Alma Mater Studiorum – Università di Bologna

DOTTORATO DI RICERCA IN

Ingegneria Biomedica, Elettrica e dei Sistemi

Ciclo 35

Settore Concorsuale: 09/E2 “Ingegneria dell’Energia Elettrica”

Settore Scientifico Disciplinare: ING-IND/33 “Sistemi Elettrici per l’Energia”

MODELS FOR RELIABILITY ESTIMATION OF HVDC CABLE SYSTEMS

Presentata da: Bassel Diban

Coordinatore Dottorato — Prof. Michele Monaci

Supervisore — Prof. Giovanni Mazzanti

Esame finale anno 2023

Acknowledgement:

To my beloved family which has always supported me…

To my home Syria which will be in the heart forever…

I would like to express my special thanks of gratitude to my supervisor Prof. Giovanni Mazzanti who helped me a lot to during the research activities.

I would like to appreciate Prof. Jérôme Castellon and Dr. Ludovic Boyer for the valuable collaboration and support.

Abstract:

The work carried out in this thesis aims at:

- studying – in both simulative and experimental methods – the effect of electrical transients (i.e., Voltage Polarity Reversals VPRs, Temporary OverVoltages TOVs, and Super imposed Switching Impulses SSIs) on the aging phenomena in HVDC extruded cable insulations. Dielectric spectroscopy, conductivity measurements, Fourier Transform Infra-Red FTIR spectroscopy, and space charge measurements show variation in the insulating properties of the aged Cross-Linked Polyethylene XLPE specimens compared to non-aged ones. Scission in XLPE bonds and formation of aging chemical bonds is also noticed in aged insulations due to possible oxidation reactions. The aged materials show more ability to accumulate space charges compared to non-aged ones. An increase in both DC electrical conductivity and imaginary permittivity has been also noticed.
- The development of life-based geometric design of HVDC cables in a detailed parametric analysis of all parameters that affect the design. Furthermore, the effect of both electrical and thermal transients on the design is also investigated.
- The intrinsic thermal instability in HVDC cables and the effect of insulation characteristics on the thermal stability using a temperature and field iterative loop (using numerical methods – Finite Difference Method FDM). The dielectric loss coefficient is also calculated for DC cables and found to be less than that in AC cables. This emphasizes that the intrinsic thermal instability is critical in HVDC cables.
- Fitting electrical conductivity models to the experimental measurements using both models found in the literature and modified models to find the best fit by considering the synergistic effect between field and temperature coefficients of electrical conductivity.

Table of Contents:

Abstract…… 4

Table of Contents……. 5

Acronyms……. 8

Chapter 1: Life estimation in HVDC cables…… 9

1.1 Thermal calculations of HVDC cables…….. 10

1.1.1 Typical structure of HVDC cables…….. 10

1.1.2 Temperature profile inside the cable layers and its environment…… 11

1.1.3 Transient temperature calculations…….. 14

1.2 Electric field calculations in HVDC cable insulation…… 17

1.2.1 Transient electric field calculations using numerical methods…… 17

1.2.2 Approximated electric field calculations using analytical methods……. 19

1.3 Model for life estimation of HVDC cables……. 20

1.3.1 Thermal life model…… 20

1.3.2 Electrical life model…….. 21

1.3.3 Electrothermal life model……. 22

1.3.4 Aging and Degradation …… 24

Chapter 2: The effect of electrical transients on HVDC cable insulation…… 27

2.1 Theoretical Introduction……. 28

2.1.1 Converters topologies…… 28

2.1.2 Voltage Polarity Reversals (VPRs)…… 30

2.1.3 Temporary Overvoltages (TOVs)…… 30

2.1.4 Superimposed Switching Impulses (SSIs)……. 32

2.2 Experimental effect of TOVs and SSIs on HVDC insulation……. 33

2.2.1 Experimental procedure……. 33

2.2.2 Specimens…….. 36

2.2.3 Characterization setup…… 38

2.2.3.1 Dielectric analyzer…….. 38

2.2.3.2 DC Conductivity measurements……. 39

2.2.3.3 Fourier Transform InfraRed spectroscopy FTIR……..... 40

2.2.3.4 Space charge measurements…… 40

2.2.4 Results…… 41

2.2.4.1 Dielectric analyzer…….. 41

2.2.4.2 DC Conductivity measurements…… 44
2.2.4.3 Fourier Transform InfraRed spectroscopy FTIR…… 44
2.2.4.4 Space charge measurements…… 48
2.2.5 Discussion …… 54
2.3 Simulative study on the effect of VPRs on the life and reliability of cable…… 56
2.3.1 VPRs…….. 54
2.3.2 Theoretical…….. 57
2.3.2.1 Transient field calculation……... 57
2.3.2.2 Life estimation…… 57
2.3.3 Case study……... 59
2.3.4 Results…… 61
2.3.4.1 Electric field distribution before, during and after VPRs…… 61
2.3.4.2 Loss of life before, during and after VPRs…… 63
2.3.4.3 Total estimated life of cable…… 65
2.3.5 Discussion…… 66
Chapter 3: Life-based design of HVDC cables…… 67
3.1 Introduction…… 68
3.2 Case study…….. 68
3.2.1 Parametric analysis…….. 68
3.2.2 Electrical transients…….. 71
3.2.3 Thermal transients…… 74
3.2.4 Life model…… 76
3.3 Results…… 78
3.3.1 Parametric analysis …….. 78
3.3.1.1 Effect of electric field and insulation thickness…… 78
3.3.1.2 Effect of conductor temperature and Temperature drop…… 80
3.3.1.3 Effect of temperature coefficient of electrical conductivity *a*…… 82
3.3.1.4 Effect of Field coefficient of electrical conductivity *b*…….. 85
3.3.1.5 Effect of soil thermal resistivity…… 87
3.3.1.6 Effect of the rated Voltage…… 87
3.3.2 Electrical transients…….. 88
3.3.3 Thermal transients…… 90
3.3.4 Electro-thermal transients …… 92
3.4 Discussion…….. 93

Chapter 4: Thermal stability in HVDC cables…… 95
4.1 Introduction…… 96
4.2 Coupled temperature and electric field calculations…….. 97
4.2.1 Calculation of insulation losses…….. 98
4.2.2 Calculation of dielectric loss coefficient…… 101
4.2.3 Calculation of the de-rating factor……. 102
4.2.4 Thermal stability conditions…….. 102
4.3 Case study……. 104
4.3.1 Characteristics of the HVDC cable…… 104
4.3.2 Temperature profile calculations……... 105
4.3.3 Insulation characteristics……106
4.4 Results……...107
4.4.1 Electric field distribution……107
4.4.2 Insulation losses……. 110
4.4.3 Temperature rise……111
4.4.4 Dielectric loss coefficient β_d……..114
4.4.5 Thermal stability diagram…….....116
4.4.6 Effect of insulation characteristics……..118
4.4.7 De-rating factor……..119
4.5 Discussion……. 120
Chapter 5: Models for electrical conductivity…….. 121
5.1 Introduction……...122
5.2 Theoretical…….....122
5.3 Application……....123
5.3.1 leakage current measurements and conductivity calculation……. 123
5.3.2 Macroscopic conductivity models……..125
5.3.3 Fitting models to experimental data……127
5.4 Results……...127
5.5 Discussion……. 136
Conclusions…….. 139
Future perspectives…….. 140
List of publications……141
References…… 144

Acronyms:

ALTs	Accelerated Life Tests
ATR	Attenuated Total Reflectance
EHVDC	Extra High-Voltage Direct Current
FTIR	Fourier Transform InfraRed spectroscopy
HV	High Voltage
HVAC	High-Voltage Alternating Current
HVDC	High-Voltage Direct Current
IEC	International Electrotechnical Commission
IPM	Inverse Power Model
IR	Infra-Red
LCC	Line Commutated Converters
LDPE	Low Density Polyethylene
LV	Low Voltage
MV	Medium Voltage
PD	Partial Discharge
PE	Polyethylene
PEA	Pulsed Electro-Acoustic
PQT	Pre-Qualification Test
RBC	Rigid Bipolar Configuration
SC	Space Charge
SSI	Superimposed Switching Impulses
TOV	Temporary Overvoltage
TT	Type Test
VEC	Voltage Endurance Coefficient
VPR	Voltage Polarity Reversal
VSC	Voltage Source Converters
XLPE	Cross-linked Polyethylene

Chapter 1

Life estimation in HVDC cables

1.1 Thermal calculations of HVDC cables:

1.1.1 Typical structure of HVDC cables:

The structure of a typical HVDC High-Voltage Direct Current HVDC extruded cable is similar to that of High-Voltage Alternating Current HVAC extruded cable, as illustrated in Figure 1.1. In Figure 1.1 (a), the cable consists of a conductor which is formed in a compact arrangement of thin round wires (either aluminum or copper) surrounded by the conductor screen then the extruded insulating material then the insulation screen, wire screen and finally the outer Polyethylene PE sheath [1]. A thin semiconductive layer (mainly made of the carbon black polymers) is extruded between the conductor and the insulation, as well as between the insulation and the metal screen. The semiconductive layers play a key role in the electric field reduction in conductor-insulation contact area.

The HVDC cable insulation is extruded around the conductor together with the inner and outer semiconductive layers thanks to the triple extrusion technique. The cable is subjected to a cross-linking process at high temperature (200÷350) °C to achieve the crosslinking of the Low Density Polyethylene LDPE and convert it to cross-linked polyethylene XLPE in the presence of a cross-linking agent. The cable is then subjected to degassing process under relatively high temperatures (i.e., ≈80 °C [2]) to remove the volatile gases which have been formed during the cross-linking process such as methane, cumyl-alcohol, and acetophenone. Followed by adding other layers on the outer semiconductive layer including water blocking tapes, wire screen, metallic laminates and plastic sheath. Other protective layers are added to submarine cables i.e., armor wires, synthetic yarns bedding to enhance the mechanical strength of the cable against possible external actions [2].

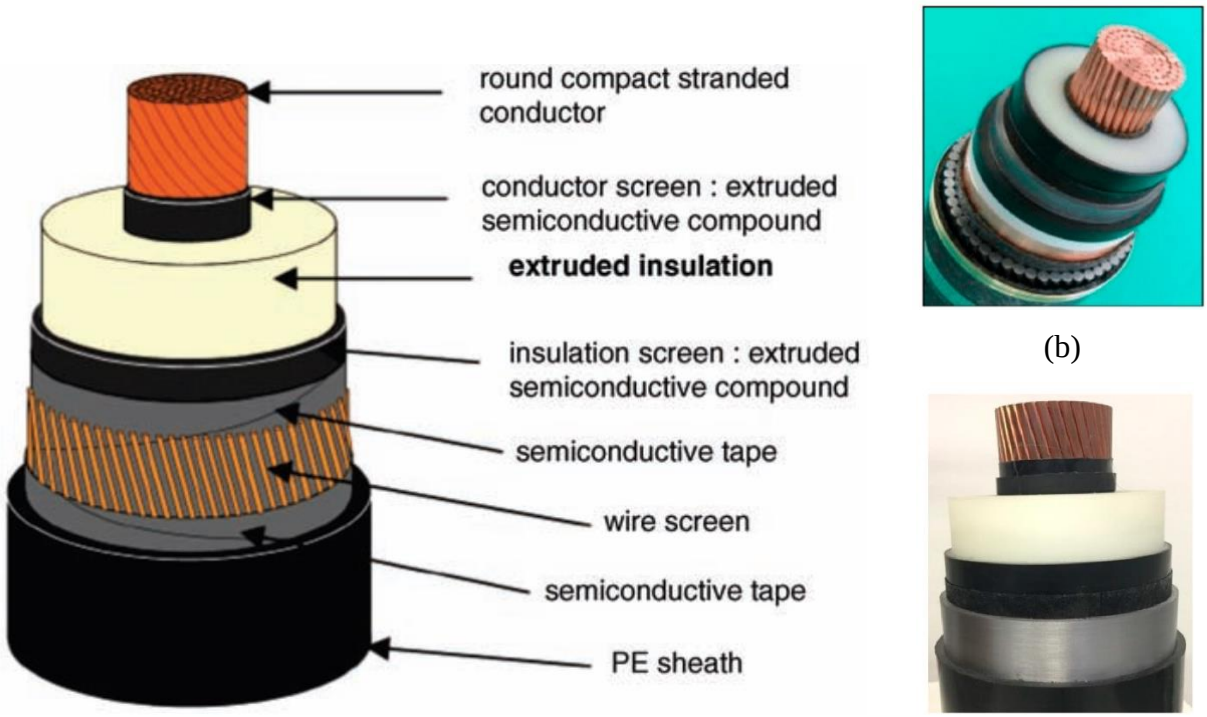

Figure 1.1 (a) Structure of a typical unipolar HVDC extruded cable, (b) XLPE-insulated HVDC subsea cable (courtesy Sumitomo Electric), (c) HPTE-insulated HVDC land cable (courtesy Prysmian). [2],[3]

1.1.2 Temperature profile inside the cable layers and its environment:

Dissimilar to Medium Voltage MV and Low Voltage LV cables, High Voltage HV cables are heavy and cannot be aerial. Thus, they are typically buried either directly under the ground or in special tunnels. Temperature calculations are prescribed by the International Electrotechnical Commission standards IEC 60287 [4], whereby the temperature drop between the conductor temperature and the ambient temperature is given by the following equation:

$$\Delta\vartheta_{tot} = \Delta\vartheta_d + \Delta\vartheta_{sh} + \Delta\vartheta_{so} \tag{1.1}$$

where: $\Delta\vartheta_d\ [°C]$ is the temperature drop inside the insulation, $\Delta\vartheta_{sh}$ is the temperature drop in the thermoplastic sheath, and $\Delta\vartheta_{so}$ is the temperature drop in the soil. $\Delta\vartheta$ can be given by the thermal Ohm's law:

$$\Delta\vartheta = R_T W \tag{1.2}$$

where $\Delta\vartheta$ $[°C]$ is the temperature drop in the considered layer, R_T $[°C\ m/W]$ is the thermal resistance of the considered layer. W [W/m] is the thermal power per unit length that crosses the considered layer. Equation (1) can be also written in the form according to [4]:

$$\begin{aligned}\Delta\vartheta_{tot} &= W_c\left(R_{T,d} + R_{T,sh} + R_{T,so}\right) + W_d\left(\beta_d R_{T,d} + R_{T,sh} + R_{T,so}\right) \\ &= \Delta\vartheta_{cl} + \Delta\vartheta_{dl}\end{aligned} \tag{1.3}$$

where: $\Delta\vartheta_{cl}$ is the temperature drop in the entire cable and soil due only to conductor losses W_c, $\Delta\vartheta_{dl}$ is the temperature drop in the entire cable and soil due only to insulation losses. $R_{T,d}, R_{T,sh}, R_{T,so}$ are the thermal resistances of the insulation, sheath, and soil, respectively. It can be clearly noticed that the thermal Ohm's law cannot be directly applied in the temperature drop calculations due to insulation losses whereby only a certain part of the heat generated inside the insulation contributes in the temperature drop, on the other hand, the other part heats up the entire insulation cross section. The latter phenomena introduces the so-called dielectric loss coefficient β_d that represents only the part of the insulation losses which contributes in the temperature drop over the insulation thickness.
The thermal resistance of the insulation or sheath can be derived by dividing the insulation (or the sheath) to infinitesimal layers whose thermal resistance per unit length of the cable can be written as follows:

$$dR_T = \rho_t \frac{dx}{2\pi x} \tag{1.4}$$

where ρ_t is the thermal resistivity of the material. Then the thermal resistance R_T can be found by integrating dR_T between the inner radius and the outer radius of the insulation (or sheath) i.e., r_i and r_o, respectively, as follows:

$$R_T = \int_{r_i}^{r_o} \rho_T \frac{dx}{2\pi x} = \frac{\rho_T}{2\pi} ln\left(\frac{r_o}{r_i}\right) \tag{1.5}$$

While the thermal resistance of the soil per unit length of the cable can be calculated according to IEC 60287 [4] using either the old version as in equation (1.6) or the new version as in equation (1.7):

$$R_{T,so} = \frac{\rho_{T,so}}{2\pi}\left\{ln\left(\frac{2b - r_{o,c}}{r_{o,c}}\right) + ln\left[1 + \left(\frac{2b}{a}\right)^2\right]\right\} \tag{1.6}$$

$$R_{T,so} = \frac{\rho_{T,so}}{2\pi}\left\{ln\left(uu + \sqrt{uu^2 - 1}\right)\right\} \tag{1.7}$$

where $r_{o,c}$ [m] is the outer radius of the cable, a [m] is the distance between cables (in case of more than one), b [m] is the burial depth, $uu = b/r_{o,c}$, $\rho_{T,so}$ is the soil thermal resistivity.
The power generated by the conductor can be calculated using the following expression:

$$W_c = R_{cc} I_c^2 \tag{1.8}$$

where I_c is the conductor's current [A], R_{cc} is the DC electrical resistance of the conductor operating at the temperature ϑ_c, which is calculated as follows:

$$R_{cc} = R_{cc,20}[1 + \alpha_{20}(\vartheta_c - 20)] \tag{1.9}$$

where α_{20} is the temperature coefficient of the electrical resistivity of the conductor at 20 °C, $R_{cc,20} = \rho_{el,20°C}/S_{eff}$ is the electrical resistance of the conductor per unit length of the cable at 20 °C, S_{eff} is the cross sectional area of the conductor, $\rho_{el,20°C}$ is the electrical resistivity of the conductor material at 20 °C.
By substituting equations (1.8), (1.9) in (1.3), the conductor temperature can be calculated using the following equation:

$$\vartheta_c = \frac{\left[R_{T,d} + \left(R_{T,sh} + R_{T,so}\right)\right]\xi I^2 + \vartheta_{ambient}}{1 - \left[R_{T,d} + \left(R_{T,sh} + R_{T,so}\right)\right]\eta I^2} \tag{1.10}$$

where $\vartheta_{ambient}$ is the ambient temperature, $\xi = R_{cc,20}(1 - \alpha_{20}20)$, $\eta = R_{cc,20}\alpha_{20}$.

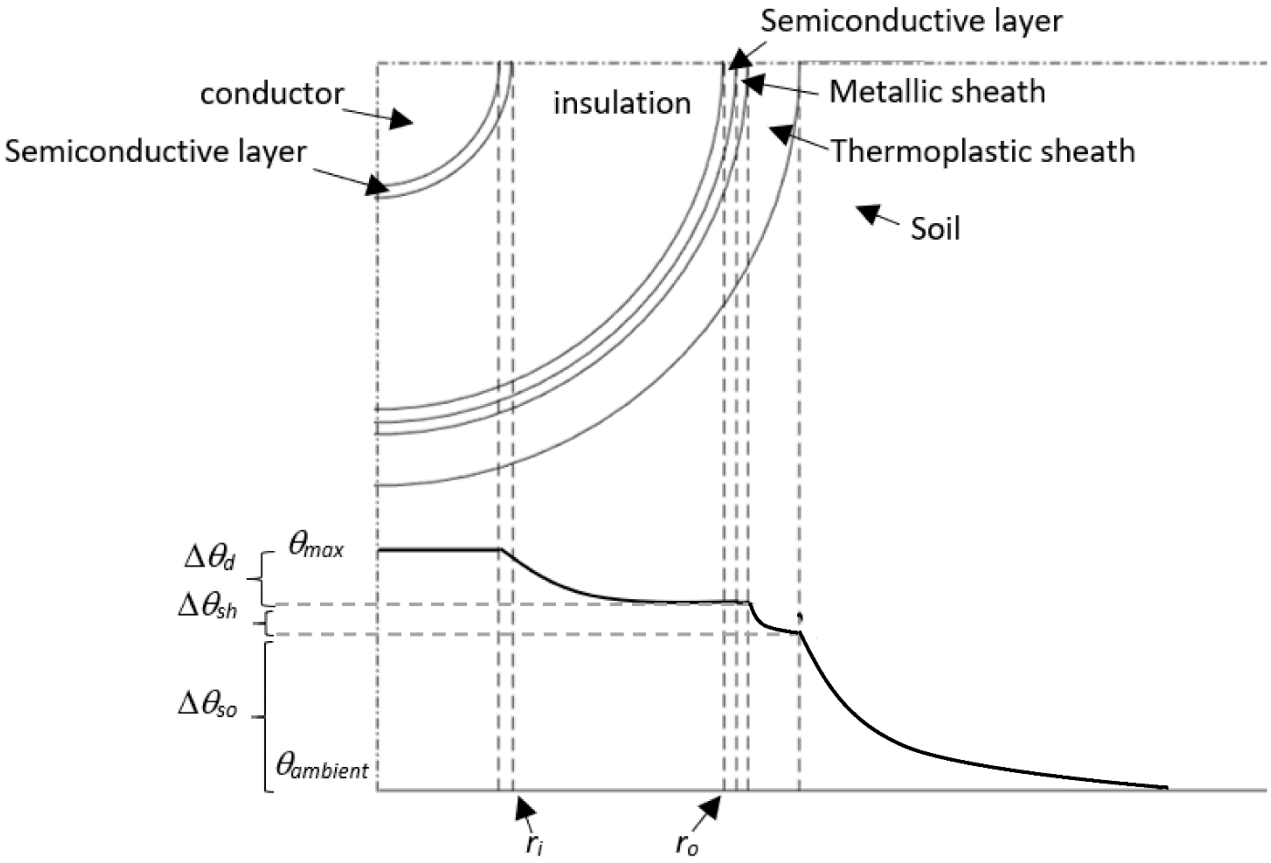

Figure 1.2 cross-sectional structure of the XLPE high voltage direct-current (HVDC) cables, with the temperature drops in the insulation, sheath and soil.

1.1.3 Transient temperature calculations:

According to IEC standards 60853-2 [5], the cable cross-sectional layers are represented by a circuit with lumped resistances and capacitances. Van Wormer's technique is used to represent the cable insulation by the equivalent thermal resistance T_1 and the equivalent thermal capacitance Q_i, as shown in Figures 1.3 and 1.4:

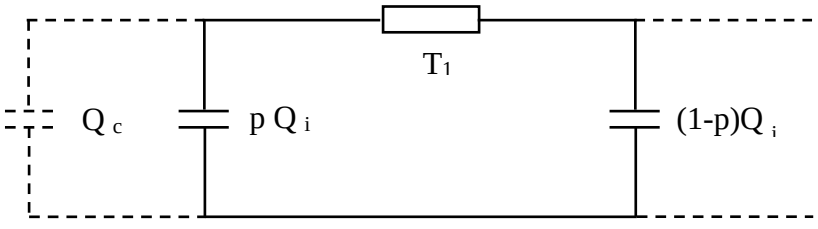

Figure 1.3 the thermal circuit representing the cable insulation.

$$p = \frac{1}{2\ln\left(\frac{D_i}{d_c}\right)} - \frac{1}{\left(\frac{D_i}{d_c}\right)^2 - 1} \qquad (1.11)$$

Where T_1 is the total thermal resistance of insulation. Q_i total thermal capacitance of insulation (or equivalent conductor in multi-core cable). Q_c is the thermal capacitance of the conductor. D_i is the outer diameter of insulation. d_c is the outer diameter of the conductor.

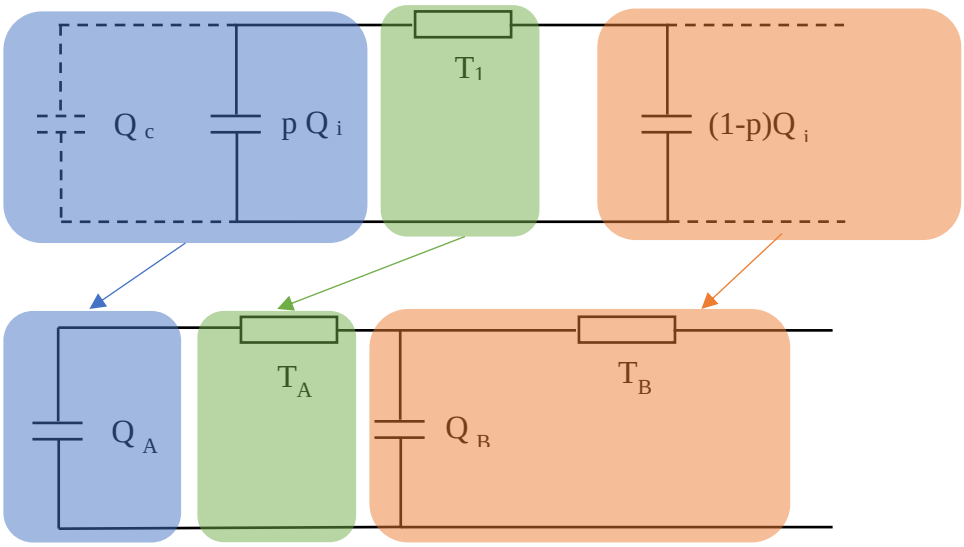

Figure 1.4 the thermal circuit representing the cable insulation with the thermoplastic sheath.

$$T_A = T_1 \tag{1.12}$$

$$T_B = q_s T_3 \tag{1.13}$$

$$Q_A = Q_c + pQ_i \tag{1.14}$$

$$Q_B = (1-p)Q_i + \frac{Q_s + p'Q_j}{q_s} \tag{1.15}$$

where T_3 is the thermal resistance of the outer thermoplastic sheath, Q_s is the thermal capacity of the electric screen, Q_j is the thermal capacity of the outer sheath, q_s = losses in conductor and sheath/losses in conductor. $p' = \frac{1}{2\log\left(\frac{D_e}{D_s}\right)} - \frac{1}{\left(\frac{D_e}{D_s}\right)^2 - 1}$, D_e *and* D_s are the outer and the inner diameters of the sheath.

The transient response $\vartheta_c(t)$ of the cable circuit to a current step can be calculated as follows:

$$M_0 = \frac{1}{2}(Q_A(T_A + T_B) + Q_B T_B) \tag{1.16}$$

$$N_0 = Q_A T_A Q_B T_B \tag{1.17}$$

$$a = \frac{M_0 + \sqrt{{M_0}^2 + N_0}}{N_0} \tag{1.18}$$

$$b = \frac{M_0 - \sqrt{{M_0}^2 - N_0}}{N_0} \tag{1.19}$$

$$T_a = \frac{1}{a-b}\left[\frac{1}{Q_A} - b(T_A + T_B)\right] \tag{1.20}$$

$$T_b = T_A + T_B - T_a \tag{1.21}$$

$$\vartheta_c(t) = \Delta W_c[\, T_a(1 - e^{-at}) + \, T_b(1 - e^{-bt})] \tag{1.22}$$

where ΔW_c is the power loss per unit length of the conductor associated with the current step, referred to the maximum temperature.

While the transient response of the cable environment to a current step is calculated according to [5] as an exponential integral expression, as follows:

$$\vartheta_e(t) = \alpha(t)\frac{\rho_{T,so}\Delta W_1}{4\pi}\left\{\left[-E_i\left(-\frac{D_e^2}{16t\delta}\right) + E_i\left(-\frac{L^2}{t\delta}\right)\right] + \sum_{k=1}^{k=N-1}\left[-E_i\left(-\frac{d_{p,k}^2}{4t\delta}\right) + E_i\left(-\frac{{d'}_{p,k}^2}{4t\delta}\right)\right]\right\} \tag{1.23}$$

where ΔW_1 is the total power loss per unit length of the cable associated with the current step, referred to the maximum temperature, $E_i(-x)$ is the exponential integral function, $\alpha(t)$ is the conductor to cable surface attainment factor, D_e is the external surface diameter of the cable, δ is the soil thermal diffusivity, t is the time from the moment of application of heating, L is the axial burial depth, $d_{p,k}$ is the distance from center of cable k to center of hottest cable p, $d'_{p,k}$ is the distance from the image of the center of the cable k to center of hottest cable p', N is the number of cables.

The temperature transient of the entire system i.e., considering the cable and its environment, can be calculated using the following equation:

$$\vartheta(t) = \vartheta_c(t) + \vartheta_e(t) \tag{1.24}$$

Then, the conductor's temperature $\vartheta_\alpha(t)$ can be calculated by considering the variation of the electrical resistance of the conductor material, as follows:

$$\vartheta_\alpha(t) = \frac{\vartheta(t)}{1 + \alpha_R(\vartheta(\infty) - \vartheta(t))} \tag{1.25}$$

where $\vartheta(\infty)$ is the conductor steady state temperature, α_R is the temperature coefficient of electrical resistivity of the conductor material.

1.2 Electric field calculations in HVDC cable insulation:

In AC cable systems, the electric field distribution inside the insulation thickness is related only to the cable geometry, as shown in Equation (1.26).

$$E_{AC}(r) = \frac{U_0}{r\ ln(r_o/r_i)} \tag{1.26}$$

where $E_{AC}(r)$ is the AC electric field distribution inside the insulation thickness, U_0 is the applied voltage, r is a generic radius inside the insulation thickness. r_i, r_o are the inner and outer insulation radii, respectively. This is because in extruded cable insulation – where the dielectric is macroscopically homogeneous – the electrical permittivity can be considered constant with the temperature variations and over the entire insulation thickness.

On the contrary, in DC cable systems the conductivity of charge carriers is ruled by both the temperature and the electric field distributions over the insulation thickness. The latter will lead to a non-linear behavior of the electrical conductivity dissimilar to the case of AC cable systems, as well as to an inherently transient distribution of DC electric field; indeed, DC electric field varies whenever the load current changes, thus involving a change in electrical conductivity, too.

1.2.1 Transient electric field calculations using numerical methods:

As a result of DC conductivity non-linearity, strictly-speaking DC electric field distribution inside the cable insulation can be only found using numerical methods that solve Maxwell's Equations (1.27–1.29) in addition to an equation (or a set of equations) which describe the charge carrier behavior inside the insulation either microscopically or macroscopically.

The macroscopic method is represented by the conductivity σ as a function of both the temperature T and the electric field E, as in Equation (1.30) for instance. The latter relationship is ruled by two (or more) coefficients used to describe the characteristics of the insulating material and found by fitting the conductivity measurements to a certain function of the temperature and the electric field. On the other hand, the microscopic models are described by the charge density as a function of physical parameters representing the charge carriers trapping, de-trapping, and mobility inside the insulation.

Gauss law	$\nabla \cdot (\varepsilon_0 \varepsilon_r \boldsymbol{E}) = \rho$	(1.27)
Current continuity	$\nabla \cdot \boldsymbol{J} = -\partial\rho/\partial t$	(1.28)
Ohm's law	$\boldsymbol{J} = \sigma \boldsymbol{E}$	(1.29)
Conductivity	$\sigma = \sigma_0 \, exp(aT + bE)$	(1.30)

where $\boldsymbol{E}$ is the electric field vector (V/m), $\varepsilon_0 = 8.854 \times 10^{-12}$ (F/m) is the vacuum permittivity, ε_r is the relative permittivity of the insulation, $\boldsymbol{J}$ is the direct conduction current density vector (A/m^2), ρ is the free charges density (C/m^3), σ is the electrical conductivity of the insulation (S/m), σ_0 is the value of σ at 0 °C and for an electric field equal to 0 kV/mm. As far as electrical conductivity σ is concerned, the empirical model suggested by Klein [6] has been used in this work, as given by Equation (4), where: *a* is the temperature coefficient of electrical conductivity (1/K or 1/°C), *b* is the stress coefficient of electrical conductivity (mm/kV, or m/MV). Other conductivity models will be extensively discussed in Chapter 5.

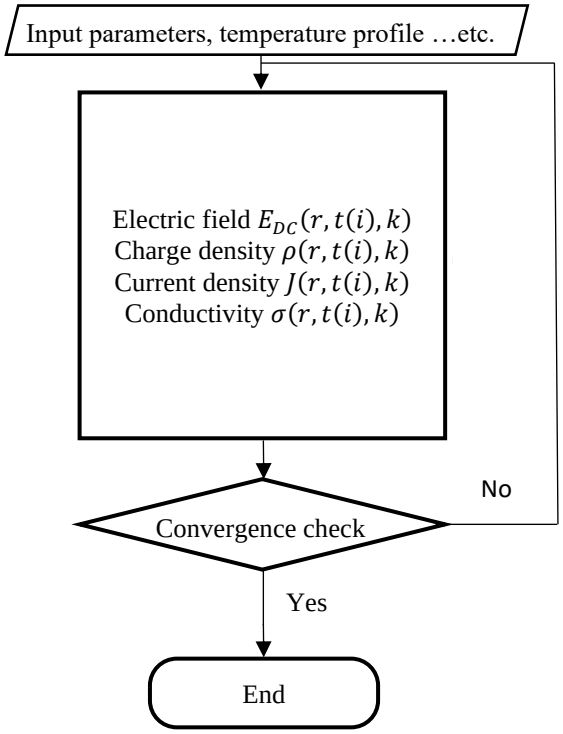

Figure 1.5 Flow chart of the procedure for iterative electric field calculation

Figure 1.5 presents the flow chart of the iterative electric field calculation using Equations (1.27–1.30) until the convergence on the electric field is reached. The field convergence is calculated using by checking the difference between the value of the electric field in the current iteration with the electric field of the last iteration, the convergence is reached when the maximum difference of the fields, at whatever generic radius r inside the insulation, is lower than or equal to a predefined error value, as follows:

$$Max\{|E(r,t,k) - E(r,t,k-1)|\} \leq \epsilon\ \% \tag{1.31}$$

where ϵ is the maximum permissible value of the field difference. Hereinafter, it is considered to be 0.1%.

1.2.2 Approximated electric field calculations using analytical methods:

The approximation first introduced by Eoll in [7] can be derived using the macroscopic conductivity Equation (1.30) (as extensively interpreted in Annex A) by introducing the approximating Equation (1.32) in Equation (1.29) yielding the Equation (1.33):

$$exp[bE(r)] \approx \left[\frac{eE(r)}{E_m}\right]^{-bE_m} \tag{1.32}$$

$$E(r) = U_0 \frac{\delta}{r_o \cdot [1 - (r_i/r_o)^{\delta}]} (r/r_o)^{\delta-1} \quad (1.33)$$

where:

$$\delta = \frac{A+B}{1+B} = \frac{\frac{aW_c}{2\pi\lambda_{T,d}} + bE_m}{1+bE_m} = \frac{\frac{aW_c}{2\pi\lambda_{T,d}} + \frac{bU_0}{r_o - r_i}}{1 + \frac{bU_0}{r_o - r_i}} = \frac{\frac{a\Delta T_d}{\ln\frac{r_o}{r_i}} + \frac{bU_0}{r_o - r_i}}{1 + \frac{bU_0}{r_o - r_i}} \quad (1.34)$$

This formula is able to estimate the electric field distribution within the insulation thickness using an analytical closed-form equation. It can be noticed in Equations (1.33) and (1.34) that the field is a function of the applied voltage, the inner and outer radii of cable insulation r_i and r_o, the temperature drop across the insulation ΔT_d, and the conductivity coefficients a and b. The absolute temperature does not contribute to the electric field distribution since only the temperature drop across the insulation appears in the formula.

1.3 Model for life estimation of HVDC cables:

Cable insulation in HV systems are subjected to many types of stresses (e.g., thermal, electrical, mechanical, and environmental … etc). The continuous stress application leads to irreversible variation in the material electrical properties until the point at which the insulation becomes unable to withstand the applied stress. For this reason, the development of life models has raised a significant attention during the last decades to estimate the remaining life (time-to-failure) of cable insulation. Life models are mainly classified as either phenomenological (macroscopic) in which a correlation between stresses is established using Accelerated Life Tests ALTs, or physical (microscopic) whereby the model is established starting from physical aging phenomena. The physical life models can be thermodynamic models [8],[9],[10], space charge SC-based models [11],[12], or partial discharge PD-based models [13],[14]. While the phenomenological life models are thermal life model, electrical life model, or electrothermal life model as follows:

1.3.1 Thermal life model

In the early 1930, Montsinger showed halving of the insulation life by increasing the temperature between 8 to 10 °C [15]. Later, the thermal degradation is represented, according to Dakin [16], by

the Arrhenius life model which depends on the Arrhenius equation of the thermal reaction rate as in Equation (1.35):

$$L(T) = L_0\, exp\left[-B\left(\frac{1}{T_0} - \frac{1}{T}\right)\right] = L_0\, exp[-BT'] \tag{1.35}$$

where $L(T)$ is the estimated life of cable at the temperature T, L_0 is the estimated life of cable at the absolute reference temperature T_0, $B = \Delta W / K_B$, ΔW is the activation energy of the main thermal degradation reaction, $K_B = 1.38 \times 10^{-23}\, J/K$ is the Boltzmann constant. Life according to this model is plotted in the so-called Arrhenius plot which has *ln*(*L*) as y-axis and -1/T as x-axis. Equation (1.35) appears in Arrhenius plot as a line with a slope of $-B$. The model's parameters can be found using tests performed in ovens in the absence of electrical stresses.

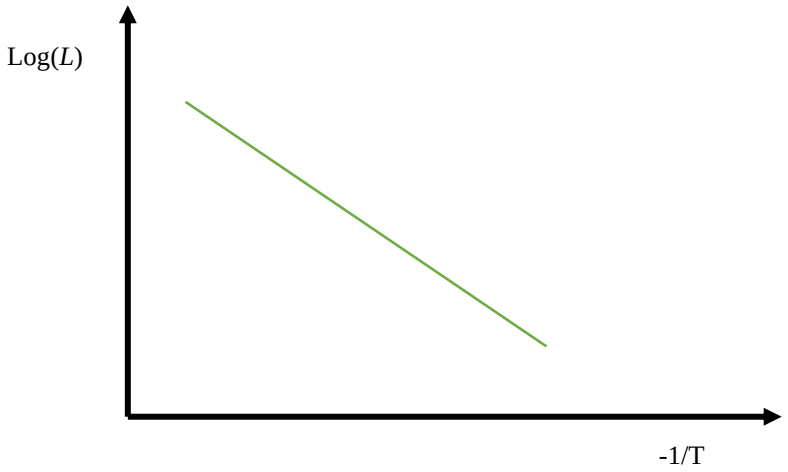

Figure 1.6 Arrhenius plot.

1.3.2 Electrical life model:

The most used electrical life model is the Inverse Power Model (IPM) which relates the life with the electric field in an inverse power function, as follows:

$$L(E) = L_0\left(\frac{E}{E_0}\right)^{-n_0} \tag{1.36}$$

where $L(E)$ is the life corresponding to the electric field E, L_0 is the life at the reference electric field E_0 (usually taken as the field bellow which the electrical aging is deemed negligible), n_0 is the voltage endurance coefficient (VEC). Note that L_0 and n_0 are relevant to a reference temperature T_0, which – in the absence of thermal stress – is the ambient temperature.

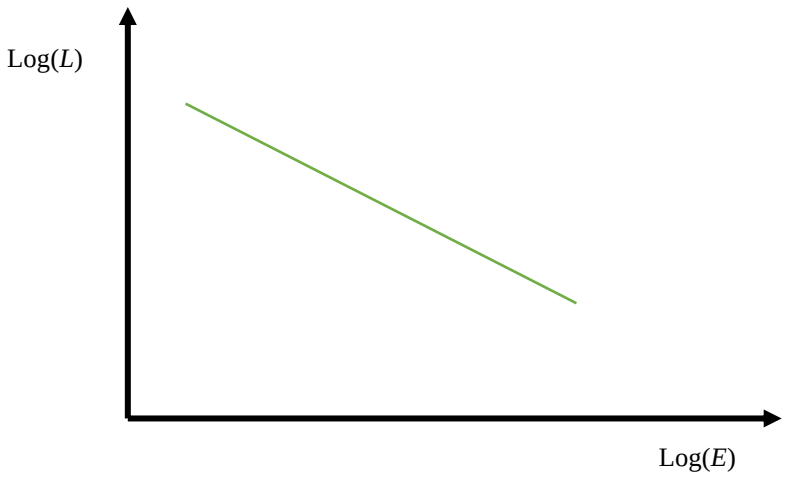

Figure 1.7 Inverse Power Model plot in log-log scale.

This model is valid only in the absence of thermal stress – or under a constant temperature - therefore, the model's parameters can be found only at a constant temperature. If this constant temperature is different from the ambient temperature, L_0 and n_0 have to be calculated considering the real temperature of the insulation, which depends on the applied thermal stress.

1.3.3 Electrothermal life model:

The electrothermal life model is a combination of the electrical and the thermal models yielding the so-called Arrhenius-IPM model. The development of this model is based on the electrical model since the electrical stress has the major effect on the cable life in HV and MV cables. Then the effect of temperature is taken into account, in addition to the synergism between the field and temperature b_{ET}, as follows:

$$L(E,T) = L_0 \left(\frac{E}{E_0}\right)^{-(n_0 - b_{ET}T')} exp[-BT'] \tag{1.37}$$

It is noteworthy to mention that $b_{ET} = 0$ represents the worst case and it is considered in this study as a conservative value.

Due to the stochastic behavior of the breakdown process, the life of cable insulation is a random variable at a given failure probability. Weibull distribution function is the best one to be used for polymeric insulations [17],[18]:

$$P(t_F,E,T) = 1 - R(t_F,E,T) = 1 - exp\left(-\left[\frac{t_F}{\alpha_t(E,T)}\right]^{\beta_t}\right) \tag{1.38}$$

where R is the reliability which is the complement to one of the probability of failure P, t_F is the P-th percentile of the electrothermal life (time-to-failure), α_t is the scale parameter of Weibull probability distribution of the life and corresponds to the 63.2-th percentile of the life, β_t is the shape parameter of Weibull probability distribution of the life.
By manipulating Equation (1.38), one can write the time-to-failure in the form:

$$t_F = [-\ln(1-P)]^{1/\beta_t}\alpha_t(E,T) \tag{1.39}$$

By substituting $\alpha_t(E,T)$ in Equation (1.39) with $L(E,T)$ in Equation (1.37), one gets:

$$t_F = [-\ln(1-P)]^{1/\beta_t}\alpha_0\left(\frac{E}{E_0}\right)^{-(n_0 - b_{ET}T')} exp[-BT'] \tag{1.40}$$

where: α_0 is the 63.2-th percentile of failure probability. The parameters in Equation (1.40) can be found by performing ALTs tests on specimens and then can be extrapolated to consider full-scale cable using the dimensional factor D:

$$L_D = L_T\left[\frac{1}{D}\cdot\frac{ln(1-P_D)}{ln(1-P_T)}\right]^{\frac{1}{\beta_t}} \tag{1.41}$$

$$D \approx \frac{l_D}{l_T}\left(\frac{r_D}{r_T}\right)^2 \tag{1.42}$$

where P_D is the failure probability for the full-scale cable, P_T is the failure probability for the specimens in the test, l_D and r_D is the length of the power cable and the radius of its conductor, respectively, l_T and r_T is the length of the specimen and the radius of its conductor, respectively.
Since L_0 (at the reference electric field E_0 and the reference ambient temperature T_0) is not easy to be found, it becomes more practical to express the life of cable with reference to the design life L_D (at the design electric field E_D and the design temperature T_D) which corresponds to a reference failure probability P_D, as follows (the complete derivation of Equation (1.43) can be found in Annex B):

$$L(E,T) = L_D\left(\frac{E}{E_D}\right)^{-[n_D - b_{ET}T'']}\left(\frac{E_D}{E_0}\right)^{b_{ET}T''} exp[-BT''] \tag{1.43}$$

where $T'' = \frac{1}{T_D} - \frac{1}{T}$, $n_D = n_0 - b\left(\frac{1}{T_0} - \frac{1}{T_D}\right)$ is the voltage endurance coefficient at the design temperature, E_D is the design electric field, E_0 is the reference electric field (see above).

It is also possible to estimate the life $L_F\ (E, T)$ at a failure probability *F* different from the design one P_D using the following equation:

$$L_F\ (E,T) = \left[\frac{-ln\ (1-F)}{-ln\ (1-\ P_D)}\right]^{1/\beta_t} L_D \left(\frac{E}{E_D}\right)^{-[n_D - b_{ET}T'']} \left(\frac{E_D}{E_0}\right)^{b_{ET}T''} exp[-BT''] \quad (1.44)$$

1.3.4 Aging and Degradation:

Aging is physically defined in [19] as the generation of free volume in the lattice; while it can be chemically defined by the formation of free radicals (or ions) in the insulation. Dissimilar to gaseous and liquid insulations, aging processes in solid dielectrics – including extruded polymers – are irreversible, whereby a scission in C–H or C–C bonds caused by electric stress, or the oxidation process of C-H bonds caused by thermal stress can take place, allowing the permanent formation of polar molecules.

Aging and degradation in insulating materials can be distinguished according to [20] using the hazard rate function:

$$h(t) = \beta . {\alpha_t}^{-\beta} . t_F^{\beta-1} \quad (1.45)$$

For values of β<1, failures occur early on; this is often referred to as "infant mortality". For β=1, failures occur randomly and spontaneously, the distribution function tends to an exponential decay, and the hazard function is constant. In this case a specimen that has been stressed for some time would be indistinguishable in terms of breakdown probability from one that has not been stressed at all. When β>1 failure becomes more likely as the specimen ages. Although there are no widely accepted definitions to distinguish ageing and degradation, degradation processes generally cause the failure rate to increase monotonically (β>2), whereas ageing may simply result in an increase in the probability of failure (2≥β>1). It may be acceptable for a commercial system to age within the design life of the product as the failure rate may still be controlled and low. Degradation, however, may cause the failure rates to increase uncontrollably [20].

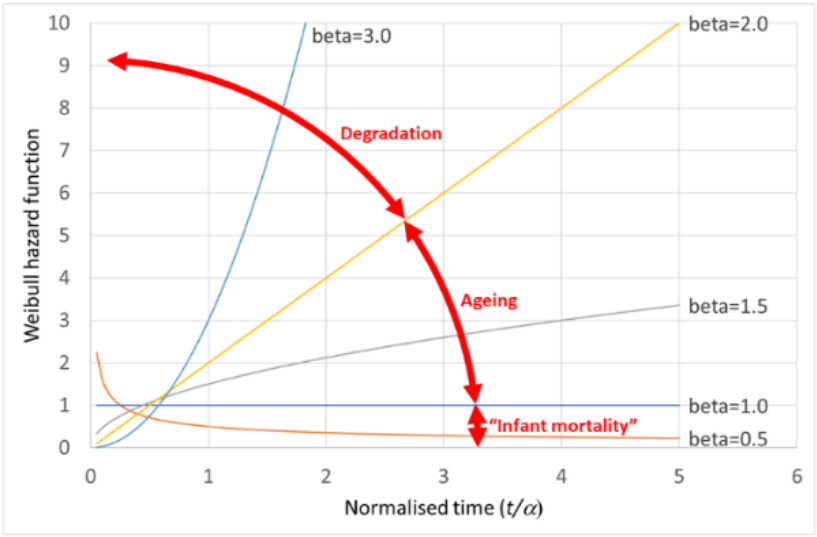

Fig. 1.8 Weibull hazard function curves vs. time to failure (normalized w.r.t. α) with conjectured ageing and degradation conditions

By following Miner's law [21], the stressing period can be divided into infinitesimal time intervals Δt_i during which both stresses can be considered constant. Then the loss of life of the cable insulation, subjected to *M* load cycles to failure, can be calculated as follows:

$$dLF = dLF(E_i(t), T_i(t)) = \frac{dt}{L[E_i(t), T_i(t)]} \tag{1.46}$$

$$\int_0^{\mathrm{L}} dLF \approx M \sum_{i=0}^{N} LF_i = 1 \tag{1.47}$$

$$LF_i = \int_0^{\Delta ti} \frac{dt}{L[E_i, T_i]} = \frac{\Delta t_i}{L[E_i, T_i]} = \frac{t_D}{L[E_i, T_i]N} \tag{1.48}$$

where the theoretically infinite number of infinitesimal time intervals *dt* making up each load cycle of duration t_d is approximated via a finite number *N* of finite subperiods Δt_i, and *L* is the life of cable.

In this way, life *L* can also be expressed as the number *M* of identical load cycles to failure, as follows:

$$M = \left(\sum_{i=0}^{N} LF_i \right)^{-1} \tag{1.49}$$

Since the thermal and electrical stresses are not constant within the insulation thickness, the total life of cable is evaluated at the point inside the insulation which has the shortest life. It is worth noting that the load cycles temperature and electric field must be identical such that (1.49) can be applied.

Chapter 2

The effect of electrical transients on HVDC cable insulation

2.1 Theoretical Introduction:

2.1.1 Converters topologies:

The converters used in HVDC cable systems fall in two categories (see Figure 2.1):

- Line Commutated Converters LCC: (or Current Source Converters CSC): these converters are based on thyristors whereby the voltage is partially controlled (it can be controllably switched on, but uncontrollably switched off) and the current is unidirectional, therefore, it can be considered a current source in the AC power system. Consequently, reversing the power flow direction can be achieved by reversing the DC voltage polarity.
- Voltage Source Converters VSC: thyristors are replaced by Insulated Gate Bipolar Transistor (IGBT) in this type of converters. This provides full controllability in switching on and off the voltage which is considered constant (using a large smoothing capacitance). In this case, reversing the power flow can be achieved by reversing the direction of current at a constant DC voltage. The main advantage of VSC HVDC systems compared to that of LCC is that in VSC systems both active and reactive powers are fully controllable independently of DC voltage level. Furthermore, self-commutated VSC allows black start since it can synthesize a balanced set of 3-phase voltages as a virtual synchronous generator able to control the reactive power on the AC side, dissimilar to the LCC which always requires reactive power from the AC grid. Another important advantage of the VSCs is the possibility of reversing the power flow by reversing the current direction without the need to reverse the voltage polarity as required in LCCs (see Figure 2.2). This is a very critical point in extruded HVDC cable insulations which is greatly affected by Voltage Polarity Reversal (VPR) events.

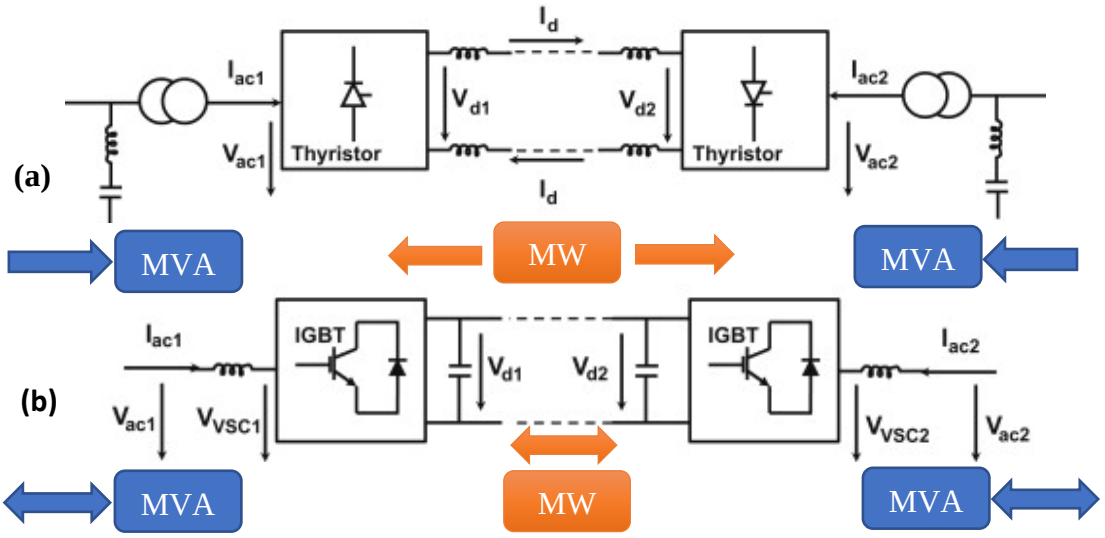

Figure 2.1 schematic of (a) LCC (b) VSC HVDC transmission systems.

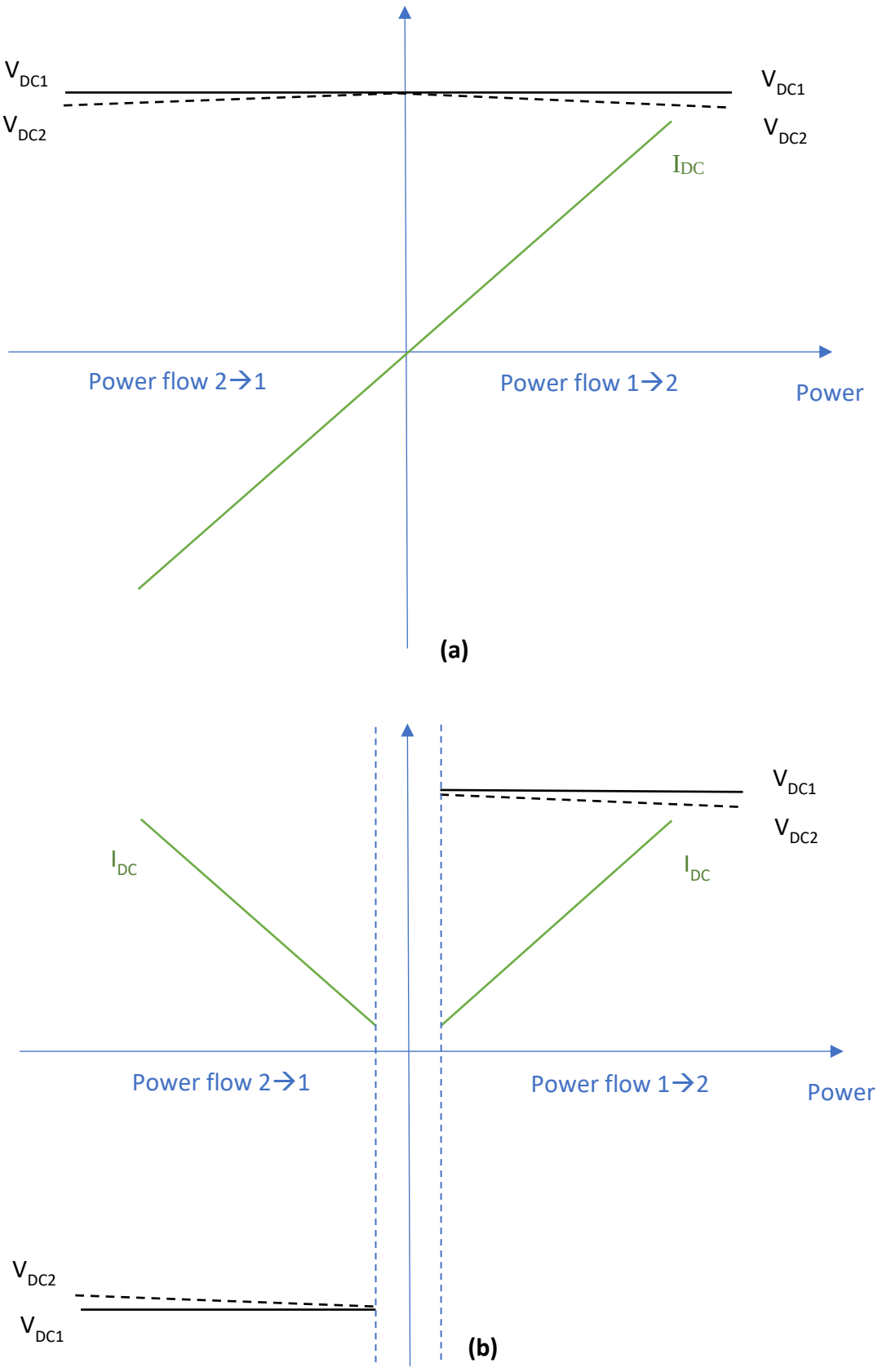

Figure 2.2 DC voltage and current controllability for (a) VSC and (b) LCC HVDC transmission systems to achieve power flow reversal.

2.1.2 Voltage Polarity Reversals (VPRs):

Voltage Polarity Reversals are used to reverse the power flow direction only in LCC cable systems. They are classified into two main categories:

- **fast VPRs:** the voltage polarity is reversed within hundreds of milliseconds, as shown in Figure 2.3a, as a fast response to contingencies in the electrical grid including either keeping the frequency within its operational limits (in the case of two unsynchronized grids) or keeping the power flow within its operational limits (in the case of one synchronized grid). This type of VPRs is not frequent in HVDC systems, as luckily also contingencies are not frequent as well. Its abrupt electrical transient may cause failure especially in extruded HVDC cable insulations [22]: for this reason, the number of fast VPRs permitted over cable life is strictly limited according to manufacturers' prescriptions.
- **slow VPRs:** the voltage is switched off within hundreds of milliseconds followed by a charge relaxation period at zero voltage, then a voltage with a reversed polarity is applied within hundreds of milliseconds, as shown in Figure 2.3b The slow PR is more frequent than the fast one in HVDC systems as it is used to meet the market needs [22]. However, also slow PRs are setting some challenge to cable insulation, therefore also the number of slow VPRs permitted over cable life is limited according to manufacturers' prescriptions, although not so strictly as fast VPRs. Despite such limitation, TSOs are striving to increase the number of slow VPRs to follow market needs as closely as possible.

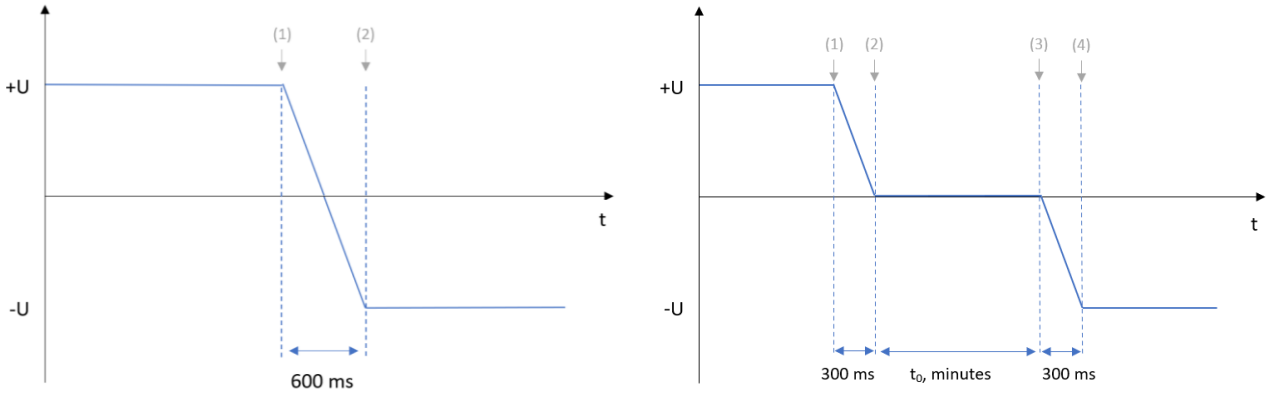

Figure 2.3 Voltage wave shape over time in (a) fast polarity reversal and (b) slow polarity reversal.

2.1.3 Temporary Overvoltages (TOVs):

Temporary Overvoltages TOVs are relatively long electrical transients that occur in VSC HVDC cable systems in both symmetric monopolar (see Figure 2.4a) and Rigid Bipolar Configuration (RBC) (see Figure 2.4b): they affect the healthy pole when the other one experiences a pole-to-ground fault.

RBC consists of a bipolar scheme without earth return or dedicated metallic return [2]. This configuration provides benefits from an economic point of view, since a return cable – found in the Bipolar Configuration with dedicated metallic return – and/or the electrode systems are avoided, which reduces the total investment costs. In addition, the RBC – in contrast to the monopolar configurations – can operate with a reduced transmission capacity in case of failure or maintenance of a converter [23]. However, the redundancy in case of pole cable failure is provided neither in the monopolar configurations nor in the RBC.

The post-fault voltage rises to reach the peak with a rise time in order of few milliseconds, then it gets limited by the surge arresters of the HVDC converter station which maintain the plateau voltage for hundreds of milliseconds until the cable is fully discharged withing few minutes (see Figure 2.5). Extensive simulations considering different fault types showed that pole-to-ground faults in the middle of the negative pole of a symmetric monopolar Voltage Source Converters VSC HVDC cable system leads to the most severe (or "worst case") TOVs on the healthy pole i.e. a voltage up to 1.8 times the pre-fault DC voltage or even higher [24].

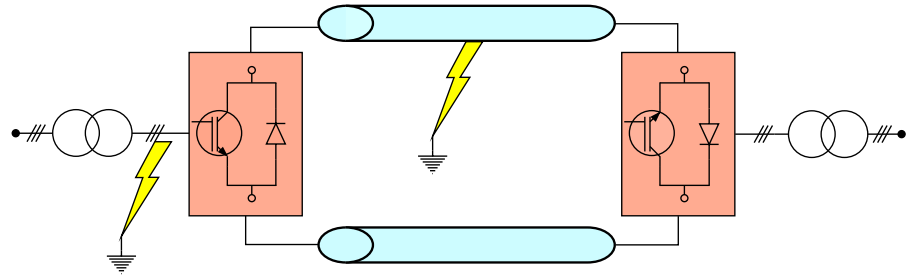

(a)

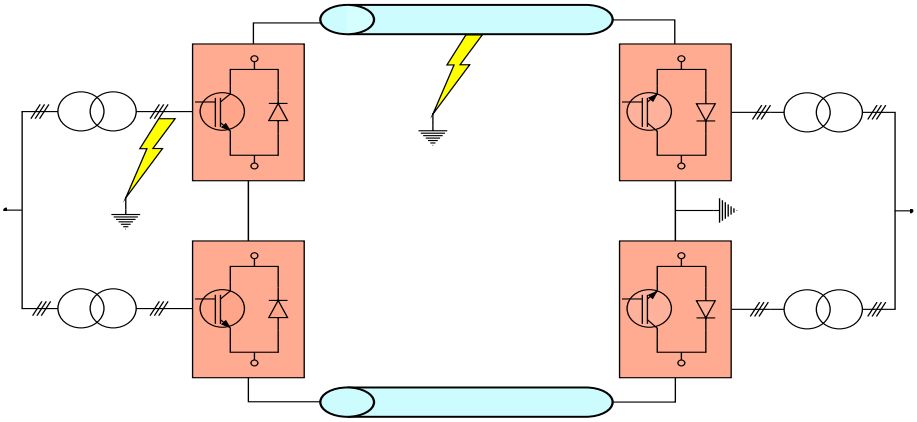

(b)

Figure 2.4 (a) symmetric monopolar and (b) Rigid bipolar configurations after [25].

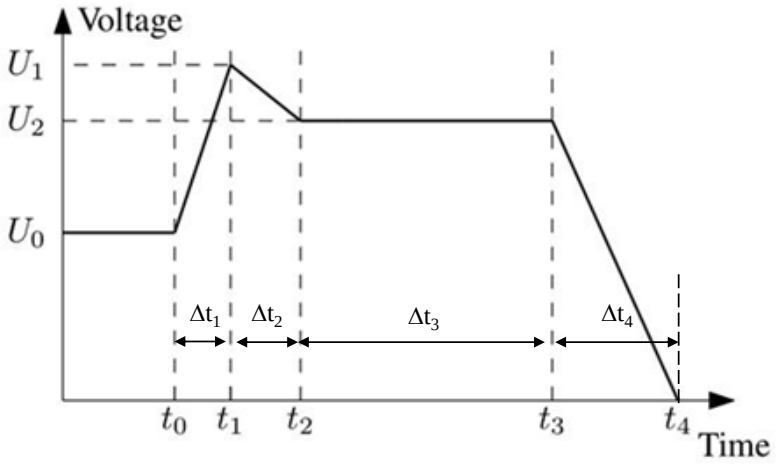

Figure 2.5 Waveshape of the Synthesized Long TOV induced on the healthy pole (After [24]).

2.1.4 Superimposed Switching Impulses (SSIs):

SSIs simulate the switching events on HVDC cable systems in qualification tests according to CIGRÉ Technical Brochure 496 [29] first and CIGRÉ Technical Brochure 852 later [74]. A SSI is a standard switching impulse superimposed onto the permanent DC voltage. The standard switching impulse is defined according to IEC Standard 60060-1 [26],[27],[28]. SSI has a rise time and a time to half-value on the tail of 250 and 2500 μs, respectively (see Figure 2.6). The peak value of the lower bound of the SSI of the same polarity superimposed to the DC voltage, $U_{P2,s,min}$, is calculated according to CIGRÉ Technical Brochure 496 [29] as follows:

$$U_{P2,s,min} = 1.15\, U_T = 1.15 * 1.85\, U_0 = 2.13\, U_0 \qquad (2.1)$$

where U_T is the voltage applied during the Type Test according to [29], while U_0 is the nominal DC voltage. As a conservative value, $2.13U_0$ is rounded to $2.2U_0$.

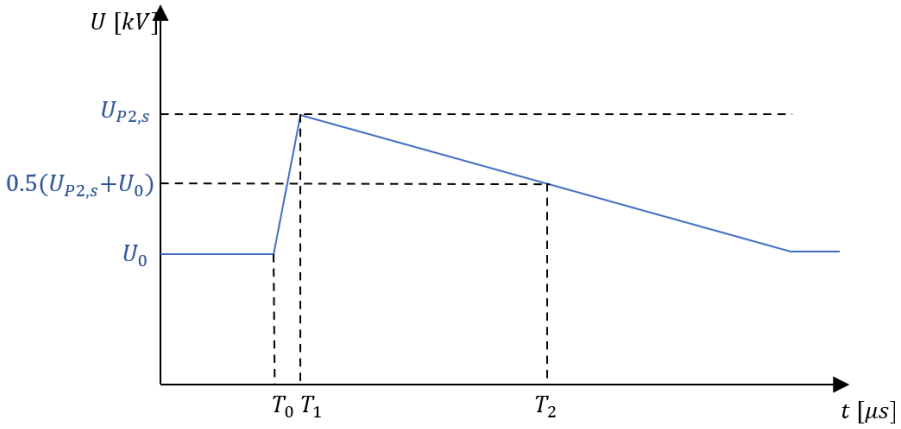

Figure 2.6 Waveshape of the SSI of the same polarity of the applied voltage superimposed on the DC voltage U_0.

2.2 Experimental effect of TOVs and SSIs on HVDC insulation

2.2.1 Experimental procedure:

This experiment consists of two main stages i.e., aging process and measurements. As it can be seen in Figure 2.7, the aging process begins with a custom-made low-voltage 13-bit digital-to-analog converter which is used as a low voltage signal generator (for either TOVs or SSIs). It is programmed to generate and replicate the impulse waveshapes shown in Figures 2.5 and 2.6 for a given number of impulses. Then, impulses in low voltage are amplified to high voltage using a Trek 30/20 high voltage amplifier (as shown in Figure 2.8). High voltage impulses are repetitively applied on XLPE specimens clamped between two circular flat electrodes (with radius of 20 mm) at room temperature (see Figure 2.9). After the aging process, both aged and non-aged specimens are characterized to assess the effect of aging on the dielectric properties and polymeric structure of XLPE. While dielectric spectroscopy and DC conductivity measurements are performed on sputtered specimens, Fourier Transform InfraRed spectroscopy (FTIR) and space charge measurements are performed on non-sputtered specimens.

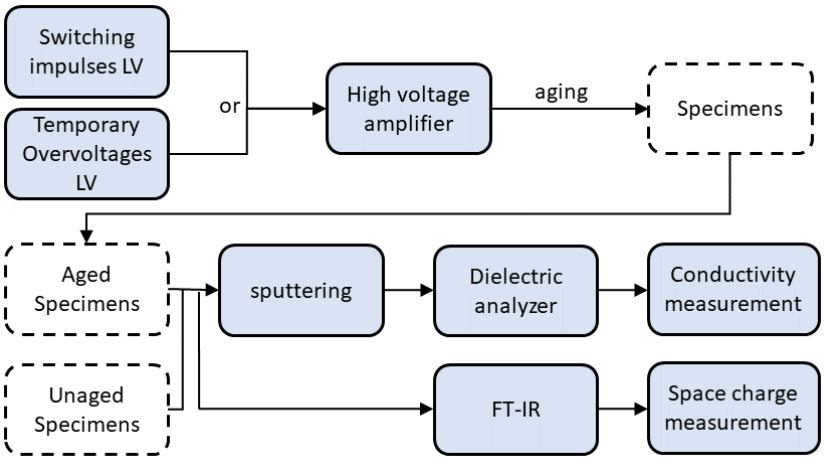

Figure 2.7 Block diagram that shows the aging and measuring processes.

(a)

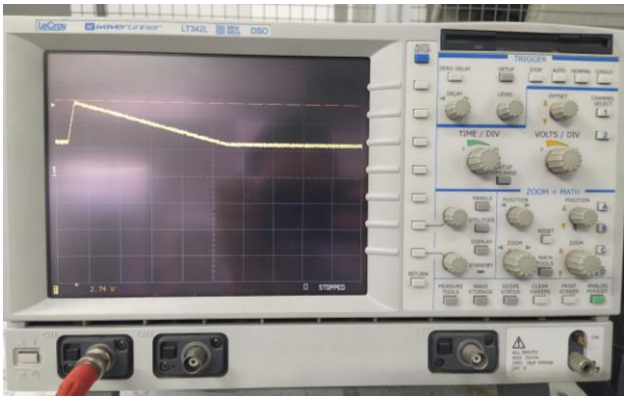

(b)

Figure 2.8 (a) High voltage amplifier Trek model 30/20, (b) the output voltage as plotted on the oscilloscope.

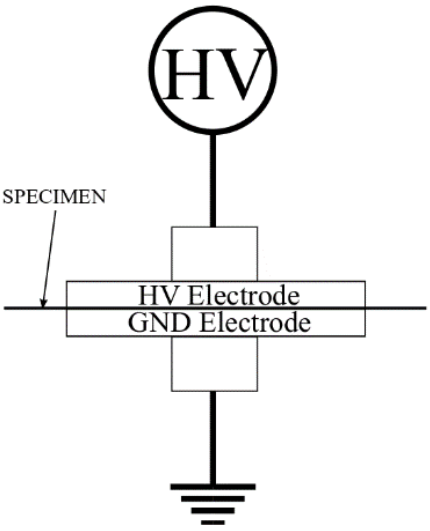

Figure 2.9 schematic of the aging setup.

Table 2.1 presents the waveshape characteristics of both TOVs and SSIs as shown in Figures 2.5 and 2.6. Where intervals of likely values are given, the numbers in bold are those chosen in this experimental work. These values are chosen so that the total number of TOVs in the test is applied in a given time interval that is not excessively long. Two durations of the test (Table 2.2) and two electric field levels (Table 2.3) are selected in these tests to simulate different numbers and amplitudes of TOVs and SSIs. For both TOVs and SSIs the number of impulses applied in the aging process are 1000 and 2000 at a frequency of 1 Hz – i.e., with a time interval of 1 (s) between each two consecutive impulses – as illustrated in Table 2.2, which includes the total duration of TOV and SSI aging tests.

It is worthwhile pointing out that – notwithstanding the pulses have the same 1 Hz frequency for both TOVs and SSIs – the total duration of TOVs aging process is much longer than that in the case of SSIs, as the duration of one single TOV (45.2 s) is much greater than that of one single SSI (4.75 ms), see Table 2.2. The frequency and number of surges applied in the aging tests are significantly greater than those encountered in service conditions; this holds especially for the TOVs, which are associated with pole faults. These values of frequency and number are chosen to accelerate the possible aging effects of TOVs and SSIs, thereby easing their detection after the tests. The chosen values of the rated electric field E_0, i.e., the DC component of the field at rated voltage U_0 are (see Table 2.3):

- 25 kV/mm, which is a typical order of magnitude of the design electric field in the state-of-the-art HVDC cables [30].
- 50 kV/mm, which represents an upper limit of the electric field in the new generation of HVDC cables (e.g., 800 kV cables), and also serves to accelerate the aging effect of electric field on dielectric properties and the aging of XLPE insulating material [31].

Values of the peak and plateau voltages for TOVs, as well as the peak voltage of SSIs, are reported in Table 2.3, for each chosen value of E_0.

Table 2.1 Worst case TOV and SSI Waveshapes Characteristics

impulse type	**symbol**	**parameter**	**value and unit**
TOV	U_a	Peak voltage	1.8 p.u.
	U_b	Plateau voltage	1.5÷1.6 p.u.
	Δt_1	Time to peak	[0.5÷5] ms **2** ms
	Δt_2	Time of peak decay	[0.5÷5] ms **2** ms
	Δt_3	Time of plateau	[100÷**200**] ms
	Δt_4	Discharge time	[30 ÷ >600] s **45** s
	T_{TOV}	Duration of TOV	45.2 s
SSI	$U_{P2,s}$	Peak voltage	2.2 p.u.
	T_1	Front duration	250 µs
	T_2	Time-to-half	2500 µs

	T_{SSI}	Duration of SSI	4.75 ms

Table 2.2 Total duration of TOV and SSI aging process

impulse type	**Time interval between consecutive impulses**	**Total duration**	
		1000 impulses	**2000 impulses**
TOV	1 s	12.8 hours	25.7 hours
SSI	1 s	17 minutes	34 minutes

Table 2.3 TOV and SSI applied voltages during the aging process

impulse type	**E_0 (kV/mm)**	**voltage type**	**value (kV)**
TOV	25	Peak (1.8 E_0)	6.75
		Plateau (1.5 E_0)	5.625
	50	Peak (1.8 E_0)	13.5
		Plateau (1.5 E_0)	11.25
SSI	25	Peak (2.2 E_0)	8.25
	50	Peak (2.2 E_0)	16.5

2.2.2 Specimens:

Specimens used in this experiment are degassed flat samples (peelings) of DC-XLPE which are initially used in the framework of the European project ARTEMIS. The thickness of each sample is measured accurately using an electronic micrometer. The measured thickness of specimens falls in the range of 0.147÷0.152 mm. Five specimens are tested for each aging case to allow a statistical processing of results. The chosen number of specimens is a compromise between the test duration (especially for TOVs, which can require up to >24 hours per specimen) and the ability to describe an average trend of the population. As a consequence of the relatively small sample and population size, Student's t-distribution with 5 degrees of freedom and a 95% confidence interval, is used to estimate the mean value of the real and imaginary permittivity, as shown in Equation (2.2):

$$\bar{m} - 2.571\ s/\sqrt{n} \leq\ \mu \leq \bar{m} + 2.571\ s/\sqrt{n} \qquad (2.2)$$

where $\bar{m}$ is the mean value of the sample, s is the standard deviation, n is the number of tested specimens and μ is the mean value of the population.

Golden electrodes were deposited on both sides of specimens by cold sputtering under 0.15 mbar pressure of Argon during 300 seconds using the setup shown in Figure 2.10 (a). This is necessary to ensure an ideal contact interface during dielectric spectroscopy. Figure 2.10 (c) and (d) shows the specimens before and after gold sputtering process.

(a)

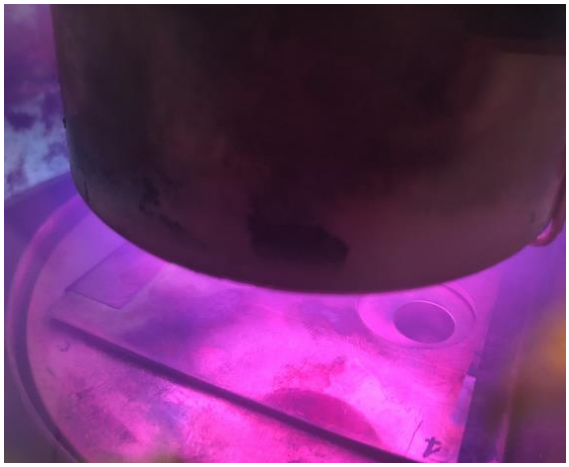

(b)

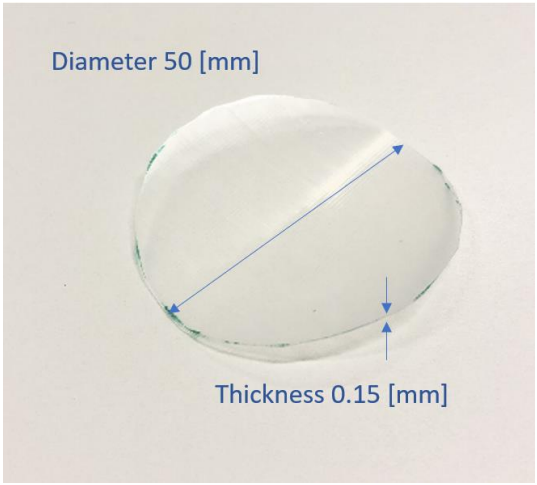

(c)

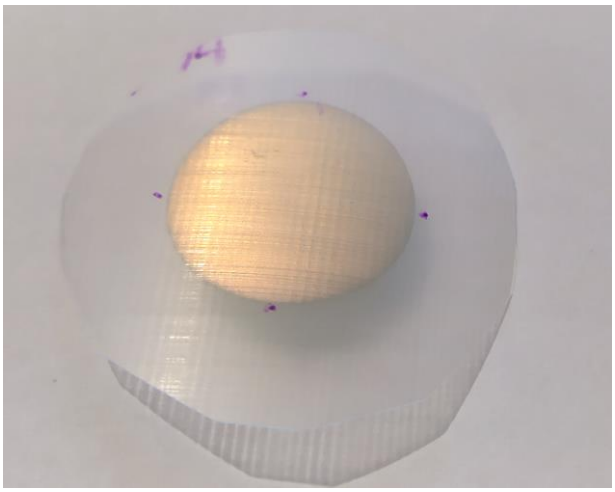

(d)

Figure 2.10 (a) Sputtering setup, (b) plasma light during sputtering process, (c) a XLPE specimen before gold sputtering, (d) the specimen after gold sputtering.

2.2.3 Characterization setup:

2.2.3.1 Dielectric analyzer:

A Novocontrol Alpha-A dielectric Analyzer (as in Figure 2.11) is used to measure the complex permittivity of aged and unaged XLPE specimens. Dielectric spectroscopy was carried out under a voltage of 3 kV (V_{rms}, to provide an electric field =20 kV/mm rms inside the 0.15-mm thick specimen), frequency range [$10^{-2} \div 10^{6}$] Hz, and a temperature of 25 (°C). The complex permittivity ε consists of real and imaginary parts, as illustrated in Equation (2.3); the real part ε' represents the dielectric constant of the material. The imaginary permittivity ε'' consists of two terms as illustrated in Equation (2.4), the first one γ/ω considers conduction process in the insulation, while the other term ε_h'' represents the contribution of dipolar losses [23].

$$\varepsilon = \varepsilon' - j\varepsilon'' \tag{2.3}$$

$$\varepsilon'' = \gamma/\omega + \varepsilon_h'' \tag{2.4}$$

where γ is electrical conductivity, ω is the angular frequency. It is worth noting that the conduction term dominates the imaginary permittivity as ω tends to 0; then, the logarithmic plot of ε'' over the applied frequency $f = \omega/2\pi$ eventually becomes a line with slope -1, below a certain frequency depending on the value of γ. Generally speaking, the higher the conductivity, the higher the frequency at which this phenomenon starts being noticeable.

The setup consists of BDS 1200 cell equipped with gold-plated electrodes where the specimen is placed in-between. The cell is connected to Alpha-A analyzer Mainframe which is connected to a PC equipped with an ad-hoc software.

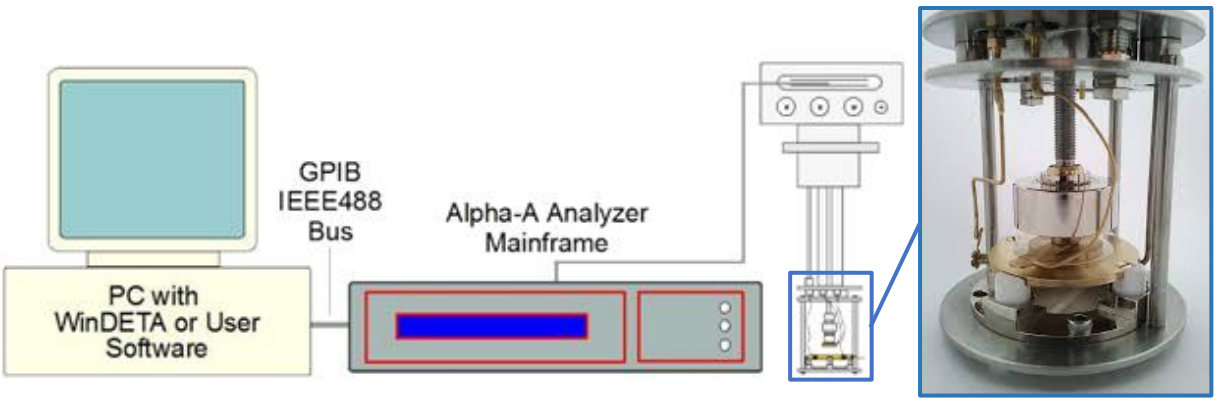

Figure 2.11 Novocontrol Alpha-A dielectric analyzer system scheme.

2.2.3.2 DC Conductivity measurements:

DC conductivity is one of the most important criteria for the selection of high voltage insulating materials used for DC applications. For this reason, DC conductivity measurements are carried out according to IEC 62631-3-1:2016 [32] in the framework of this experimental activity, to find out the effect of impulses (SSIs and TOVs) aging on the DC conductivity of XLPE flat specimens. The setup consists of an insulated cell in which three electrodes are placed as shown in Figure 2.12. The upper electrode is connected to the DC power supply which is kept at 3 kV during the experiment to provide an electric field =20 kV/mm inside the 0.15-mm thick specimen. The lower electrode is connected to the picoampere meter. While the guard ring is connected to earth to remove stray currents and ensure that the measured current is only the conduction current flowing in the bulk of the dielectric specimen. Due to the flat geometry of the test cell, the apparent conductivity can be calculated using the following equation:

$$\sigma = \frac{J}{E} = \frac{I\,d}{A\,U} \tag{2.5}$$

where σ is the conductivity (S/m), J is the current density (A/m^2), I is the current (A), E is the electric field (V/m), A is the effective electrode area, U is the applied voltage (V), d is the insulation thickness (m).

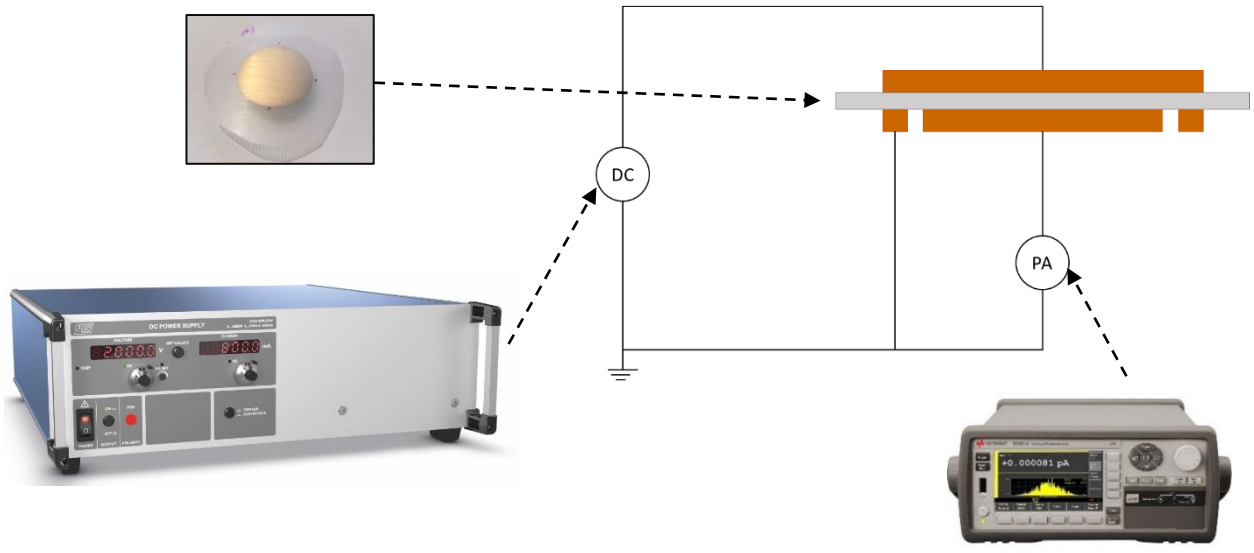

Figure 2.12 schematic of the DC conductivity measurement setup.

2.2.3.3 Fourier Transform InfraRed spectroscopy (FTIR):

Fourier Transform InfraRed spectroscopy FTIR is used to detect the molecular composition of XLPE specimens. FTIR can detect the formation of new functional groups and characterizing bonding information using the transmittance (or the absorbance) in a certain frequency range of the wavelength commonly indicated by its reciprocal, which is the wavenumber (cm^{-1}). A Bruker ALPHA FTIR Spectrometer equipped with Attenuated Total Reflectance (ATR) with diamond crystal accessory allowing to measure solid specimens' chemistry is used to characterize the aged specimens as well as the unaged ones to compare them and detect any variation of the XLPE material or formation of new aging bonds. The ATR tool allows for direct spectra recording on solid samples without specific preparation, thus being more representative of the actual specimen chemistry. Figure 2.13 illustrates the concept of FTIR where an Infra-Red IR beam is directed toward ATR diamond crystal in which the beam is internally reflected on the specimen's surface. The outgoing beam is analyzed and plotted using an ad-hoc PC software [33].

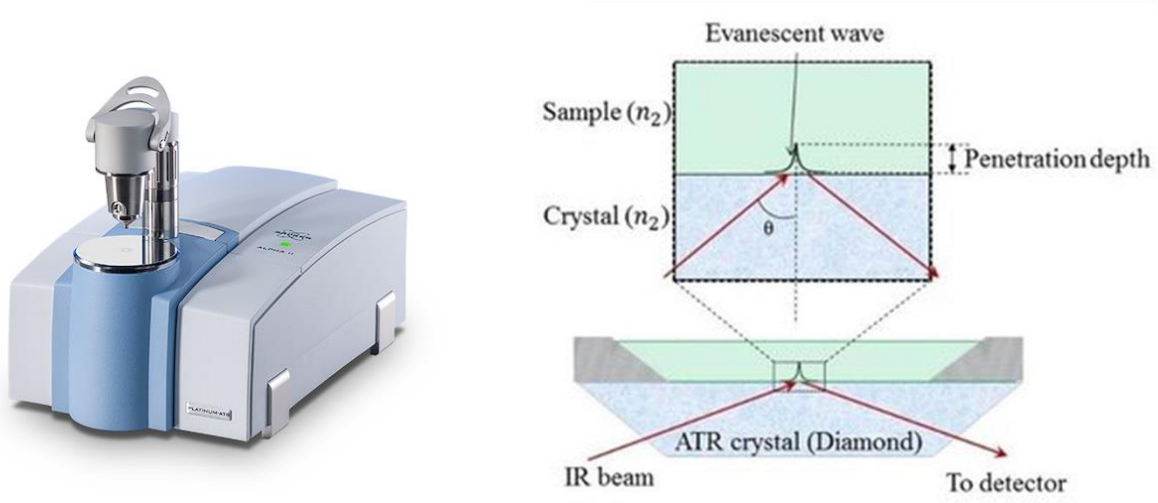

(a) (b)

Figure 2.13 Fourier Transform InfraRed spectroscopy (a) test setup, (b) concept of the measurement .

2.2.3.4 Space charge measurements:

Pulsed Electro-Acoustic (PEA) method of Space Charge SC measurement is used to detect any possible aging in the insulating material i.e., XLPE by comparing the measurements of both aged and non-aged specimens. The schematic of the SC measurement setup is shown in Figure 2.14b. It basically consists of two electrodes where the flat specimen is placed in between with adding a thin semi-conductive flat layer between the specimen and both electrodes. A drop of silicon oil is used to ensure continuous acoustic properties for the propagating waves. The HVDC power supply is used to apply a certain electric filed inside the specimen (here it is 20 kV/mm). While the pulse generator aims at generating electrical pulses which induce a transient displacement of the space charges along

the thickness direction as a result of Coulomb effect. The latter displacement causes pressure waves with amplitude proportional to the local charge density. The pressure waves propagate inside the specimen with the speed of sound in the insulating material. The pressure waves are detected by the transducer (piezoelectric sensor) which converts them into electrical waves. Then, the voltage signals are subjected to deconvolution process (signal processing) to obtain the charge density distribution inside the specimen as well as its evolution over time [34], [35]. The SC measurement are performed under both the ambient temperature i.e., 25 (°C) and the typical design temperature of HVDC cables i.e., 70 °C.

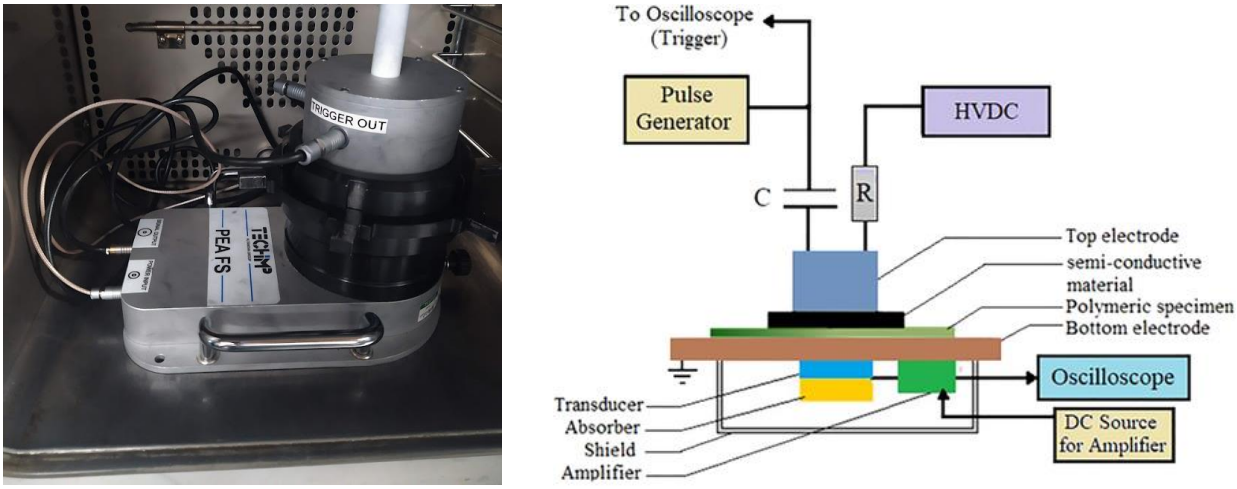

(a) (b)

Figure 2.14 Pulsed Electro-Acoustic method of space charge measurement (a) PEA cell, (b) schematic of the setup .

2.2.4 Results:

2.2.4.1 Dielectric analyzer:

Figure 2.15 presents in each curve the mean value (for the 5 specimens) of the imaginary permittivity with respect to the frequency in the range $[10^{-2} \div 10^{6}]$ when the specimens are aged by TOVs in Figure 2.15(a) and SSIs in Figure 2.15(b). The mean value of ε" shows peaks of different amplitudes and different corresponding frequencies. These peaks are dependent on the amplitude of the applied electric field and the duration of the aging process. In addition, a more careful inspection reveals that the higher the field applied on the samples, the more evident the peak of ε". In particular, it is possible to note that the tests performed with E_0=25 kV/mm yield peaks of ε" that are considerably lower than those performed with E_0=50kV/mm. Furthermore, it can be noticed that, at a given amplitude of the applied stress, the peak of ε" is higher for the test with 2000 impulses with respect to that with 1000 impulses. Indeed, this Figure emphasizes that, for E_0=25 kV/mm, ε" has peaks in a range of frequencies between 10^0 and 10^2 Hz (yellow and red curves), while the curves corresponding to E_0=50

kV/mm have permittivity peaks in the range 10^2 and 10^4 Hz. Hence, the longer the aging duration, the stronger the aging effect of the TOV on the dielectric properties of the extruded insulation. While increasing the aging field shifts the peaks towards higher frequencies beside the overall increase in the amplitude. The latter suggests the formation of polar molecules due to the aging process, which in turn increase the dipolar losses in the range [1÷10^4] Hz.

Moreover, Figure 2.15 indicates that, especially at 50 kV/mm, the aging effect on conductivity in case of SSIs is greater than that in case of TOVs, although the polarization peaks in both TOVs and SSIs have approximately the same order of magnitude. This result might indicate an increase of the electrical conductivity γ of aged insulation, compared to the non-aged one. Such increase should result in higher values of the term γ/ω in Equation (2.4), and an increase of the imaginary part of permittivity with a linear trend with slope of -1, as ω tends to 0 in bi-logarithmic scale, which is confirmed by conductivity measurement results. This tendency suggests a general increase of dielectric losses due to electrical aging caused by these transient voltage waveforms at high fields. This might set a challenge especially to the new generation of HVDC extruded insulation.

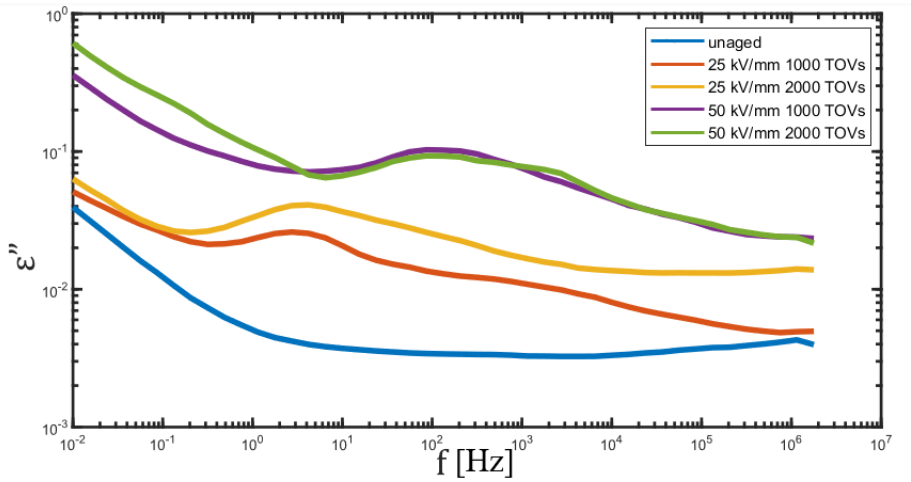

(a)

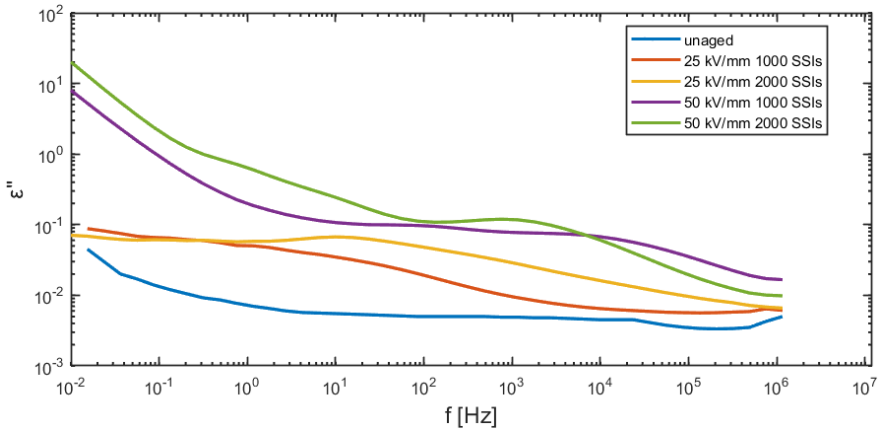

(b)

Figure 2.15 The mean value of the imaginary permittivity vs frequency in a log-log scale for both unaged and aged specimens with two different values of number (1000 and 2000) and amplitude (E_0=25 kV/mm and 50 kV/mm) of (a) Temporary Overvoltages TOVs (after[25]) and (b) Superimposed Switching Impulses SSIs.

Figure 2.16 illustrates the real permittivity variation after the aging of specimens using SSIs. It is clearly seen that only a slight increase in the real permittivity can be noticed for frequencies greater than 10^4 due to aging process. However, for lower frequencies i.e. [10^{-2}÷10^4], the real permittivity increases as the frequency tends to 0; such increase is mild at E_0=25 kV/mm, more significant at E_0=50 kV/mm, especially as the number of impulses is increased from 1000 to 2000. Also the slope increment is greater for higher amplitude of the SSIs impulses.

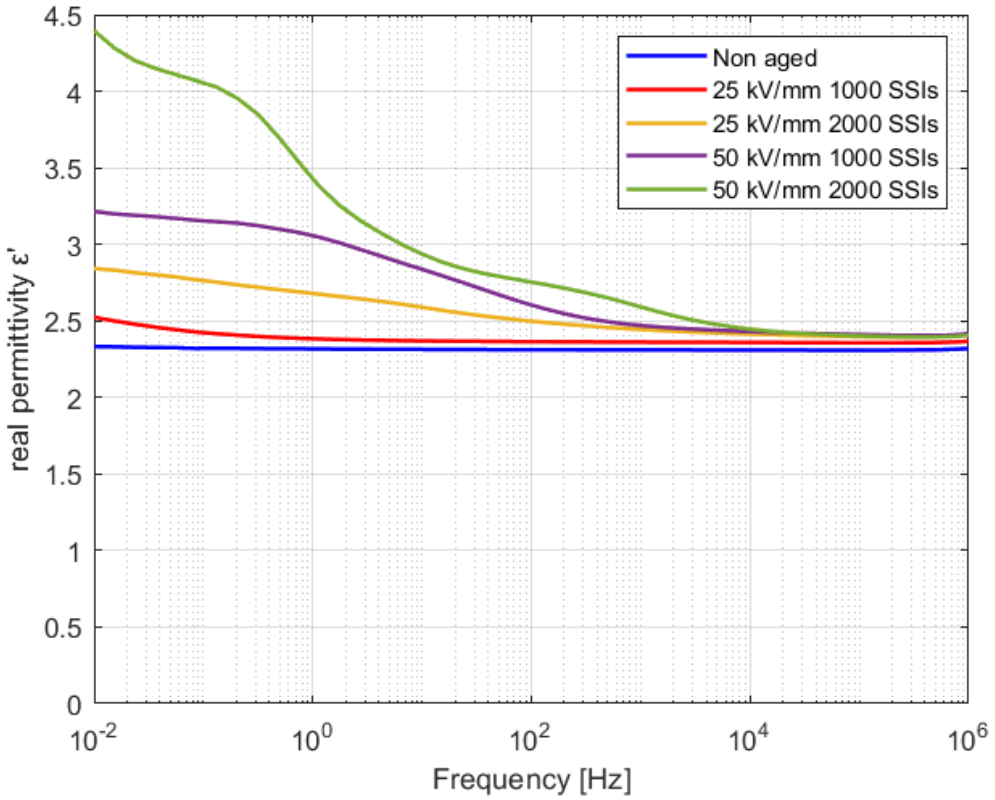

Figure 2.16 The mean value of the real permittivity vs frequency in a semi-log scale for both unaged and aged specimens with two different values of number (1000 and 2000) and amplitude (E0=25 kV/mm and 50 kV/mm) of Superimposed Switching Impulses SSIs.

2.2.4.2 DC Conductivity measurements:

Figure 2.17 shows the conductivity evolution over time until 80,000 s (≈22 hours) calculated from the polarization current for non-aged specimens (black curve) and specimens aged by 2000 SSIs at E_0=25kV/mm (blue curve) and E_0=50kV/mm (red curve) at room temperature. The results are processed using Matlab (10'th-order one-dimensional median filter) to make the results comparable. It can be noticed that the specimens reach the stability after 70,000 s (≈20 hours) showing an increase in the conductivity as a result of the aging process. The electrical conductivity is increased after the aging process due to SSIs: at 25 kV/mm it is increased by ≈ 25 %, but it is particularly doubled at 50 kV/mm. As the electrical conductivity is one of the most critical properties used to assess the overall

quality and performance of HVDC cable insulation, these measurements suggest that for the new generation of HVDC extruded cables a high number of switching impulses might set a challenge to the useful service life of the cable.

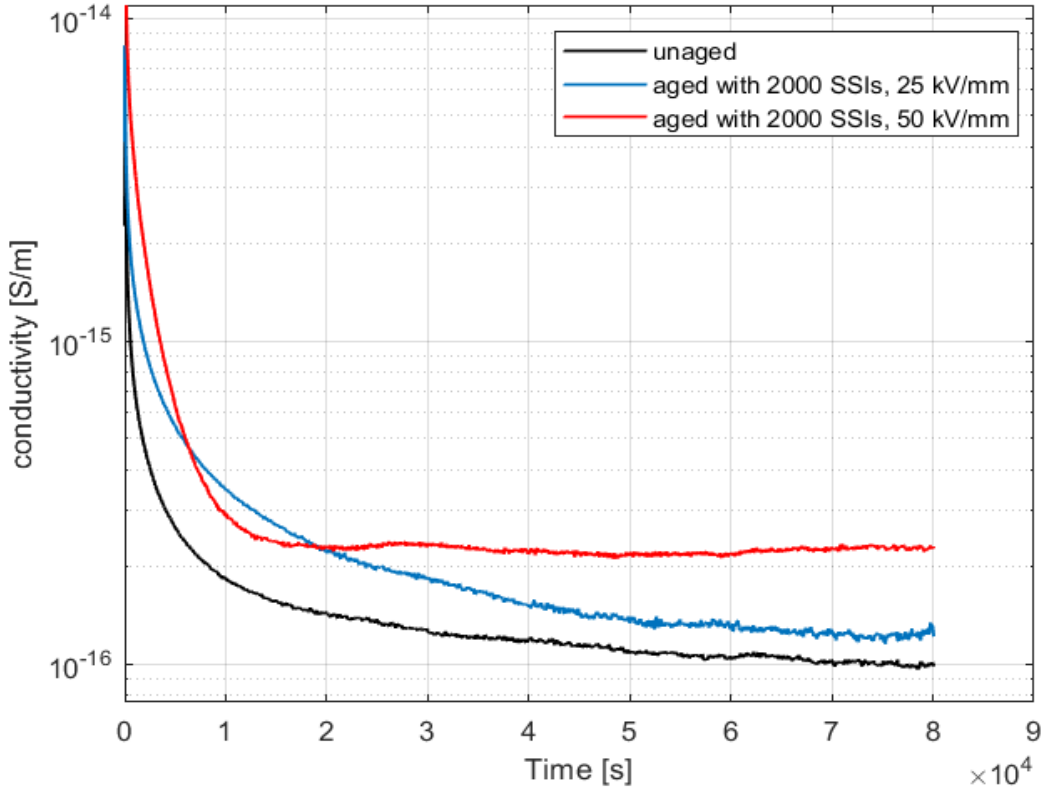

Figure 2.17 DC current measurements on a specimen aged by 2000 SSIs for E_0=25 kV/mm and E_0=50 kV/mm at 25 °C and electric field E =20 kV/mm.

2.2.4.3 Fourier Transform InfraRed spectroscopy (FTIR):

Figure 2.18 shows the results of FTIR spectroscopy measurements performed for unaged and aged specimens subjected to either TOVs (Figure 2.18(a)) or SSIs (Figure 2.18(b)). Those Figures plot the transmittance of the IR waves in a certain range of the wave length represented here by the wavenumber [400 ÷ 4000] cm^{-1}. Polyethylene (PE) is characterized by 3 strong absorption peaks or conversely transmittance drops, (they are referred to as "absorption peaks" hereafter) [36] attributed to the aliphatic chain:

- 2870 cm^{-1} corresponds to the stretching vibration of the C–H bond of methylene which includes two peaks: 2915 cm^{-1} and 2850 cm^{-1} for CH_2 asymmetric and symmetric stretching, respectively;
- 1460 cm^{-1} corresponds to the bending vibration of the methylene C–H bond;

- 720 cm^{-1} corresponds to the rocking vibration of the methylene C–H bond.

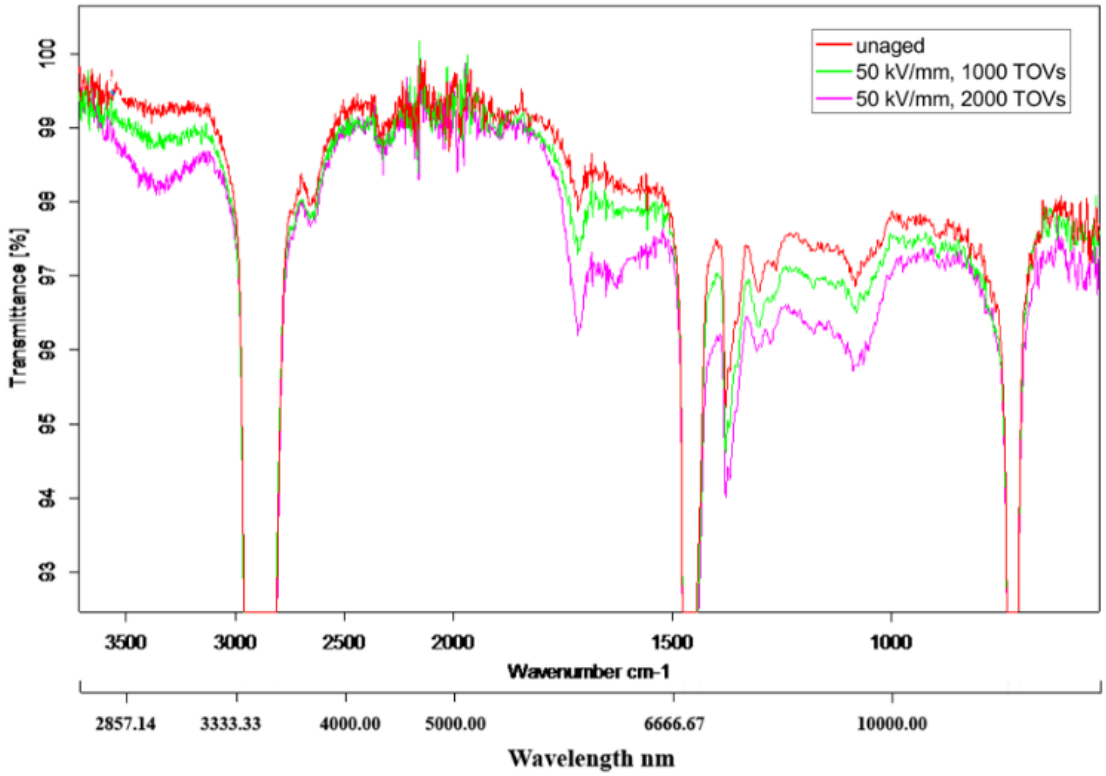

(a)

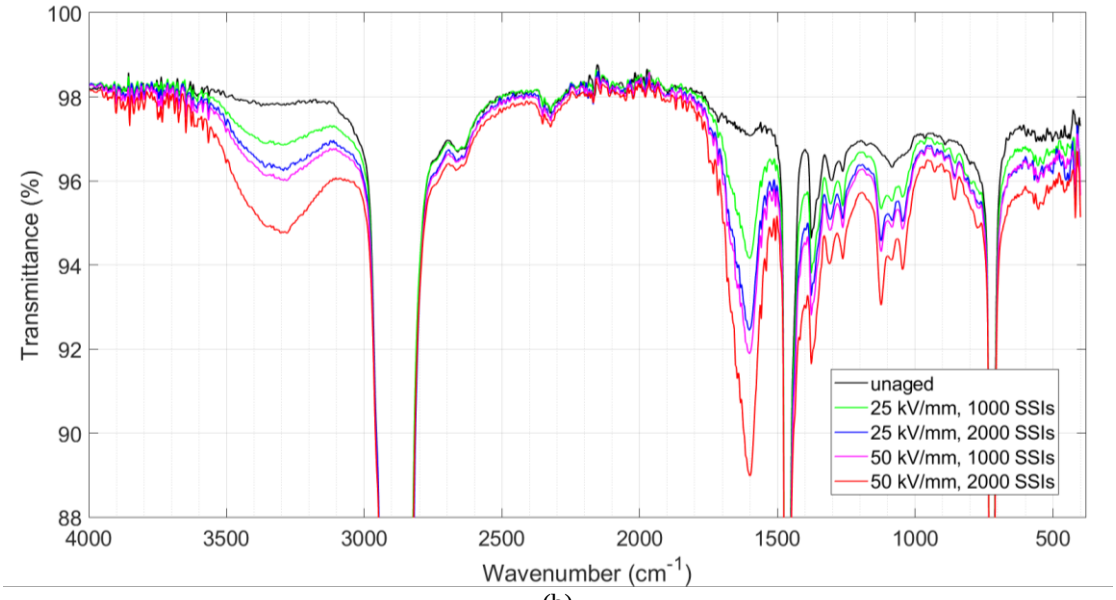

(b)

Figure 2.18 The mean value of the transmittance of non-aged samples and samples aged by (a) Temporary Overvoltages TOVs (after[25]) and (b) Superimposed Switching Impulses SSIs, measured by Fourier Transform Infrared Spectroscopy FTIR.

Additionally, other smaller peaks can be observed at the wave numbers 1377, 1306 and 1176 which corresponds to CH_3 symmetric deformation, twisting deformation and wagging deformation

respectively (see strong peaks in the insets of Figure 2.19). While the aforementioned characteristics are related to the unaged and aged XLPE samples, both TOVs and SSIs aging processes cause a considerable variation in the transmittance at certain wavenumber bands as follows:

1) A decrease of the IR transmittance (increase of absorption) at 3 wavenumber bands is observed by comparing the unaged mean curve with the mean curve of samples aged by either TOVs or SSIs:

- [740÷1450], the absorption peak of C=C bond increased with aging field's amplitude and time. The latter change might be related to oxidative cracking reaction which leads to the formation of aging products belonging to the vinylene group [37],[38]. Additionally, the peaks in this band might be also caused by the vibrations of –C–O–C– ether bonds [39],[40].
- [1500÷1750] cm^{-1}: the absorption peak in this regions is ascribed to the possible formation of C=O and C=C bonds. Free radicals caused by the C–C bond rupture might be combined with oxygen to form carbonyl groups C=O, carboxylic acid RC(=O) OH, ketones RC(=O) R' or ester RC(=O) OR' [40].
- [3000÷3500] cm^{-1}, the absorption peak at this wavenumber is typical of the O-H stretching that might belong either to the formation of carboxylic acid groups R–COOH and hydroxyl groups R–OH [41] both resulting from oxidative ageing processes;

2) An increase of the IR transmittance (decrease of absorption) of characteristic XLPE peaks (720, 1460, 2850 to 2915 cm^{-1}) after the aging process. This could be a result of molecular chain scissions in XLPE by which the above-mentioned aging byproducts are formed. Figure 2.19 presents the full scale plot of the FTIR spectroscopy for unaged samples and samples aged with SSIs highlighting three clearly increasing absorption peaks in three zoom-in insets.

As a comparison between the FTIR results of samples aged by TOVs and SSIs, it can be seen in Figure 2.18 that the transmittance of IR is reduced in SSIs approximately twice that in case of TOVs, for the same E_0 and the number of impulses. This might be the cause of the different levels of conductivity increase noticed in the previous section. Consequently, according to the results of these measurements the effect of the applied SSIs on the aging of the tested XLPE insulation specimens seems to be more severe than that of the applied TOVs, although the duration of an SSI is much shorter than that of a TOV. On the other hand, the insulating material aged with SSIs is subjected to a peak electric field 20% greater than that in the case of TOV aging. This result highlights the strong impact of a small increase in the applied field on aging. The long plateau duration of TOVs seems to

have no noteworthy effect on the aging of XLPE, compared to the effects of a higher field, despite a shorter duration of the stress.

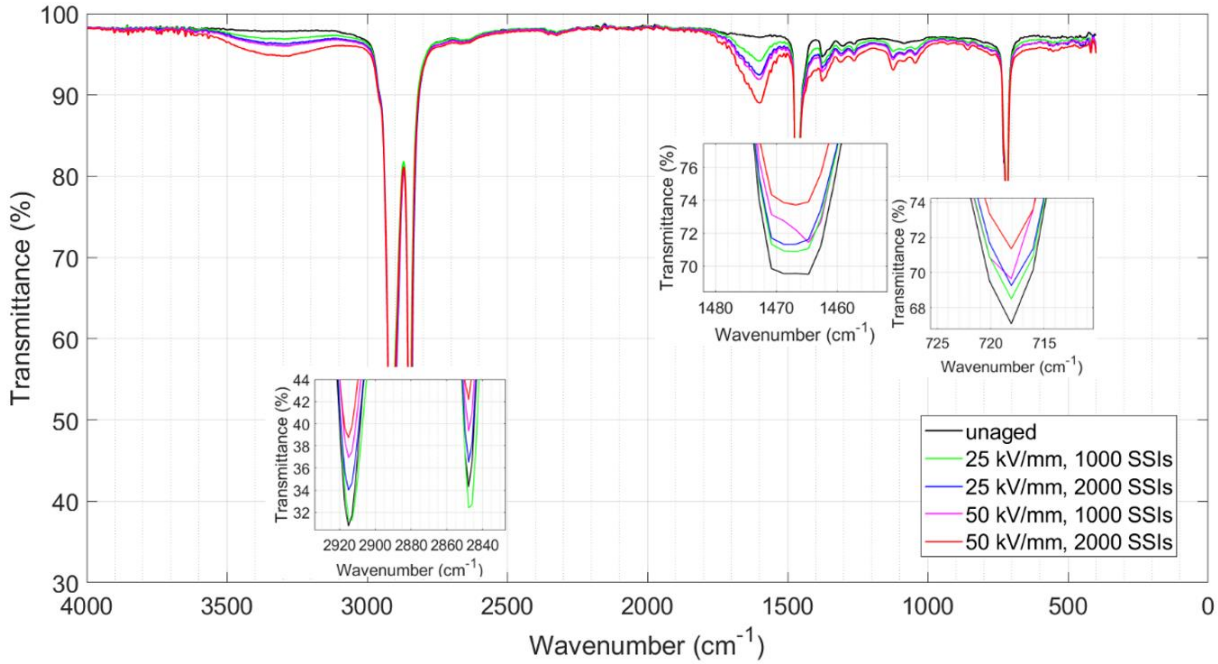

Figure 2.19 The mean value of the transmittance of non-aged samples and samples aged by Superimposed Switching Impulses SSIs, measured by Fourier Transform Infrared Spectroscopy FTIR highlighting the variation of transmittance drops of XLPE in 3 zoom-in insets.

2.2.4.4 Space charge measurements:

Figure 2.20 shows the space charge distribution inside the non-aged and aged specimens (with Superimposed Switching Impulses SSIs onto a DC field E_0=50 kV/mm) at 25°C and 70 °C. By comparing Figures 2.20 (a) and (b), it can be noticed that space charges accumulate in the mid insulation at 25°C. However, at 70 °C, more space charges accumulate in mid-insulation in addition to homo-charges accumulation near electrodes.

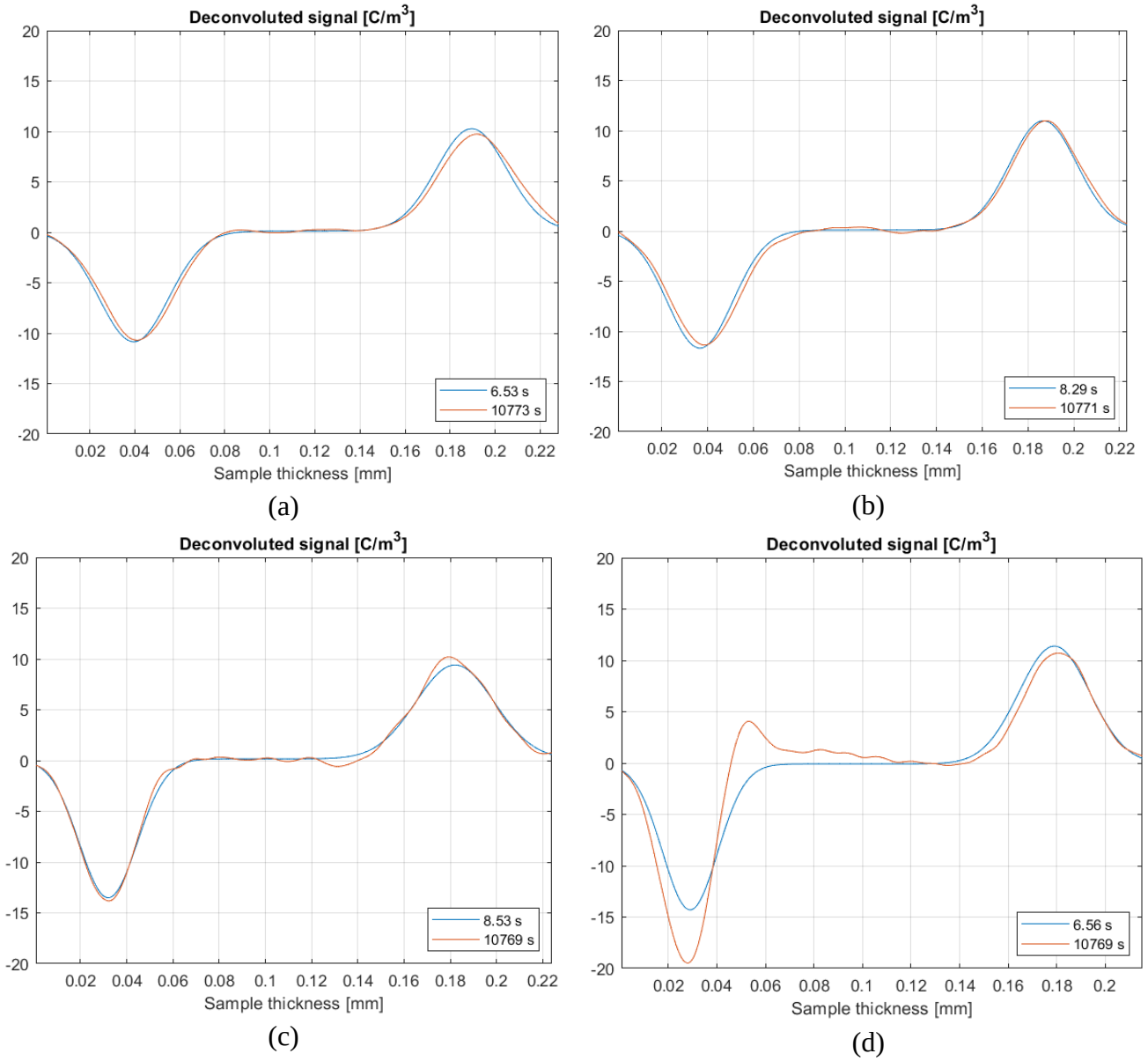

Figure 2.20 Space charge measurements using Pulsed Electro-Acoustic method PEA of:
(a) non-aged specimens at 25 °C
(b) aged specimens E_0=50 kV/mm, 2000 impulses at 25 °C
(c) non-aged specimens at 70 °C
(d) aged specimens E_0=50 kV/mm, 2000 impulses at 70 °C

Figure 2.21 shows space charge evolution over time during polarization period (from 0 to 10400 s) and depolarization period (from 10400 to 14000 s) for non-aged and aged specimens at 25 °C and 70 °C. The formation of hetero-charges at 25 °C and both hetero- and homo-charges at 70 °C can be noticed by comparing the non-aged (Figures a and c) and the aged (Figures b and d) specimens. It is worth noting from both polarization and depolarization periods that the aged XLPE tends to store more charges compared to the non-aged XLPE, in particular with a massive increase of heterocharges.

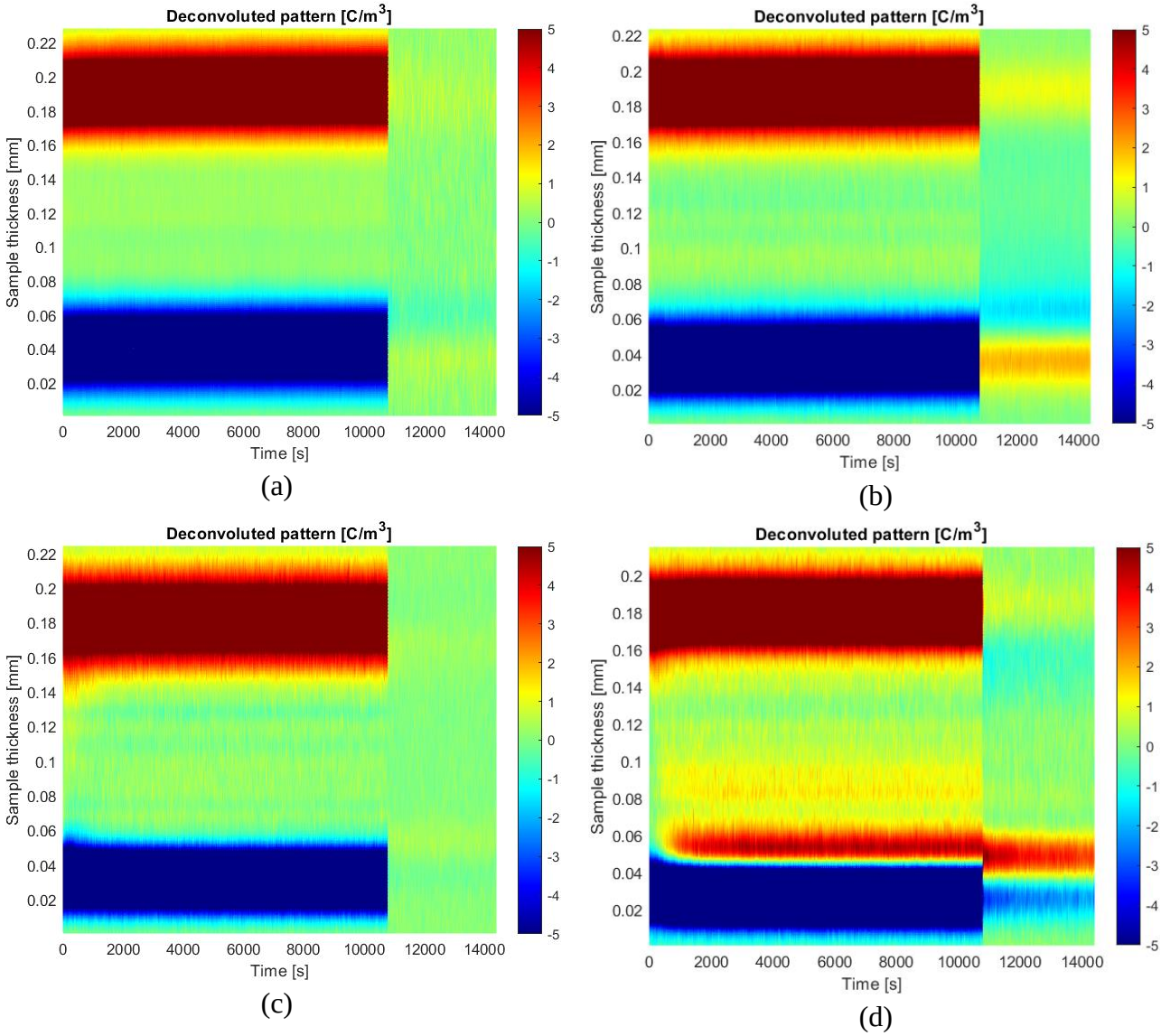

Figure 2.21 Space charge evolution over time for:
(a) non-aged specimens at 25 °C
(b) aged specimens E_0=50 kV/mm, 2000 impulses at 25 °C
(c) non-aged specimens at 70 °C
(d) aged specimens E_0=50 kV/mm, 2000 impulses at 70 °C

Figure 2.22 shows the space charge evolution over time with zoom-in charge densities in the range [-2,2] to highlight the space charge accumulation near the electrodes as well as in the mid insulation. It can be noticed by comparing Figures 2.22 (a) and (b) that hetero charges accumulate in the specimen as positive charges represented by yellow color accumulate closer to the earthed electrode, while negative charges represented by blue color accumulate closer to the HV electrode. A greater space charge accumulation can be clearly noticed at 70 °C by comparing Figures 2.22 (c) and (d).

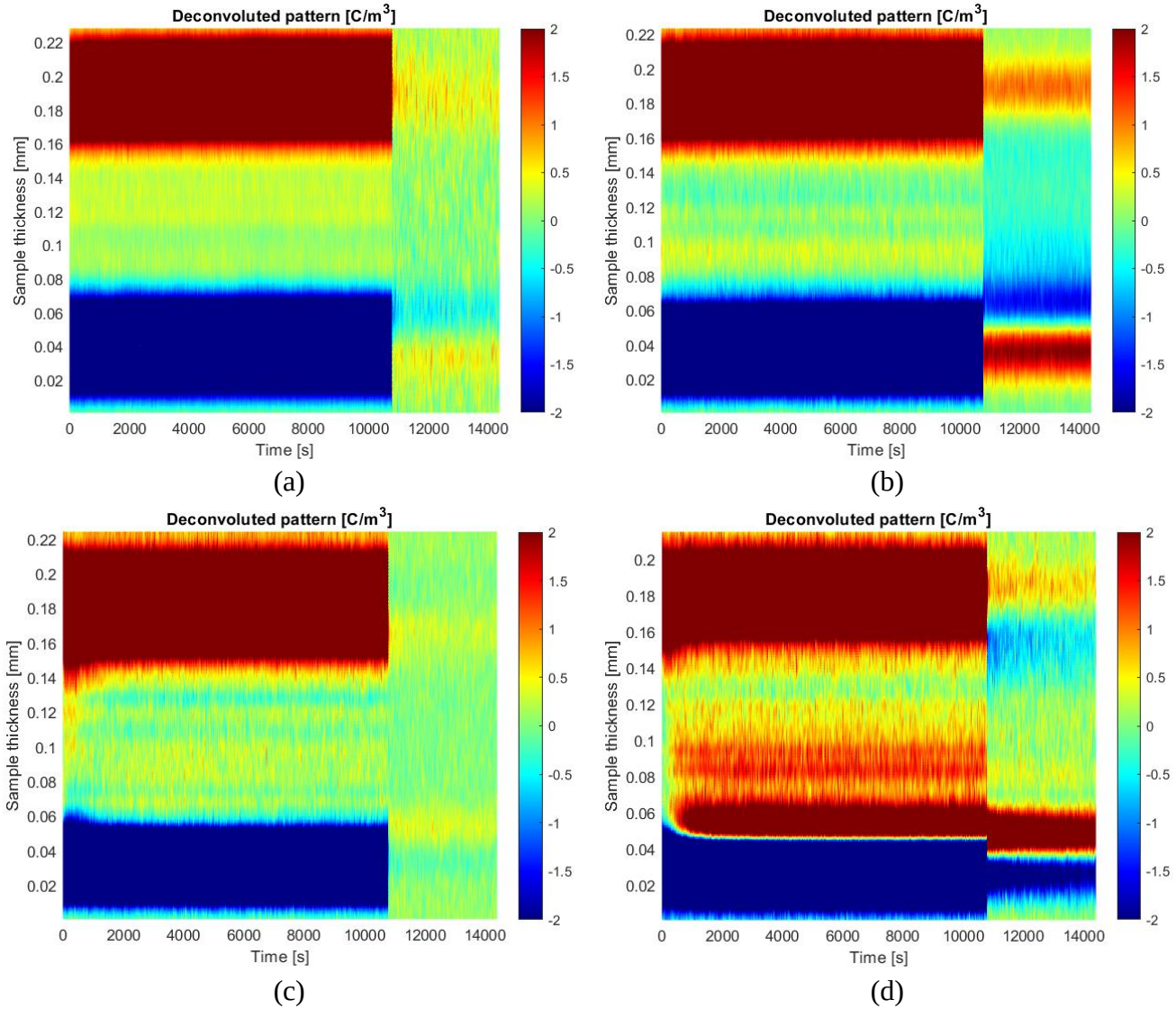

Figure 2.22 Space charge evolution over time with zoom-in charge densities in the range [-2,2] (C/m^3) for:
(a) non-aged specimens at 25 °C
(b) aged specimens E_0=50 kV/mm, 2000 impulses at 25 °C
(c) non-aged specimens at 70 °C
(d) aged specimens E_0=50 kV/mm, 2000 impulses at 70 °C

Figure 2.23 shows the electric field distribution inside the specimen as well as its evolution over time during polarization and depolarization periods. The homo-charges accumulated near the conductor reduces the field as represented by the green and yellow colors. The space charges accumulated in the mid insulation increase the local electric field as can be clearly seen in Figure 2.23 (d) represented by the dark red.

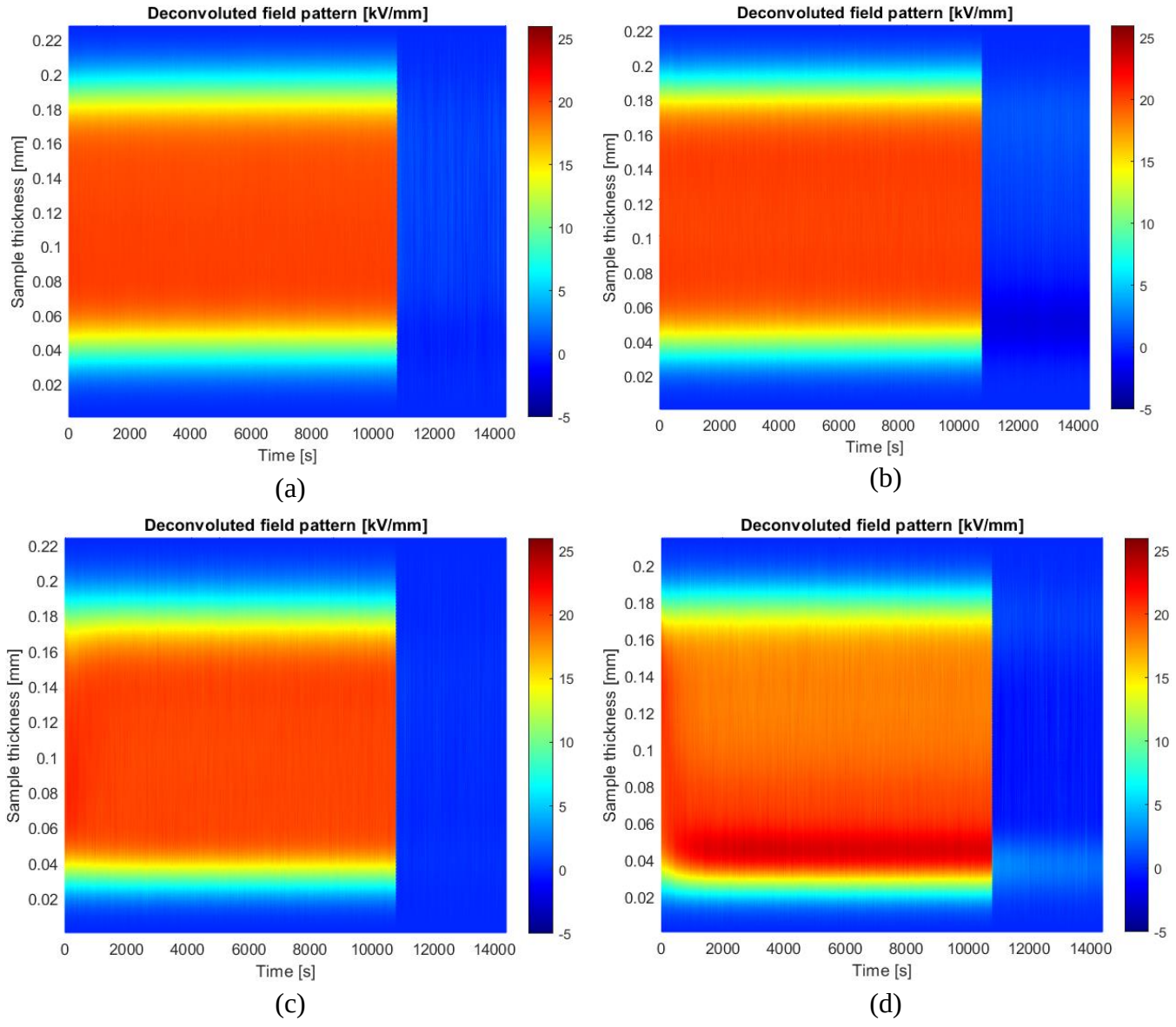

Figure 2.23 Electric field evolution over time for:
(a) non-aged specimens at 25 °C
(b) aged specimens E_0=50 kV/mm, 2000 impulses at 25 °C
(c) non-aged specimens at 70 °C
(d) aged specimens E_0=50 kV/mm, 2000 impulses at 70 °C

Figure 2.24 shows the probability density function (pdf) of the trap depth for both non-aged and aged specimens at 25 °C and 70 °C calculated using kernel density estimation. It is clear that at both temperatures the aging of the specimens leads to a shift of the pdf peak towards a higher trap depth i.e., from 0.88 eV to 0.94 eV at 25 °C and from 1.01 eV to 1.08 eV.

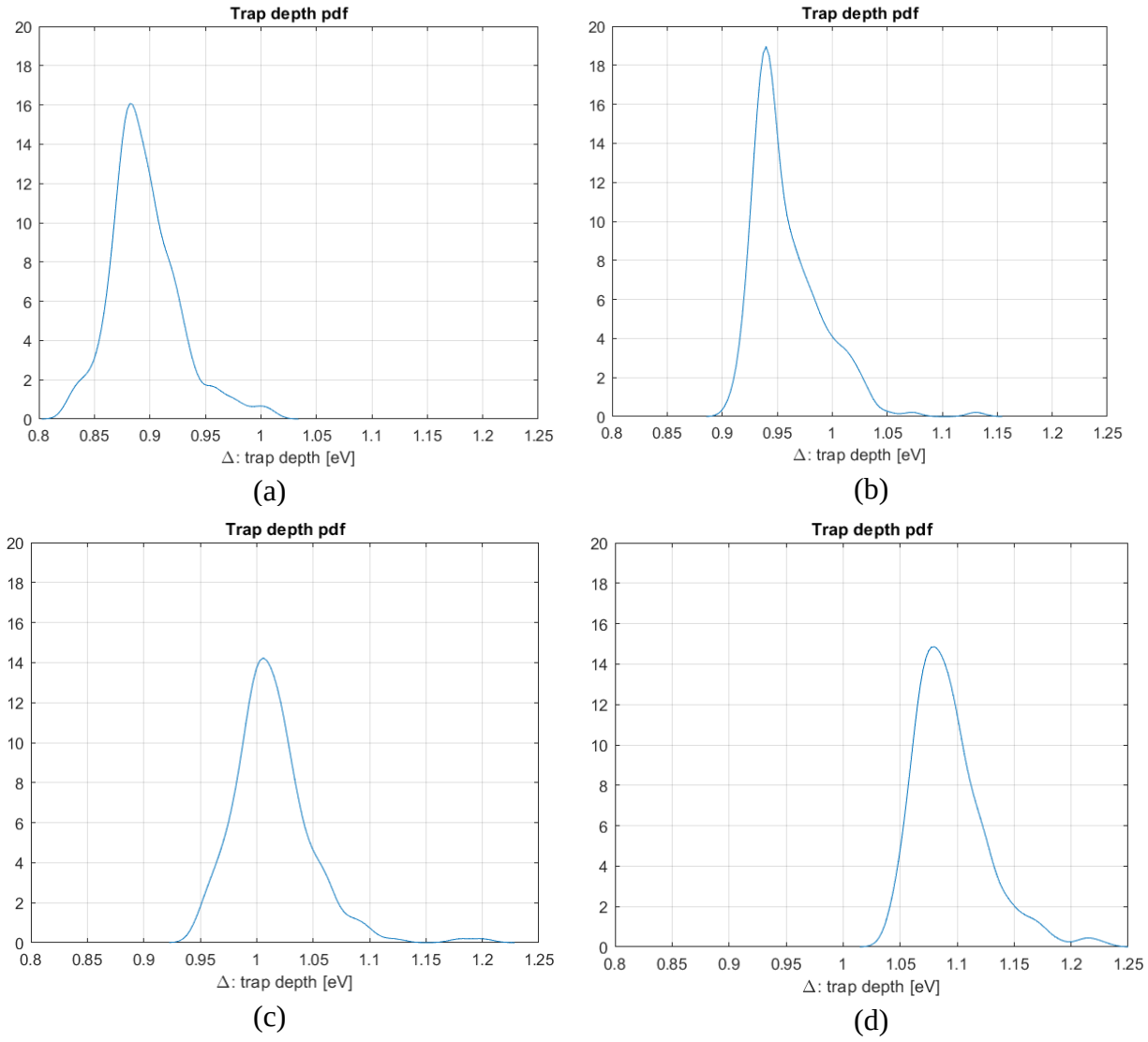

Figure 2.24 probability density function (pdf) of the trap depth for:
(a) non-aged specimens at 25 °C
(b) aged specimens E_0=50 kV/mm, 2000 impulses at 25 °C
(c) non-aged specimens at 70 °C
(d) aged specimens E_0=50 kV/mm, 2000 impulses at 70 °C

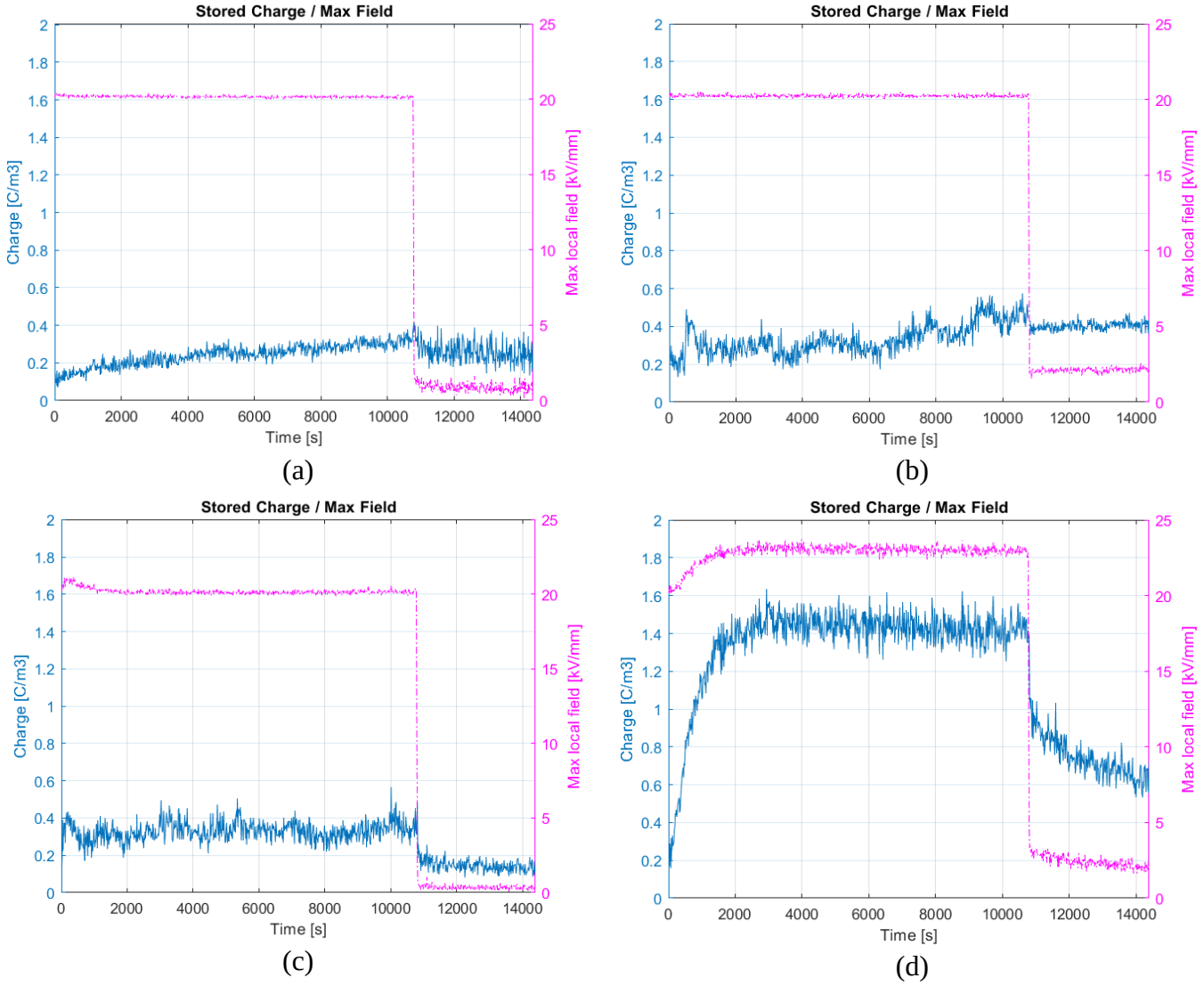

Figure 2.25 The stored charge density (in blue) and the maximum electric field (in pink) for:
(a) non-aged specimens at 25 °C
(b) aged specimens E_0=50 kV/mm, 2000 impulses at 25 °C
(c) non-aged specimens at 70 °C
(d) aged specimens E_0=50 kV/mm, 2000 impulses at 70 °C

Figure 2.25 shows the mean value of the stored charge density (in blue) and the maximum electric field (in pink) inside the specimen for non-aged and aged specimens at 25 °C and 70 °C. By comparing Figures 2.25 (a) and (b), it can be noticed that the stored charges are doubled at the end of polarization period (i.e., at 10400 s). While it is increased 5 times at 70 °C when comparing Figures 2.25 (c) and (d) at 10400 s. This confirms that the ability of the aged XLPE to store charges is "relatively" high compared to the non-aged specimens in Figures (a) and (c) where the charge evolution curve is approximately constant, while it is clearly increasing in the case of aged specimens Figures (b) and (d). During depolarization period (i.e., between 10400 s and 14000 s), the space

charge relaxation takes place gradually in a speed which depends on both the temperature and the ability of the insulation to store space charges. It can be noticed that the higher the temperature, the fastest the dissipation of the stored charges. At 25 °C in Figure 2.25 (b), the stored charges remain at the end of the experiment at 14000 s, while at 70 °C in Figure 2.25 (d), the charges are relaxed gradually, however, the steady-state is not reached at the end of the experiment at 14000 s.
The maximum electric field presented in the pink curves in Figure 2.25 gives an indication how the specimen is stressed before and after the aging process. In the case of non-aged specimens, Figures 2.25 (a) and (c), the evolution of the maximum electric field during the polarization period is approximately constant at 20 kV/mm, while it is < 1 kV/mm during the depolarization period. In the case of aged specimens, Figures 2.25 (b) and (d), the evolution of the maximum electric field during the polarization period is approximately constant at 20 kV/mm at the room temperature, while it is increasing to reach a value of 26 kV/mm at 70 °C.

2.2.5 Discussion:

Many proposals of the electrical aging mechanisms in polymeric insulations can be found in the literature [42],[43]. In [42], experimental results suggest that most physical and chemical aging processes occurs in cavities inside the insulation or at its interfaces. Two mechanisms of electrical aging can be distinguished according to the amplitude of the electric field distributed inside the insulation:

- low (operational) electric fields: electrons in sub-excitation state are not expected to cause a chemical damage but a morphological change in the insulating material, where the electron moves as a polaron or by trapping/detrapping with energy that is sufficient to break only intermolecular bonds [42].
- high electric field: when a high electric field is applied on the insulation, hot electrons in microcavities in the bulk probably gain sufficient energy to cause intramolecular bonds rupture (i.e. C-H or C-C bonds in the molecular structure) in the insulation surface near the voids [42], which in turn allows oxidation reactions and the formation of aging products. Dissado, Mazzanti, and Montanari in [44] introduced an electronic aging model in the presence of space charges due to the reduction of the free-energy barrier from Δ to $\Delta(E) < \Delta$ as illustrated in Figure 2.26. The reduction in the free-energy barrier could be translated into fatigue in the Van der Waals bonds leading to free-volume rearrangement [45]. The latter likely induces partially reversible / partially permanent deformation of the insulation leading

at the end to microcavities formation and expansion [44]. Ionization in the gaseous molecules in microcavities might contribute to the aging process, since it triggers and sustains localized electrical discharges within the insulation which increase the chemical damage inside the dielectric [42].

Other aging phenomena attributed to relatively long impulse duration i.e. TOV might be fast charge packets. Fast packets are clusters of electrons or ions with a high mobility value. Such packets could cause space charge layer accumulation inside the insulation which is expected to accelerate and enhance the above-mentioned space charge electronic aging. This phenomenon is not likely to occur in SSI because its duration is much shorter [46]. Another possible mechanism could be involving electromechanical stresses [47] able to cause local and global plastic strain and craze formation, from which energetic phenomena (such as partial discharges) can start incepting, eventually bringing the insulation to failure.

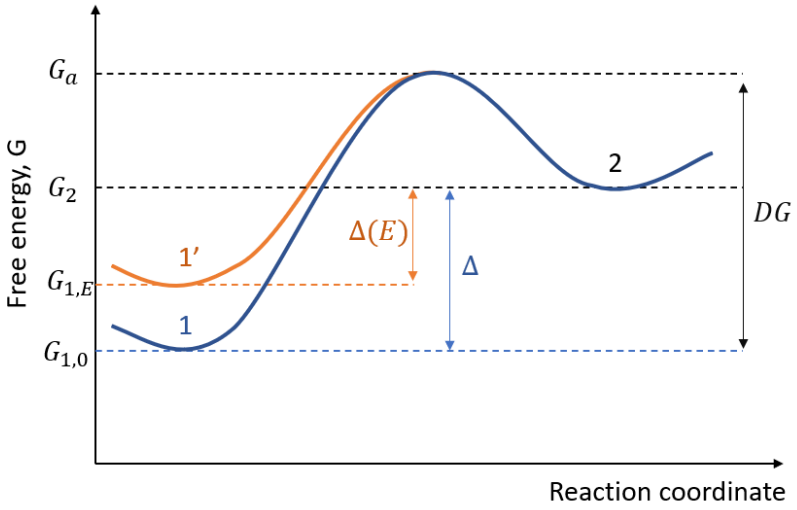

Figure 2.26 Free energy diagram in the presence of electric field (after [40]).

Space charge measurements show a noticeable variation in the electrical properties of the aged XLPE including the more ability to store space charges which is considered critical for HVDC applications where hetero-charges increase the electric field locally. Although homo-charges reduces the electric field near the electrodes, it becomes hetero-charges during Voltage Polarity Reversal VPR giving a high field that might cause failure or affect the reliability of the complete HVDC system.

2.3 Simulative study on the effect of VPRs on the life and reliability of cable:

2.3.1 Voltage Polarity Reversals (VPRs):

Voltage Polarity Reversals VPRs are transient events in HVDC cable systems that use Line Commutated Converters LCC to reverse the power flow in the electrical grid. Fast VPR events take place as a response to serious contingencies to keep the grid frequency within its operational limit in unsynchronized grids or to keep the power flow within its operational limits in synchronized grids. While slow VPRs are scheduled transient events that aim to reverse the power flow to meet the electricity market needs [48]. As the fast VPR events are linked to contingencies, they are not frequent in HVDC systems, unlike the slow VPR events which are linked to frequent variations in the electricity market. In fast VPR the voltage is switched off and reversed from U_0 to $-U_0$ within few hundreds of milliseconds as shown in Figure 2.27(a) between the time markers (1) and (2), creating two electric field transients Tr1 and Tr2 due to the residual space charge accumulated before the VPR under DC voltage. In slow VPR, the voltage is switched off from U_0 to 0 within few hundred of milliseconds during Tr 1 (1)→(2), then the voltage is kept zero for some minutes during Tr 2 (2)→(3) followed by a voltage reversal from 0 to $-U_0$ within hundreds of milliseconds during Tr 3 (3)→(4). The period at which the voltage is kept zero (t_0) serves as a relaxation period for the space charge accumulated in the cable insulation revealing the electrical stress to which the cable is subjected during Tr 4, as shown in Figure 2.27(b) [22].

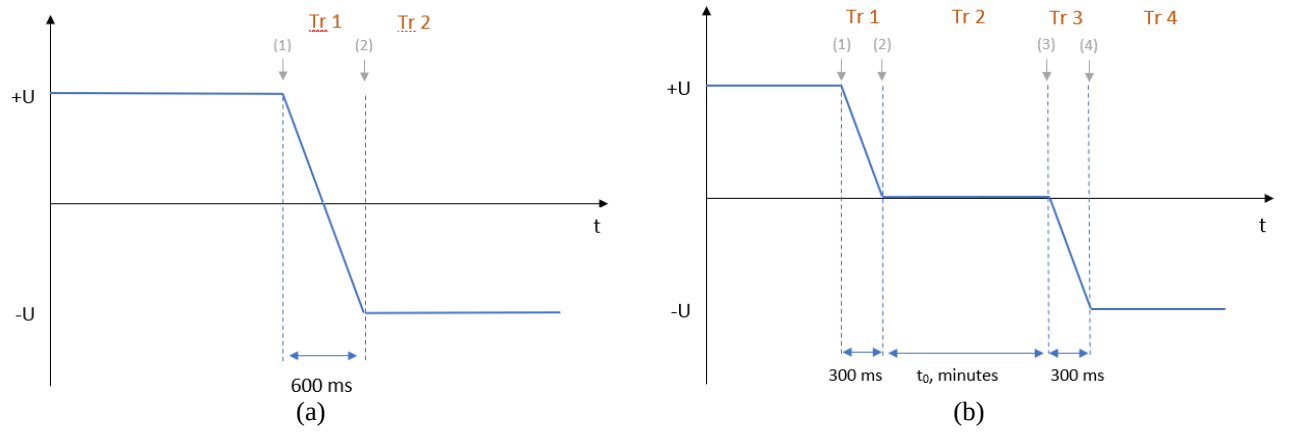

Figure 2.27 Voltage wave shape in (a) fast polarity reversal, and (b) slow polarity reversal. The markers (1), (2), (3), and (4) are the beginning instants of the transients Tr 1, Tr 2, Tr 3, and Tr 4, respectively.

2.3.2 Theoretical:

2.3.2.1 Transient field calculation:

The electric field in the insulation is calculated numerically by solving Maxwell's equations i.e. Equations (1.27) – (1.29) in addition to the conductivity equation (1.30) which macroscopically describes the relationship between the conductivity on one side and the temperature and the field on the other side. Figure 2.28 shows a flowchart of the transient electric field calculation during the slow VPR transients (*i*=1 to 4).

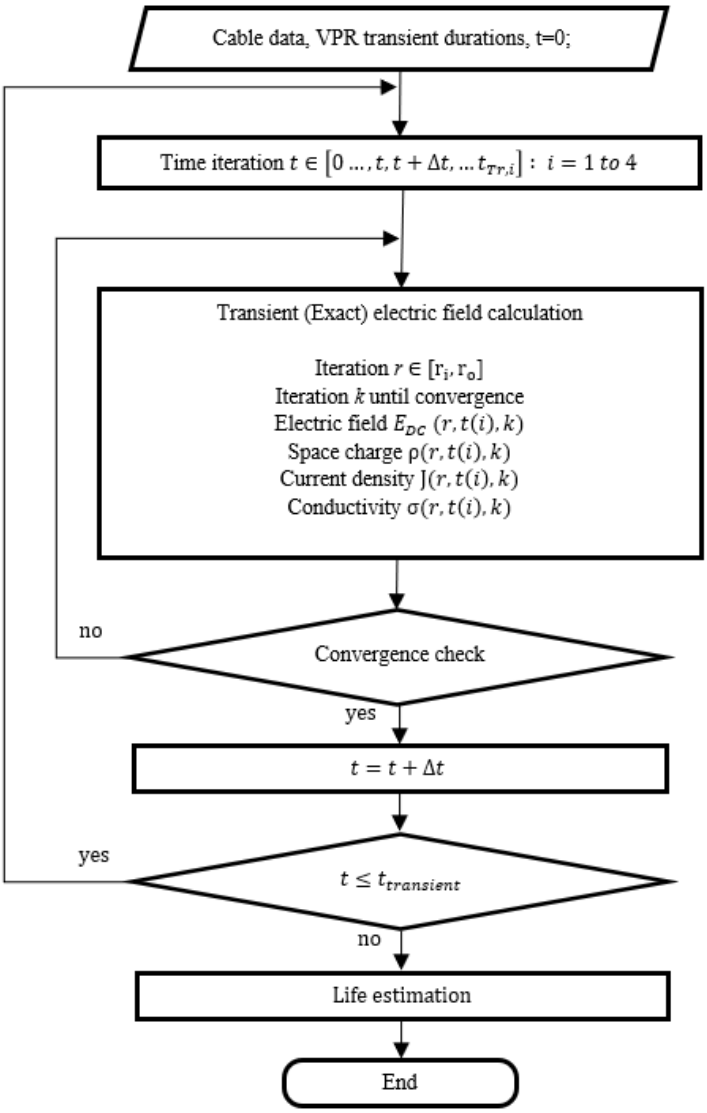

Figure 2.28 Flowchart of the transient electric field calculation and the life estimation during the slow VPR transients.

2.3.2.2 Life estimation:

The lifetime of the cable is estimated according to the electrical Inverse Power Model (IPM) and Arrhenius thermal model as expressed in the following equation:

$$L(E,T) = L_D.[E/E_D]^{-n_D}\, exp\,(-B(1/T_D - 1/T)) \tag{2.6}$$

where: $L(E,T)$ is life at a DC electric field E and temperature T (in K). E_D, T_D and L_D are design electric field, temperature and life respectively, n_D is the value of the voltage endurance coefficient (VEC) at temperature T_D, $B = \Delta W/k_B$, ΔW is the activation energy of the main thermal degradation reaction (in J), $k_B = 1.38 \times 10^{-23}\, J/K$ is the Boltzmann constant. The life is estimated at each infinitesimal time interval dt in the range $[0 \ldots, t, t + \Delta t, \ldots t_{tr}]$ of the total transient period t_{tr}. Then, the loss of life during one transient LF_{tr} can be calculated according to Miner's law of the cumulated aging during all infinitesimal time intervals dt [21], as follows:

$$LF_{tr}(r) = \int_0^{t_{tr}} \frac{dt}{L[E(r,t),T(r,t)]} \tag{2.7}$$

where $L[E(r,t),T(r,t)]$ is life obtained from (2.6).

The loss of life LF_{ss} during the steady state period of the cable's operation t_{ss} can be estimated similarly using the following equation:

$$LF_{ss}(r) = \int_0^{t_{ss}} \frac{dt}{L[E(r,t),T(r,t)]} = \frac{t_{ss}}{L[E(r),T(r)]} \tag{2.8}$$

where $L[E(r),T(r)]$ is life obtained from (2.6) and t_{ss} is calculated by subtracting the total period $t_{tr,tot}$ at which the cable is subjected to *n* transients from a reference period of time t_{tot}:

$$t_{ss} = t_{tot} - t_{tr,tot} = t_{tot} - n\, t_{tr} \tag{2.9}$$

Accordingly, the loss of life during both the steady state and the transient periods can be calculated as follows:

$$LF_{tot}\big(E(r),T(r)\big) = LF_{ss}\big(E(r),T(r)\big) + \sum_{i=1}^{n} LF_{tr,i}\big(E(r),T(r)\big) \tag{2.10}$$

Then, the lifetime of the cable at each generic radius r can be calculated using the total reference period t_{tot}, as follows:

$$L\big(E(r),T(r)\big)=\frac{t_{tot}}{LF_{tot}\big(E(r),T(r)\big)} \tag{2.11}$$

The life of cable is defined at the insulation radius which has the shortest lifetime over the insulation thickness between the inner insulation r_i and the outer insulation r_o:

$$L=\min_{r_i\le r\le r_o}\Big(L\big(E(r),T(r)\big)\Big) \tag{2.12}$$

2.3.3 Case study:

Table 2.4 illustrates the main characteristics of the 500-kV XLPE-insulated cable in addition to the laying environment that are used in both thermal and electrical calculations in this study. The temperature profile is calculated according to the transient thermal model of the cable layers in addition to the surrounding environment as described in IEC Standard 60853-2 [5]. More details about the transient temperature calculations can be found in Chapter 1. The insulation thickness is divided into 25 equally distributed points for Finite Difference Method FDM simulation performed in Matlab environment. The conductor's temperature is assumed to be constant during the steady-state period t_{ss}, however, it becomes transient during the slow VPR events for the sake of accuracy [49]. Figure 2.29 shows the temperature distribution inside the insulation thickness within 30 minutes of the period t_0.

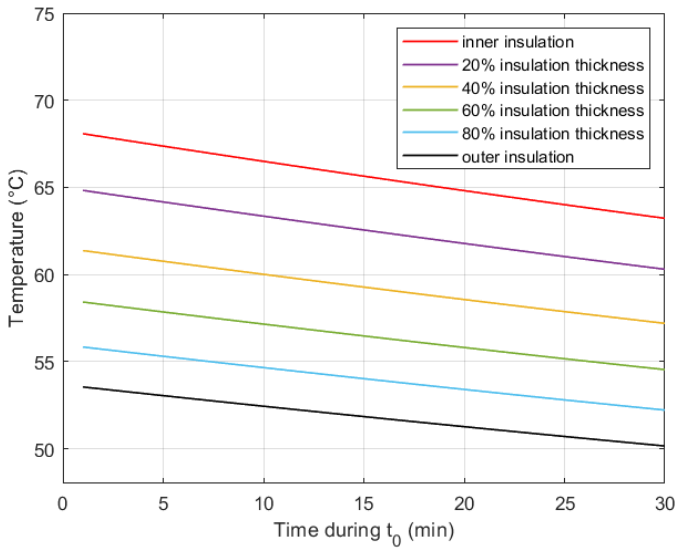

Figure 2.29 Temperature distribution within the insulation thickness during 30 minutes of the zero voltage period t_0 of the slow VPR.

Table 2.4 The characteristics of the case-study cable and the laying environment.

Parameter	**value**
Rated power (bipolar scheme) (MW)	1920
Rated voltage (kV)	500
Conductor Material	Cu
Insulation Material	DC-XLPE
Relative permittivity ε_r	2.3
Rated conductor temperature (°C)	70
Ambient temperature ϑ_a (°C)	20
Conductor cross-section (mm^2)	2000
Inner semiconductor thickness (mm)	2
Inner insulation radius r_i (mm)	27.2
Insulation thickness (mm)	28.1
Outer insulation radius r_o (mm)	55.3
Outer semiconductor thickness (mm)	1
Metallic shield thickness (mm)	1
Thermoplastic sheath thickness (mm)	4.5
Thermal resistivity of dielectric [K.m/W]	3.5
Thermal resistivity of sheath [K.m/W]	3.5
Thermal resistivity of soil [K.m/W]	1.3
Burial depth *bb* (m)	1.3
Design life L_D (years)	40
t_{tot} (year)	1
Temperature coefficient of conductivity *a* (1/°C)	0.084

Field coefficient of conductivity b (mm/kV)	0.0645

Table 2.5 shows the characteristics of the fast and slow VPR events investigated in this study. The number of VPR events is chosen according to [50] to occur from many times per year to many times per week.

Table 2.5 Characteristics of VPR events.

Parameter	**value**
Transient type	Fast and slow VPR
Frequency of VPR events [50]	0 VPR/year
	1 VPR/year
	1 VPR/month
	2 VPRs/month
	1 VPR/week
	2 VPRs/week
	1 VPR/day
t_0	0 (fast VPR)
	10 min
	20 min
	30 min

2.3.4 Results:

2.3.4.1 Electric field distribution before, during and after VPRs:

Figure 2.30 shows the transient electric field calculated inside the insulation thickness according to Equations (1.27)–(1.30) during one (a) fast VPR (b) slow VPR with t_0=10 min (c) slow VPR with t_0=20 min (d) slow VPR with t_0=30 min. In all cases, the initial point of the transient is always assumed that the cable has already reached the resistive electric field distribution as shown in the black solid curve in Figure 2.30. In Figure 2.30(a) the fast VPR first transient Tr 1 lasts 600 ms as illustrated in the dash-dotted curves, reaching the solid red curve at the end of Tr 1. Then, the transient

Tr 2 starts leading to charge relaxation within the insulation (the dotted curves) recovering at the end the resistive electric field distribution. Figure 2.30(b) shows the field distribution during the slow VPR whereby 4 transients take place Tr 1, Tr 2, Tr 3, and Tr 4 (see Figure 2.27). The only difference from fast VPR is that in slow VPR, the period Tr 2 allows a charge relaxation while the voltage is zero making the electric field low compared to the typical design fields of HVDC cables (see the dashed curves in Figure 2.30(b)). The latter reduces the electric field at the beginning of Tr 4 (the solid red curve) compared to that in the fast VPR in Figure 2.30 (a). Figures 2.30 (c) and 2.30 (d) show more charges relaxation when t_0 increases from 10 to 20 minutes, however, the difference becomes barely noticeable when t_0 increases from 20 to 30 minutes.

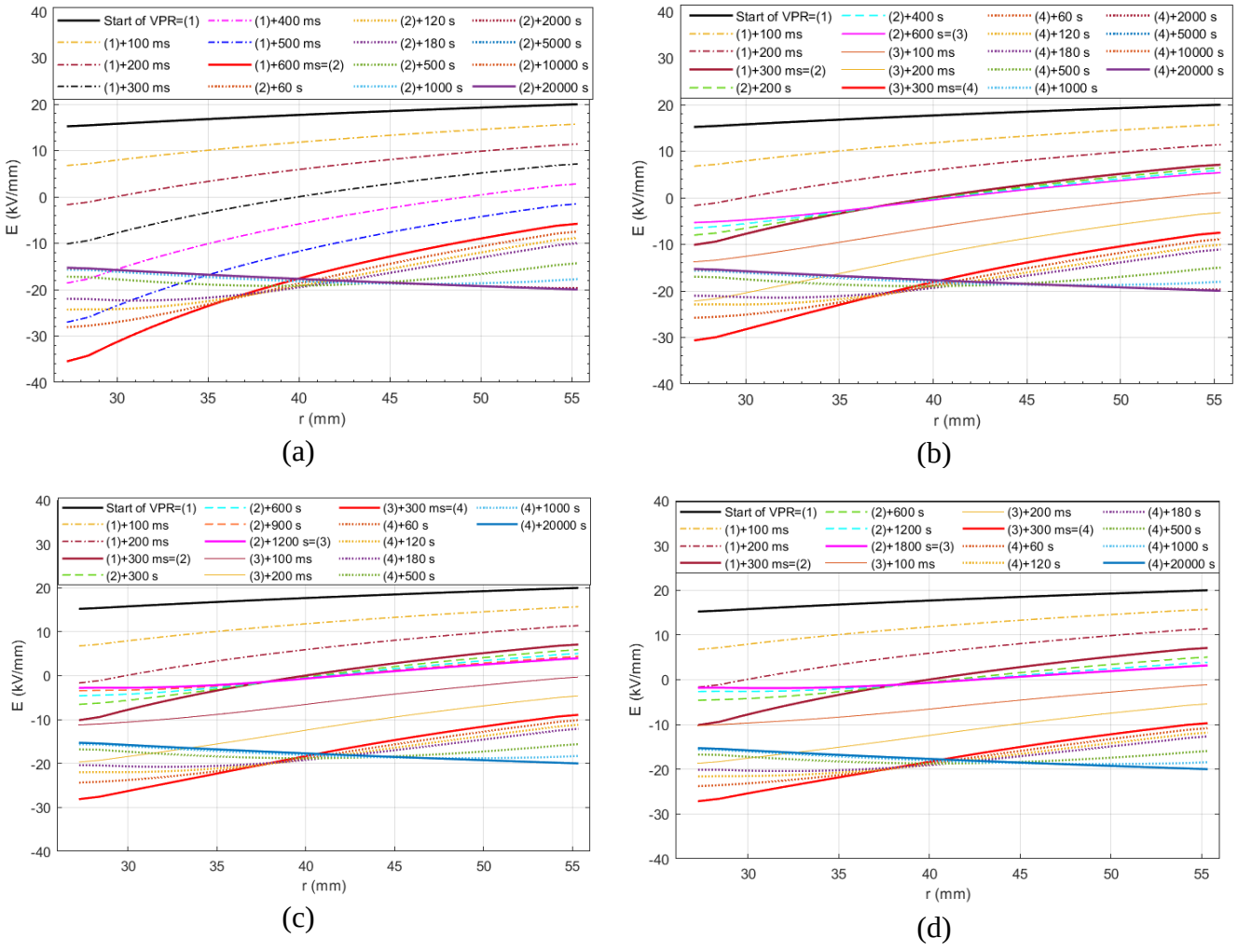

Figure 2.30 The electric field distribution in the HVDC cable insulation thickness before, during and after (**a**) fast VPR, (**b**) slow VPR with t_0=10 min, (**c**) slow VPR with t_0=20 min, (**d**) slow VPR with t_0=30 min. the markers (1), (2), (3), and (4) are defined in Figure (2.27)

2.3.4.2 Loss of life before, during and after VPRs:

Figure 2.31 demonstrates the loss of life estimated inside the insulation thickness during one (a) fast VPR (b) slow VPR with t_0=10 min (c) slow VPR with t_0=20 min (d) slow VPR with t_0=30 min. In Figure 2.31(a), the first transient Tr 1 of the fast VPR (the green solid curve) causes a relatively high loss of life in the inner insulation, while it has a low loss of life in the outer half of the insulation thickness. Nevertheless, the main loss of life occurs during the second transient Tr 2 (the red solid curve) whereby it dominates that of the Tr 1. The latter can be justified by the duration of both transients Tr1 and Tr 2 which last hundreds of milliseconds and minutes, respectively. Figures 2.31(b), 2.31 (c), and 2.31(d) show similar patterns of the loss of life during the 4 transients Tr 1, Tr 2, Tr 3, and Tr 4 highlighted in blue, green, yellow and red, respectively. While Tr 1 stresses the outer insulation, Tr 3 stresses the inner insulation and Tr 2 stresses the inner and the outer insulations. Tr 4 still has the main contribution in the loss of life with many order of magnitudes higher values. It is worth noting that the loss of life during Tr 2 is always lower than that in both Tr1 and Tr 2 together, although Tr 2 lasts for minutes while Tr1 and Tr 3 last hundreds of milliseconds. The latter shows that slow VPR reduces the loss of life compared to the fast VPR due to the reduced electric stress during t_0. Overall, only the transient after VPR (red solid curves) has noticeable effect on the life of cable.

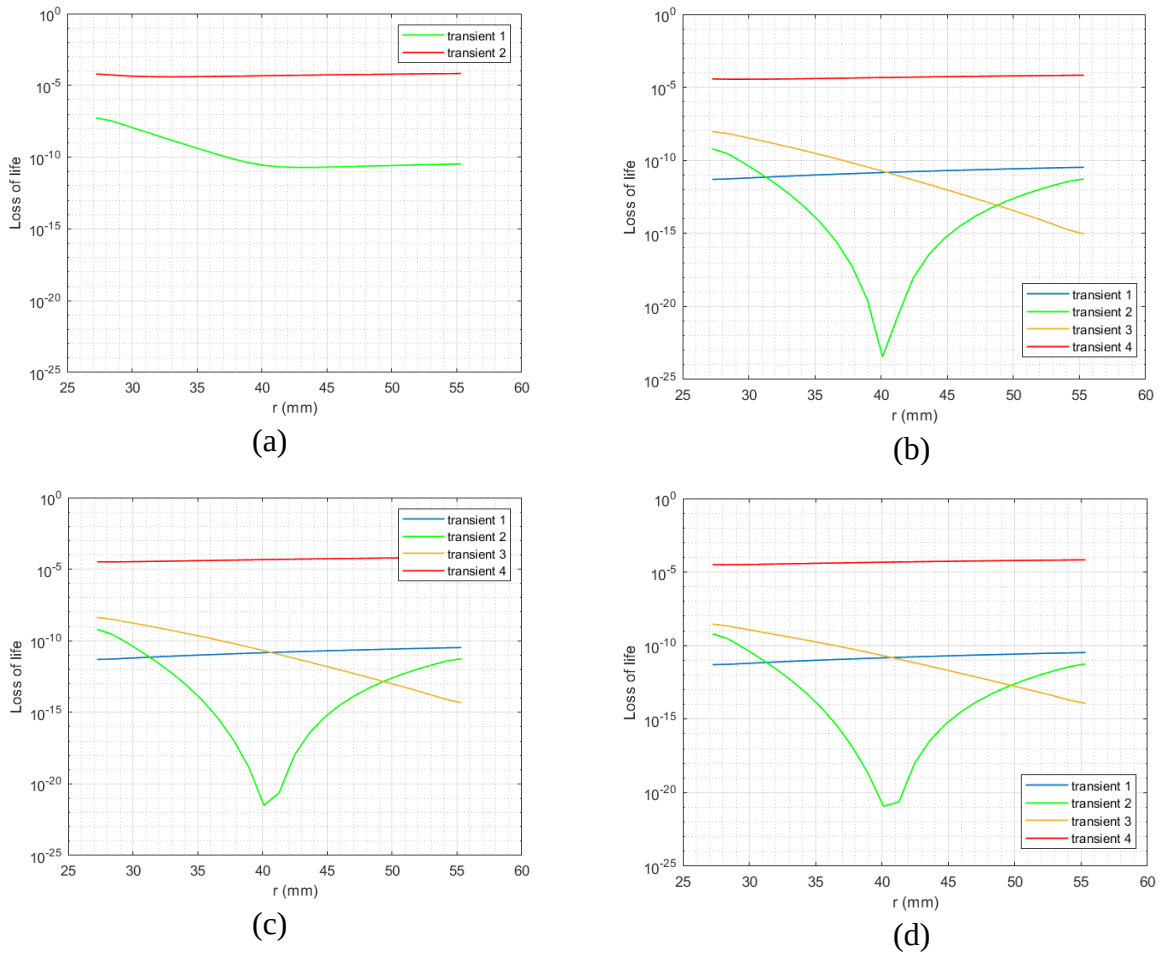

Figure 2.31 The loss of life of the case-study HVDC cable during all transients of (**a**) 1 fast VPR, (**b**) 1 slow VPR with t_0=10 min, (**c**) 1 slow VPR with t_0=20 min, (**d**) 1 slow VPR with t_0=30 min. The transients 1, 2, 3, and 4 are defined in Figure (2.27).

Figure 2.32 presents the total loss of life during the steady state and all transients (1 VPR/day) estimated according to Equation (2.10) for fast and slow VPRs considering t_0=10, 20, and 30 min (black, red, green and blue curves, respectively). It can be noticed that both fast and slow VPRs stress the inner insulation, although the outer insulation is still the most stressed point in all cases. 1 fast VPR/day makes the loss of life at the inner insulation just lower that that at the outer insulation. While 1 slow VPR/day has lower effect on the loss of life of the insulation. The latter effect becomes lower when t_0 increases until it becomes barely noticeable for t_0=30 min.

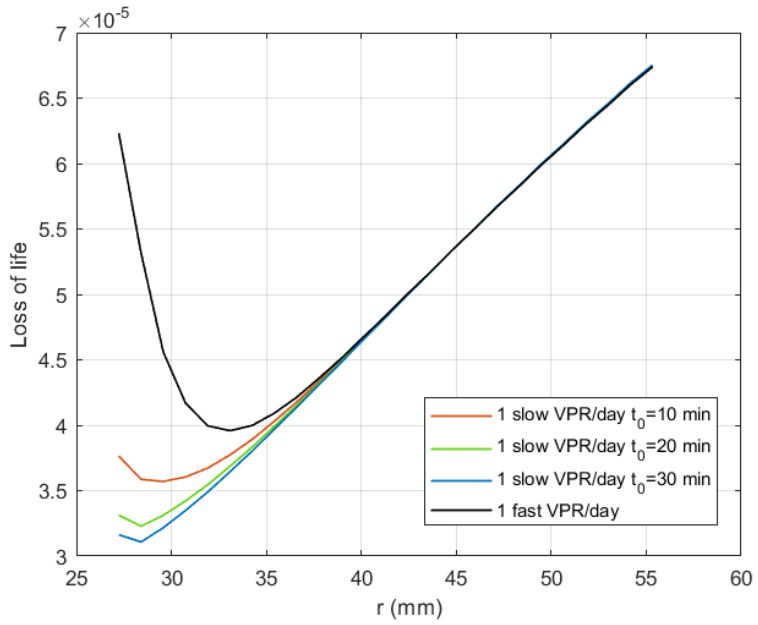

Figure 2.32 The total loss of life of the case-study HVDC cable subjected to 1 VPR/day.

2.3.4.3 Total estimated life of cable:

Figure 2.33 shows the life of cable subjected to different number of VPR events according to Table 2.5, (a) fast VPR (b) slow VPR with t_0=10 min (c) slow VPR with t_0=20 min (d) slow VPR with t_0=30 min. All Figures have the same steady-state curve (black curve) whereby the cable is subjected only to the steady-state period without any transient. The cable life is defined by the life of the outer insulation which is the most stressed point in this case. By increasing the number of transients, the inner insulation becomes more stressed until it reaches 44 years in the case of 1 fast VPR/day, 73 years for 1 slow VPR/day with t_0=10 min, 83 years for 1 slow VPR/day with t_0=20 min, and 83 years for 1 slow VPR/day with t_0=10 min, 87 years for 1 slow VPR/day with t_0=20 min. However, in all cases the life of cable is still 40 years as defined by the point which has the shortest life i.e. the outer insulation.

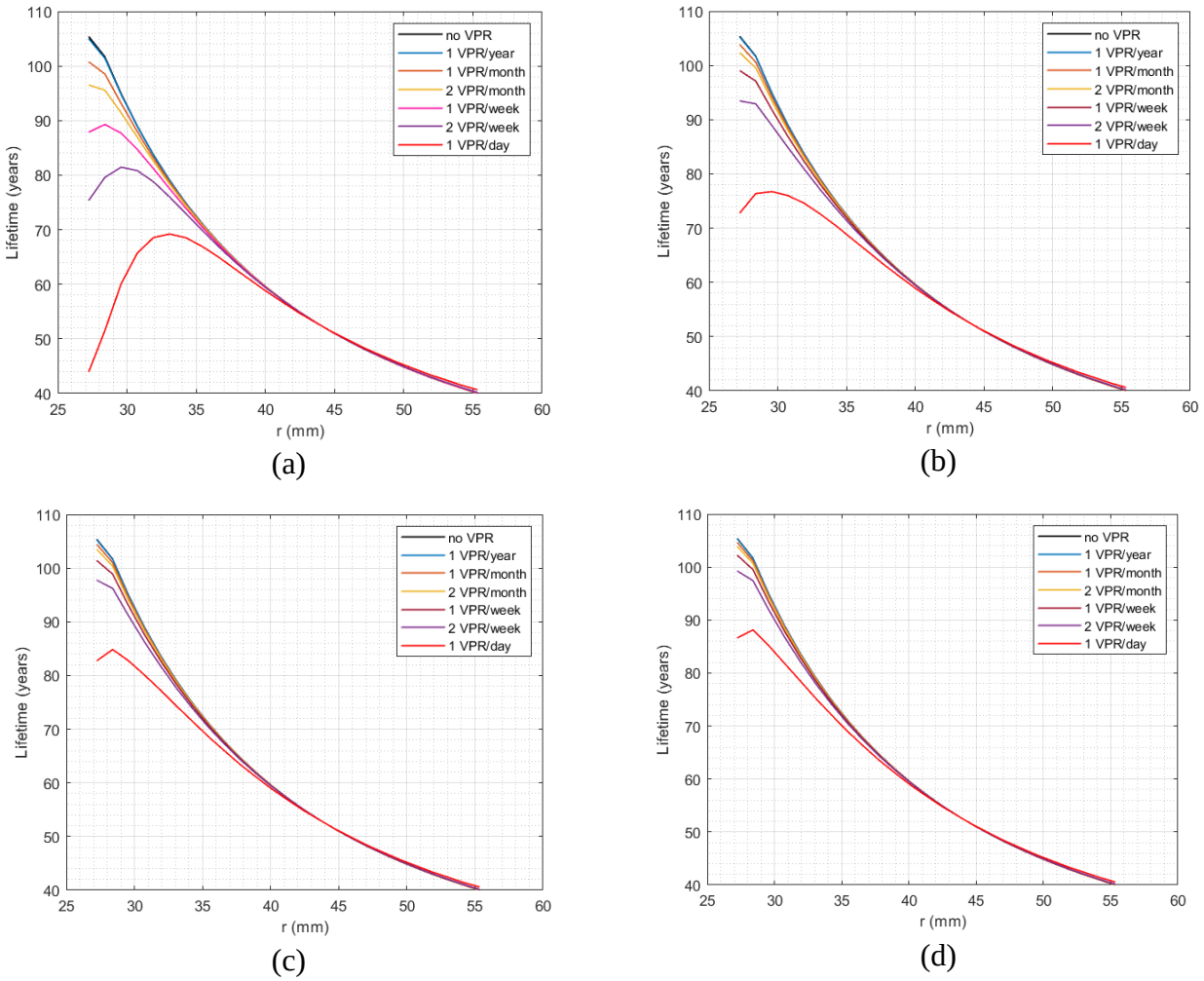

Figure 2.33 The life of cable subjected to different number of VPRs ranging from 1 VPR/year to 1 VPR/day, (**a**) fast VPR, (**b**) slow VPR with t_0=10 min, (**c**) slow VPR with t_0=20 min, (**d**) slow VPR with t_0=30 min.

2.3.5 Discussion:

The results presented in this study highlight the effect of VPR events on the life of cable. The electric field distribution is significantly affected by the transients leading to a non-monotonous life distribution inside the insulation thickness. Furthermore, the results demonstrate the significant effect of fast VPRs on the life of cable compared to that of slow VPRs. While 1 fast VPR/month reduces the local life in the inner insulation by ≈ 10%, 1 VPR/day causes a life reduction by 60%. The latter affirms the importance of avoiding the fast VPR as much as possible or replace it with slow VPR where possible, since the same number of slow VPRs can enhance the life reduction by [40÷50]% compared to the fast VPRs. This is justified by the reduction of the maximum transient electric field after VPR because of the relaxation of the residual charges in the insulation during the period at which the voltage is kept zero t_0. The results also show that the reduction of the life loss by increasing t_0 is more effective in the first 10 minutes, then it gradually decreases as t_0 becomes longer (and the transient electric field becomes lower and the conductivity becomes lower), then the time constant of the insulation increases.

Chapter 3

Life-based design of HVDC cables

3.1 Introduction:

HVDC cable technologies have been getting more attention during the last decades, especially with the booming use of renewable energy sources [2]. This implies the need to transmit these energies to energy demand centers, accordingly, the need to raise the voltage and power of HVDC cable systems to reduce the losses as much as possible. In this regard - and due to the rising appeal of cables vs overhead lines in land and submarine links - some huge HVDC projects have been and are currently being installed, such as the land German corridors (525 kV) [51], using both Cross-linked Polyethylene (XLPE) and innovative High Performance Thermoplastic Elastomer (HPTE) extruded cables, and the Western Link project between Scotland, England and Wales (600 kV), using Mass Impregnated - Paper Poly-propylene Laminate (MI-PPL) cables. A higher voltage (640 kV) HVDC-XLPE cable system was also fully qualified [31].

As readily seen, these latter developments are also driven by the progressive development of innovative HVDC insulating materials. This is a consequence of the continuous desire to extend the limits of transmission systems to higher and higher capacities, increasing transmission voltages and/or ampacity.

In this chapter, the following points are investigated:

- Parametric analysis of the life-based geometric design of HVDC cables.
- the effect of Temporary OverVoltages (TOVs) and Super-imposed Switching Impulses (SSI) on the life-based geometric design of HVDC cables since higher voltage necessarily means greater and more severe electrical transients [52],[53].

3.2 Case study:

3.2.1 Parametric Analysis:

In this study, the DC electric field is calculated depending on the analytical closed-form formula introduced by Eoll in Equations (1.33) and (1.34), instead of the exact iterative method calculated using Maxwell's Equations (1.27) to (1.30). The main reason is that a great number of designs is tested here, the latter makes applying the iterative method at each design is time consuming.

Table 3.1 Main design parameters of the HVDC cable

Cable parameters	**Symbol and unit**	**value**
Design life	L_D [years]	**40**
Voltage Endurance Coefficient n_D	[a.u.]	**10**

Design temperature	T_D (=T_{ro}) [°C]		**55**
Design electric field	E_D [kV/mm]		**20**
Rated voltage	U_0 [kV]		**320**
			525
			640
Maximum conductor temperature	T_{max} [°C]		**70**
			90
Temperature coefficient of conductivity	a [$°C^{-1}$]	a_L	0.042
		a_M	**0.084**
		a_H	0.168
Stress coefficient of conductivity	b [mm/kV]	b_L	**0.03**
		b_M	0.06
		b_H	0.12
Thermal resistivity of dielectric	$\rho_{T,d}$ [K.m/W]		**3.5**
Thermal resistivity of sheath	$\rho_{T,sh}$ [K.m/W]		**3.5**
Thermal resistivity of soil	$\rho_{T,so}$ [K.m/W]		1
			1.3
			1.5
			1.7

Table 3.1 presents the main design parameters of the HVDC cable. For some of them multiple values are considered, in the framework of a dedicated parametric analysis. The bold numbers are the values of a reference cable design, with inner and outer insulation radii set to (r_i, r_o) = (21.4, 39.7) mm, whose design life is 40 years. In particular, the bold values of *a* and *b* are typical values for DC-XLPE insulation according to scientific literature [54]; the other two values of *a* and *b* are generated by halving and duplicating the medium values, thereby yielding the so called low values a_L,b_L and high

values a_H,b_H, respectively. The actual values of the compounds used by the various manufacturers are in fact confidential, but they can be deemed to span over the chosen intervals reported in Table 3.1.

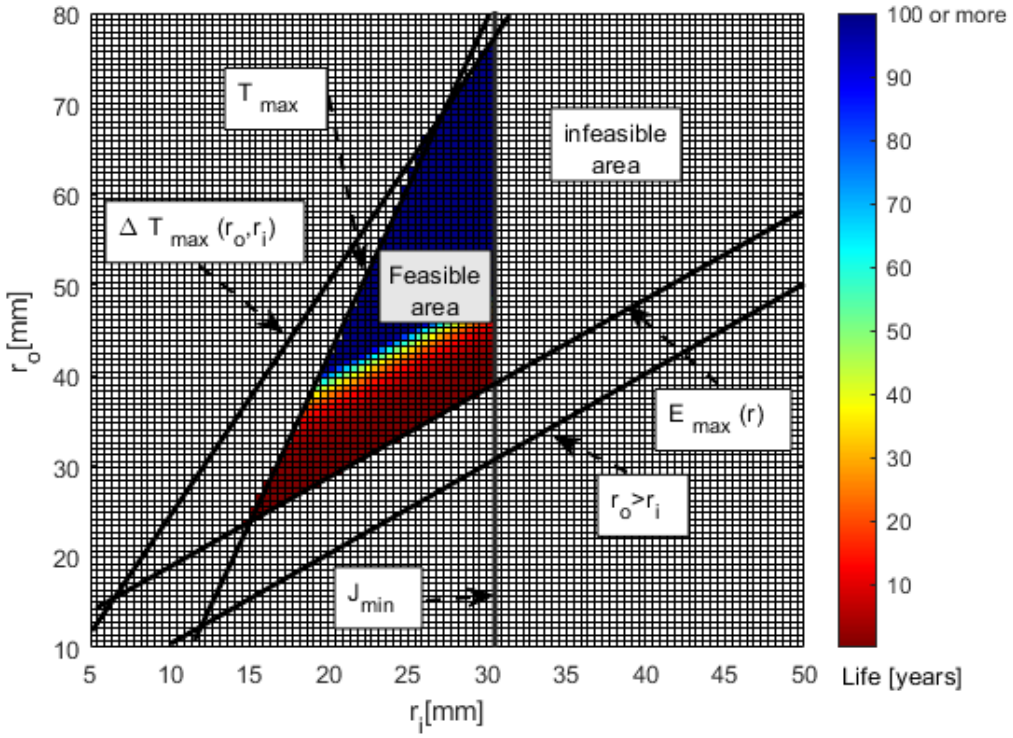

Figure 3.1 Life map in linear scale for hot cable, highlighting the constraints defining the feasible design area.

All possible cable designs are simulated – with inner and outer insulation radii spanning over the following ranges: $(r_i, r_o) = (5 \div 50{,}10 \div 80)\ mm$ – using an ad hoc Matlab code to calculate the life of each design. This procedure results in a two-dimensional graph as in Figure 3.1, where the "feasibility loci" of the life map are defined by the limits given by 5 constrained quantities, i.e.:

1) maximum dielectric temperature T_{max}
2) maximum temperature drop across the insulation, ΔT_{max}
3) maximum electric field E_{max}.
4) minimum conductor current density J_{min}
5) maximum extrusion radius $r_{o,max}$.

Although the minimum design life $L_m > L_D$ (green and blue areas) is highlighted in the results, shorter life designs which satisfies constraint 3) (red area) are also investigated for the sake of completeness. These limits are as stated in Table 3.2 on the basis of typical manufacturing constraints, in addition to the case in which ΔT_{max} is not limited by any constraint. It is worth noting that the positive thickness condition i.e., $r_o > r_i$ is always redundant since it is implicitly included in the

maximum electric field condition. Hereinafter, only the latter will be considered. On the contrary, the maximum extrusion radius is necessary to consider the technical limits of available industrial extruders. The minimum conductor current density J_{min} represents the minimum utilization limit of the conductor cross section below which the conductor cross section becomes excessively large.

Table 3.2 Constrained quantities and the relevant limits

Feasible area conditions	**Limit value**
$J > J_{min}$ [A/mm²]	**0.6**
Maximum extrusion radius $r_{o,max}$ $[mm]$	**80**
$r_o > r_i\ (redundant)$ & $max\big(E(r)\big) < E_{max}$	$\boldsymbol{E_{max} = 40\ kV/mm}$
$T(r_i) < T_{max}$	$\boldsymbol{T_{max} = 70\ °C}$
	$T_{max} = 90\ °C$
$\Delta T = T(r_i) - T(r_o) < \Delta T_{max}$	$\Delta T_{max} = 10\ °C$
	$\Delta T_{max} = 15\ °C$
	$\boldsymbol{\Delta T_{max} = 20\ °C}$
	ΔT_{max} has no limit

3.2.2 Electrical transients:

In this study, voltage polarity reversal (VPR) is studied as an electrical transient due to its severe effect on HVDC polymeric cables. VPRs in HVDC systems can be of two types, namely fast and slow VPRs as defined in section 2.3.1.

VPRs can be divided into 2 parts [48]:

1) a first transient referred hereafter to as tr_1, occurring while the polarity of the applied voltage is reversed (i.e. $+U_0 \rightarrow -U_0$ or $-U_0 \rightarrow +U_0$). This transient lasts hundreds of milliseconds in fast VPRs, while it lasts a few minutes in normal operation;

2) a second transient, referred hereafter to as tr_2, is the field transient occurring after the VPR, when the voltage applied is opposite to the voltage before the VPR.

This study investigates only fast VPRs. As such:

a) during the first electrical transient the field distribution within the cable switches from the initial resistive to a subsequent quasi-capacitive distribution;

b) during the second electrical transient the charges inside the insulation thickness redistribute within a period ranging between minutes to hours, until the electric field reaches a resistive distribution. For the sake of simplicity and computational efficiency, the electric field variation during such second electrical transient is represented here according to the following approximated exponential model, previously introduced in [48],[55], and validated in [22] giving uncertainty lower than 2% for fast VPR, see Fig. 1:

$$E(r,t) = E_2(r) + [E_1(r) - E_2(r)] \cdot exp(-t/\tau_E(E,T)) \tag{3.1}$$

where t is the generic time, $\tau_E(E,T)$ is the electrical time constant of the insulating material of the cable, which is given in DC systems by the following equation:

$$\tau_E(E,T) = \varepsilon/\sigma(E,T) \tag{3.2}$$

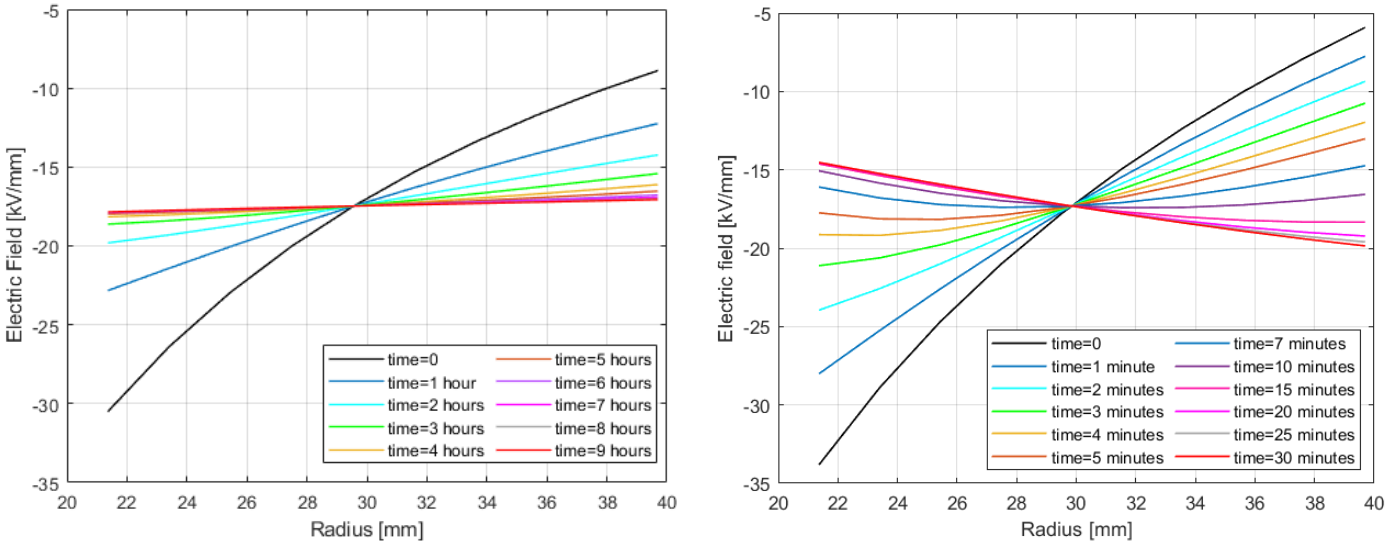

(a) (b)

Figure 3.2 Electric field variation over the period $5\tau_E$ during the second electrical transient after a fast VPR from $+U_0 \rightarrow -U_0$ for the so-called reference cable in hot conditions and (a) $a = 0.042$ and (b) $a = 0.084$. The main design data of the reference cable are listed in bold in Table 3.1.

$E_1(r)$, and $E_2(r)$ are the electric fields at the beginning of the second transient tr_2 and at the steady state after the VPR, respectively. The profiles within insulation thickness of $E_1(r)$ and $E_2(r)$ during the second electrical transient after a VPR from $+U_0$ to $-U_0$ for the so-called reference cable (the main design data of the reference cable are listed in bold in Table 3.1) in hot conditions are

represented in Figure 3.2 by the black and red curves, respectively. Those fields are given by the following equations [56]:

Transient
$$E_1(r) = E_{DC} - 2E_{ac}(r) = E_{DC} - 2U_0/r \ln(r_o/r_i) \quad (3.3)$$

Steady state
$$E_2(r) = -E_{DC} \quad (3.4)$$

Due to the negligible time duration of the first transient tr_1 in fast polarity reversal, only the second transient tr_2 will be investigated in this study. It is also worth noting that the time between two consecutive VPRs is assumed to be greater than or equal to $5\tau_E$ i.e., hence the steady state is supposed to be always reached after tr_2.

Table 3.3 shows the parameters of the electrical transients considered in this study. The initial electric field is the electric field directly after fast polarity reversal whereas the steady-state field is the resistive DC electric field distribution. It is worth noting that the time required to reverse the applied voltage is neglected here, being much shorter than the dielectric relaxation transient considered in Equation (3.2) (hundreds of milliseconds vs. minutes to hours). The electrical transients are applied during t_{tr}, while the resistive DC electric field is used for the calculations during t_{ss}. The number of electrical transients falls in the range from 1 transient per month up to 10 transients per day, as polarity reversals occur from few times per year to many per week according to [50] (it should also be pointed out that 10 events are an upper limit of transients within one single day, which occurs only on a minority of the overall service days of the cable system). However, this number is limited in this study to 2 electrical transients per day when considering low values of the temperature coefficient of conductivity, a, causing the increase of the time constant of the insulation, as shown in Figure 3.3. A higher number of transients in this case would make the transients period longer than the total period $t_{tr} > t_{tot}$.

Table 3.3 Parameters and Characteristics of Electrical Transients

Parameter	symbol		Value
State 1	E_1		E distribution directly after polarity reversal (6)
State 2	E_2		Resistive electric field distribution (7)
Direction			$tr2: E_1 \rightarrow E_2$, tr_1 is neglected
Transient equation			(4)
Electrical time constant	τ_E		(5)
Transients frequency	n_E	a_L	0

			1 per month
			1 per week
			2 per week
			1 per day
			2 per day
		a_M	0
			1 per month
			1 per week
			2 per week
			1 per day
			2 per day
			5 per day
			10 per day

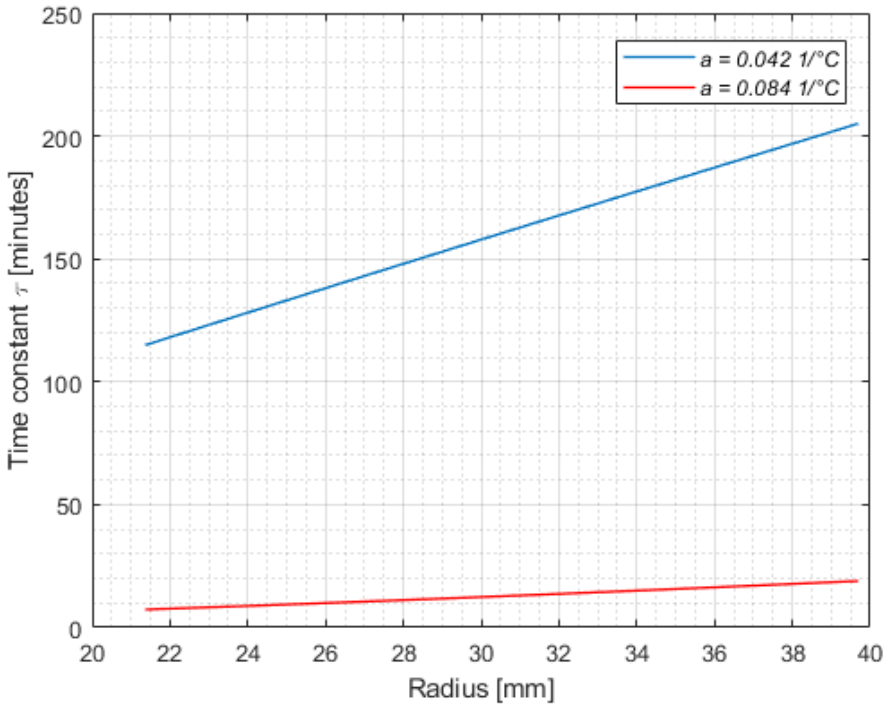

Figure 3.3 Electrical time constant $\tau = \varepsilon/\sigma$ for a hot reference cable ($r_i = 21.4$, $r_o = 39.7$ mm), for $a = 0.042$ and $a = 0.084$.

3.2.3 Thermal transients:

Thermal transients reflect the load cycles to which the cable is subjected throughout the year due to the load variation and in turn the variation in heat dissipation from the conductor across the insulation,

see Figure 3.4 (the LT→HT transient and HT→LT transient are described in Table 3.4). Strictly speaking, the rigorous treatment of such thermal transients would require the use of high order "ladder-type" equivalent thermal models made of multiple cascaded series thermal resistances and shunt thermal capacitances, as prescribed by Standard IEC 60853 [5]. However - again for the sake of simplicity and computational efficiency - the thermal transients are also represented here according to the following approximated exponential model:

$$T(r,t) = T_2(r) + [T_1(r) - T_2(r)] \cdot exp(-t/\tau_T) \tag{3.5}$$

where $T_1(r)$ is the initial temperature and $T_2(r)$ is the steady-state temperature. Equation (3.5) is the step response of a simplified first-order thermal circuit in which both the initial and the steady-state temperature is pre-defined to assure that the steady state temperature is reached and the load cycle is fully represented by the transient.

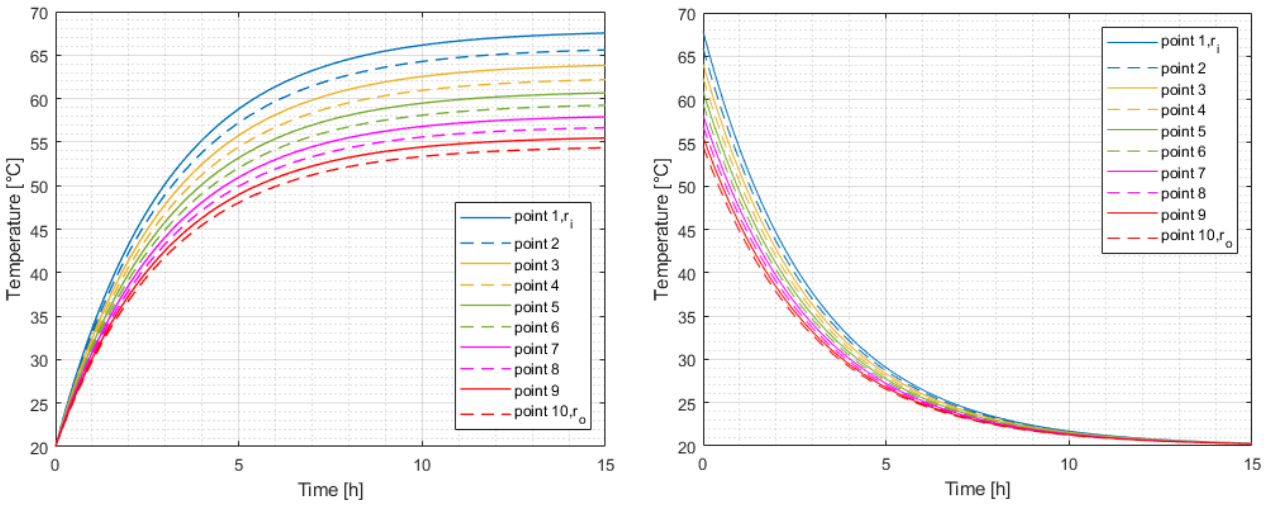

(a) (b)

Figure 3.4 Temperature transients over time = $5\tau_T$ at 10 evenly spaced points inside the insulation thickness (a) $LT \rightarrow HT$ transient and (b) $HT \rightarrow LT$ transient. The LT→HT transient and HT→LT transient are described in Table 3.4.

The validation of the approximated exponential transient thermal model vs. the higher order models recommended by IEC 60853 for MV and HV cables can be found in [57],[58],[59],[60]. The temperature distribution within the insulation thickness $T(r)$ is found from considerations detailed in [5],[61], bringing to the following equation:

$$T(r) = T(r_i) - [T(r_i) - T(r_o)]\, ln\left(\frac{r}{r_i}\right) / ln\left(\frac{r_o}{r_i}\right) \tag{3.6}$$

Table 3.4 presents the parameters of the thermal transients. Two types of thermal transients are investigated i.e., heating transient ($T_1 \rightarrow T_2$) and cooling transient ($T_2 \rightarrow T_1$), applied on the cable

during the transient period t_{tr}. A full load (hot cable) is used for steady-state calculations during t_{ss}. Thermal time constant τ_T ranges from 1 hour to many hours depending on the surrounding environment, burial depth …etc [62], [63]. In this study, two values of the thermal time constant are investigated i.e., 1 hour corresponding to air environment and 3 hours for soil environment. One transient per day is chosen for this study, i.e., one cycle includes both thermal transients ($T_1 \rightarrow T_2$ and $T_2 \rightarrow T_1$) every other day.

Table 3.4 Parameters and Characteristics of Thermal Transients

Parameter	**Symbol and unit**	**Value**
State 1 of $T_{conductor}$	T_1 [°C]	20 (Ambient temperature)
State 2 of $T_{conductor}$	T_2 [°C]	70 (Full load temperature)
Direction		$T_1 \rightarrow T_2$
		$T_2 \rightarrow T_1$
Transient equation		(8)
Thermal time constant	τ_T [h]	1
		3
Transients frequency	n_T	0
		1 per day

3.2.4 Life model:

Life estimation is based on the Inverse Power Model (IPM) and Arrhenius electro-thermal life models which can be expressed as follows:

$$L(E,T) = L_D.[E/E_D]^{-n_D} exp(-B(1/T_D - 1/T)) \quad (3.7)$$

where: $L(E,T)$ is life at a DC electric field E and temperature T (in K). E_D, T_D and L_D are design electric field, temperature and life respectively, n_D is the value of the voltage endurance coefficient (VEC) at temperature T_D, $B = \Delta W/k_B$, ΔW is the activation energy of the main thermal degradation reaction (in J), $k_B = 1.38 \times 10^{-23}\, J/K$ is the Boltzmann constant.

Considering a reference time t_{tot} (e.g. $t_{tot} = 1yr$), a steady state fraction, t_{ss}, can be defined as:

$$t_{ss} = t_{tot} - t_{tr} \quad (3.8)$$

where t_{tr} is the cumulative duration of all transient periods occurring within the same reference time t_{tot}. Consequently, the loss of life occurring during the steady state period t_{ss} within the reference time t_{tot} can be written as follows, according to Miner's law of cumulated aging [21]:

$$LF_{ss}\big(E(r),T(r)\big) = \int_{t=0}^{t_{ss}} \frac{dt}{L_{ss}\big(E(r,t),T(r,t)\big)} = \frac{t_{ss}}{L_{ss}\big(E(r),T(r)\big)} \tag{3.9}$$

where L_{ss} is life obtained from (3.7), and fields and temperatures are considered constants (since that is the case during t_{ss}). Accordingly, life loss during a single transient can be found by:

$$LF_{tr,i}\big(E(r),T(r)\big) = \int_{t=0}^{5\tau} \frac{dt}{L_{tr}\big(E_i(r,t),T_i(r,t)\big)} \tag{3.10}$$

where τ is the time constant, it is either the time constant of the electrical transient τ_E or the time constant of the thermal transient τ_T depending on the type of the transient. L_{tr} is life obtained from Equation (3.7), and considering both the electrical and thermal fields, E_i, T_i are variables with time and the type of the transient i.e. electrical or thermal. The total loss of life occurring within t_{tot} can be attained by cumulating the loss of life during both the steady-state period LF_{ss} and a number *n* of transient events:

$$LF\big(E(r),T(r)\big) = LF_{ss}\big(E(r),T(r)\big) + \sum_{i=1}^{n} LF_{tr,i}\big(E(r),T(r)\big) \tag{3.11}$$

Then, the life (e.g., in years) of insulation at different points in the cable insulation thickness can be estimated as follows:

$$L\big(E(r),T(r)\big) = t_{tot}/LF\big(E(r),T(r)\big) \tag{3.12}$$

Then, cable life is defined by the shortest life found within the insulation thickness:

$$L = \min_{r_i \le r \le r_o} \Big(L\big(E(r),T(r)\big)\Big) \tag{3.13}$$

3.3 Results:

3.3.1 Parametric analysis:

Figure 3.1 shows the life colormap of the HVDC cable reference design (bold values in Table 3.1 and Table 3.2). As a consequence, life is displayed as a gradient distributed between red (shortest life) and blue (longest life). For better visualization of the life map plots, the color scale is limited to values ranging $(0 \div 100)$ years (i.e. >100 years until 10^6 years, are also represented by the same color, i.e. dark blue). Yellow, green and blue areas are the feasible design areas, and the white surrounding area outside the boundaries is infeasible, due to the violation of one (or more) of the conditions stated in Table 3.2.

3.3.1.1 Effect of electric field and insulation thickness:

Figure 3.5, which reports life in log scale, shows the great sensitivity of life to inner and outer insulation radii: a 1-mm uncertainty of these radii leads to many years variation in the electrothermal life of cable. This is mainly justified by the great effect of electric field variation (which in turn strongly depends on the inner and outer radii of the insulation as shown in Eoll's Equation (1.33)) on HVDC cable insulation life. On the other hand, the same uncertainty would not be able to give a sensitive modification of the temperature gradient, and life consequently (considering the typical activation energy of HVDC cable insulation). This is the reason why the equi-life loci (points having the same color) are practically parallel to the maximum electric field limit, whereas the effect of the temperature is barely noticed. This means that the electric field impact dominates the thermal impact in the life map. To separate the electrothermal impact, the relative electric field and relative temperature are plotted separately in Figure 3.6(a) and 3.6(b), respectively. By comparing those two Figures, it can be clearly seen that the electric field is extremely sensitive to the cable geometries, while the temperature varies only slightly with the variation of the cable geometries.

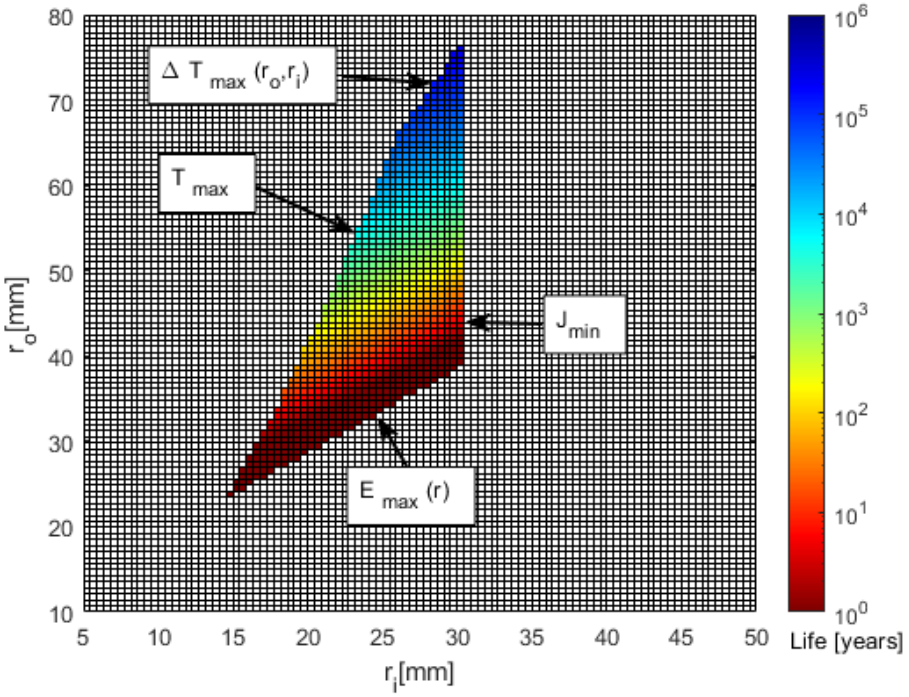

Figure 3.5 Life map in logarithmic scale for a hot cable

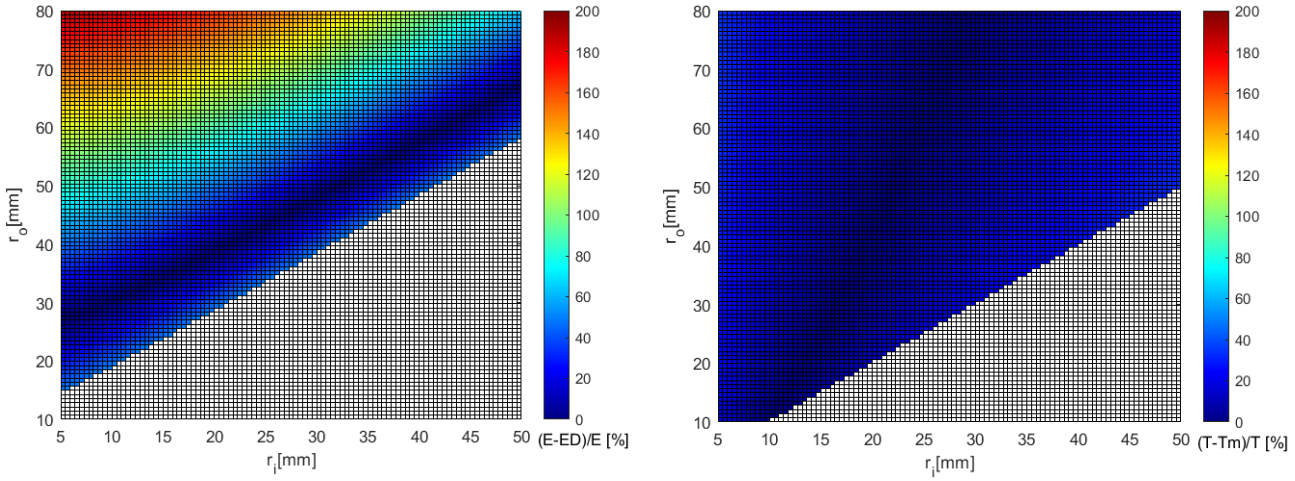

(a) (b)

Figure 3.6 Percentage relative variations of (a) electric field and (b) temperature, for all possible cable designs.

While Figures 3.1, 3.5 are life maps, Figure 3.7 is a "field differential map" that reports the difference between the field at inner and outer insulation, $\Delta E = E(r_i) - E(r_o)$ for the cable in (a) hot and (b) cold conditions. This illustrates the field inversion phenomenon across the insulation of hot HVDC cables (Figure 3.7(a)) vs. the quasi-capacitive electric field distribution of the cold cable (Figure 3.7(b)). It is necessary to limit the field inversion in HVDC cables (when $\Delta E < 0$), which is greater with thinner insulation and vice versa.

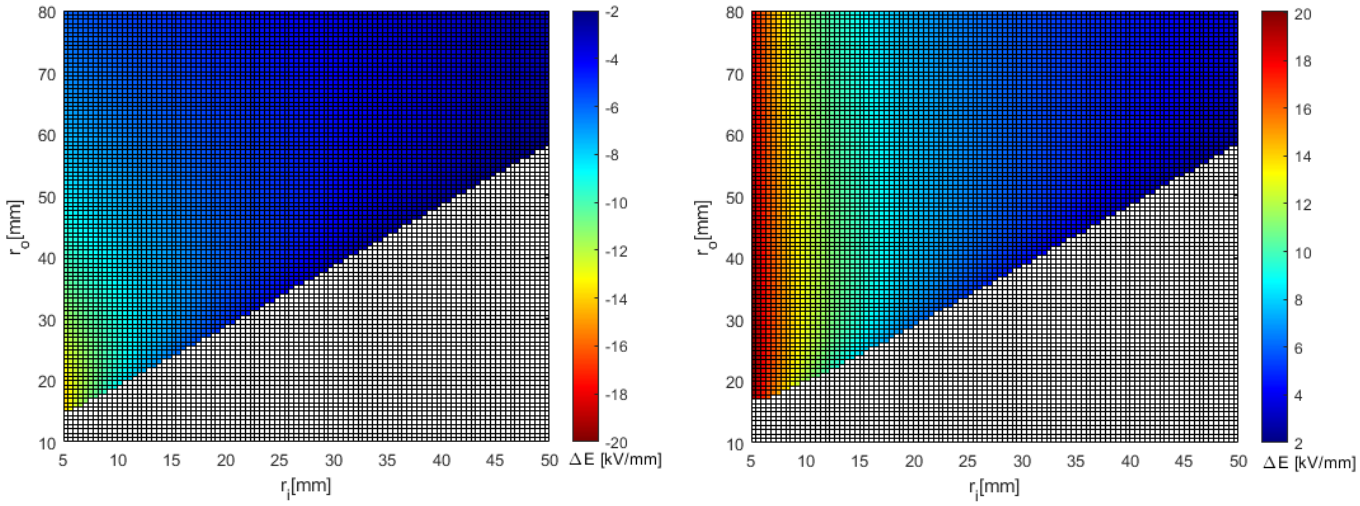

(a) (b)

Figure 3.7 Electric field difference between the inner and the outer insulation $\Delta E = E(r_i) - E(r_o)$ for (a) hot cable (field inversion), and (b) cold cable (quasi-capacitive field distribution).

3.3.1.2 Effect of conductor temperature and Temperature drop:

Figure 3.8 shows the life map of HVDC cable designs with the constraints on maximum insulation temperature T_{max} and on temperature drop across the insulation ΔT_{max} set – for the sake of parametric analysis – to all values in Table 3.2, i.e. 70°C (the reference cable design) and 90°C for T_{max}, 20°C (reference design), 15°C and 10°C for ΔT_{max}. ΔT_{max} is a limit usually set by the TSOs before the cable manufacturing process, to control the field inversion phenomenon and reduce HVDC cables losses. Feasibility loci can be found on the right side of the lines defined by both T_{max} and ΔT_{max}.

It is seen that the greater the maximum conductor temperature, the smaller the allowed insulation radii (r_i, r_o) and the overall size of the cable. Momentarily neglecting ΔT_{max} and increasing the maximum conductor temperature from 70 to 90 °C, the insulation radii of a cable having design life of 40 years can significantly be reduced, from (r_i, r_o) = (19, 37) mm to (9, 31) mm, (see Figure 3.8). This leads to a great reduction in the conductor radius but conversely a small increase in the insulation thickness. However, such a value violates one of the limits in Table 3.2 on temperature drop across the insulation, as $\Delta T_{max} > 20$ °C (see Figure 3.9). This implies that the advantage of an increased feasible area due to maximum conductor temperature rise is limited by ΔT_{max}, e.g. for $\Delta T_{max} = 10$ or 15 $°C$ respectively no or very small benefits can be attained by increasing T_{max} above 70 °C, as readily seen from Figure 3.8. On the other hand, for $\Delta T_{max} = 20\ °C$, the feasible area can be extended up to (14, 35) mm for $L_D = 40$ years. As a result, developing insulating materials able to withstand higher temperatures can scale the overall cable dimensions down only when a suitable temperature gradient can also be allowed. Since those results come from the necessity to limit field inversion, which in turn is affected by both temperature and field coefficients of conductivity, their effects will be discussed in the next sections.

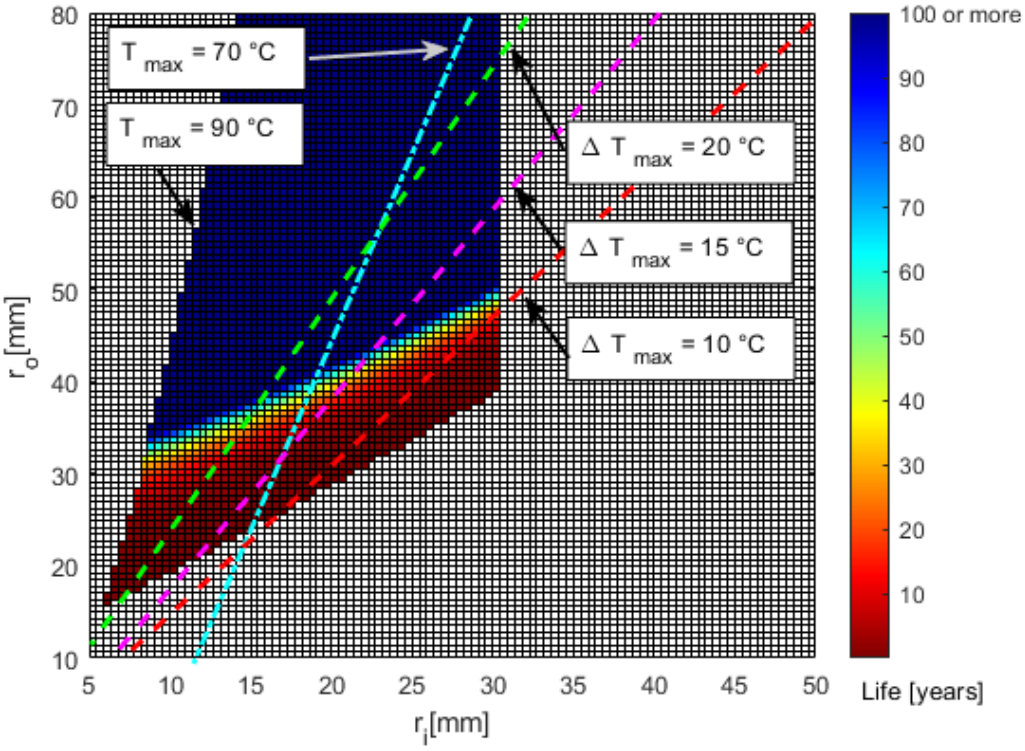

Figure 3.8 Life map in linear scale for 3 different values of the maximum temperature drop inside the insulation thickness ΔT_{max} and 2 values of the maximum conductor temperature T_{max}.

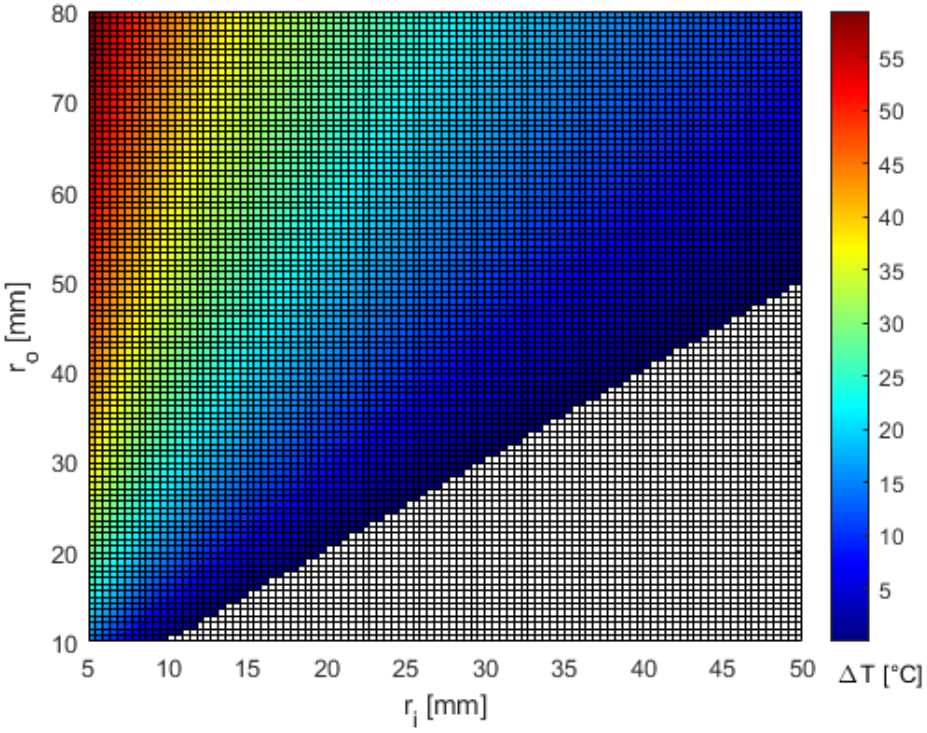

Figure 3.9 Temperature drop ΔT = $T(r_i)$ - $T(r_o)$ map between the inner insulation (T_{max}) and the outer insulation $T(r_o)$.

3.3.1.3 Effect of temperature coefficient of electrical conductivity *a*:

Temperature coefficient of electrical conductivity a has a major effect on the resistive electric field distribution inside the insulation of HVDC cables and in turn on cable life (Figures 3.10, 3.11, 3.12). For the sake of comparison, the 3 values of a from Table 3.1 are used to plot these Figures. It must be specified that results of field distribution in those figures are valid only for one geometry ($r_i = 21.4, r_o = 39.7$) and are intended to be used only to describe the main conceptual reasons driving the influence of coefficient a on life. Using the same values of this coefficient, with different inner or outer radii, would result in a different kind of electric field and temperature distribution. It is worth noting that the same design geometry is chosen in previous studies neglecting here the presence of the semi-conductive layers.

The trend of the influence of a on L is nonlinear (Figure 3.10), since the electric field distribution is deeply affected by such parameter. Indeed, for lower values of a, the maximum electric stress is found near the inner electrode, and will be reduced for increasing levels of a, until field inversion is achieved. In those conditions L_{min} will tend to increase. Once field is inverted, the maximum field will be found near the outer radius of the insulation, and a further increase of a will result in the increase of stresses and reduction of L_{min}. Therefore, reducing a does not necessarily lead to an increase in the life of the cable, due to the non-linear effects of a on the maximum electric field in the insulation, hence life. Consequently, an optimal value of a exists for each cable design, which guarantees a uniform distribution of life (and semi-uniform distribution of field) inside the insulation thickness. The optimal value of a for the reference cable is $a = 0.063\ °C^{-1} < a_{XLPE} = 0.084\ °C^{-1}$. Field and life distributions inside cables with insulations characterized by the chosen values of a listed in Table 3.1 can be seen in Figures 3.10 , 3.11, and 3.12 justifying the overlap of the 40-year equi-life lines for both a_L and a_M in Figure 3.13 (obtained for a_M). This figure also shows the 40-year equi-life line for a_H (grey-dashed line): as it can be seen, it moves toward greater cable dimensions. This emphasizes the importance of developing new materials having moderate a.

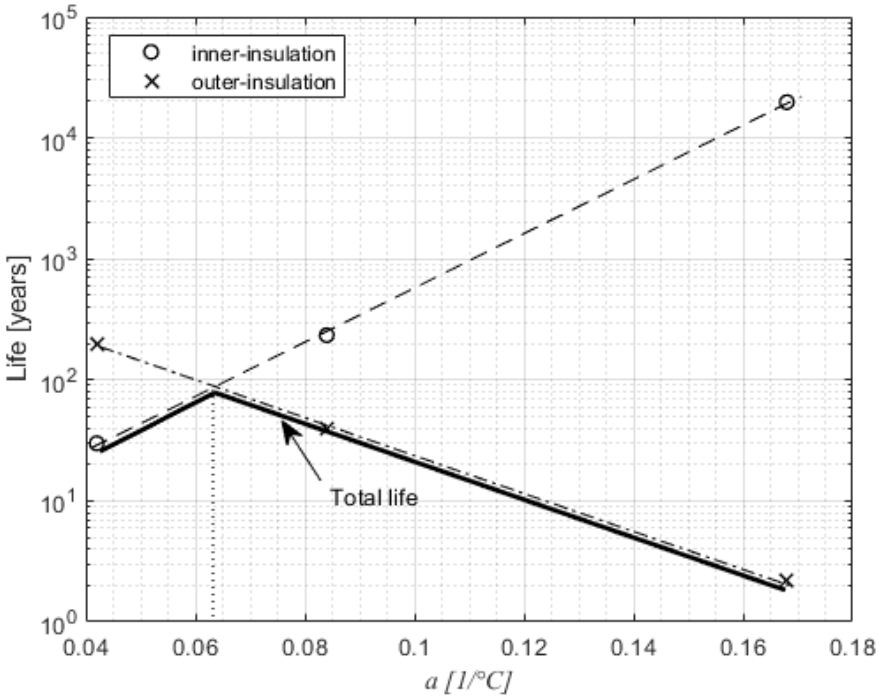

Figure 3.10 Estimated life of the insulation at the inner and outer radii for different values of *a* for the hot cable. where an optimum can be identified.

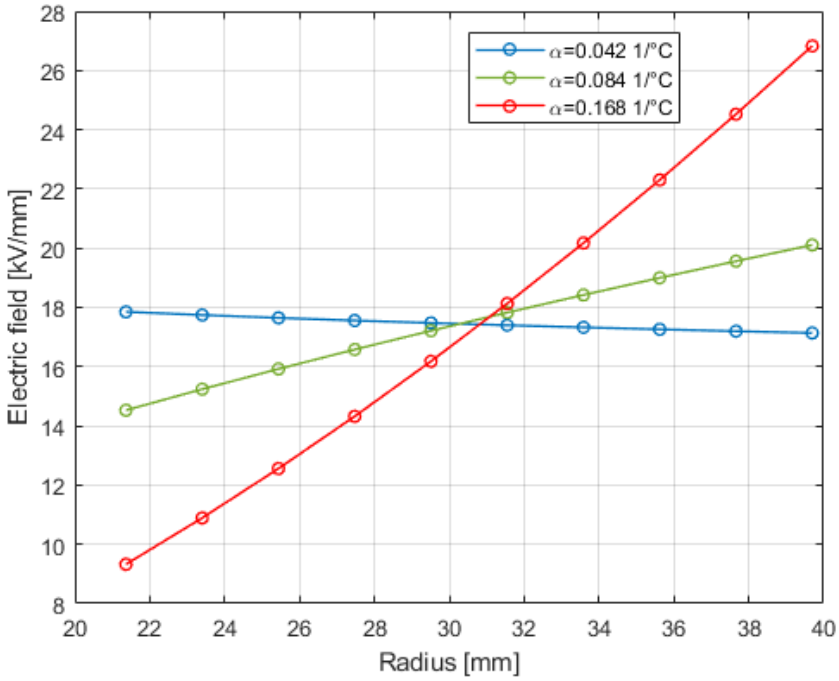

Figure 3.11 DC field profile in the insulation of the reference design cable (21.4, 39.7) mm for the 3 values of *a* from Table 3.1, and hot cable.

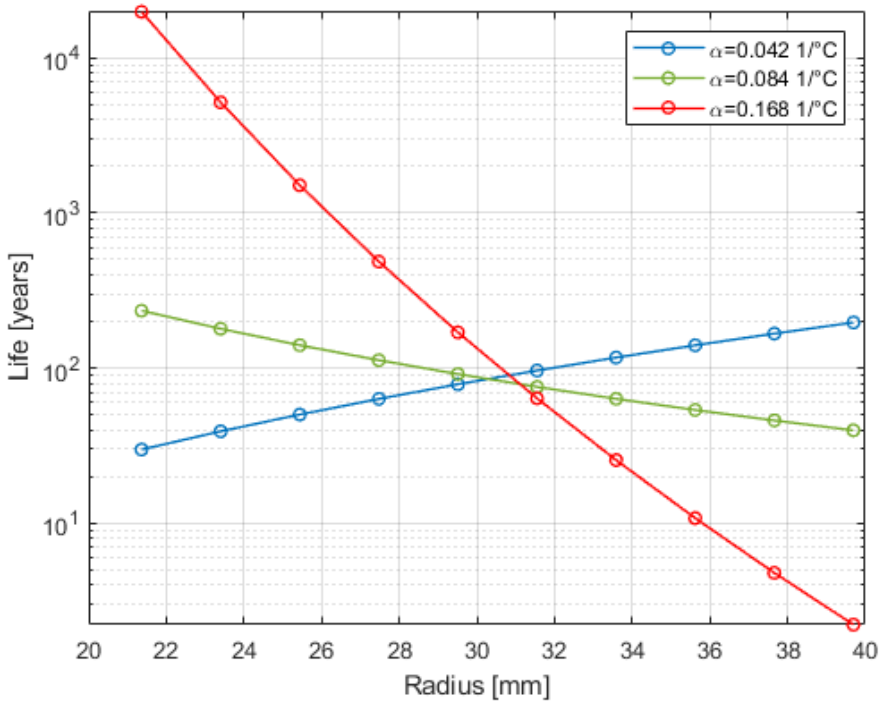

Figure 3.12 Life distribution inside the insulation of the reference design cable in log scale for the 3 values of *a* from Table 3.1, and hot cable.

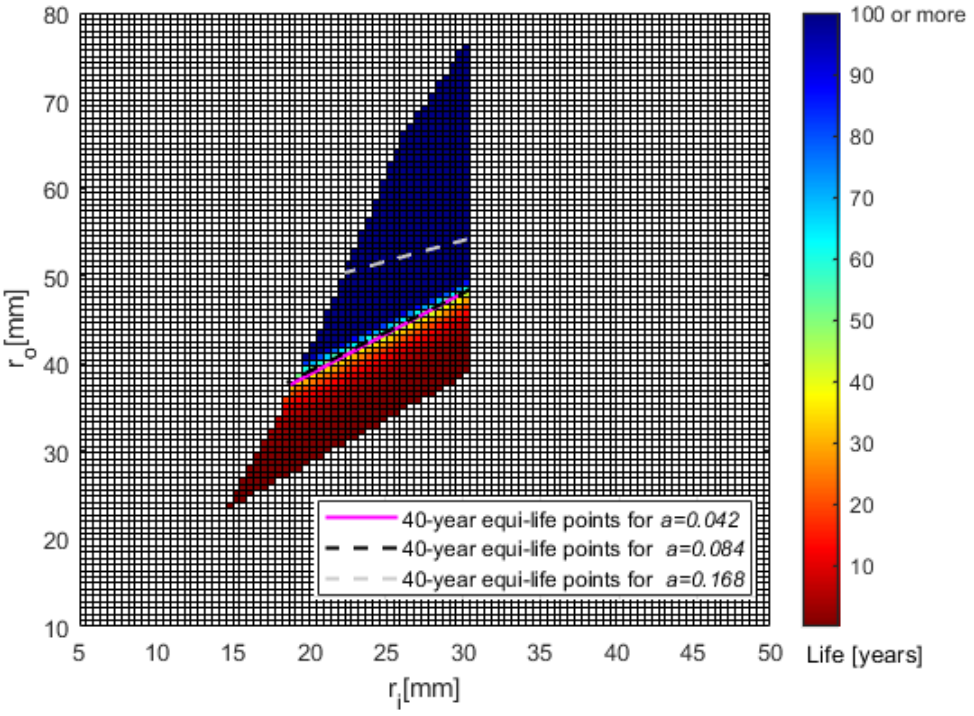

Figure 3.13 Life map in linear scale for temperature obtained for coefficient of conductivity $a = a_M$ and hot cable. The 40-year equi-life loci for a_L, a_M, a_H are also shown. a_L, a_M lines are overlapped.

3.3.1.4 Effect of Field coefficient of electrical conductivity *b*:

To investigate the effect of *b* on HVDC cable life, the 3 values of *b* in Table 3.1 are used. Figure 3.14 shows a positive effect of increasing *b* on reducing the field inversion ΔE between the inner and the outer insulation. This positive effect can be seen also in the life distribution across the insulation, Figure 3.15, where the life distribution becomes flatter by increasing *b*, and the life in the most stressed point raises from 40 years for b_L=0.03 to 56 years for b_M=0.06 and 81 years for b_H=0.12. Figure 3.16 shows that the 40 years equi-life points slightly shift downward, as *b* varies from b_L to b_H, reducing the feasible outer insulation radii by only ≈ 1 mm. However, the effects of *b* are great only if the field inversion is great (i.e. for materials characterized by high values of the parameter a), hence while its impact is minor for the case reported, it will become much more important for materials and conditions with a stronger attitude to invert field distribution.

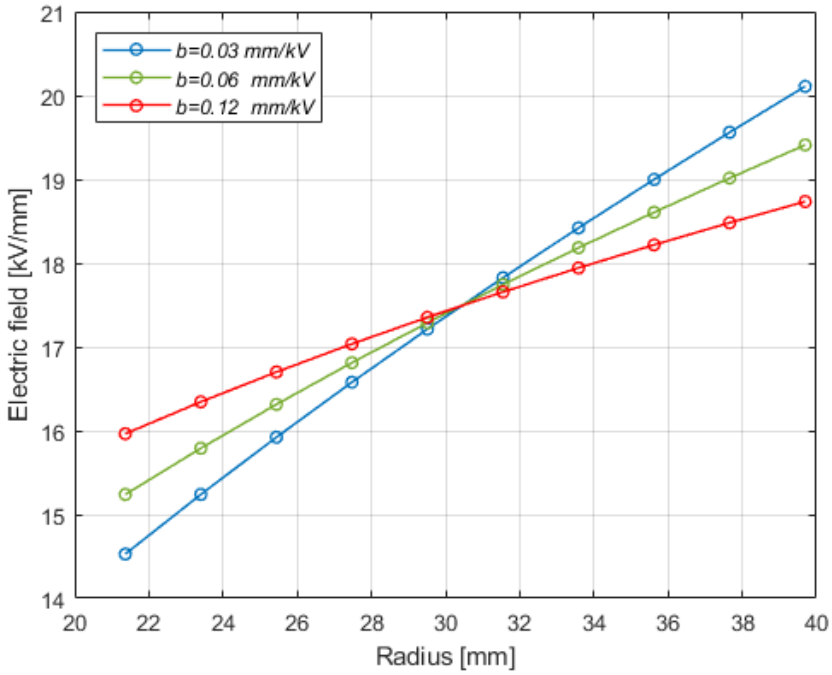

Figure 3.14 DC field profile in the insulation of the reference design cable (21.4, 39.7) mm for the 3 values of *b* from Table 3.1, and hot cable.

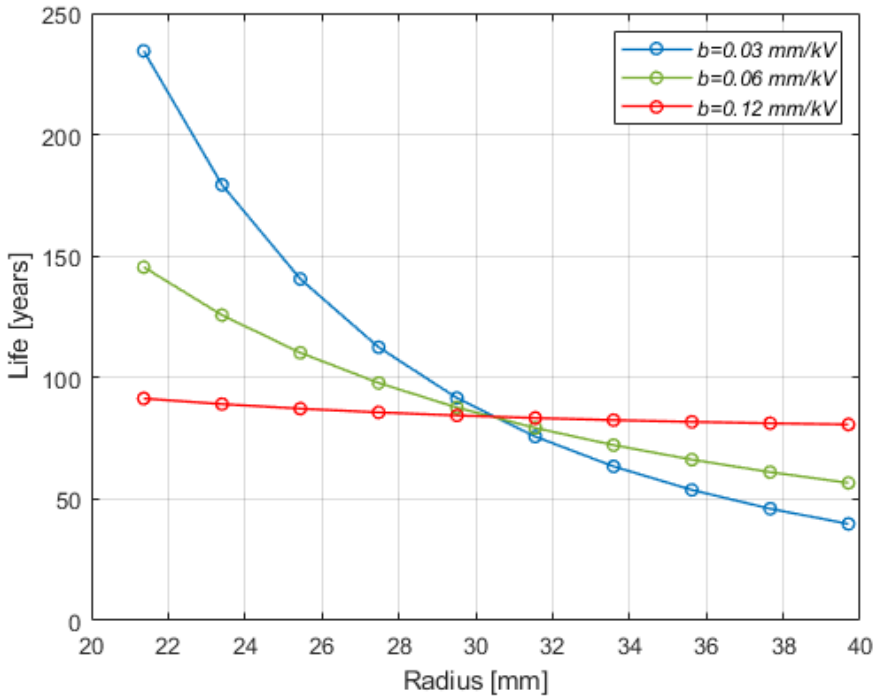

Figure 3.15 Life distribution inside the insulation of the reference design cable in log scale for the 3 values of b from Table 3.1, and hot cable.

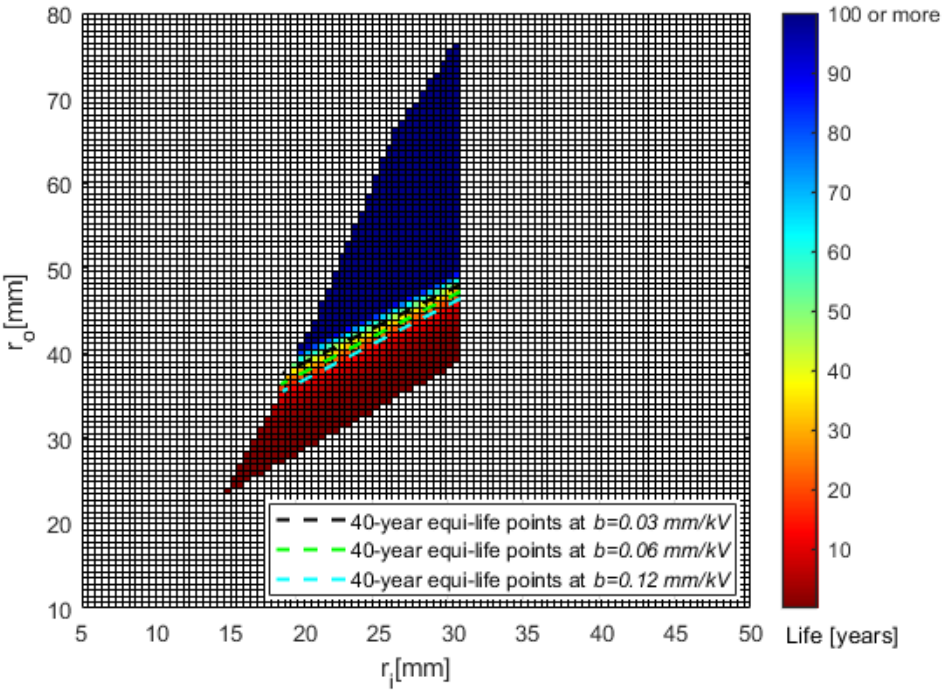

Figure 3.16 Life map in linear scale for field coefficient of conductivity $b=b_L$ and hot cable. The 40-year equi-life loci for b_L, b_M, b_H are also shown

3.3.1.5 Effect of soil thermal resistivity:

Figure 3.17 illustrates the effect of soil thermal resistivity on HVDC cables design, which in turn affects the geometries characterized by $T(r_i) = T_{max} = 70\ °C$. It shows that a considerable reduction in the feasible design area is attained by increasing the thermal resistivity of the surrounding soil, until the feasible area vanishes for $\rho_{T,so} > 1.7\ K.m/W$; this is fully consistent with the life estimates obtained in [64]. Let us recall from IEC 60287-3-1:2017, Annex A [65], that $\rho_{T,so} = 1\ K.m/W$ represents the moist soil in autumn or spring, $\rho_{T,so} = 1.3\ K.m/W$ is the typical value of the partially dry soil thermal resistivity in summer (recommended for current-carrying capacity calculations), whereas greater values tend to the fully dry soil. This emphasizes the importance of the backfill to avoid unacceptably great cable dimensions. It is worth noting that neither the intrinsic, nor the interactive thermal instability is considered in this study [66].

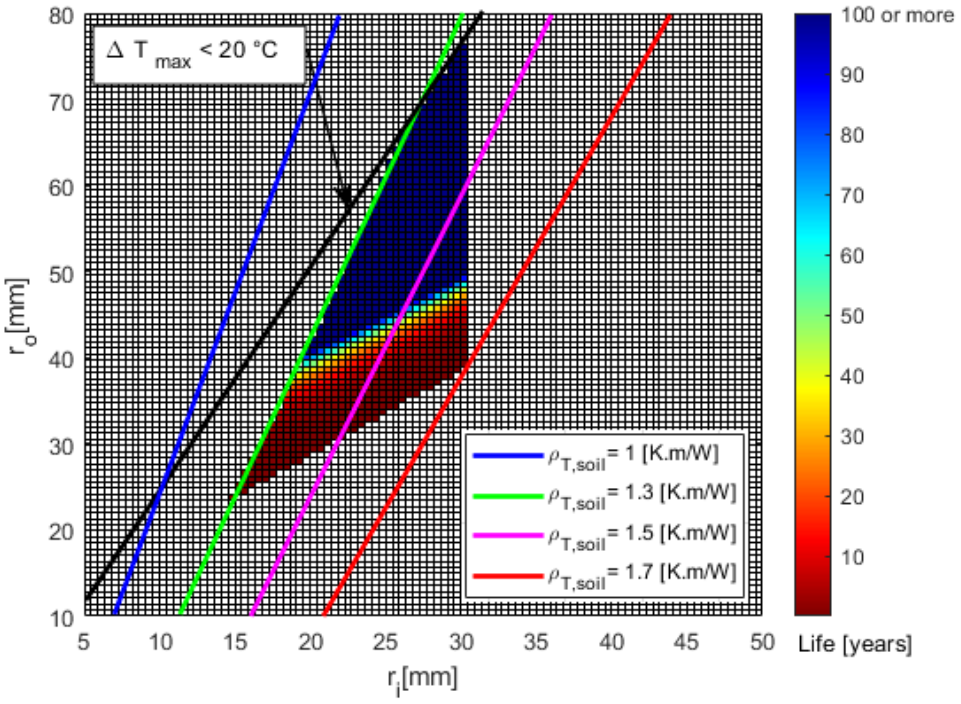

Figure 3.17 Life map in linear scale for 4 different values of the soil thermal resistivity.

3.3.1.6 Effect of the rated Voltage:

Figure 3.18 shows the effect of voltage U_0 on the life map of HVDC cables, increasing it from 320 kV (reference design value) to 525 kV and 640 kV, while keeping the other parameters, such as ampacity, unchanged. As expected, the rated voltage rise leads to a shift of the feasible design area toward greater dimensions of both the conductor and the insulation (Figure 3.18). It can be also noticed that the limits T_{max}, ΔT_{max} and J_{min} are still unchanged, because the current carrying capacity of the cable is still the same, giving greater cable power values for greater voltages.

Variations of both r_i and r_o are necessary to maintain feasibility when U_0 is increased, since a greater insulation thickness is required to keep the electric field distribution and the life to suitable values. On the other hand, the restraint in ΔT_{max} must also be respected. An increase of only r_o would lead to increasing values of ΔT_{max}, due to worse heat exchange conditions. Hence, the dimension r_i must change as well, allowing for both reduced local electric fields and admissible values of temperature gradients. The effect of voltage explains the need to develop new insulating materials having better endurance to DC voltage (thus, higher maximum applied DC field) and/or appropriate values of temperature and field coefficients of conductivity *a* and *b*, such that equi-life points move downward when applying higher voltages, e.g. 800 kV.

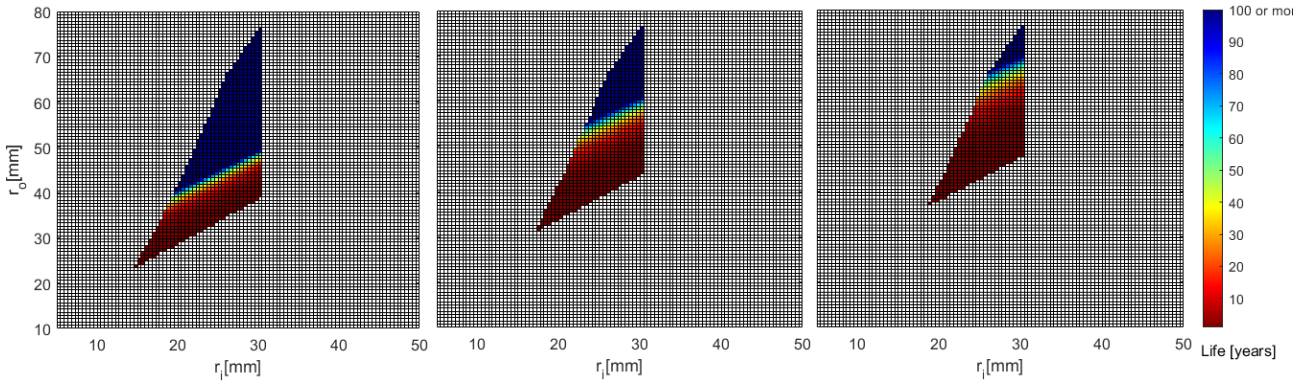

(a) (b) (c)

Figure 3.18. Life map of HVDC cable in linear scale for hot cable and applied voltage = (a) 320 kV, (b) 525 kV, (c) 640 kV.

3.3.2 Electrical transients:

Electrical transients, with reference to Table 3.3, are applied on the cable for two values of *a* (low and medium), for the sake of comparison. Figure 3.19 shows that the greater the frequency of electrical transients, the shorter the life. The latter demonstrates the need to enlarge the cable geometries to sustain the design life as the frequency of transients - thus their number over a given period - increases, which in turn shifts the equi-life loci upward. Comparing Figure 3.19(a) to 3.19(f), a more severe effect of transients on cable life can be noticed when the dielectric is characterized by a low value of *a*. In the worst case simulated here ($a = a_L$, Figure 3.19(a), 3.19(b), and 3.19(c)), two polarity reversals per day are enough to increase the cable design thickness by ≈ 10 mm. On the other hand, when $a = a_M$ (Figure 3.19 (d), 3.19 (e), and 3.19 (f)), insulation thickness increases by ≈ 5 mm for the same frequency of transients. This is justified by the fact that low values of *a* will also imply lower values of conductivity. This will in turn increase the electrical time constant, hence the duration of transient conditions during which the insulation will locally have to withstand enhanced fields. For the sake of clarity, the life distribution inside the insulation thickness can also be analysed. In Figure 3.20(a) and 3.20(b), it can be seen how electrical transients have a more detrimental effect on the

inner insulation of dielectrics with lower values of *a*, since in this case the electric field is always maximum near the inner conductor of the cable (see Figure 3.20(a)). For higher values of *a*, the life distribution pattern can be non-monotone, due to field inversion. In this case, at steady state the outer insulation will be more stressed than the inner insulation, while the opposite occurs during transient conditions (Figure 3.20(b)). As a result, when no transients are considered, life is always related to the failure of the outer insulation. Introducing a number of transients, however, will modify life distribution and, from a certain amount (e.g. 1 electrical transient per day), life minimum can shift towards the inner insulation. This is also the reason why Figure 3.19(d) and 3.19(e) seem identical. It can be also noticed in Figure 3.19 that the increase in the inner insulation radius leads to a significant reduction of the effect of electrical transients on the life (i.e. 40-year life loci are converging). This is caused by the reduction of both steady state and transient electric field inside the insulation thickness.

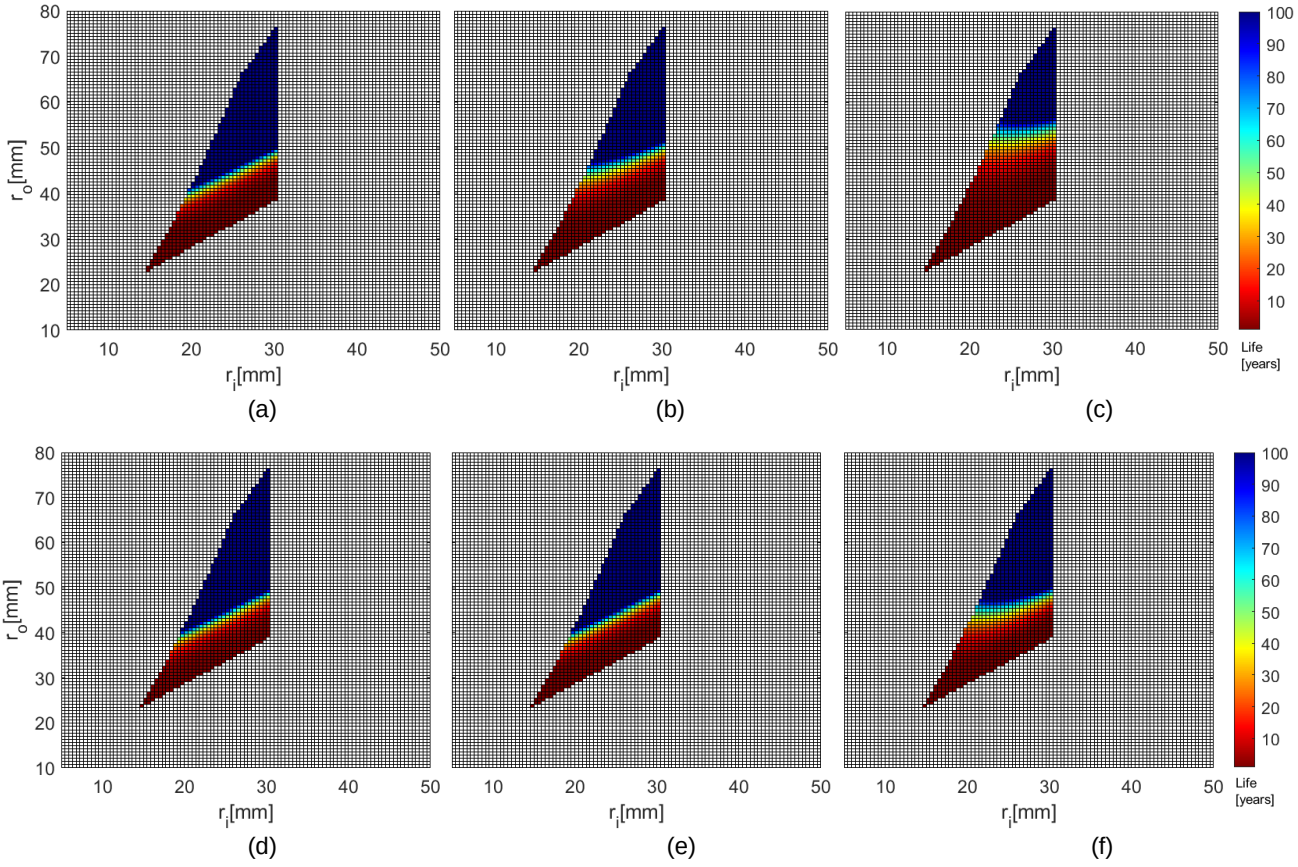

Figure 3.19 The effect of electrical transients on the life map for hot cable (a) $a = 0.042$, no transients, (b) $a = 0.042$, 2 transients per week, (c) $a = 0.042$, 2 transients per day, (d) $a = 0.084$, no transients, (e) $a = 0.084$, 2 transients per week and (f) $a = 0.084$, 2 transients per day.

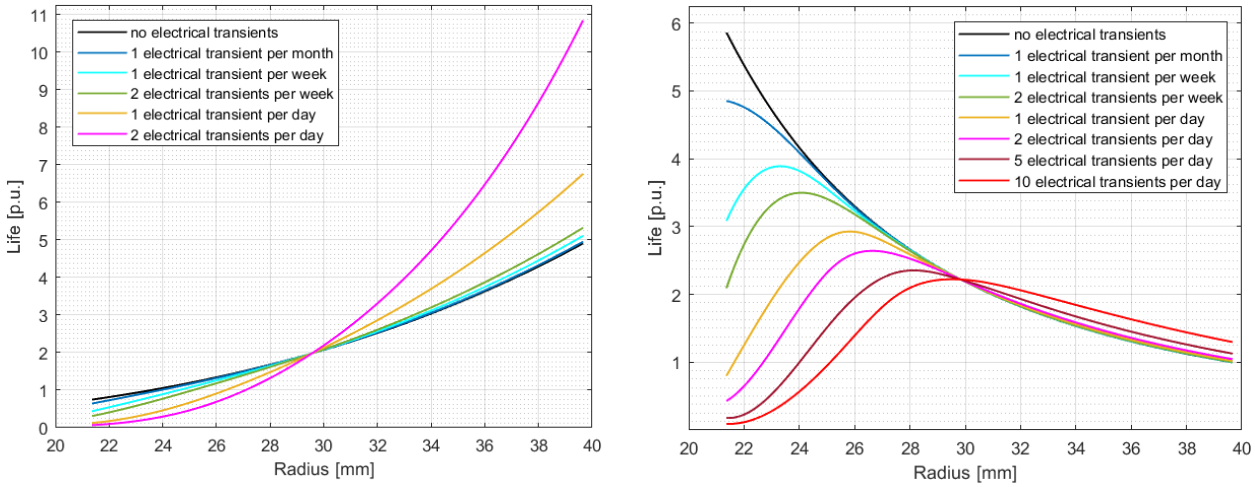

(a) (b)

Figure 3.20 Life distribution in p.u. (base value is design life L_D) inside the insulation thickness in linear scale for several numbers of electrical transients for a hot reference cable ($r_i = 21.4$, $r_o = 39.7$ mm) and (a) $a = 0.042$ and (b) $a = 0.084$.

3.3.3 Thermal transients:

Thermal transients are applied on the cable in the form of load cycles, each cycle consists of two transients LT→HT and HT→LT according to Table 3.4, see Figure 3.4. Figure 3.21 illustrates electric field variation over time for both types of thermal transients. It can be noticed that the electric field distribution is quasi-capacitive in the cold cable, since an isothermal condition is considered at this stage. Hence, conductivity will be almost homogeneous (as only a slight effect of field coefficient *b* is observed), and field distribution in DC will be practically the same as in AC. Hence, the inner insulation is the most stressed part of the insulation at this stage. On the contrary, in the hot cable, the electric field distribution becomes resistive and the outer insulation is the most stressed point. Results from simulations considering a constant applied voltage $U = U_0$ and thermal transients with different time constants (Figure 3.22) show that life minimum is generally found in the outer insulation, since field redistribution due to thermal transients are usually faster than in the cases discussed in section 3.3.2, hence most of life reduction will be due to steady state conditions. It can also be seen that more thermal transients can relieve the electro-thermal stress during insulation life, for two reasons:

1) both LT→HT and HT→LT transients are characterized by a lower average temperature of the various points within the insulation compared to the unperturbed conditions of the hot cable at rated temperature, thereby reducing the thermal stress and aging within the insulation.
2) both LT→HT and HT→LT transients extend the amount of time characterized by intermediate field distributions, when a lower maximum value of the field is found in the insulation (Figure 3.21). As a result, life in the insulation is increased for longer values of the thermal time constant τ_T (Figure 3.22).

The effect on life of thermal transients due to exclusively thermal stresses at different values of τ_T can be noticed considering the insulation at $r \approx 30\ mm$, where the electric field is mostly constant during thermal transients (Figure 3.21). Considering this point, life increases by 67% in the case of $\tau_T = 3\ h$ due to the sole contribution of an average thermal stress reduction HT→LT.

Figure 3.23 shows the effect of temperature transients on life map, with different time constants. Due to the positive effects of longer thermal time constants, smaller design geometries of the cable are allowed for the same life. In other words, equi-life loci are shifted toward smaller insulation thicknesses. Life minimum (hence cable life) in the reported case is always found in the outer insulation, but it should be mentioned that this is not the case when no field inversion is present at steady state (i.e. materials with lower values of the temperature coefficient a, as can also be seen in the Section 3.3.4).

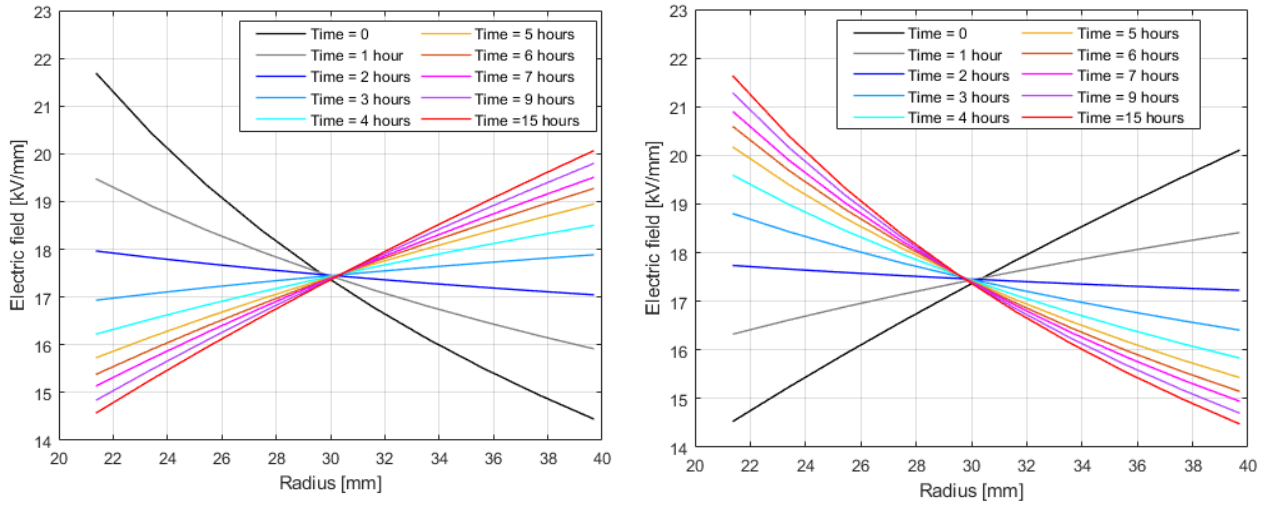

(a) (b)

Figure 3.21 Electric field during thermal transients (a) T1→ T2 transient and (b) T2→ T1 transient.

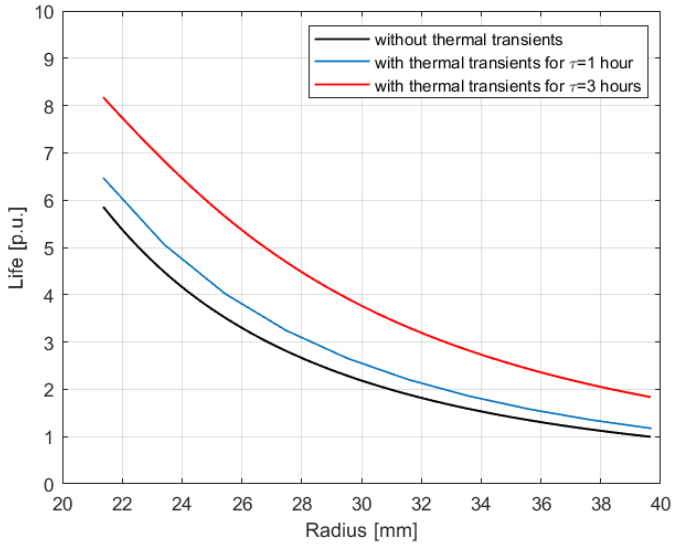

Figure 3.22 Life distribution in p.u. (base value is design life L_D) inside the insulation thickness for different values of the thermal time constant τ_T

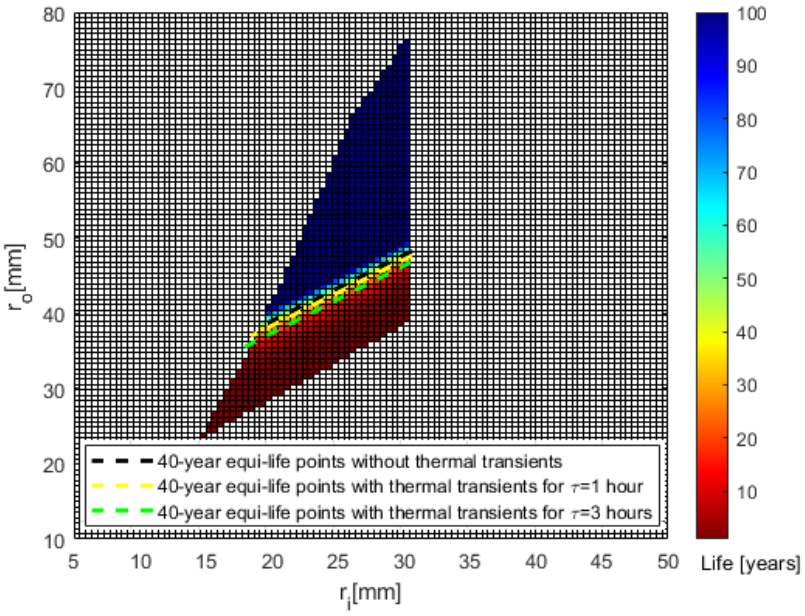

Figure 3.23 The effect of thermal transients on the life map.

3.3.4 Electro-thermal transients:

Figure 3.24 illustrates the combined effect of electrical and thermal transients on the total life of cable. One thermal and one electrical transients per day are applied in a non-simultaneous way on the reference cable, considering $a = 0.042$ (Figure 3.24(a)) and $a = 0.084$ (Figure 3.24(b)). Results show, in the red curve, the combined effect of electrical and thermal transients on the life of different points distributed within the insulation. The case represented in Figure 3.24(a) shows that the combination of electrical and thermal transients does not induce a substantial difference on cable life, since its minimum is always found near the inner insulation, and the effect of electro-thermal transients are similar to that of the sole electrical transients. This can be explained reminding that most of life loss of the inner insulation is occurring during transients, when local field is increased. A closer look reveals a mild increase of life minimum in the case of electrothermal transients, due to slightly lower average temperatures experienced by the insulation during life (which is the reason behind the life increase observed with purely thermal transients). Life near the outer insulation is, on the other hand, higher in the presence of combined transients since it will benefit from both the local electric field reduction due to the electrical part of transients, and an average lower temperature due to the thermal part of transients. As can be noticed, life distribution after combined transients is monotonically increasing since both thermal and electrical stresses are generally decreasing with the considered radius. On the other hand, the case of Figure 3.24(b) shows that life distribution following combined transients can also be non-monotone. That is the case when the average electric stress is distributed in a non-monotone manner (as mentioned in Section 3.3.2), while thermal stress is monotonous. As a result, life of insulation near the inner conductor is, as before, similar for both the

electrical and combined transients, for the same reason discussed above. On the other hand, results closer to the outer regions are mostly similar to life in the case of thermal transients, since the influence of electrical transients is negligeable (notice that in Figure 3.24(b) life with and without electrical transients are practically the same in those regions). To further emphasize the role played by electrical transients, the quite severe – and far from reality, see above - case where 10 electrical transients per day take place throughout the cable life (combined or not with thermal transients) has also been considered in Figure 3.24(b). In this case, the cable life at inner insulation is dramatically reduced with respect to design life. It must be noticed that this study shows the effect of transients on only electrothermal life of cable. Other types of stress are out of the scope of this study. In fact, thermal load cycles cause consecutive heating (expansion) and cooling (contraction) of the cable components, resulting in radial and circumferential stresses in the insulation [67].

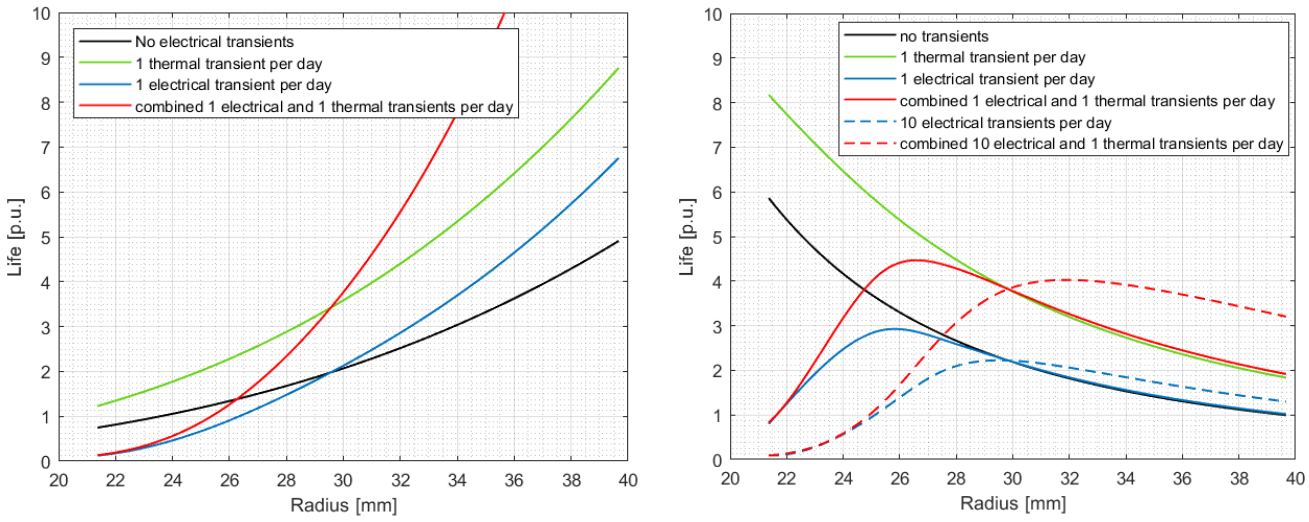

Figure 3.24 Total life of a hot reference cable with combined non-simultaneous electrical and thermal transients for (a) $a = 0.042$ and (b) $a = 0.084$.

3.4 Discussion:

The comprehensive Figure 3.25 illustrates the effects on the feasible design area of HVDC cable life map when varying the 6 parameters analyzed, i.e., T_{max}, ΔT_{max}, $\rho_{T,so}$, U_0, a and b. T_{max} decrease shifts its limit toward greater conductor dimension (rightward). ΔT_{max} decrease rotates its limit clockwise, i.e., toward thinner insulation and lower conductor temperature. $\rho_{T,so}$ rise shifts T_{max} limit quasi-parallelly toward greater conductor and outer insulation radii, which reduces the conductor temperature for the same rating. Rated voltage rise, for the same ampacity, shifts the whole feasible design area upward, i.e., toward greater conductor radius, outer insulation radius and insulation

thickness, all together. The increase in field coefficient of electrical conductivity *b* slightly shifts the equi-life points downward in the life map, i.e., toward smaller conductor and outer insulation radii. On the contrary, increasing temperature coefficient of electrical conductivity *a* shifts the equi-life points in the life map upward, i.e., toward greater conductor radius, insulation thickness and outer insulation radius, all together.

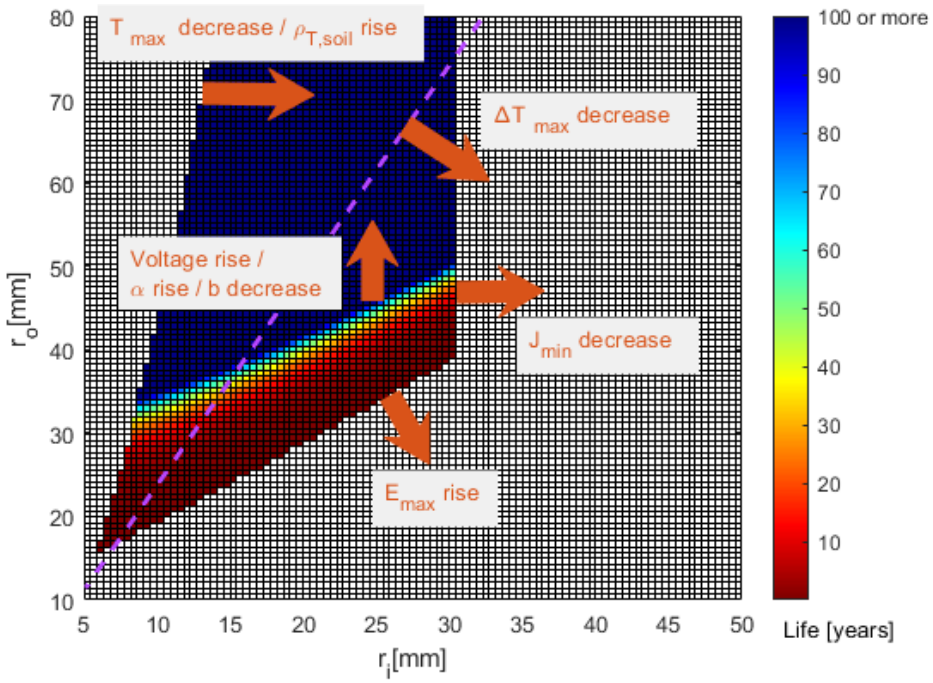

Figure 3.25 Effect of variation of T_{max}, ΔT, $\rho_{T,so}$, J_{min}, *voltage*, *a* and *b* on the feasible design area of HVDC cables.

The field enhancement in the inner insulation due to electrical transients leads to life reduction of the cable. This shifts the equi-life loci toward greater cable radii. A material characterized by lower temperature coefficient of electrical conductivity, *a*, enhances this detrimental effect due to an increased electrical time constant of the dielectric, requiring longer time to reach stability (hence an extension of high local stress conditions). Conversely, thermal transients relieve the average thermal stress applied on the insulation, increasing insulation life and extending feasibility towards smaller cables. The effects of the combination of those transients are dependent on two separate contributions: one negative, from the electrical part of the transient, and one positive, from the thermal part of the transient. The resulting cable life is generally similar to the one found after an equal amount of purely electrical transients, with minor benefits from temporary temperature reduction.

Chapter 4

Thermal stability in HVDC cables

4.1 Introduction:

High voltage direct-current (HVDC) cables have progressively been used in high voltage (HV) transmission systems to meet the increasing energy demand [2]. For this reason, cable manufacturers are working on innovative materials to withstand higher voltages to meet the increasing demand. So far, HVDC cables have been qualified at rated voltages up to 640 kV [31]. The increase in both the applied voltage and the electric field justifies the need to investigate the insulation losses (i.e., dielectric losses or leakage current losses), which may lead to temperature rise and in some cases to thermal instability (thermal runaway) [68]. In AC cables, insulation losses are caused not only by the leakage (conduction) of current through the dielectric material, but also by dielectric polarization losses—mainly associated with dipolar hysteresis losses—which tend to overwhelm conduction losses. On the contrary, in DC cables, insulation losses are fully driven by leakage current [2].

Intrinsic thermal instability was studied by Whitehead and O'Dwyer [69],[70]. They worked on thick plane insulations with a constant boundary temperature, which is not fully comparable to this study where the temperature profile is transient according to CIGRÉ Technical Brochure 496 [29] for a cable buried in soil (not a constant boundary temperature). Whitehead found that intrinsic thermal instability occurs at a critical temperature rise (due to only insulation losses) as low as 10 °C [69]. Fallou [71], Brazier [72] and Jeroense and Morshuis [56] studied the so-called "interactive" thermal instability of cables, which occurs in the presence of thermal interaction of the cable with the outer environment. The authors in [56] studied the interactive thermal instability of 450 kV paper-insulated cable and found that the insulation losses become significant for sheath temperatures >70 °C, and interactive thermal instability becomes inevitable for sheath temperatures >83 °C. Eoll first introduced and studied the intrinsic instability of HVDC cables, which can occur even in the absence of thermal interaction with the outer environment [7]. Reddy et al. also studied the intrinsic thermal instability of HVDC cables, considering a 21.7-mm-thick Cross-Linked Polyethylene XLPE-insulated cable at a constant temperature of the metallic screen/sheath, fixed at 25 °C to study the sole effect of the electric field on the thermal stability; the authors calculated the intrinsic Maximum Thermal Voltage (i.e., the maximum DC voltage above which no stability is achieved) and found that interactive Maximum Thermal Voltage will certainly have a lower value. They found out that the critical temperature rise, at which the intrinsic instability takes place, depends almost solely on the insulating material [73].

In this chapter, the intrinsic thermal instability will be investigated—due to either the electric field rise or to the effect of cable insulation characteristics—in XLPE-insulated HVDC cables buried in soil. Compared to the above-mentioned papers, the case study tackled first considers a constant interaction of the cable buried in soil having a constant thermal resistivity (neglecting soil drought).

Furthermore, for the sake of completeness and comparison this study considers two different voltage ratings of XLPE-insulated HVDC cables, 320 kV and 500 kV, which involve different insulation thicknesses, so as to analyze the effect of different cable insulation designs.

Thermal stability is investigated from two intrinsic perspectives:

- The insulation material characteristics, focusing here on the electrical conductivity coefficients of both temperature and electrical stress, *a* and *b*, respectively.
- The electric field variation as a result of the applied voltage variation. This might happen during testing at very high and/or increasing voltage levels, e.g., during thermal stability tests.

This study also aims at finding the critical values of the conductivity coefficients which guarantee a thermally stable operation of the cable under different applied voltages (and, in turn, in different electric fields).

4.2 Coupled temperature and electric field calculations

Thermal instability of both 320 and 500 kV XLPE-insulated HVDC cables are investigated as a function of cable insulation characteristics, represented by the temperature and stress coefficients (*a*, *b*) of electrical conductivity of the extruded dielectric and the insulation thickness. The effects of these parameters on temperature rise due to insulation losses and, consequently, on the thermal instability. The flow chart presented in Figure 4.1 explains step by step the algorithm implemented for such assessment. First, the temperature profile of load cycles according to CIGRÉ Technical Brochure 496 [29] is calculated using the CIGRE transient thermal network model following the guidelines of Standard IEC 60853-2 [5]. Then, the transient electric field inside the insulation of the cable subjected to load cycles is calculated using both Maxwell's Equations (1.27) – (1.29) and the macroscopic conductivity Equation (1.30), followed by the calculation of insulation losses and the resulting temperature rise. Finally, the thermal stability diagram is found for both studied cables. It is noteworthy in Figure 4.1 that in this study the temperature profile is updated with iterations at each time instant.

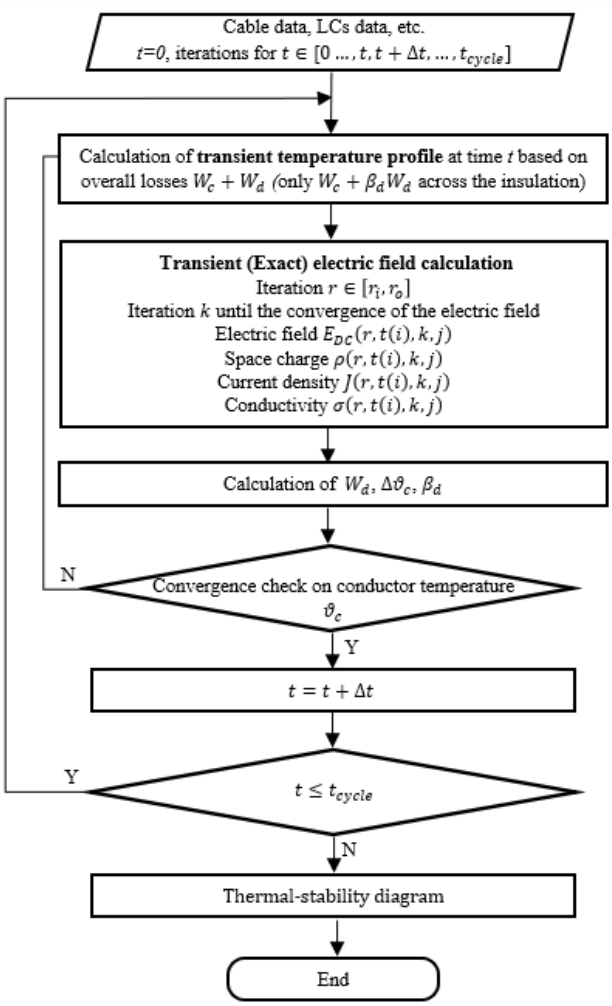

Figure 4.1 Flowchart shows the algorithm implemented for the calculation of the electric field, insulation losses and thermal stability

4.2.1 Calculation of insulation losses:

The temperature rise in the insulation can be found by solving the heat transfer Equation (4.1) in cylindrical coordinates in the steady-state form ($\partial T/\partial t = 0$):

$$\frac{1}{r}\frac{d}{dr}\left(\frac{r}{\rho_{th}}\frac{dT}{dr}\right) = -w_d \tag{4.1}$$

where r is the generic radial coordinate in cable insulation, ρ_{th} is the thermal resistivity of the insulation, T is the temperature, w_d is the per unit volume power generated due to insulation losses; it represents the source term in the equation and can be found as follows:

$$w_d = \boldsymbol{J}.\boldsymbol{E} = \boldsymbol{J}.\frac{\boldsymbol{J}}{\sigma} = \frac{J^2}{\sigma} = \frac{I^2}{(A)^2.\sigma} = \frac{I^2}{(2\pi r)^2.\sigma} \tag{4.2}$$

where J is the current density inside the insulation, A is the lateral surface area of one meter length of the cylindrical cable at a generic radius r (see Figure 4.2), and σ is the electrical conductivity of the insulation at the radial coordinate r.

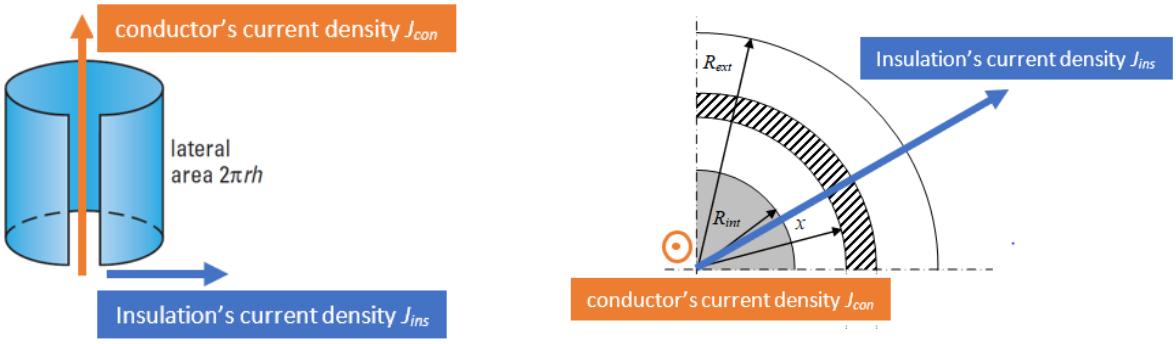

(a) (b)

Figure 4.2 The conductor's and insulation's current densities from (a) 3D perspective, (b) cross-sectional 2D perspective.

By manipulating (4.1), one obtains:

$$\frac{d^2T}{dr^2} + \frac{1}{r}\frac{dT}{dr} = -\rho_{th} w_d \tag{4.3}$$

where the negative Right-Hand Side RHS refers to the reduction of temperature in the direction of which the finite difference method (FDM) is used to solve (4.3), namely, the temperature variation from the inner-insulation towards the outer-insulation is always a temperature drop. The total dielectric losses in the unit length of cable insulation can be obtained using the following equation, which is derived by integrating (4.2) in cylindrical coordinates:

$$W_d = \int_0^1 \int_{\varphi_1}^{2\pi} \int_{r_i}^{r_o} w_d r \, dr \, d\varphi \, dz = \int_{\varphi=0}^{2\pi} \int_{r_i}^{r_o} \frac{I^2}{(2\pi r)^2 . \sigma} r \, dr \, d\varphi \tag{4.4}$$

$$W_d = \frac{I^2}{2\pi} \int_{r_i}^{r_o} \frac{1}{r . \sigma} \, dr \tag{4.5}$$

As a result of the discretization in *r* axis, the electrical conductivity is considered constant within the infinitesimal differences *dr*. Consequently, Equation (4.5) can be simplified to an integrable form in each infinitesimal interval $\Delta r = r_{i+1} - r_i$, as follows:

$$W_d = \frac{I^2}{2\pi}\sum_{i=1}^{n}\frac{1}{\sigma_i}\int_{r_i}^{r_{i+1}}\frac{dr}{r} = \frac{I^2}{2\pi}\sum_{i=1}^{n}\frac{1}{\sigma_i}\left[\ln\left(\frac{r_{i+1}}{r_i}\right)\right] \tag{4.6}$$

Boundary conditions:

1) Inner boundary conditions: Neumann boundary conditions are applied to the inner insulation near the conductor surface. The RHS of (4.7) refers to the heat flowing from the conductor to the insulation due to conductor losses in the *r* axis where the temperature drop takes place.

$$\frac{r}{\rho_{th}}\frac{dT}{dr}\Big|_{r = r_{in}} = \frac{W_c}{2\pi} \tag{4.7}$$

$$-T_1 + T_2 = \frac{\Delta r\, \rho_{th}\, W_c}{2\pi\, r_{in}} \tag{4.8}$$

where T_1 and T_2 are the temperatures at the first and second points of the mesh in the inner insulation.

2) Outer boundary conditions: Neumann boundary conditions are applied to the outer insulation, where the heat flow in the direction of the *r* axis consists of both the heat generated due to conductor losses and the heat generated due to insulation losses. A ghost point n + 1 is placed at the metallic/screen sheath whose temperature is calculated using (4.10). This gives a more realistic simulation of heat flow in the thermoplastic sheath (which, contrary to the metallic sheath, has a non-negligible thermal resistance) and in the surrounding soil resulting in a more realistic metallic sheath temperature (see both Annex C and Annex D).

$$\frac{r}{\rho_{th}}\frac{dT}{dr}\Big|_{r = r_{out}} = -\left(\frac{W_c}{2\pi} + \frac{W_d}{2\pi}\right) \tag{4.9}$$

$$T_{n+1} = (W_c + W_d)(R_{T,Sh} + R_{T,So}) \tag{4.10}$$

where $R_{T,Sh}$ is the thermal resistance of the thermoplastic sheath, $R_{T,So}$ is the thermal resistance of the surrounding soil.

4.2.2 Calculation of dielectric loss coefficient:

According to IEC Standard 60287, the temperature drop can be re-written as in (4.11) [4]:

$$\begin{aligned}\Delta\vartheta &= W_c\left(R_{T,d} + R_{T,sh} + R_{T,so}\right) + W_d\left(\beta_d R_{T,d} + R_{T,sh} + R_{T,so}\right) \\ &= \Delta\vartheta_{cl} + \Delta\vartheta_{dl}\end{aligned} \tag{4.11}$$

where: $\Delta\vartheta_{cl} = W_c\left(R_{T,d} + R_{T,sh} + R_{T,so}\right)$ is the temperature drop over the whole cable and soil layers due only to the conductor losses, $\Delta\vartheta_{dl} = W_d\left(\beta_d R_{T,d} + R_{T,sh} + R_{T,so}\right)$ is the temperature drop over the whole cable and soil layers due only to the insulation losses, and β_d is the dielectric loss coefficient. It is only added to the insulation temperature drop term, because only a part of insulation losses contribute in the temperature drop inside the insulation. The other part of the insulation losses contributes instead in heating the entire insulation cross-section.

By manipulating (4.11), one obtains the following Equation (4.12) which is used to calculate the dielectric loss coefficient of DC cable insulation:

$$\beta_d = \frac{\Delta\vartheta_{dl} - W_d(R_{T,sh} + R_{T,so})}{W_d\, R_{T,d}} \tag{4.12}$$

By calculating β_d, the temperature drops in the insulation, sheath and soil, due to both conductor and insulation losses, can be found using (17)–(19), respectively:

$$\Delta\vartheta_d = R_{cc} I_c^2 R_{T,d} + W_d \beta_d R_{T,d} \tag{4.13}$$

$$\Delta\vartheta_{sh} = R_{cc} I_c^2 R_{T,sh} + W_d R_{T,sh} \tag{4.14}$$

$$\Delta\vartheta_{so} = R_{cc} I_c^2 R_{T,so} + W_d R_{T,so} \tag{4.15}$$

where I_c is the conductor's current [A], R_{cc} is the DC electrical resistance of the conductor operating at the temperature ϑ_c as defined in Equation (1.9).

4.2.3 Calculation of the de-rating factor:

Since the load current and its heat flow inside the insulation play an important role in the stability of HVDC cables, the calculation of the de-rating factor is needed to accurately define the stability limits. The power generated by the conductor current per meter cable is given by (4.16):

$$W_c = R_{cc} I_c^2 \tag{4.16}$$

Accordingly, the de-rating factor can be calculated using (22):

$$DF = \frac{I_c}{I_{c,n}} = \sqrt{\frac{W_{c,n} - W_d}{W_{c,n}}} \tag{4.17}$$

where $W_{c,n}$ [W/m] are conductor losses per meter cable at the rated current $I_{c,n}$ [A], W_d are the insulation losses per meter cable [W/m], I_c [A] is the de-rated conductor current equivalent to the conductor losses considering insulation losses $W_{c,n} - W_d$ [W/m].

4.2.4 Thermal stability conditions:

The stability study can be carried out using the so-called thermal stability diagram (Figure 4.3). The diagram consists of two basic curves:

1. The heat generation curve (red solid curve in Figure 4.3) refers to the heat generated within the cable due to both insulation losses and conductor losses $W_d + W_c$.
2. The heat dissipation line (blue solid line in Figure 4.3) refers to the heat dissipated outside the cable through the insulation, thermoplastic sheath and soil, W_o. This full straight line is defined using two parameters:

    - The thermal resistance of the insulation, thermoplastic sheath and soil, represented by the reciprocal of the slope of the dissipation line. The higher the thermal resistance, the lower the slope, resulting in a higher temperature w.r.t the same losses, see dashed blue line in Figure 4.3;

    - The ambient temperature, the intersection of the dissipation line with the temperature axis. As the ambient temperature rises, the dissipation line shifts in the direction of the temperature rise without variation in the slope, see dash-dotted blue line in Figure 4.3.

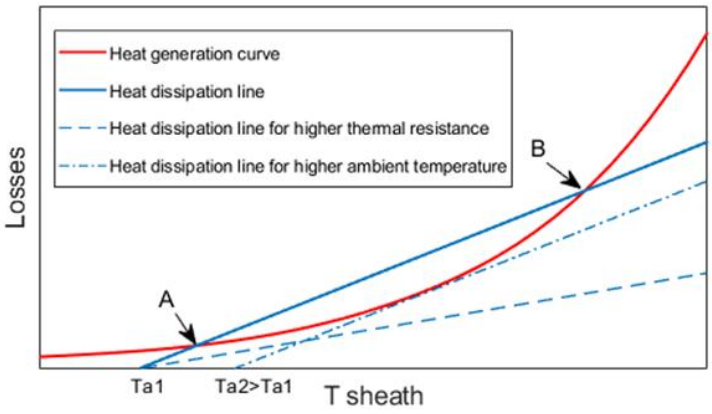

Figure 4.3 Thermal stability diagram.

Thermal instability occurs when thermal equilibrium cannot be achieved. A stable thermal equilibrium is reached only when the total heat of both conductor and insulation losses is equal to the heat dissipated from the cable [72]. This condition known as stable equilibrium is shown in Figure 4.3 in the point (A), i.e., the first intersection between the generation curve and the dissipation line. Two cases of thermal instability were considered:

$$W_o > W_{diss} \tag{4.18}$$

$$W_o = W_{diss}\ , \frac{\partial W_o}{\partial T} \geq \frac{\partial W_{diss}}{\partial T} \tag{4.19}$$

where W_o stands for the total losses $[W/m]$, W_{diss} is the heat dissipation $[W/m]$. The second case of thermal instability refers to the so-called “unstable equilibrium” in which an equilibrium exists but even a slight temperature rise leads eventually to instability. The latter is shown in Figure 4.3 in the point (B).

Thermal instability is of two types:

1. Intrinsic thermal instability:

   In intrinsic thermal instability, there is no external interaction with the cable, namely no interaction between the cable layers and the outer environment. This type of instability depends on the characteristics of the insulation (dielectric material and insulation thickness) and on the electric field, regardless of the external thermal resistance variation. This type of instability is not associated with a runaway increase in the temperature of the metallic sheath (which in practice coincides with the temperature in the outer insulation surface, since the

thermal resistance of the metallic sheath is negligible) unlike the interactive instability [7]. Thus, it occurs even at ambient temperature in the case of unloaded cable [73]. Referring to Figure 4.3, it can be said that intrinsic thermal instability corresponds to shifting the red curve upwards until an intersection with the blue curve—namely thermal equilibrium—cannot be achieved anymore, even by moving the operating point along the red curve to the right.

2. Interactive thermal instability:

In interactive thermal instability, an interaction between the cable and the ambient leads to runaway if the equilibrium cannot be reached. In this type of instability, variation of external thermal resistance or variation in the ambient temperature are necessary for the runaway to take place [73]. Referring to Figure 4.3, it can be said that interactive thermal instability corresponds to shifting the blue curve to the right and/or tilting it downward until the equilibrium (intersection with the solid blue curve) cannot be achieved anymore. Indeed, Figure 4.3 shows that:

i) for a value of the ambient temperature $\geq T_{a2}$ (dash-dotted line), equilibrium cannot occur, and thermal instability takes place;

ii) the increase in the thermal resistance of the surrounding soil (dashed line) leads to inevitable thermal instability because the equilibrium cannot exist.

Both intrinsic and interactive instability terminate with the same failure mechanism, which includes an extreme variation in the temperature distribution inside the insulation leading to an extreme rise of the electric field to values greater than the intrinsic dielectric strength of the insulation, and eventually the breakdown occurs [7].

4.3 Case study

4.3.1 Characteristics of the HVDC cable:

The main characteristics of the 320 kV and 500 kV HVDC cables are reported in Table 4.1. The thermal properties of the cable and the environment are reported in Table 4.2.

Table 4.1 Characteristics of the HVDC cables under study.

Parameter	500 kV Cable	320 kV Cable
Rated power (bipolar scheme) (MW)	1920	1105
Rated voltage (kV)	500	320

Conductor Material	Cu	Cu
Insulation Material	DC-XLPE	DC-XLPE
Relative permittivity ε_r	2.3	2.3
Rated conductor temperature (°C)	70	70
Ambient temperature ϑ_a (°C)	20	20
Conductor cross-section (mm²)	2000	1600
inner insulation radius r_i (mm)	27.2	24.6
Insulation thickness (mm)	28.1	17.9
Outer-insulation radius r_o (mm)	55.3	42.5
Design life L_D (years)	40	40
Design failure probability P_D (%)	1	1
Rated or design current (ampacity) $I_{c,n}$ (A)	1920	1727

Table 4.2 Thermal characteristics of the cables and the surrounding environment.

	Thermal Resistivity	**Thermal Resistance**	
		500 kV	**320 kV**
insulation	3.5	0.447	0.365
Thermoplastic sheath	3.5	0.0421	0.054
Soil	1.3	0.769	0.818

4.3.2 Temperature profile calculations:

The temperature profiles within the insulation of the 320 kV and 500 kV HVDC cable are calculated for the 24-h load cycles mentioned in CIGRÉ Technical Brochure 496 and prescribed during prequalification tests and type tests (see Figure 4.4). It is worth recalling briefly that the 24-h load cycles prescribed in [29] consist of at least 8 h of heating followed by at least 16 h of natural cooling, during at least the last 2 h of the heating period, a conductor temperature ≥ rated conductor temperature and a temperature drop across the insulation ≥ rated temperature drop shall be maintained. The insulation thickness is divided by n = 50 points into 49 layers which have a thickness $\Delta r = r_{i+1} - r_i = (r_o - r_i)/(n-1) = 0.365\ [mm]$ each. The time step is set to be 1 (s) that is found to achieve the stability of the algorithm especially for high values of the electric field and the conductivity.

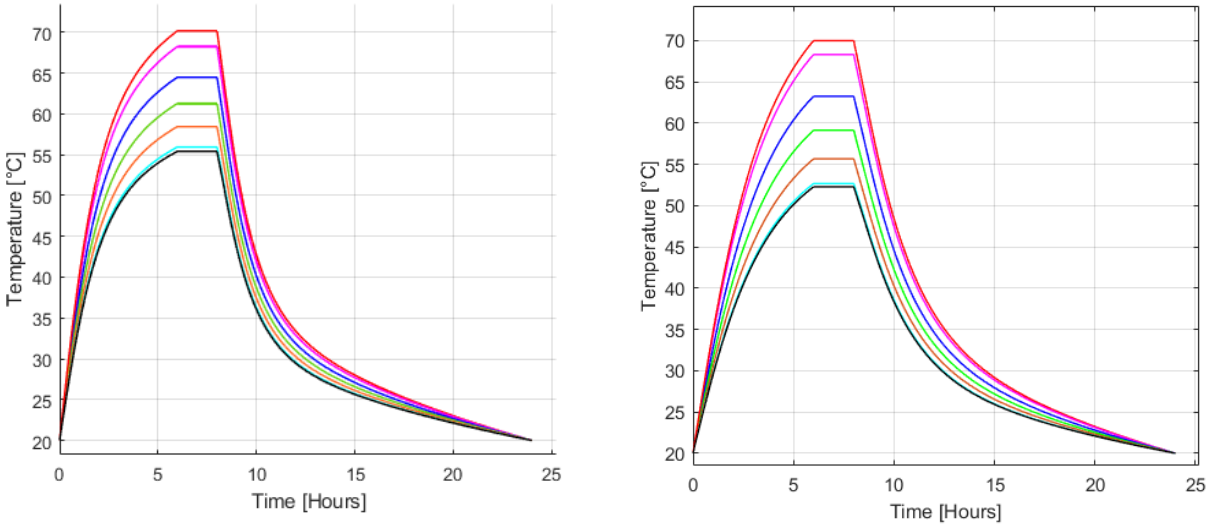

(a) (b)

Figure 4.4 The temperature profile of (a) 320 kV cable, (b) 500 kV cable at five points inside the insulation in the case of applying a 24-h load cycle according to CIGRÉ Technical Brochure 496.

4.3.3 Insulation characteristics:

Many empirical models have been introduced in the literature to represent the relationship between electrical conductivity and both temperature and electric stress variations for different types of insulation [54]. However, as pointed out above, the empirical model suggested by Klein [6] has been used in this study (see Equation (1.30)). As far as this model is concerned, many values of conductivity coefficients *a*, *b* can be found in literature [54]; however, the set of values reported in [54] is considered in this study (see Table 4.3), of which the medium set of values corresponds to the XLPE, the low set of values corresponds to paper insulations and the high set corresponds to thermoplastic insulations.

Table 4.3 The conductivity coefficients of HVDC cable insulation for different types of dielectrics.

Type of Dielectric	***a* (1/°C)**	***b* (mm/kV)**
Paper	0.074	0.018 ÷ 0.029
Thermoset	0.084 ÷ 0.101	0.0645
Thermoplastic	0.104 ÷ 0.115	0.034 ÷ 0.128

Focusing on thermoset extruded dielectrics for HVDC cables, to which the XLPE insulation of the treated cables belong, let us take the medium set of values of conductivity coefficients a_M = 0.084 1/°C, b_M = 0.0645 mm/kV as a reference. Due to the high sensitivity of the conductivity to *a*, *b* coefficients, more extreme values of *a*, *b*—which may fit future insulations—are considered in this

study, by taking the medium set of values a_M,b_M as the base set (multiplier $M = 1$) and multiplying them by proper values of the multiplier M, as shown in Table 4. In more detail:

- An extremely low set, a_L,b_L, is obtained by multiplying a_M,b_M by $M = 0.5$;
- An extremely high set, a_{VH},b_{VH}, is obtained by multiplying a_M,b_M by $M = 2$;
- The interval $[a_L,b_L \div a_{VH},b_{VH}]$ is divided into 16 equally distributed sets of a,b values, each identified in Table 4.4 by the corresponding value of the multiplier M of the medium set a_M,b_M.

Table 4.4 sets of coefficients a, b representing the characteristics of the insulating material.

Classification	**Symbols of the *a,b* Set**	**M (Multiplier of a_M,b_M)**	***a* (1/°C)**	***b* (mm/kV)**
Low set	a_L,b_L	0.5	0.042	0.032
		0.6	0.05	0.0387
		0.7	0.059	0.045
		0.8	0.067	0.052
		0.9	0.076	0.058
Medium set	a_M,b_M	1	0.084	0.0645
		1.1	0.092	0.071
High set	a_H,b_H	1.2	0.101	0.0774
		1.3	0.109	0.0839
		1.4	0.118	0.0903
		1.5	0.126	0.0968
		1.6	0.134	0.1032
		1.7	0.143	0.1097
		1.8	0.1512	0.116
		1.9	0.156	0.1225
Very high set	a_{VH},b_{VH}	2	0.168	0.129

4.4 Results

4.4.1 Electric field distribution

Figure 4.5 presents the electric field distribution inside the insulation for both 320 kV cable (Figure 4.5(a)) and 500 kV cable (Figure 4.5(b)) during the first 24-h load cycle of the load cycle period

according to CIGRÉ Technical Brochure 496 at a voltage equal to rated voltage U_0. Therefore, the electric field distribution in the first instance is a capacitive distribution. The DC electric field distribution for the cold cable is presented in the blue curve (24 h curve).

In the simulations, different voltages—up to 4.5 times the rated voltage—are applied to the 320 kV XLPE-insulated cable, thereby obtaining the profiles within cable insulation of electric field, electrical conductivity and leakage current, shown in Figures 4.6–4.8, respectively.

In more detail, Figure 4.6 presents the DC electric field profiles for (a) the cold cable at ambient temperature, (b) the hot cable (i.e., rated current flowing in the conductor, as prescribed in CIGRÉ Technical Brochure 496 for the 24-h load cycles of the high load period). The maximum mean electric field is ≈80 kV/mm in case of applied voltage = 4.5 U_0; the electric field inversion phenomenon is observed in the hot cable (Figure 4.6(b)). Figure 4.7 demonstrates the effect of the applied voltage and temperature on the electrical conductivity in the insulation: it can be seen that the conductivity varies by [1.4 ÷ 2] orders of magnitude between the cold cable (Figure 4.7(a)) and the hot cable (Figure 4.7(b)). Moreover, it is worth noting that the conductivity of the inner insulation is much greater than that of the outer insulation for the hot cable due to the high temperature of the conductor. This difference in conductivity distribution inside the insulation is lesser in the cold cable because in this case the temperature is constant over the insulation and the quasi-capacitive electric field is the only variable quantity in the conductivity expression (1.30). Figure 4.7 also illustrates the effect of the applied voltage (i.e., the electric field) on the conductivity of XLPE insulation, which rises by ≈1.5 orders of magnitude when rising the voltage from U_0 to 4.5 U_0. Figure 4.8 presents the leakage current for 320 kV XLPE-insulated cable for the considered applied voltages during the first 24-h load cycle of the load cycle period according to CIGRÉ Technical Brochure 496. It is clear that the leakage current increases by ≈2.5 orders of magnitude by applying 4.5 U_0.

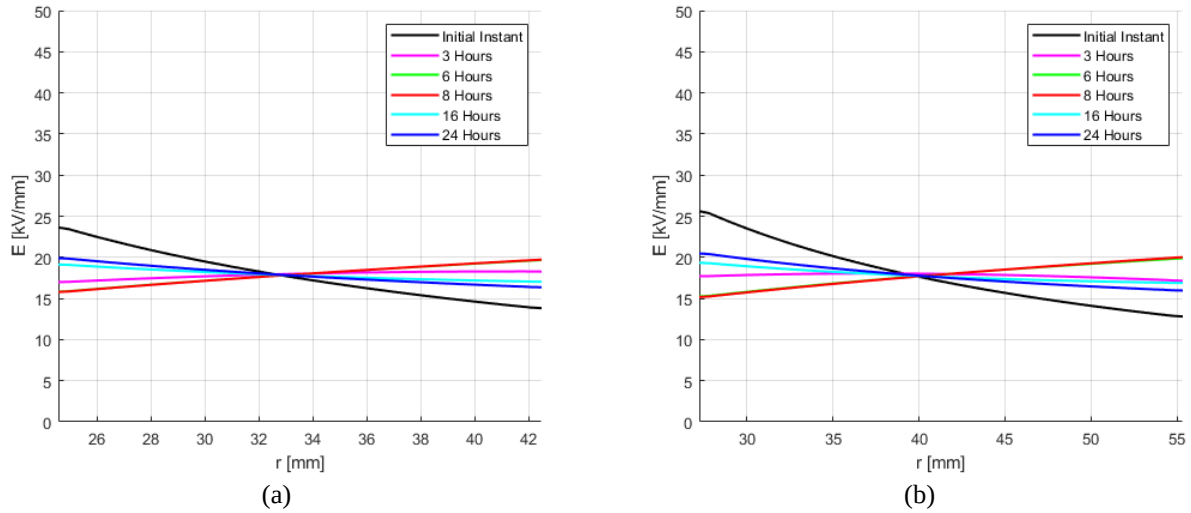

Figure 4.5 The electric field distribution in the insulation of (a) 320 kV cable, (b) 500 kV cable, during the first 24-h load cycle of the load cycle period according to CIGRÉ Technical Brochure 496.

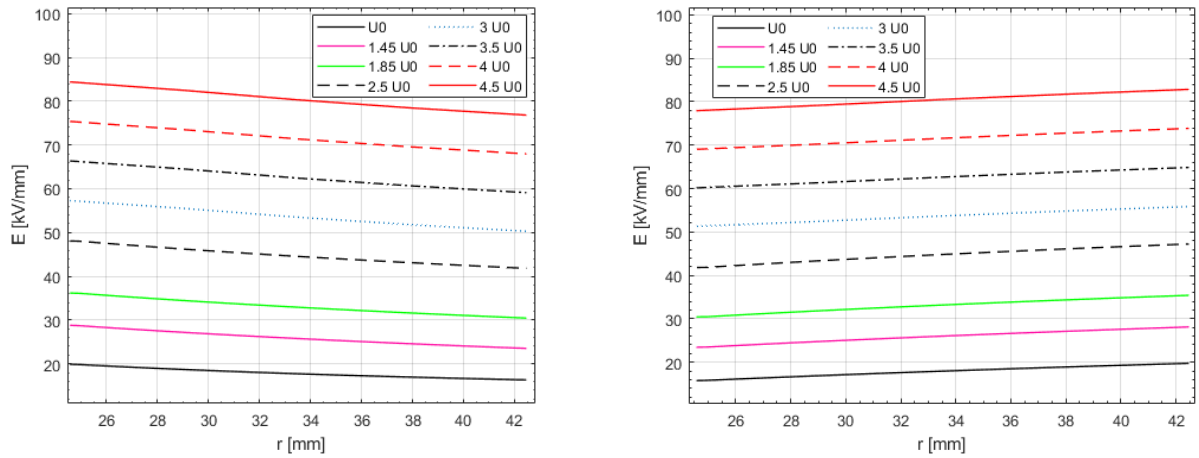

(a) (b)

Figure 4.6 The DC electric field profiles in the insulation of the 320 kV cable for different applied voltages: (a) at the ambient temperature (cold cable), (b) in the high load period according to CIGRÉ Technical Brochure 496 (hot cable).

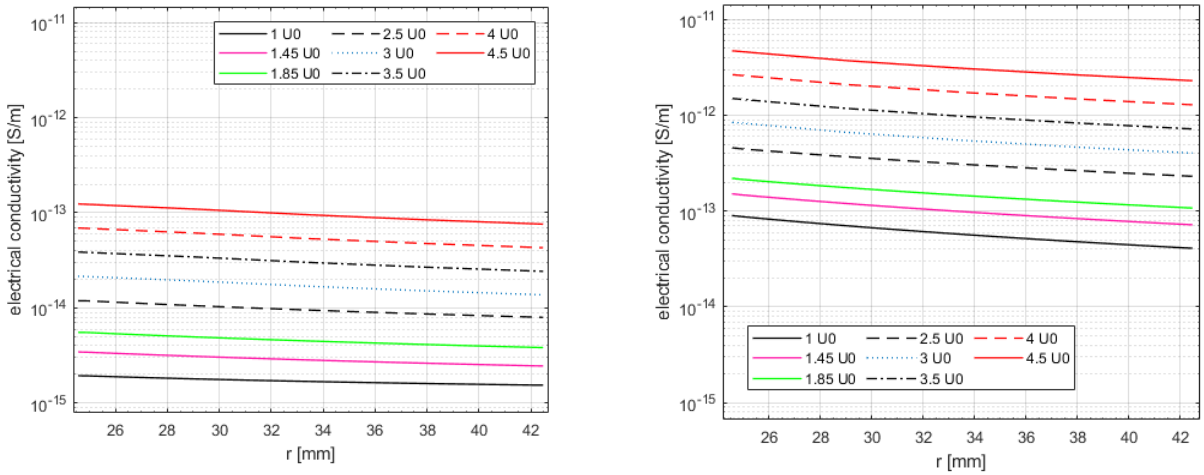

(a) (b)

Figure 4.7 The electrical conductivity profiles in y-log scale inside the insulation of the 320 kV cable for the different applied voltages: (a) at the ambient temperature (cold cable), (b) in the high load period according to CIGRÉ Technical Brochure 496 (hot cable).

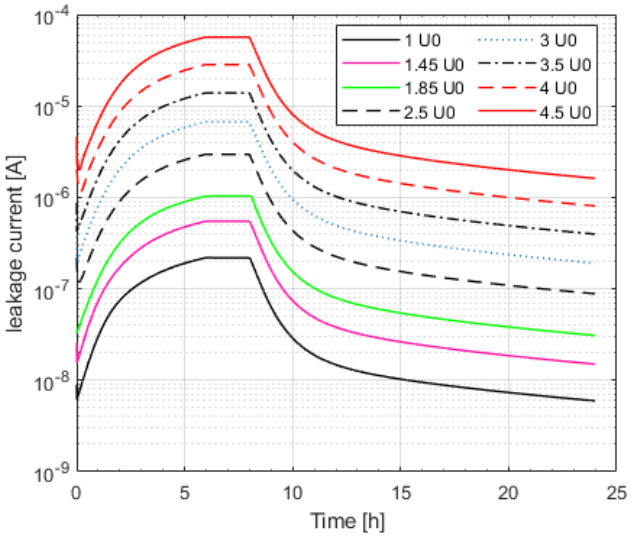

Figure 4.8 The leakage current of the 320 kV cable in y-log scale for different applied voltages during the first 24-h load cycle of the load cycle period according to CIGRÉ Technical Brochure 496.

4.4.2 Insulation losses

Figure 4.9 shows the insulation losses during the first 24-h load cycle compared to the conductor losses in both linear and logarithmic y-scale for both the 320 kV and 500 kV cables subjected to many values of the applied voltage starting from U_0, 1.45 U_0 and 1.85 U_0, which correspond, respectively, to the rated voltage, pre-qualification test (PQT) voltage and type test voltage (TT). It can be seen from Figure 10 that the insulation losses at rated voltage U_0, PQT voltage = 1.45 U_0 and TT voltage = 1.85 U_0 are hardly noticeable compared to conductor losses, having maximum values of (0.06, 0.2, 0.6 W), respectively, which can be deemed negligible compared to the conductor losses ≈40 W. Although TT voltage is the most severe condition to be continuously applied on the cable, higher values of the applied voltage are also considered to reach high enough values of insulation losses to cause thermal instability. It is evident that the insulation losses of the 500 kV cable are approximately 1.5 times greater than that of the 320 kV cable (the same as the ratio between their insulation thicknesses). Therefore, the thicker the insulation is, the greater the insulation losses are. This ratio may be different according to the cable's temperature and time during the load cycle, namely, this can be justified by the field inversion phenomenon which takes place in DC cables, during which the electric field in the outer insulation becomes greater than that in the inner insulation.

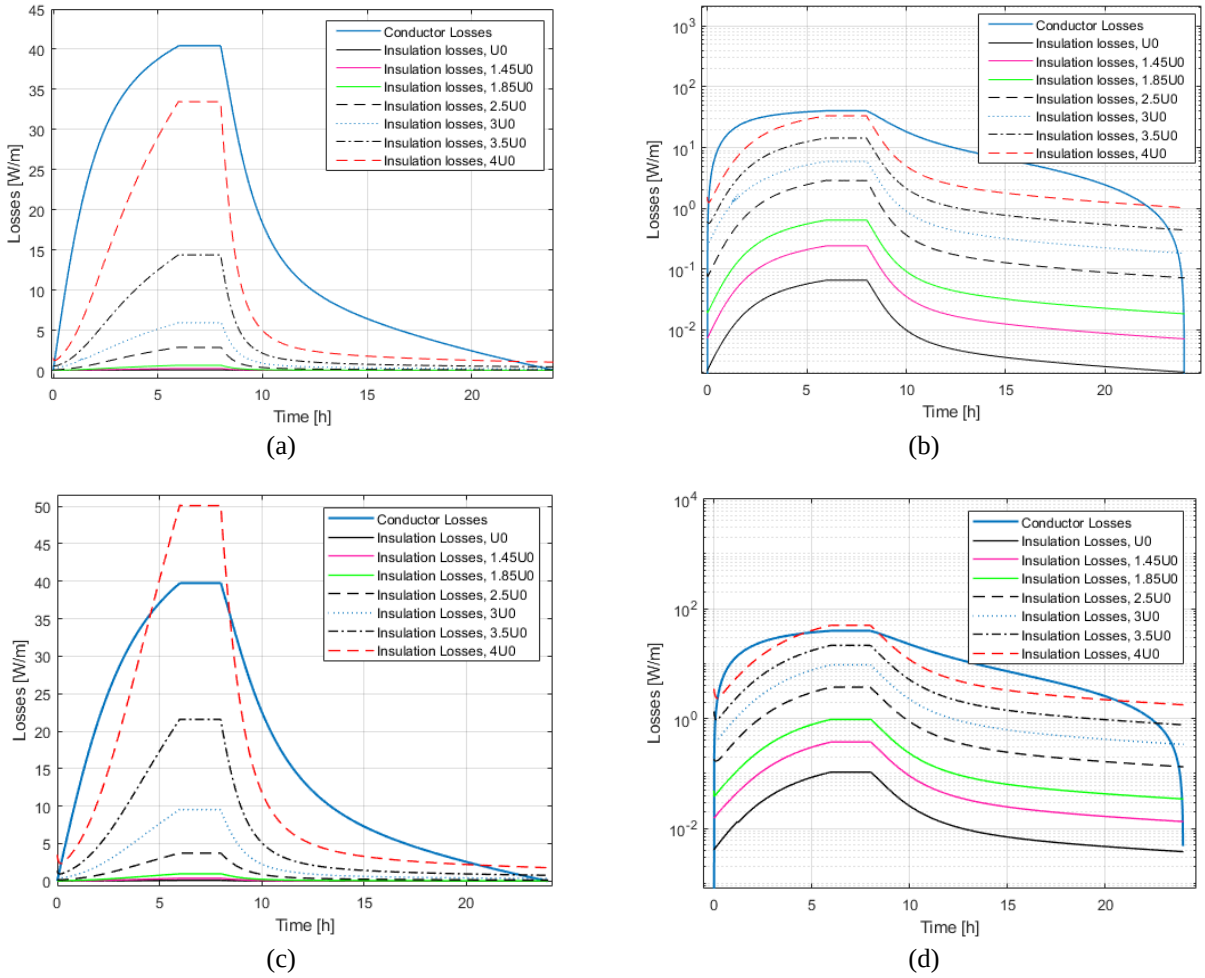

Figure 4.9 The insulation losses of (a,b) the 320 kV cable and (c,d) the 500 kV cable in both linear (a,c) and logarithmic (b,d) y-scale during the first 24-h load cycle of the load cycle period.

4.4.3 Temperature rise

Many runs of the code have been performed to obtain the temperature rise in the insulation of the hot cable (i.e., with rated current flowing in the conductor) due to insulation losses —calculated according to Equations (4.1) – (4.10) — added to conductor losses. As a further verification, the results obtained have been also checked by calculating—in alternative to (4.2)—per unit dielectric losses as $w_d = \sigma E^2$ and the results have been found to be the same. Different values of a, b coefficients are considered to show the effect of the cable characteristics on the insulation losses and consequently on the temperature rise.

It can be noticed from Figure 4.10 that the temperature rise due to insulation losses is strongly dependent on the values of conductivity coefficients of temperature and electric field for the 320 kV cable. In Figure 4.10(a) the low values of a, b (a_L, b_L) lead to weak dependency of the conductivity on the temperature and the electric field giving a temperature rise of 0.5 [°C] which is not enough for

thermal runaway to take place. Figure 10(b) shows the case of a_M, b_M, where a considerable temperature rise due to insulation losses can be noticed; the temperature rise is negligible for rated voltage, PQT voltage and TT voltage, it increases by ≈ [2 ÷ 3] °C for 2.5 U_0 and thereafter exponentially increases exceeding 30 °C for 4U_0. Figure 10(c) shows the case of the high set a_H, b_H, in which even a moderate increase of the applied voltage with respect to U_0 (e.g., PQT and TT voltages) leads to a temperature rise of [1 ÷ 3] °C; the temperature rise becomes ≈10 °C for an applied voltage equal to 2.5 U_0, namely more than three times than in the case of a_M, b_M.

Coming to the 500 kV cable in case of a_M, b_M—a set of conductivity coefficients which fits well on the average the overall behavior to XLPE insulating materials—in Figure 4.11 it can be noticed that the temperature rise is greater than that of the 320 kV cable, due to the greater insulation thickness—since the electric field and the conductor temperature are similar in both cables.

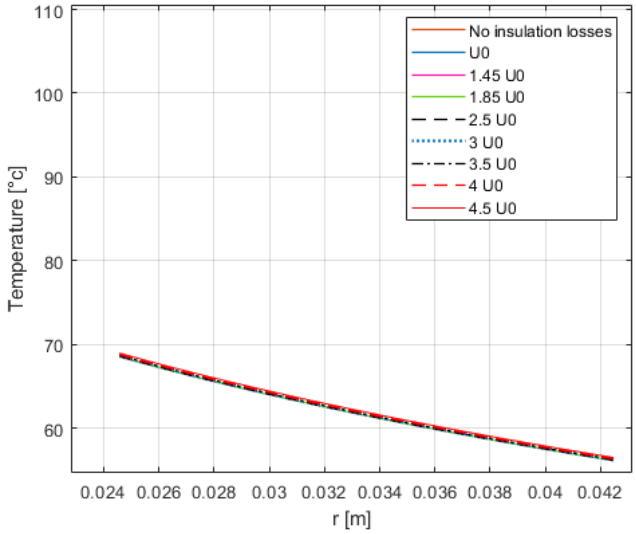

(a)

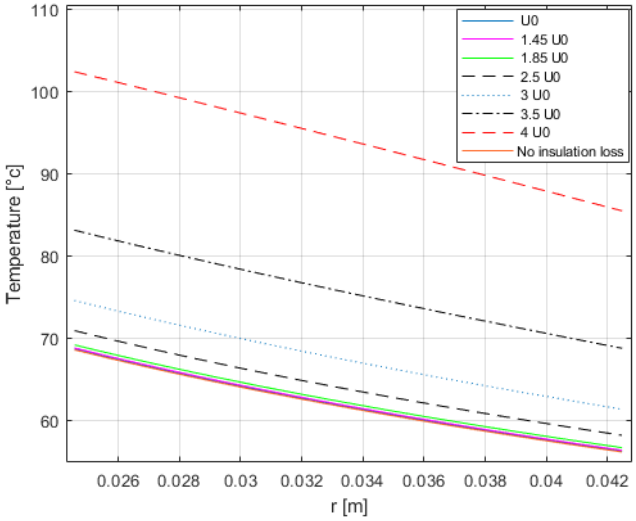

(b)

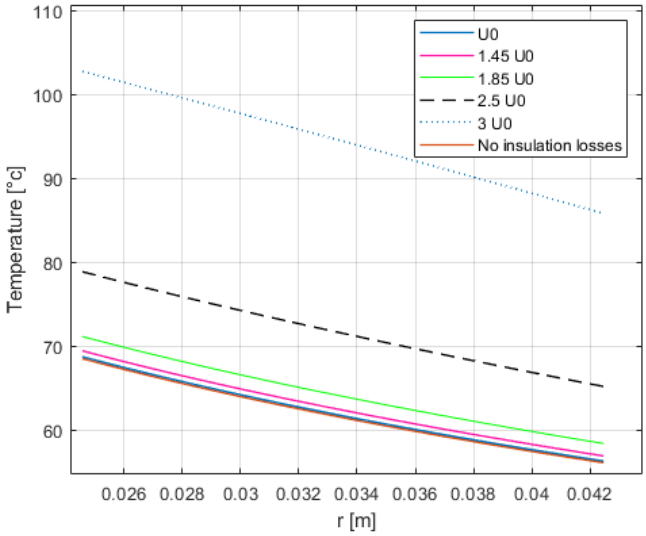

(c)

Figure 4.10 The temperature rise of the hot vable due to insulation losses added to conductor losses vs. the position within the insulation thickness for increasing values of applied voltages with 3 sets of conductivity coefficients: (a) a_L, b_L; (b) a_M, b_M; (c) a_H, b_H. 320 kV cable.

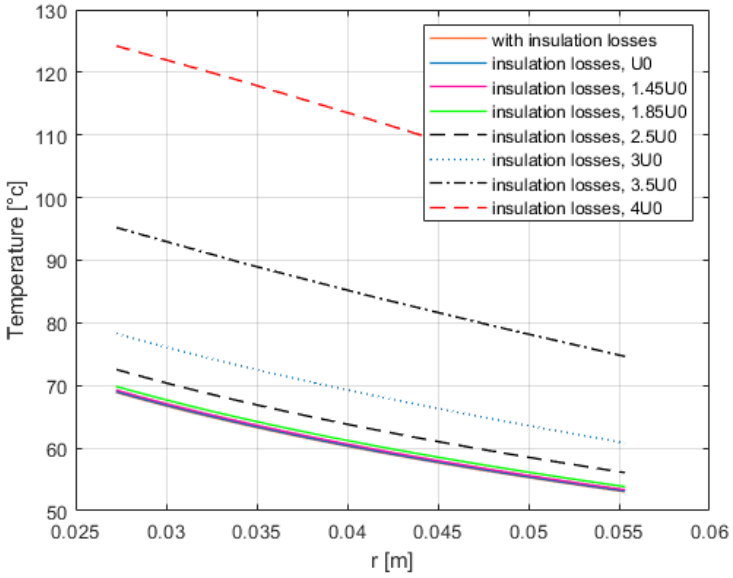

Figure 4.11 The temperature rise of the hot cable due to insulation losses added to conductor losses vs. the position within the insulation thickness for increasing values of applied voltages up to 4.5 times the rated voltage with the medium set of conductivity coefficients a_M, b_M. 500 kV cable.

4.4.4 Dielectric loss coefficient β_d

Figure 4.12 shows the values of β_d for the 320 kV cable, obtained using relationship (4.12) calculated at each time step $\Delta t = 1\ (s)$ during the first 24-h load cycle of the load cycle period after [29]. Similar curves are obtained for all values of applied voltages, all sets of *a* and *b* coefficients, as well as for the 500 kV cable. The capacitive electric field distribution at the beginning of the first load cycle gives a value of $\beta_d = 0.5$, which agrees with the value of β_d mentioned in IEC 60853-2 for AC cables. Then, it goes down within 30 min to fall within the range $\beta_d = [0.38 \div 0.4]$ which represents the typical range of values of β_d for DC cables. As explained here below, this result is consistent with the well-known fact that the electric field of inner insulation in DC is lower than that in AC: this already holds for the unloaded cable (compare in Figure 4.5 the black curve = AC electric field vs. the blue curve = DC electric field at ambient temperature), but it holds a fortiori as the cable is loaded (see warmer color curves in Figure 4.5, corresponding to higher cable load and temperature). Thus, compared to AC cables, the insulation losses in DC cables move towards the outer insulation, i.e., they are lower in the inner insulation and higher in the outer insulation, as readily seen from the alternative expression of per unit volume dielectric losses:

$$w_d = \boldsymbol{J}.\boldsymbol{E} = \sigma E^2 \tag{4.20}$$

(for the loaded cable at outer insulation the quadratic increase in losses due to the higher electric field overwhelms the decrease in losses due to the slight conductivity drop because of lower temperature). Now, by carefully inspecting Equations (4.11) and (4.12) it can be understood that, physically, the parameter β_d represents the "equivalent"—from the viewpoint of the overall temperature drop across insulation $\Delta\vartheta_d$ —fraction of dielectric losses W_d crossing the whole thermal resistance of the insulation, hence, it is the part of the dielectric losses which cause a temperature drop inside the insulation. Consequently, it is reasonable that β_d is lower in DC than in AC, as dielectric losses in DC cables move towards outer insulation. By comparing the updated version of "Recommendations for Testing DC Extruded Cable Systems for Power Transmission at a Rated Voltage up to 500kV, CIGRÉ Technical Brochure 496, 2012." [29] which is "Recommendations for testing DC extruded cable systems for power transmission at a rated voltage up to and including 800 kV, 2021" [74], it can be noticed that the minimum temperature drop inside the insulation thickness is also limited (in addition to the limit of the maximum temperature drop inside the insulation thickness). As a result, a minimum temperature drop inside the insulation thickness is required to ensure enough heat flux from the conductor towards the surrounding environment.

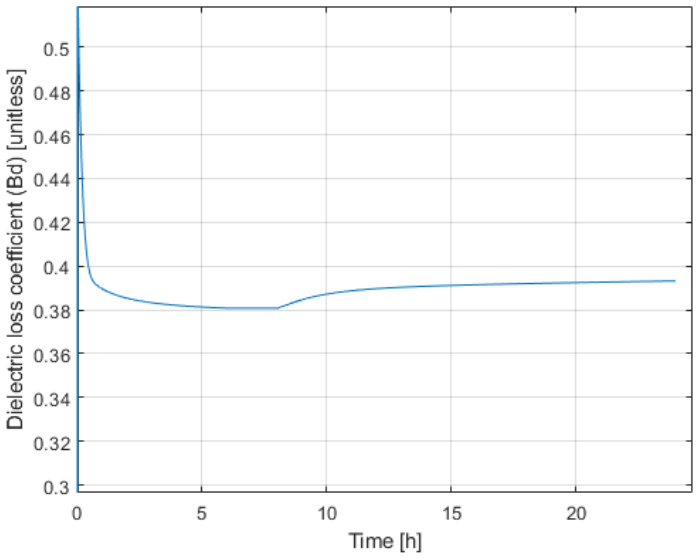

Figure 4.12 Dielectric loss coefficient β_d during the first 24-h load cycle of the load cycle period after [29]. 320 kV cable.

4.4.5 Thermal stability diagram

Figure 4.13 is the so-called "thermal stability diagram" of the 320 kV (Figure 4.13(a)) and of the 500 kV (Figure 4.13(b)) cables for different values of applied voltage: with reference to Equations (4.18), and (4.19), it shows the insulation losses W_d (colored curves) and the dissipation losses W_{diss} (black

straight line) on the *y*-axis as a function of the metallic sheath temperature T_{sheath} on the *x*-axis. The metallic sheath temperature in turn varies with conductor temperature according to the $\Delta\vartheta_{cl}$ term in (4.11). From this diagram the so-called maximum thermal voltage (MTV) can be attained, namely the maximum value of the applied DC voltage above which no equilibrium is achieved in the design conditions of the environment. For both 320 kV and 500 kV XLPE-insulated cables, the medium set of conductivity coefficients (a_M, b_M) is considered for the sake of brevity.

Figure 4.13 shows that the higher the applied voltage, the higher the insulation losses, which reduces the maximum (or critical) value of cable current I_{crit} that keeps the cable thermally stable. I_{crit} is obtained from the value of losses found on the *y*-axis as a complement of the insulation losses to the dissipation line. This implies a reduction in cable load current from the rated current in the design conditions of the environment, I_D (cable ampacity), to critical current I_{crit}: such a load reduction is necessary to avoid thermal instability.

Let us focus for the sake of illustration on Figure 4.13(a): for instance, in the absence of dielectric losses a metallic sheath temperature of 50 °C corresponds to a conductor temperature of 62.5 °C, as obtained from Equation (4.11) without insulation losses and for a conductor current lower than cable ampacity (note that conductor temperature in the absence of dielectric losses reaches 70 °C when conductor current is equal to cable ampacity and metallic sheath temperature is equal to 55 °C, see Figure 4.4(a)). In the case of applied voltage equal to 3.5 times the rated voltage = 1120 kV, the insulation losses are equal to 8.4 W (see point A in Figure 4.13(a)) and lead to temperature rise of 8.5 °C in the inner insulation (again from Equation (4.11)). Then, as pointed out above, the critical value of cable current I_{crit} can be derived from the vertical distance along *y*-axis from the dissipation line (see point B in Figure 4.13(a)), which is ≈26 W and corresponds to a conductor temperature of 52 °C in the absence of insulation losses. However, this case falls within the "unstable equilibrium" expressed by conditions (4.19); namely, an equilibrium exists, but even a slight temperature rise leads eventually to instability, unless the cable is further underloaded.

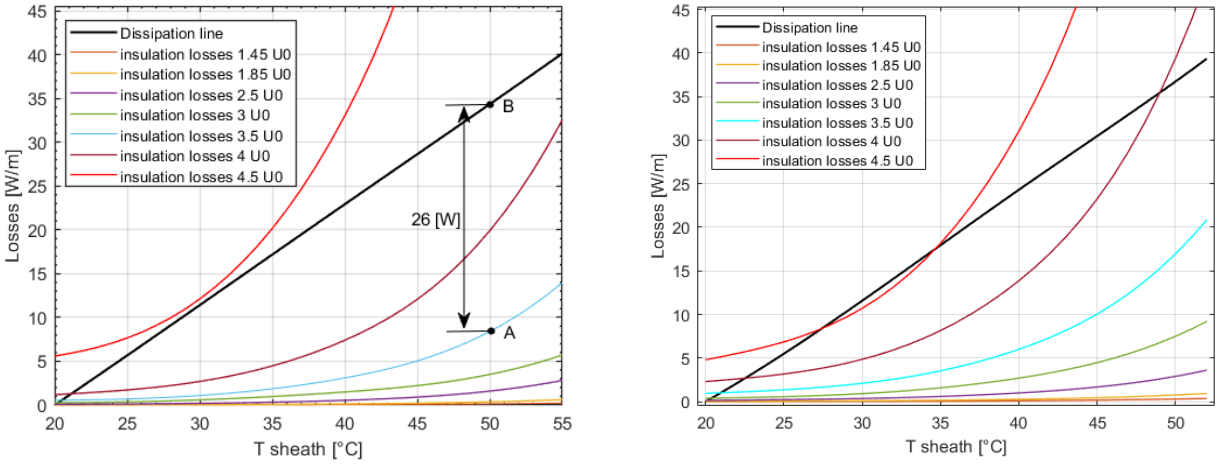

Figure 4.13 The thermal stability diagram for (a) the 320 kV cable and (b) the 500 kV cable for different applied voltages up to 4.5 times the rated voltage.

For low applied voltages, in which two equilibrium points can be found, both conditions in Equation (4.19) need to be satisfied to reach the instability. In other words, to ensure thermal stability, a stable equilibrium must exist ($W_o = W_{diss}$ & $\partial W_o/\partial T < \partial W_{diss}/\partial T$). Figure 4.13(a) shows that a stable thermal equilibrium exists up to $3U_0 \approx 1000$ *kV* (54 *kV/mm*)—among the considered values of the applied voltages—for a fully loaded (i.e., conductor current equal to cable ampacity) 320 kV XLPE cable buried in soil. When higher voltages are applied, conductor current has to be progressively reduced with respect to cable ampacity to keep the cable thermally stable, until conductor current reaches zero at $4.5U_0$. Thus, in unloaded cable subjected to $4.5U_0$ no equilibrium between the insulation losses and the heat dissipation exists and thermal instability eventually occurs starting from a temperature rise equal to only 5 °C, then, raising the metallic sheath temperature and moving the operating point towards the direction of the metallic sheath temperature rise (to the right here) until an intersection between the generation curve and the dissipation line exists, if any. Otherwise, thermal instability will be inevitable as occurs anyway in case of $4.5U_0$, which is the first case of thermal instability, as in Equation (4.18).

Coming now to Figure 4.13(b)—the same as Figure 4.13(a) but for the 500 kV cable (a_M, b_M)—the thermal runaway of intrinsic nature occurs at voltages slightly greater than 4.5 $U_0 \approx$2250 kV, although the mean electric field necessary to reach thermal instability in unloaded cable is almost the same in both cables having different thicknesses. For lower voltages $[2.5 \div 4]$ U_0, it can be noticed from Figure 4.13(b) that the insulation losses are greater than those of the 320 kV cable at the same voltages, with a more significant exponential rise. This implies more load reduction is required to avoid thermal instability, thus, worsening the stability and loading conditions.

Figure 4.13(b) shows that a stable thermal equilibrium exists up to $2.5U_0$ = 1250 *kV* (45 *kV/mm*)—among the considered values of the applied voltages—for a fully loaded 500 kV XLPE cable buried in soil. Thus, this voltage value can be deemed as the maximum thermal voltage of these cables.

4.4.6 The effect of insulation characteristics

For the sake of the generality of the obtained results, the results for different electrical conductivity characteristics of cable insulation are obtained as can be seen in Figure 4.14, which shows the insulation losses as a function of mean electric field in the insulation over a wide range of values of mean electric field (from the rated one up to 100 kV/mm) for different *a, b* coefficients (see Table 4.4) at the maximum conductor losses (full load) for the 320 kV cable. This figure highlights the importance of the insulating material, represented here by the temperature and electric stress coefficients of electrical conductivity, on the thermal stability of the cable. The very high *a, b* coefficients give rise to very high insulation losses compared to conductor losses. Some thermoplastic materials tend to have *a, b* coefficients up to 0.15, 0.128, respectively, which is referred to as *M* = 1.8 in Figure 4.14 and Table 4. According to the simulations summarized in Figure 4.14, materials having such characteristics would not have acceptable thermal stability properties for the insulation of HVDC cables. For materials having the so-called "high" values of *a, b* coefficients, namely a_H, b_H with M = 1.2 in Table 4.4, the insulation losses are low up to TT voltage = 1.85 U_0, then they exponentially increase for greater electric fields. Coming to the medium set of *a, b* coefficients, taken as a reference (M = 1 in Table 4.4) since they correspond to typical XLPE insulation for HVDC cables [54], it leads to a more stable behavior with low insulation losses up to *E* = 40 kV/mm which is a conservative value and greater than the electric field in case of type test at 1.85 U_0 (the most severe DC voltage to be continuously applied to the cable in tests after [29]). For higher values of the electric field corresponding to a voltage up to $3U_0$, the insulation losses increase, however, a stable equilibrium can be attained; both stable and unstable equilibrium can be reached for voltages greater than $3U_0$ (according to loading conditions); but instability becomes inevitable for field values corresponding to a voltage equal to or higher than $4.5U_0$. The lower set of values of *a, b* (M = 0.8, 0.9) which are typical of paper insulations [54] make the intrinsic thermal instability unlikely to take place even for high values of the electric field, say, higher than ≈70 kV/mm. The lowest set of values of *a, b* coefficients (which, to the best of the authors' knowledge, does not correspond to any known insulating material used in HVDC applications, but is considered here for the sensitivity analysis), it does not give an insulation loss temperature rise greater than 6 °C for the highest electric field considered in this study.

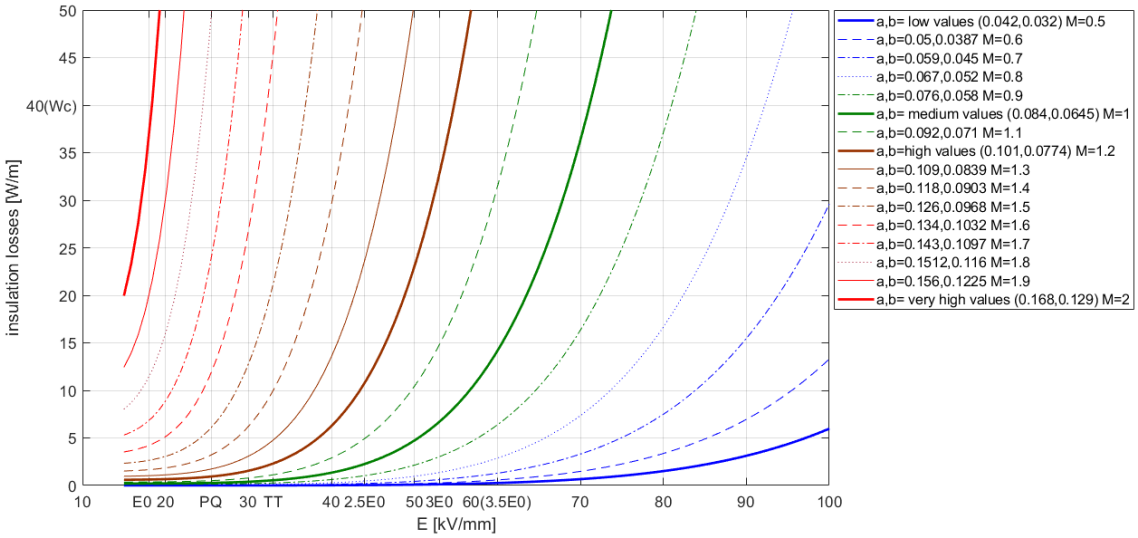

Figure 4.14 The insulation losses vs. the mean electric field in the insulation for different values of temperature and stress coefficients of electrical conductivity *a*, *b* as reported in Table 4.4 at the maximum conductor losses (full load).

4.4.7 De-rating factor

Figure 4.15 demonstrates the de-rated conductor current, the so-called I_c in Equation (4.16), (Figure 4.15(a)) and the de-rating factor, *DF* in Equation (4.17), (Figure 4.15(b)) with respect to the applied voltage ranging from U_0 to 3 U_0. Greater voltages are not studied since $3.5U_0$ or higher voltages lead to unstable equilibrium at losses equivalent to the rated current $I_{c,n}$ as discussed in Section 4.4.5 and shown in Figure 4.13. Figure 4.15 shows that at the rated voltage *DF* = 1, *DF* becomes lower than 0.99 at ≈1.8 U_0 and then it drops dramatically until the voltage $3U_0$ where it reaches a value *DF* = 0.93 for 320 kV cable and *DF* = 0.88 for 500 kV cable. The results also clearly show that the 500 kV cable is more de-rated than the 320 kV cable for the same multiplier of the applied voltage.

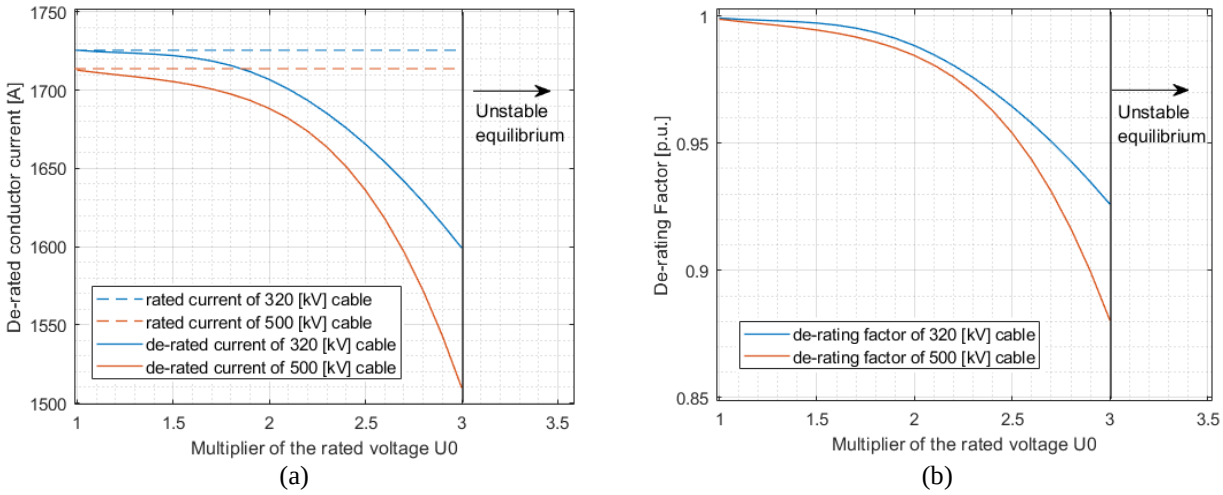

Figure 4.15 (a) The de-rated conductor current w.r.t times the rated voltage, (b) de-rating factor w.r.t times the rated voltage for both the 320 kV and 500 kV cables.

4.5 Discussion

For the 320 kV cable, the $4.5U_0 \approx 1400$ kV curve in Figure 4.13a refers to thermal instability of an intrinsic nature: no load current is required for instability to take place because of the extreme temperature rise inside the insulation without temperature runaway near the metallic sheath; in this case, the instability occurs even at the ambient temperature, because the insulation losses are enough to heat up the insulation and move the operating point towards higher temperatures (towards right on the red curve Figure 4.13) until the breakdown occurs due to the absence of any type of equilibrium. The insulation losses which lead to thermal instability can be found from Figure 4.13, then the resulting temperature rise is calculated from Equation (4.11) considering the value of $\beta_d = 0.4$ to obtain $\Delta\vartheta_d = 5\ ℃$ at $\vartheta_a = 20\ ℃$. This study shows that thermal instability occurrence is possible even at lower applied voltages because of its dependency on the load current. This value is lower than those found in the literature, which range between [8 ÷ 22] °C for a constant metallic sheath temperature fixed at the ambient temperature according to Whitehead, Eoll and Reddy. Reddy et al. found that the maximum thermal voltage is equal to 1300 kV at a rated current = 1400 [A] for a 17.9-mm-thick XLPE cable. The soil environment can be a reasonable justification of this difference.

Coming to the 500 kV cable, the results of this study show an increase in the insulation losses in the case of 500 kV cable compared to the 320 kV cable. Those results are approximately consistent with Reddy's results in which the intrinsic maximum thermal voltage increases with the insulation thickness to reach a value ≈1800 kV for an insulation thickness ≈28 mm under load, whereas for the 500 kV cable, the intrinsic instability is guaranteed for applied voltages greater than 2250 kV even in unloaded cable. (The results are not fully comparable due to the difference in the inner insulation radius). Another interesting result (see Figure 4.13) is that the mean electric field, necessary for intrinsic thermal runaway to take place ≈4.5 U_0, is not noticeably affected by the variation of the cable thickness and this result is consistent with Reddy *et al.* [73]. The results shown in Section 4.5 lead to the conclusion that the greater the insulation thickness is, the more underloading is required to sustain the stability.The most important novelty in this study is the relationship between insulation losses and the conductivity coefficients of temperature and electric field, *a, b*, for different electric fields up to 100 kV/mm, which has not been extensively studied in the literature so far, mainly due to the lack of available values of *a*, *b*. The results show high dependency of the insulation losses on the electrical conductivity coefficients of temperature and electric field. The calculation of the value of dielectric loss coefficient β_d for DC cables compared to AC cables is also another novelty in this study, making the temperature calculations possible if the insulation losses are known. Furthermore, the dielectric loss coefficient for DC cables is found to be $\beta_{d\_DC} = 0.4$ which is lower than its value for AC cables $\beta_{d\_AC} = 0.5$. The latter highlights the fact that thermal instability is critical in DC cable.

Chapter 5

Models for electrical conductivity

5.1 Introduction:

DC electrical conductivity is considered one of the most critical parameters in determining the validity of a certain insulating material in DC systems. The main reason is the dependency of the electric field distribution on the conductivity (which in turn depends on both the temperature and the electric field) in DC cable systems as the poling DC field causes space charge mobility, trapping and/or de-trapping inside the cable insulation hence changing the capacitive electric field distribution into more complicated field distribution, dissimilar to the AC system where the electric field is still capacitive due to the absence of such space charge accumulation and mobility [75]. Physical models for describing the space charge behavior inside the insulation have been introduced with the proper fitting parameters to the space charge measurements (e.g., bipolar charge transport equation) [76]. Another simpler method for describing the space charge behavior is to be represented by the electrical conductivity in a phenomenological way, where the electrical conductivity is represented by a closed-form function to the temperature and electric field, then the charge density can be calculated as the charges accumulated at the discontinuities of permittivity and conductivity from Equation (5.1) [2]. The former methods are called physical (or microscopic) models, while the latter are called phenomenological (or macroscopic) models for DC electrical conductivity.

$$\rho = J.\nabla\left(\frac{\varepsilon}{\sigma}\right) \tag{5.1}$$

While physical models are mainly used in numerical calculations in the full cables and accessories (joints and terminations) as a compromise with the difficulty in both finding its fitting parameters and its application, the macroscopic models are mainly directed to the applications where preliminary field calculations are required (e.g., cable design and standardization) due to its simplicity in both finding the fitting parameters and its application. In this chapter, the experimental conductivity measurements performed by L. Boyer *et. al.* in SuperGrid institute in [77] are fit to the macroscopic DC conductivity models mostly found in the literature. Furthermore, the latter models are modified in such a way that the experimental data have a better fit to those new models.

5.2 Theoretical:

The fitting method used in this study is the least squares in which coefficients of the best fit are obtained by minimizing the residual (i.e., the difference between the fit and the data), as follows:

$$r_i = y_i - \hat{y}_i \tag{5.2}$$

$$\min(S) = min\left[\sum_{i=1}^{n} {r_i}^2\right] = min\left[\sum_{i=1}^{n} (y_i - \hat{y}_i)^2\right] \quad (5.3)$$

Where n is the number of data points. S is the sum of squares to be minimized. r_i are the residuals of the i'th data point. y_i is the i'th data. $\hat{y}_i$ is the i'th fit to data.

The electrical conductivity in DC cables are described by non-linear equations. Therefore, a non-linear least-squares method will be used in this application where the coefficients cannot be estimated using simple matrices. Hence, an iterative method is used as follows:

- Start with an initial estimate of each coefficient considered in the model based on the experience with fitting of similar models found in the literature.
- Produce a fitted surface for the current set of coefficients.
- Adjust the set of coefficients using one of the following algorithms:
  1) Levenberg-Marquardt: it is usually used when coefficients constraints are not provided.
  2) Trust-region: it is more efficient but it requires coefficients constraints to be provided.
- Produce new fit and iterate until a minimum is found.

5.3 Application:

5.3.1 Leakage current measurements and conductivity calculation:

Boyer *et. al* have performed current measurements on a cable with 5-mm-thick XLPE insulation in [77]. The current measurement was carried out by the means of a shunt resistor between the outer screen and the ground pit at three temperatures i.e., 19°C, 45°C and 75°C in polarization/depolarization cycles with a minimum duration of 1 hour each under applied voltages ranging between 15 kV and 165 kV. The leakage current was measured by summing the averaged values over the last 10 minutes of each polarization or depolarization stage. To calculate the conductivity, the electric field is assumed capacitive when the time constant is great enough to keep a quasi-capacitive field distribution within the insulation thickness during polarization or depolarization stages. The latter assumption becomes not accurate at high fields and/or temperatures (i.e., the green points in Figures 5.1 and 5.2).

$$\sigma = \frac{J}{E} = \frac{I}{2\pi r l} . \frac{r\ ln(r_o/r_i)}{U} = \frac{I\ ln(r_o/r_i)}{2\pi l\ U}\ [S/m] \quad (5.4)$$

where σ is the apparent conductivity [S/m], r_i is the inner-insulation radius [m], r_o is the outer-insulation radius [m], U is the applied voltage [V], l is the length of cable in [m], I is the measured leakage current [A]

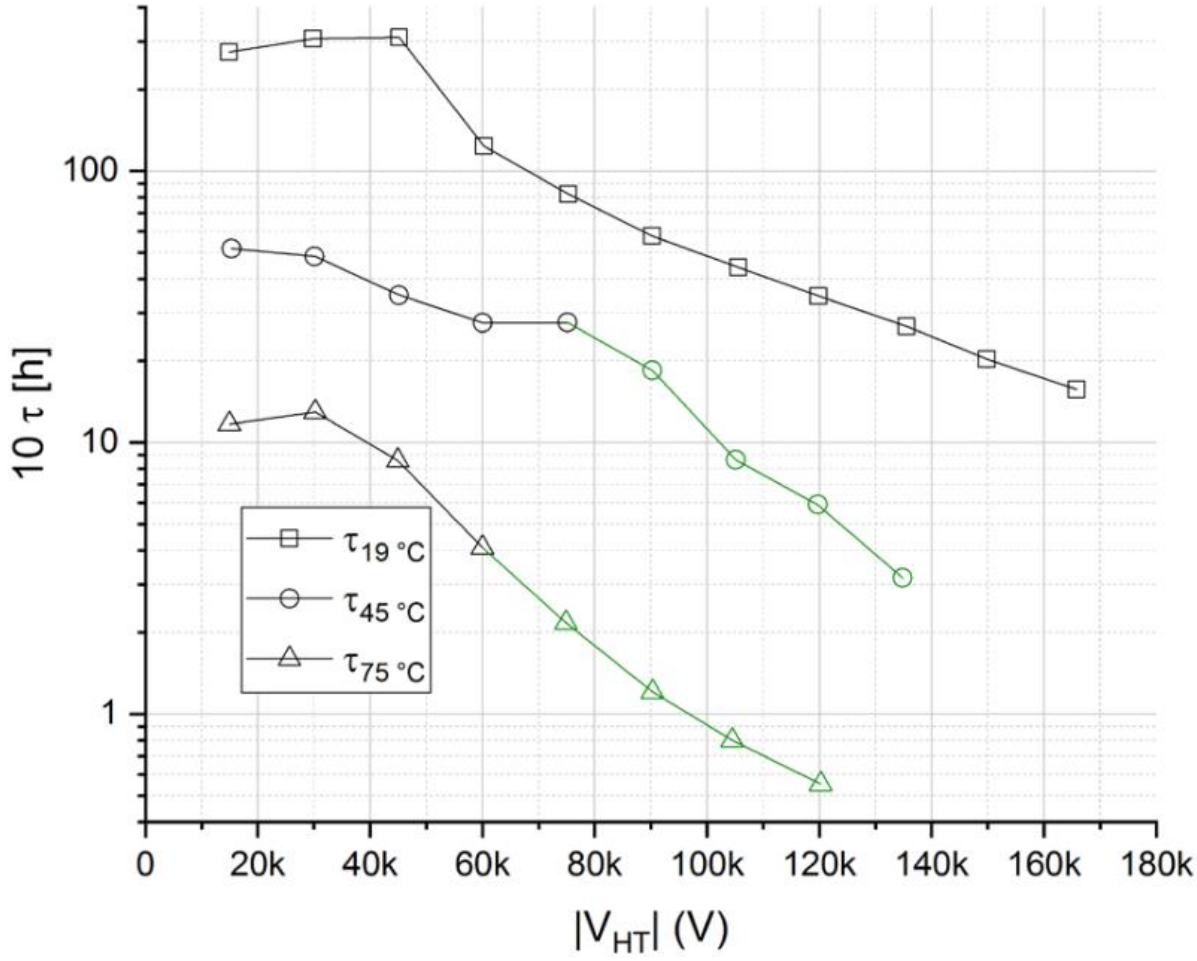

Figure 5.1 The time to stability required to reach a resistive field distribution inside the cable insulation for different voltages and temperatures. After [77]

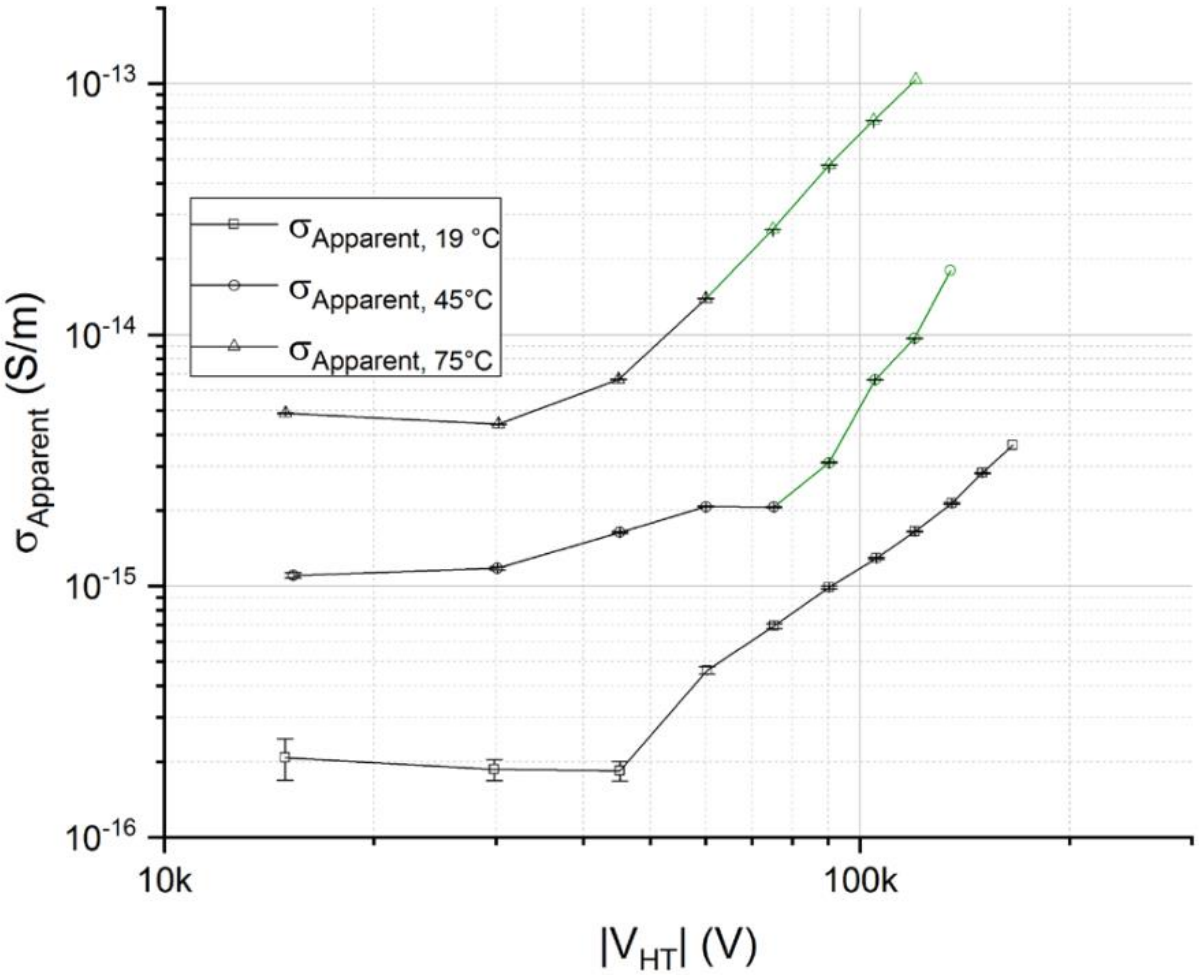

Figure 5.2 The apparent conductivity calculated for different voltages and temperatures. After [77]

5.3.2 Macroscopic conductivity models:

Model 1:

The empirical model first introduced by Klein in [6] which has exponential dependencies on both temperature and electric field:

$$\sigma = \sigma_0 \, exp(aT + bE) \tag{5.5}$$

T and E are independent variables. σ is a dependent variable. σ_0, a, and b are the parameters to be fit.

Model 2:

This model is similar to Model 1, however, the field coefficient is assumed to have a linear function with respect to the temperature to represent the a mutual increase of the conductivity due to both the

temperature and the field together. This synergism is represented in this model by the coefficient c. Model 2 has also exponential dependencies on both temperature and electric field, as follows:

$$\sigma = \sigma_0 \, exp(aT + (b + cT)E) \tag{5.6}$$

where *T* and *E* are independent variables. σ is a dependent variable. σ_0, a, b, and c are the parameters to be fit.

Model 3:

This empirical model can be also found in the literature, it has an exponential dependency on the temperature and a power dependency on the electric field:

$$\sigma = \sigma_0 \, exp(aT) \, E^{\gamma} \tag{5.7}$$

where *T* and *E* are independent variables. σ is a dependent variable. σ_0, a, and γ are the parameters to be fit.

Model 4:

In this model the dependency of the conductivity is Boltzmann- (or Arrhenius-) like on the temperature whereas it is a quasi-hyperbolic sine function with respect to the electric field.

$$\sigma = \sigma' \, exp\left(-\frac{G_a}{k_B T}\right) sinh(cE).E^{\gamma} \tag{5.8}$$

where *T* and *E* are independent variables. σ is a dependent variable. σ', G_a, c, and γ are the parameters to be fit. G_a is the thermal activation energy governing the temperature dependence of the conductivity (*eV*), k_B is Boltzmann constant 8.62×10^{-5} (*eV/K*). Although this model is also phenomenological as the other four models, its dependencies on the temperature and the electric field are related to the physical processes of the charge carriers which occur inside the insulation. While the relationship with the temperature in the first term follows the Arrhenius relationship of the chemical reaction rate, the second term of the conductivity can be justified by the hopping and ionic conduction processes inside the insulation in a quasi-hyperbolic sine function [78].

Model 5:

This empirical model was used in [79]. The dependency is Arrhenius-like on the temperature and exponential on the electric field.

$$\sigma = \sigma_0 \, exp(-a/T + bE) \tag{5.9}$$

where T and E are independent variables. σ is a dependent variable. σ_0, a, and b are the parameters to be fit.

5.3.3 Fitting models to experimental data:

MATLAB curve fitting tool is used in this study to fit the 5 models to experimental data. The fitting to the logarithmic function of Equations (5.5) to (5.9) is chosen instead of the fitting to the conductivity itself. The reason is that the conductivity varies over many orders of magnitude [$10^{-16} \div 10^{-13}$] which gives extreme weight to the residual errors r_i of the conductivity points with high conductivity (temperatures and fields), while it gives negligible weight of the points with low conductivity (low temperatures and fields). Hence, Equation (5.3) becomes as follows:

$$min\,(S) = min\left[\sum_{i=1}^{n} {r_i}^2\right] = min\left[\sum_{i=1}^{n} \left(ln(\sigma_i) - ln(\hat{\sigma}_i)\right)^2\right] \tag{5.10}$$

First, all conductivity models are fit to the experimental data. Then, the models having the best fit is further investigated

5.4 Results

Model 1:

This model (having constant a, b) fits the sole temperature or field variation. The error increases for high (or low) temperatures and fields together. The model is good overall.

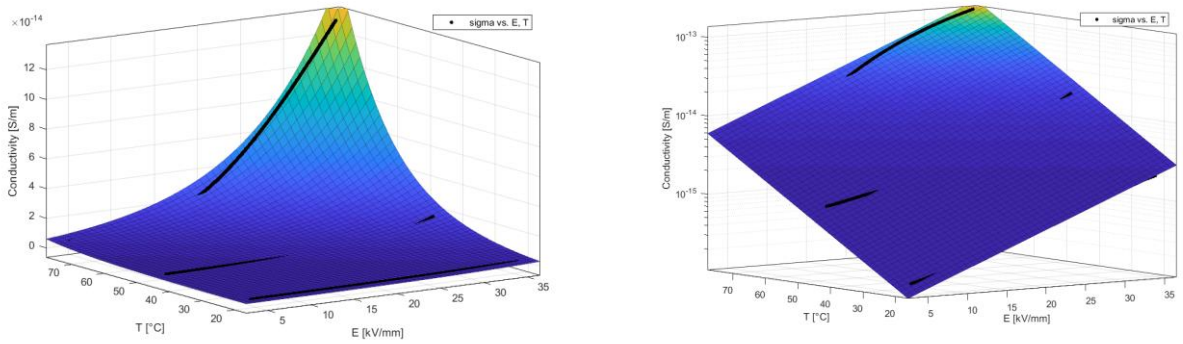

(a) (b)

Figure 5.3 Conductivity fitting of model 1 as a function of temperature and electric field in 3D plot in (a) linear scale and (b) z-log scale. The black curves are the experimental data and the colored surface is the fitting.

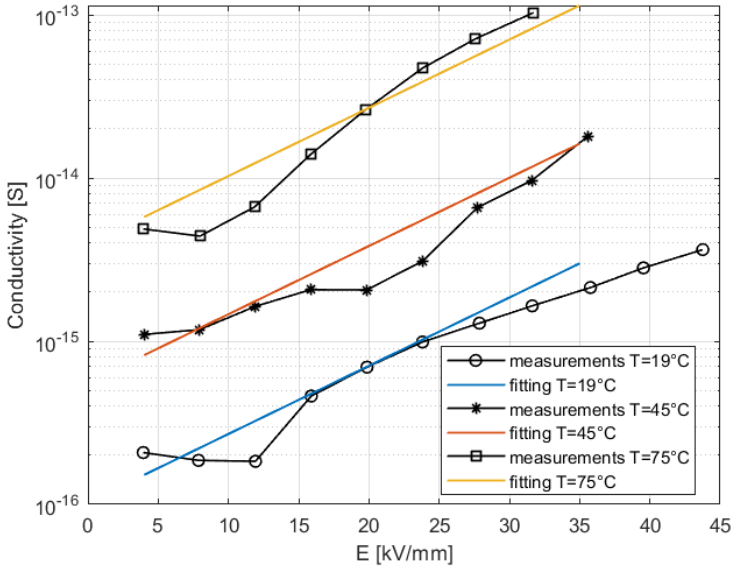

Figure 5.4 Conductivity fitting of model 1 as a function electric field at 3 temperatures. The black curves are the experimental data and the colored curves are the fitted curves.

Model 2:

This model has the best fit over other proposed models as it fits the experimental data for both low and high temperatures and/or electric fields. The term $b + cT$, as a temperature-dependent field coefficient, increases the field dependency at high temperatures. It is slightly more conservative than model 1 at 75 °C.

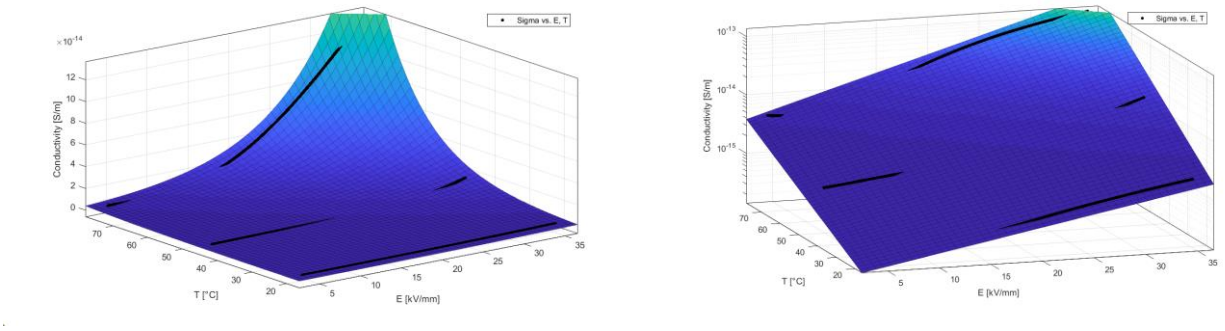

(a) (b)

Figure 5.5 Conductivity fitting of model 2 as a function of temperature and electric field in 3D plot in (a) linear scale and (b) z-log scale. The black curves are the experimental data and the colored surface is the fitting.

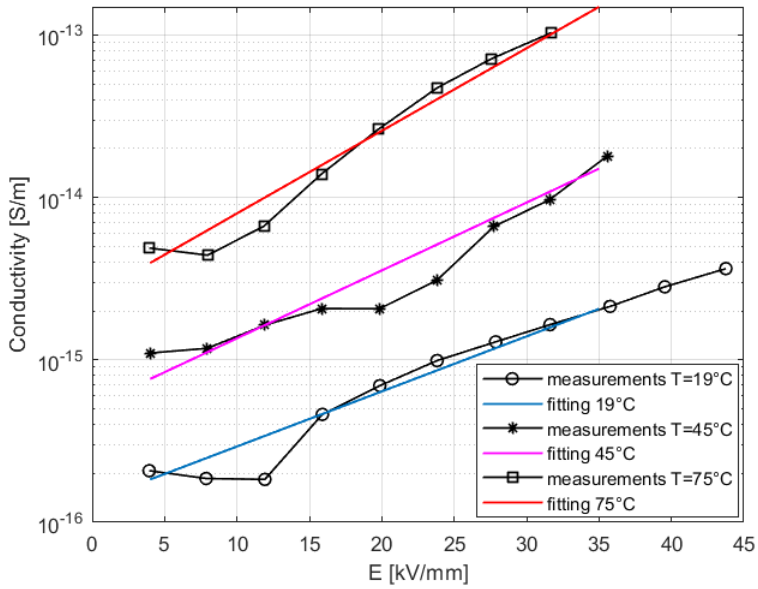

Figure 5.6 Conductivity fitting of model 2 as a function electric field at 3 temperatures. The black curves are the experimental data and the colored curves are the fitted curves.

Model 3:

It has the worst fit of the experimental data overall, as it is not conservative at low and high fields, but overconservative in the studied range of fields at 45°C and 75°C.

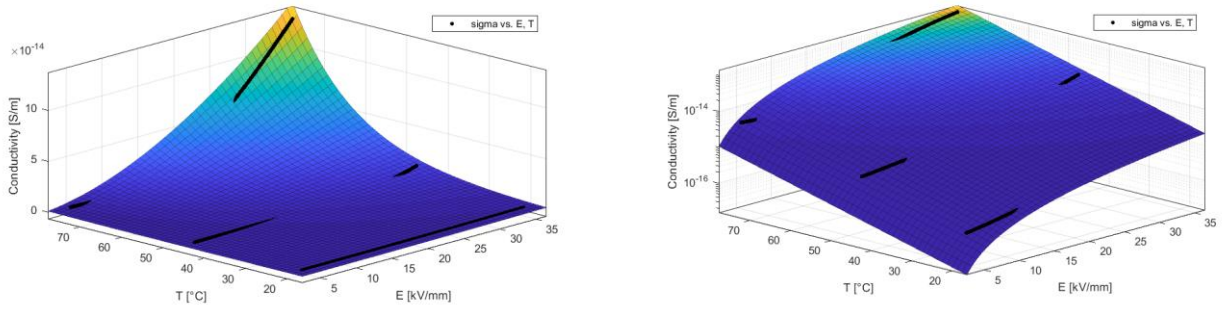

(a) (b)

Figure 5.7 Conductivity fitting of model 3 as a function of temperature and electric field in 3D plot in (a) linear scale and (b) z-log scale. The black curves are the experimental data and the colored surface is the fitting.

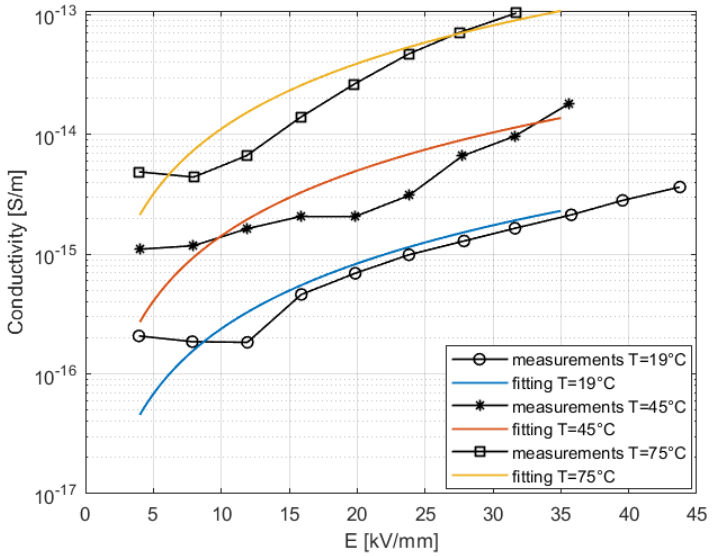

Figure 5.8 Conductivity fitting of model 3 as a function electric field at 3 temperatures. The black curves are the experimental data and the colored curves are the fitted curves.

Model 4:

This model is good overall, however, it is more conservative at 45°C, less conservative at 19°C and slightly less conservative at 75°C for high fields, compared to model 2.

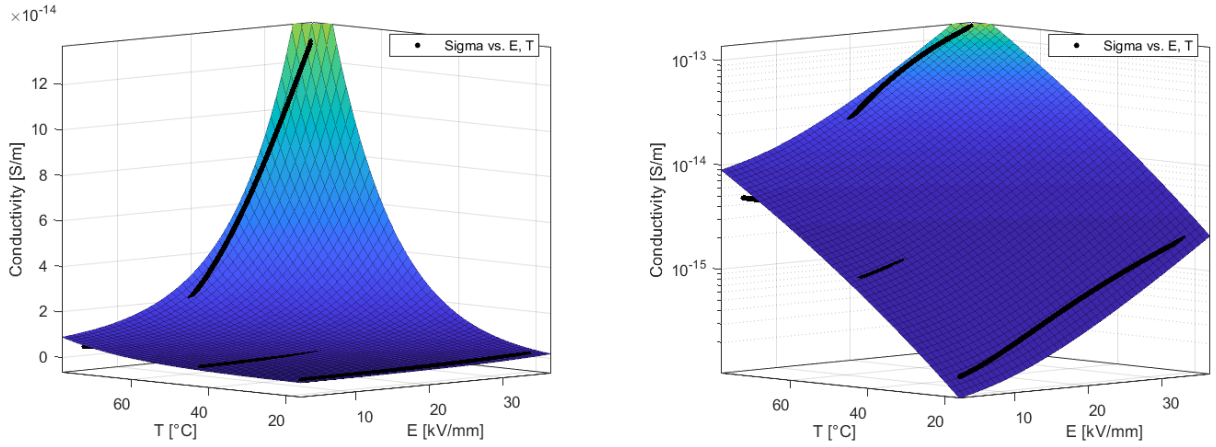

(a) (b)

Figure 5.9 Conductivity fitting of model 4 as a function of temperature and electric field in 3D plot in (a) linear scale and (b) z-log scale. The black curves are the experimental data and the colored surface is the fitting.

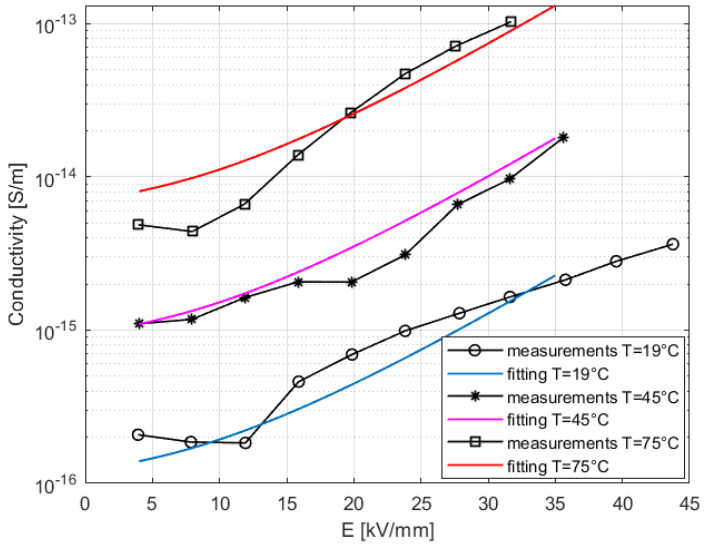

Figure 5.10 Conductivity fitting of model 4 as a function electric field at 3 temperatures. The black curves are the experimental data and the colored curves are the fitted curves.

Model 5:

The model does not perfectly fit for all temperatures, especially, at 19°C where it is not conservative at low fields but overconservative at high fields.

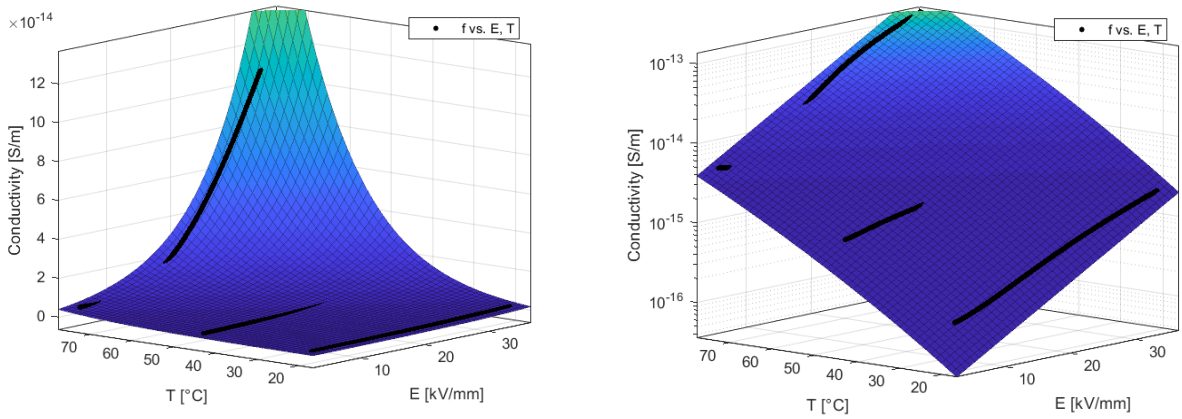

(a) (b)

Figure 5.11 Conductivity fitting of model 5 as a function of temperature and electric field in 3D plot in (a) linear scale and (b) z-log scale. The black curves are the experimental data and the colored surface is the fitting.

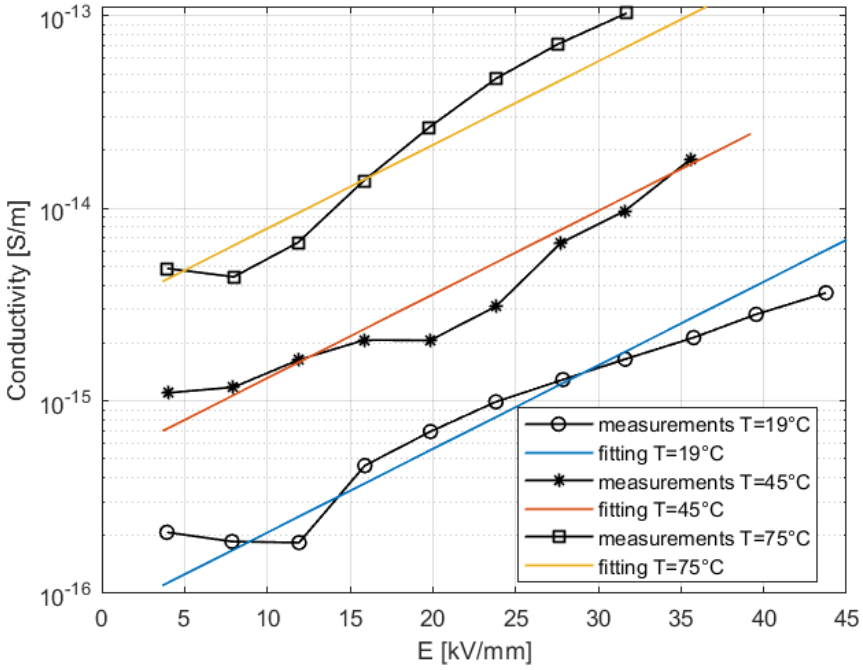

Fitting only points with high accuracy:

As mentioned in section 5.3.1, the points where the capacitive field distribution is guaranteed have higher accuracy in conductivity calculation compared to other points. Therefore, model 2 will be more investigated considering only the latter points (highlighted in red in Figures 5.13 and 5.14) by weighting them 1 in the least-squares formulation, while other points are weighted 0 (neglected from calculations). In this case, the following coefficients have been found for model 2:

$$\sigma_0 = 1.1 \times 10^{-16} (S/m)$$

$$a = 0.038 \left(\frac{1}{°C}\right)$$

$$b = 0.044 \left(\frac{mm}{kV}\right)$$

$$c = 1 \times 10^{-3} \left(\frac{mm}{kV.°C}\right)$$

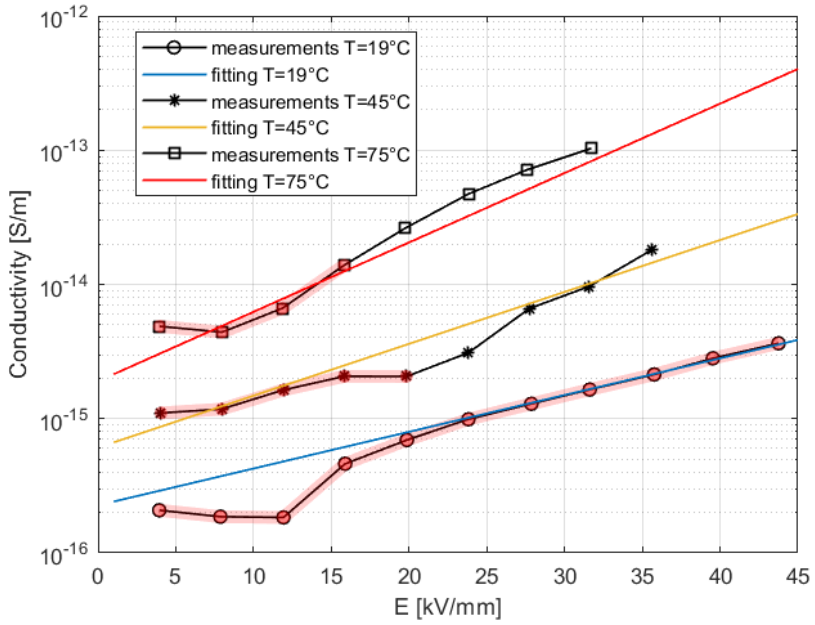

Figure 5.13 Conductivity in log-linear scale fitting of model 2 as a function electric field at 3 temperatures. The black curves are the experimental data and the colored curves are the fitted curves. Points highlighted in red are weighted 1 and all other points are weighted 0.

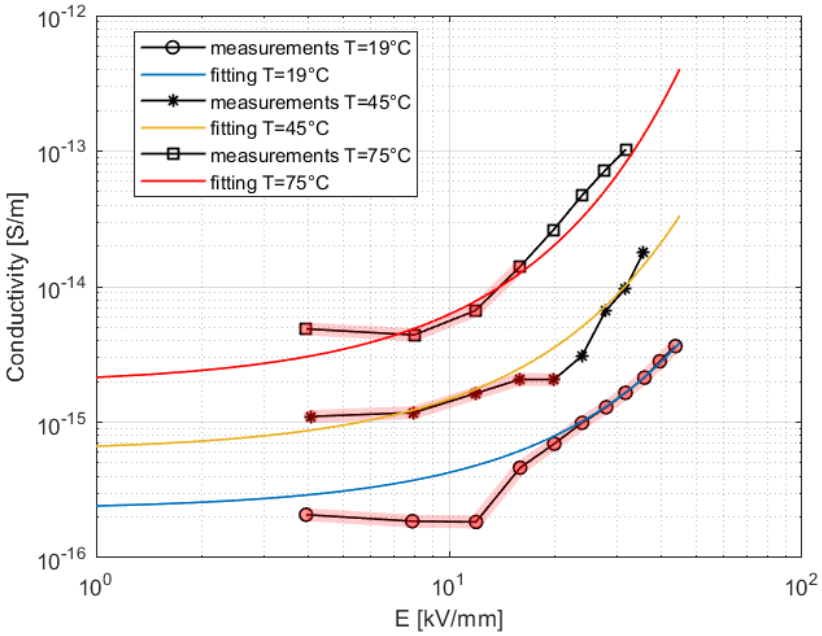

Figure 5.14 Conductivity in log-log scale of model 2 as a function electric field at 3 temperatures. The black curves are the experimental data and the colored curves are the fitted curves. Points highlighted in red are weighted 1 and all other points are weighted 0.

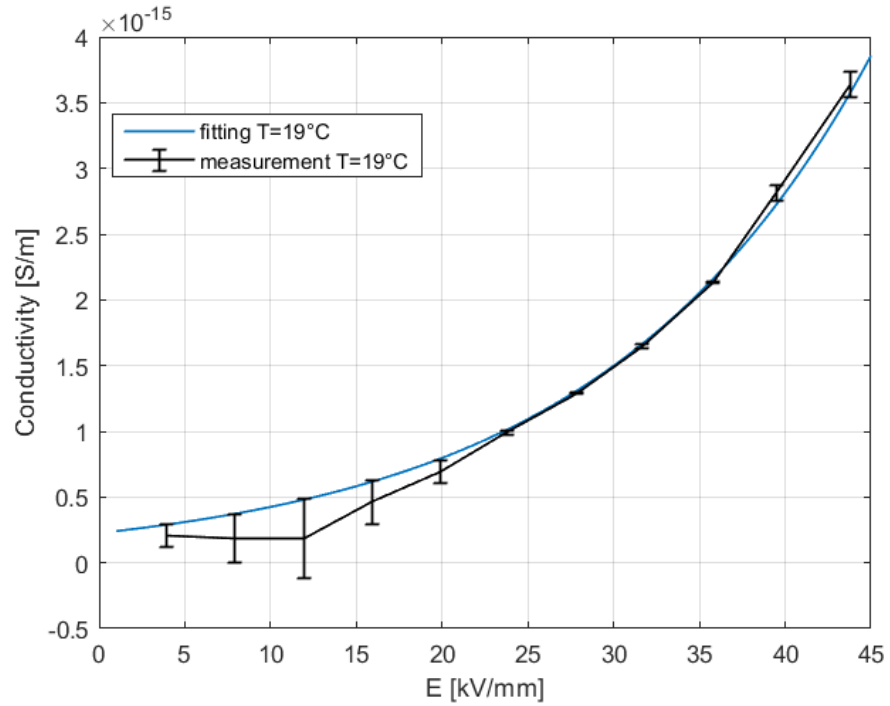

Figure 5.15 Conductivity of model 2 as a function electric field at 19°C with error bars. The black curve is the experimental data and the blue curve is the fitted curves.

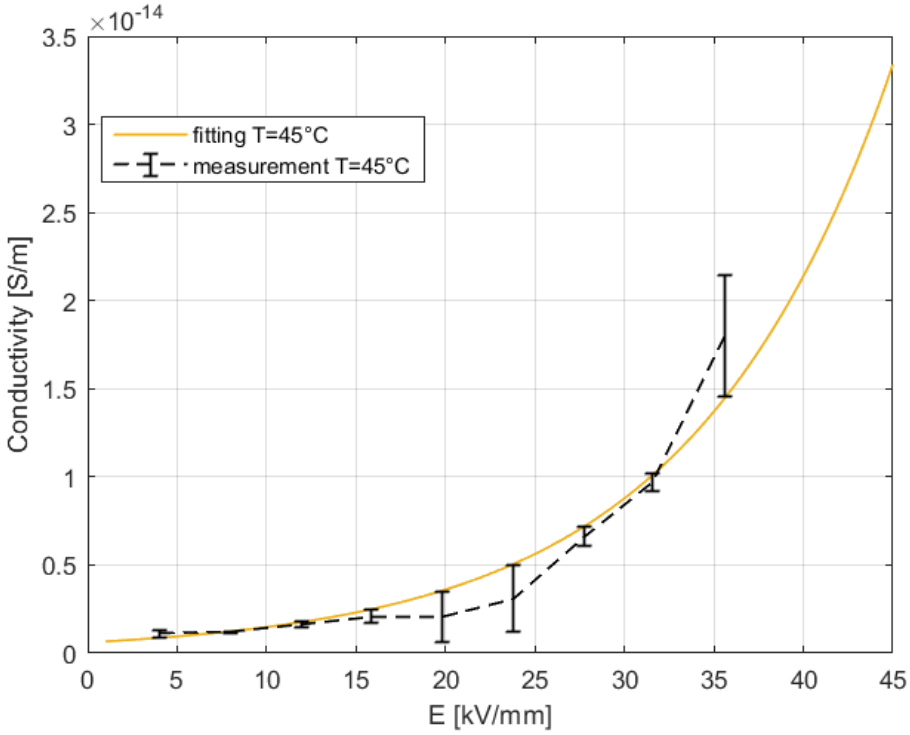

Figure 5.16 Conductivity of model 2 as a function electric field at 45°C with error bars. The black curve is the experimental data and the yellow curve is the fitted curves.

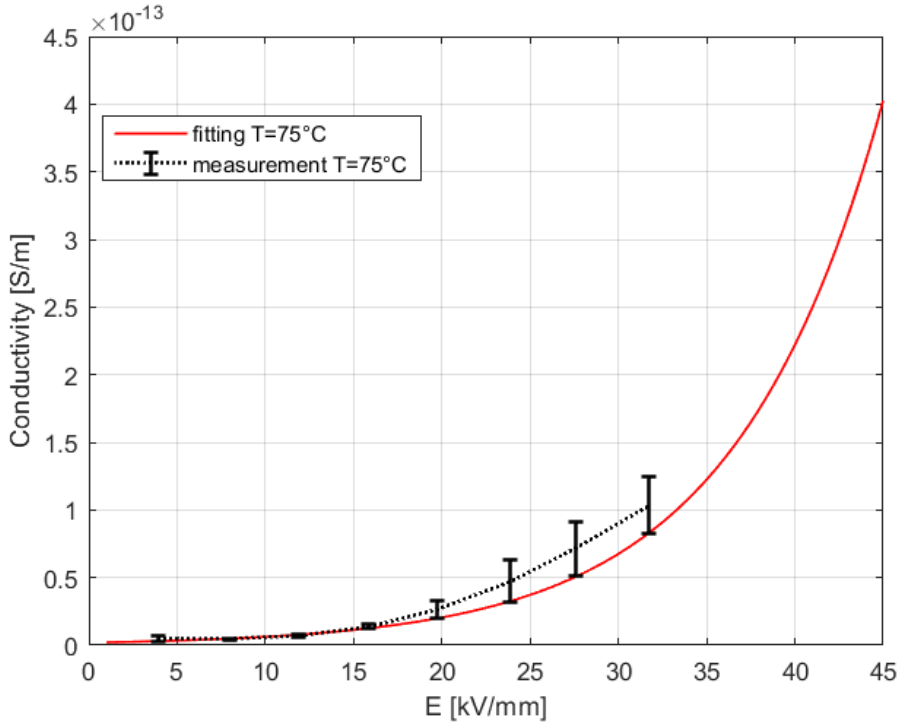

Figure 5.17 Conductivity of model 2 as a function electric field at 75°C with error bars. The black curve is the experimental data and the red curve is the fitted curves.

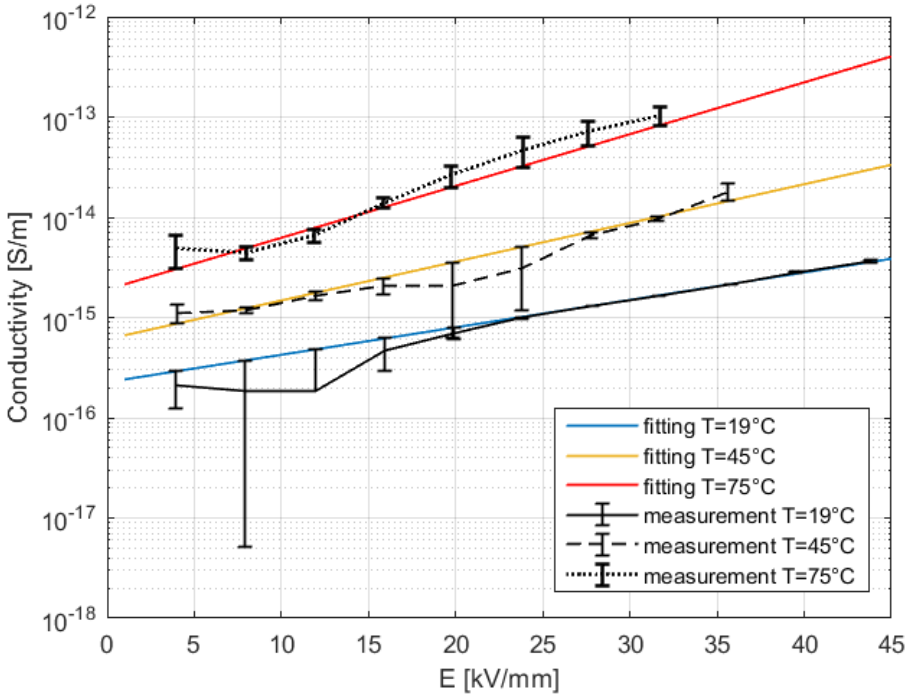

Figure 5.18 Conductivity of model 2 in log-linear scale as a function electric field at 3 temperatures with error bars. The black curves are the experimental data and the colored curve is the fitted curves.

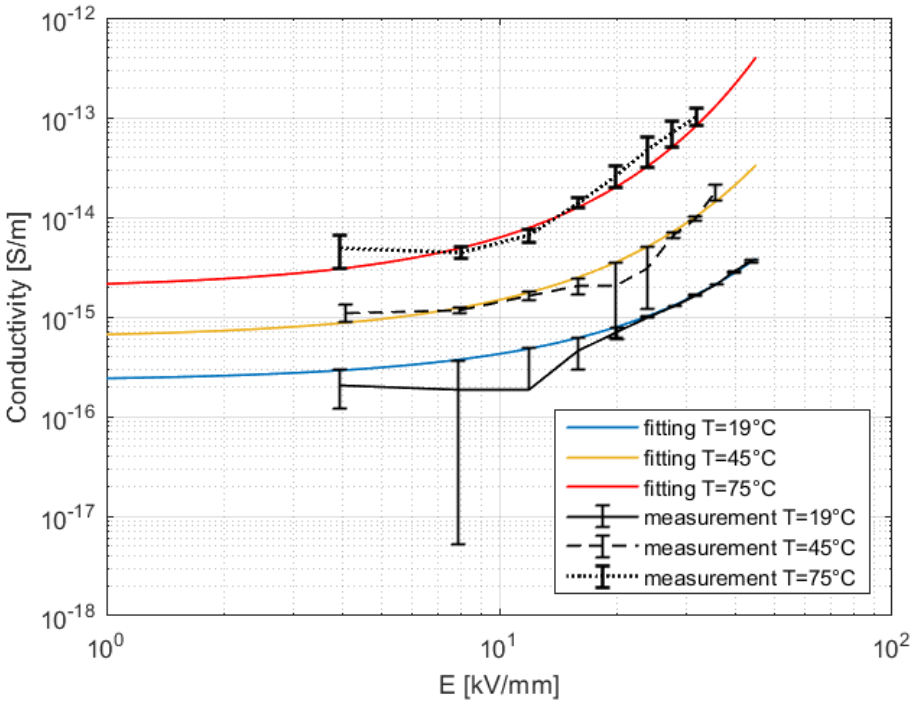

Figure 5.19 Conductivity of model 2 in log-log scale as a function electric field at 3 temperatures with error bars. The black curves are the experimental data and the colored curve is the fitted curves.

5.5 Discussion

Overall, the constants σ_0, σ' fit in this paper are comparable to the ones found in the literature. All models show similar (or lower) temperature dependency of the conductivity "*a*". While they have higher field dependency "*b*" compared to the values found in the literature by comparing Table 5.1 and Table 5.2.The difference of the temperature coefficient "*a*" could be related to the different manufacturing and processing techniques of the DC-XLPE studied here on mini cables compared to that found in the literature and performed on flat specimens. It is worth also noting that the temperature fit in this study is the conductor temperature which is subjected to a temperature drop inside the insulation, while the flat specimens are in isothermal conditions when the measurements from the literature are carried out. Further investigations are necessary to figure out the effect of the temperature gradient on the apparent conductivity measurements in mini- or full-size cables. The electrode/insulation interface might have the key role in the value of the field coefficient "*b*". Indeed, many studies in the literature concluded that both charge injection and extraction at the semicon/insulation interface (the case of mini- and full-size cables) are comparable. While metal electrodes (the case of conductivity measurements on flat specimens) has a high injection but low extraction of charge carriers, hence, it tends to accumulate homo charges which reduces the electric field as well as the injection itself (which is a function of the electric field). This might justify the

considerable increase of the field coefficient "*b*" of the conductivity when scaling up the flat specimens (with metalized electrodes) to mini- or full-size cables (with semicon electrodes). It could be argued that the coefficients fit using conductivity measurements on metal electrodes might not be conservative and not fully representative of the phenomena that occur in full-size cables. However, further investigations are required to fully confirm this conclusion.

The ohmic conductivity corresponds to low electric fields i.e., approximately lower than 10 kV/mm. The Space Charge Limited Conduction SCLC covers both operational electric fields and relatively high electric fields i.e., >8 –12 kV/mm. It can be also noticed that model 2 – in which the synergism between temperature and field coefficients is considered – has the best fit among all studied models. The best fit of the empirical model 2 can be physically justified by:

a dominance of Schottky injection mechanism (as discussed in [77]) for temperatures up to 45 °C. This mechanism is empirically represented by a field- and temperature- driven exponential function.

a possible dominance of Poole-Frenkel conduction (as discussed in [77]) at 75°C that assists the thermally activated hopping process which is empirically described by the synergistic coefficient "*c*" in model 2 as a synergistic thermally ruled increment in the field-driven term of the electrical conductivity. Although this type of conduction mechanism has been observed at 75°C (in [77]), a constant value of "*c*" is assigned for all temperatures. Further future development of the model could be finding a threshold "T_{th}" of the temperature above which this conduction mechanism become obvious, which requires more conductivity measurements at different temperatures.

Table 5.1 Summary of fitting coefficients found in this study.

	Equation*	σ_0, σ'	a, G_a	b	c	γ
Model 1	$\sigma = \sigma_0\, exp(aT_c + bE_k)$	3×10^{-17}	0.065 (1/°C)	0.09628 (mm/kV)	-	-
Model 2	$\sigma = \sigma_0\, exp(aT_c + (b + cT_c)E_k)$	5×10^{-17}	0.052 (1/°C)	0.06477 (mm/kV)	6.9760e-04 (mm/kV °C)	-
Model 3	$\sigma = \sigma_0\, exp(aT_c)\, {E_k}^{\gamma}$	1×10^{-18}	0.06865 (1/°C)	-	-	1.81 (unitless)
Model 4	$\sigma = \sigma' exp\left(-\frac{G_a}{k_B T_K}\right) sinh(cE_V).\, {E_V}^{-\gamma}$	30	0.6353	-	1.43e-07	0.9327

			(eV)		(m/V)	(unitless)
Model 5	$\sigma = \sigma_0\, exp(-a/T_K + bE)$	5×10^{-7}	6600 (K)	0.1 (mm/kV)	-	-

* T_c is the temperature in °C.

T_K is the temperature in K.

E_k is the electric field in kV/mm

E_V is the electric field in V/m

Table 5.2 Summary of fitting coefficients found in the literature.

	Reference	σ_0, σ' **[S/m][A/m²]**	a, G_a	b	c	γ
Model 1	[80]	1×10^{-16}	0.1 (1/°C)	0.03 (mm/kV)	-	-
	[54]	1×10^{-17}	0.084 (1/°C)	0.0645 (mm/kV)	-	-
Model 2	Not found	-	-	-	-	-
Model 3	[81] For *DC PPLP*	9×10^{-20}	0.06 (1/°C)	-	-	1.8 (unitless)
Model 4	[79],[82],[83],[84]	30	0.6353 (eV)	-	2.7756e-07 (m/V)	1 (unitless)
	[84]	3.6783×10^{7}	0.98 (eV)	-	1.086e-07 (m/V)	1 (unitless)
	[85]	1×10^{14}	1.48 (eV)	-	2e-07 (m/V)	1 (unitless)
Model 5	[86],[87]	2.2896×10^{-6}	7600 (K)	0.27756 (mm/kV)	-	-

Conclusions:

- The effect of VPRs on the life of extruded cables is significant. The main reason is the high electric field caused by the space charge accumulation in the insulation thickness, in addition to the relatively long time required to reach the steady-state after VPR compared to other types of electrical transients (e.g., TOVs and SSIs).
- Fast VPRs are more critical to extruded cables compared to slow VPRs because the relaxation period in the slow VPRs helps in the reduction of charges accumulated inside the insulation.
- Experimental investigation on the effect of TOVs and SSIs on the extruded cable insulation shows an evident change in the insulating properties by comparing non-aged and aged specimens.
    1) Dielectric spectroscopy shows an increase in the imaginary permittivity in the frequency band that corresponds to dipolar polarization. The latter means the formation of polar molecules inside the XLPE chemical structure.
    2) FTIR measurements show a decrease in the 3 absorption peaks of XLPE as well as an increase in the absorbance in other wavenumber bands. The former is an indication to scission in the single chemical bonds in XLPE, while the latter means the formation of new aging chemical bonds (e.g., carbonyl groups, carboxylic acid, and hydroxyl groups) throughout oxidation reactions.
    3) Space charge measurements show an increase in the space charges accumulation in mid insulation, in addition to more homo-charge accumulation in near the electrodes at high temperature which becomes critical to the insulation in the case of VPRs. A shift of the trap depth distribution towards higher value is also noticed in the aged specimens which means more deep traps due to the aging process.
    4) Conductivity measurements show and increase in DC electrical conductivity due to the aging process.
- The electric field has a dominant effect on the design of HVDC cables as the equi-life loci are found to be parallel to the maximum field limit. Considering the effect of electrical transients in the design will lead to an increase in the cable geometries (i.e., inner and outer insulation radii) proportionally to the number of transients per year.
- Intrinsic thermal instability is critical in HVDC cables, considering a significant effect of the conductivity coefficients (representing the insulation characteristics). The dielectric loss coefficient β_d is found to be lower in DC than that in AC i.e., $\beta_{d\_DC} = 0.4 < \beta_{d\_AC} = 0.5$ due to the shift of the insulation losses towards the outer insulation as a result of the field inversion phenomenon in DC cables.

Future perspectives:

The effect of transients on the field enhancement during VPRs could be more stressful in some points inside the insulation when the physical model of charge carriers is considered in the field calculations compared to the macroscopic conductivity models. A future research direction could be studying the effect of transients (TOVs, SSIs, VPRs) on the life estimation of the cable insulation using those models.

Extending this study to cable accessories (i.e., joints and terminations) could also be a future research topic, as the majority of failures occurs in the accessories.

Moreover, the continuous need to raise the voltage and the applied electric field inside the cables pushes towards finding new insulating materials with space charge mitigation, hence, lesser effect of VPRs (or other transients) on the cable insulation.

List of publications

1) B. Diban and G. Mazzanti, "The effect of temperature and stress coefficients of electrical conductivity on the life of HVDC extruded cable insulation subjected to type test conditions," in IEEE Transactions on Dielectrics and Electrical Insulation, vol. 27, no. 4, pp. 1313-1321, Aug. 2020, doi: 10.1109/TDEI.2020.008772.
2) G. Mazzanti, B. Diban, E. Chiodo, P. De Falco, L.P.D. Noia, “Forecasting the Reliability of Components Subjected to Harmonics Generated by Power Electronic Converters”. Electronics 2020, 9, 1266.
3) D. Fabiani, G. Mazzanti, S.V. Suraci, B. Diban, “Preliminary development and application of a stress-strength model for reliability estimation of aged LV cables for nuclear power plants”, Proc. IEEE ICD 2020, pp. 37-40, Valencia, Spain, 6-31 Jul. 2020, Virtual Edition.
4) G. Mazzanti, P. Seri, B. Diban, S. Stagni, “Preliminary experimental investigation of the effect of long temporary overvoltages on the reliability of HVDC extruded cables”, Proc. IEEE ICD 2020, pp. 49-52, Valencia, Spain, 6-31 Jul. 2020, Virtual Edition.
5) J.C. Fothergill, G. Mazzanti, B. Diban, “Identifying electrical ageing in polymeric insulation”, Proc. IEEE ICD 2020, pp. 53-56, Valencia, Spain, 6-31 Jul. 2020, Virtual Edition.
6) B. Diban, G. Mazzanti, I. Troia, “Preliminary Estimation of The Effect of Insulation Losses on HVDC Cable Reliability,” IEEE Conference on Electrical Insulation and Dielectric Phenomena (CEIDP), 2020.
7) G. Mazzanti, B. Diban, “Parametric Analysis of HVDC Extruded Cable Reliability for Different Cable Designs,” IEEE Conference on Electrical Insulation and Dielectric Phenomena (CEIDP), 2020.
8) B. Diban, G. Mazzanti, “The Effect of Insulation Characteristics on Thermal Instability in HVDC Extruded Cables,” Energies 2021, 14, 550. https://doi.org/10.3390/en14030550.
9) G. Mazzanti and B. Diban, "The Effects of Transient Overvoltages on the Reliability of HVDC Extruded Cables. Part 1: Long Temporary Overvoltages," in IEEE Transactions on Power Delivery, doi: 10.1109/TPWRD.2021.3049269.
10) G. Mazzanti and B. Diban, "The Effects of Transient Overvoltages on the Reliability of HVDC Extruded Cables. Part 2: Superimposed Switching Impulses," in IEEE Transactions on Power Delivery, doi: 10.1109/TPWRD.2021.3049283.
11) D. Fabiani, G. Mazzanti, S.V. Suraci and B. Diban, “Innovative Development and Application of a Stress-Strength Model for Reliability Estimation of Aged LV Cables for Nuclear Power Plants”, IEEE TDEI Transactions on Dielectrics and Electrical Insulation.

12) B. Diban, G. Mazzanti, N. Guerrini, and I. Troia, “Deeper insight into the relationship between experimental expressions of conductivity and DC electric field in cables,” IEEE Electrical Insulation Conference (EIC), June 2021.
13) N. Guerrini, I. Troia, G. Mazzanti, and B. Diban, “Evaluation and Analysis of the Impact of the Leakage Current on HVDC R&D and Qualification Tests on Power Cables,” IEEE Electrical Insulation Conference (EIC), June 2021.
14) G. Mazzanti, P. Seri, and B. Diban, “Preliminary Experimental Investigation of the Effect of Superimposed Switching Impulses on XLPE-insulated HVDC Cables,” IEEE Electrical Insulation Conference (EIC), June 2021.
15) B. Diban, G. Mazzanti, I. Troia, and N. Guerrini, “The Effect of Ambient Thermal Properties on Transient Electric Field Distribution and Life Estimation in Underground HVDC Cable Insulation,” IEEE Conference on Electrical Insulation and Dielectric Phenomena (CEIDP), 2021.
16) G. Mazzanti, and B. Diban, “Broadening the Simulative Analysis of the Effects of Long Temporary Overvoltages on the Reliability of HVDC Cables,” IEEE Conference on Electrical Insulation and Dielectric Phenomena (CEIDP), 2021.
17) N. Guerrini, G. Mazzanti, B. Diban, and I. Troia, “Validation of Mechanical Features of HPTE Insulation for EHV DC Land Cable Systems,” IEEE Conference on Electrical Insulation and Dielectric Phenomena (CEIDP), 2021.
18) N. Guerrini, G. Mazzanti, B. Diban, and I. Troia, “Investigation on online fault location techniques during factory testing on manufactured cable lengths,” IEEE Conference on Electrical Insulation and Dielectric Phenomena (CEIDP), 2021.
19) B. Diban, G. Mazzanti and P. Seri, "Life-based Geometric Design of HVDC cables. Part 1: Parametric Analysis," in IEEE Transactions on Dielectrics and Electrical Insulation, doi: 10.1109/TDEI.2022.3168369.
20) B. Diban, G. Mazzanti and P. Seri, "Life-based Geometric Design of HVDC Cables. Part 2: Effect of Electrical and Thermal Transients," in IEEE Transactions on Dielectrics and Electrical Insulation, 2022, doi: 10.1109/TDEI.2022.3212974.
21) A. Tzimas et al., "Feasibility of Space Charge Measurements on HVDC Cable Joints: Study Group—IEEE DEIS Technical Committee “HVDC Cable and Systems:”," in IEEE Electrical Insulation Magazine, vol. 38, no. 5, pp. 18-27, September/October 2022, doi: 10.1109/MEI.2022.9858040.
22) A. Cristofolini, B. Diban, G. Mazzanti, G. Pierotti and A. Popoli, "Focusing on the Effects of Longitudinal Heat Exchange on Electric Field and Temperature Distribution in HVDC

Cable," 2022 IEEE 4th International Conference on Dielectrics (ICD), 2022, pp. 206-209, doi: 10.1109/ICD53806.2022.9863530.

23) B. Diban, G. Mazzanti, M. Marzinotto and A. Battaglia, "Calculation of Electric Field Profile within HVDC Cable Insulation in the Presence of Voltage Polarity Reversals," 2022 IEEE 4th International Conference on Dielectrics (ICD), 2022, pp. 13-16, doi: 10.1109/ICD53806.2022.9863466.
24) B. Diban, G. Mazzanti, M. Marzinotto, and A. Battaglia, «Life Estimation of HVDC Cables Subjected to Fast and Slow Polarity Reversals", submitted to Energies (MDPI) 2022**.**
25) B. Diban, G. Mazzanti and P. Seri, "Experimental Investigation of the Effect of Transient Overvoltages on XLPE-insulated HVDC Cables," submitted to IEEE Transactions on Dielectrics and Electrical Insulation, 2022.

References

[1] B. DIBAN,. "Life Estimation Of HVDC Cables Subjected To Qualification Test Conditions.," MSc thesis, University of Bologna, 2019.

[2] G. Mazzanti and M. Marzinotto, Extruded Cables for High Voltage Direct Current Transmission: Advances in Research and Development, ser. Power Eng. Ser.. Hoboken, NJ, USA: Wiley/IEEE, Jul.2013.

[3] G. Mazzanti "Issues and Challenges for HVDC Extruded Cable Systems.," *Energies* Vol. 14, no. 15, p. 4504, 2021.

[4] IEC 60287. Electric cables—Calculation of the Current Rating Equations (100% Load Factor) and Calculations of Losses; Part 1-1; 1-2, 1-3, 2-1, 3-1, Series (Ed.2-2020); International Electrotechnical Commission IEC: Geneva, Switzerland, 2020

[5] IEC 60853-2. Calculation of the Cyclic and Emergency Current Rating of Cables, Part 2: Cyclic Rating of Cables Greater Than 18/30 (36) kV and Emergency Ratings for Cables of All Voltages; Ed. 1.0; International Electrotechnical Commission IEC: Geneva, Switzerland, January 1989.

[6] Klein, N. Electrical Breakdown in Solids. *Adv. Electr. Electron. Phys.* 1969, *26*, 309–424.

[7] C.K. Eoll."Theory of Stress Distribution in Insulation of High Voltage d.c. Cables. PartI," IEEE Trans. Electr. Insul., Vol. EI-10, No. 1, pp. 27–35, March 1975.

[8] Endicott, H.S.; Hatch, B.D.; Sohmer, R.G. Application of the Eyring model to capacitor aging data. IEEE Trans. Comp. Parts 1965, 12, 34–41.

[9] Montanari, G.C.; Mazzanti, G. From thermodynamic to phenomenological multi-stress models for insulating materials without or with evidence of threshold (XLPE cables). J. Phys. D Appl. Phys. 1994, 27, 1691–1702.

[10] Crine, J.P. On the interpretation of some electrical aging and relaxation phenomena in solid dielectrics. IEEE Trans. Dielectr. Electr. Insul. 2005, 12, 1089–1107.

[11] Mazzanti, G.; Montanari, G.C.; Dissado, L. Electrical aging and life models: The role of space charge. IEEE Trans. Dielectr. Electr. Insul. 2005, 12, 876–890.

[12] Zuo, Z.; Dissado, L.A.; Yao, C.; Chalashkanov, N.M.; Dodd, S.J.; Gao, Y. Modeling for life estimation of HVDC cable insulation based on small-size specimens. IEEE Electr. Insul. Mag. 2019, 36, 19–29.

[13] Mazzanti, G.; Montanari, G.C.; Civenni, F. Model of inception and growth of damage from microvoids in polyethylene-based materials for HVDC cables—Part 1: Theoretical approach. IEEE Trans. Dielectr. Electr. Insul. 2007, 14, 1242–1254.

[14] Mazzanti, G.; Montanari, G.C.; Civenni, F. Model of inception and growth of damage from microvoids in polyethylene-based materials for HVDC Cables—Part 2: Parametric investigation and data fitting. IEEE Trans. Dielectr. Electr. Insul. 2007, 14, 1255–1263.
[15] V. M. Montsinger, “Loading transformers by temperature,” Transactions of the American Institute of Electrical Engineers, vol. 49, no. 2, pp. 776-790, 1930.
[16] T. W. Dakin, "Electrical Insulation Deterioration Treated as a Chemical Rate Phenomenon," in Transactions of the American Institute of Electrical Engineers, vol. 67, no. 1, pp. 113-122, Jan. 1948.
[17] W. Mosch and W. Hauschild. Statistical Techniques for HV Engineering. Peter Peregrinus, London, 1992.
[18] W. Nelson. Applied Life Data Analysis, Wiley, New York, 1982.
[19] L. Dissado, and J. C. Fothergill. *Electrical degradation and breakdown in polymers*. Vol. 9. Iet, 1992.
[20] J. C. Fothergill, G. Mazzanti and B. Diban, "Identifying Electrical Ageing in Polymeric Insulation," 2020 IEEE 3rd International Conference on Dielectrics (ICD), Valencia, Spain, 2020, pp. 53-56, doi: 10.1109/ICD46958.2020.9341973.
[21] Miner, Milton A. "Cumulative damage in fatigue." (1945): A159-A164.
[22] B. Diban, G. Mazzanti, M. Marzinotto, A. Battaglia, "Calculation of Electric Field Profile within HVDC Cable Insulation in the Presence of Voltage Polarity Reversals," in IEEE Int. Conf. Dielectr. ICD 2022, Palermo, 2022.
[23] G. Mazzanti, P. Seri, B. Diban and S. Stagni, "Preliminary Experimental Investigation of the Effect of Long Temporary Overvoltages on the Reliability of HVDC Extruded Cables," 2020 IEEE 3rd International Conference on Dielectrics (ICD), 2020, pp. 49-52.
[24] M. Saltzer, M. Goertz, S. Wenig, H. Saad, W. Leterme, J.I. Juvik, R.D. Zhang, C. Bartzsch, A. Crippa, V. Joubert, T. Karmokar, B. Khodabakchian, L. Colla, P. Chakraborty, A. Tzimas, S. Nyberg, M. Fu, A. Kothari, A.K. Saha, G. Mazzanti, M. Nguyen-Tuan, J. Mathot, and Y. Fan, “Overvoltages experienced by DC cables within an HVDC transmission system in a rigid bipolar configuration”, JICABLE’15, paper C5.1, Versailles (France), June 23-27 2019.
[25] S. stagni, “Experimental evaluation of dielectric aging due to long TOV application in XLPE-insulated HVDC cables”, master thesis, University of Bologna, 2019.
[26] IEC 60060-1, High-voltage test techniques. Part 1: General definitions and test requirements, Ed. 3, 2010.
[27] G. Mazzanti and B. Diban, "The Effects of Transient Overvoltages on the Reliability of HVDC Extruded Cables. Part 1: Long Temporary Overvoltages," in IEEE Transactions on Power Delivery, doi: 10.1109/TPWRD.2021.3049269.

[28] G. Mazzanti and B. Diban, "The Effects of Transient Overvoltages on the Reliability of HVDC Extruded Cables. Part 2: Superimposed Switching Impulses," in IEEE Transactions on Power Delivery, doi: 10.1109/TPWRD.2021.3049283.

[29] Recommendations for Testing DC Extruded Cable Systems for Power Transmission at a Rated Voltage up to 500kV, CIGRÉ Technical Brochure 496, 2012.

[30] A. Bareggi et al. "Current and future applications of HPTE insulated cables systems," Paper B1-307, CIGRÉ Science & Engineering, no.13, pp. 34-44, Feb. 2019.

[31] M. Jeroense, P. Bergelin, T. Quist, A. Abbasi, H. Rapp, and L. Wang, "Fully qualified 640 kV underground extruded DC cable system," paper B1-309, 2018 CIGRE Session, 2018.

[32] IEC 62631-3-1:2016 Dielectric and resistive properties of solid insulating materials - Part 3-1: Determination of resistive properties (DC methods) - Volume resistance and volume resistivity - General method.

[33] Diban, Bassel; Mazzanti, Giovanni; Mazzocchetti, Laura; Seri, Paolo "Experimental Investigation of the Effect of Transient Overvoltages on XLPE-insulated HVDC Cables.," TechRxiv. Preprint., 2022 https://doi.org/10.36227/techrxiv.21641504.v2.

[34] A. Tzimas et al., "Feasibility of Space Charge Measurements on HVDC Cable Joints: Study Group—IEEE DEIS Technical Committee "HVDC Cable and Systems:"," in IEEE Electrical Insulation Magazine, vol. 38, no. 5, pp. 18-27, September/October 2022, doi: 10.1109/MEI.2022.9858040.

[35] Tefferi, Mattewos, "Characterization of Conduction Properties of DC Cable Dielectric Materials" (2019). Doctoral Dissertations. 2246.

[36] J. V. Gulmine, et al. "Polyethylene characterization by FTIR," Polymer testing, vol. 21, no. 5, pp. 557-563, 2002.

[37] B. Ouyang, H. Li, X. Zhang, S. Wang and J. Li, "The role of microstructure changes on space charge distribution of XLPE during thermooxidative aging," IEEE Trans. Dielectr. Electr. Insul., vol. 24, no. 6, pp. 3849-3859, 2017.

[38] Y. Liu, H. Liu, L. Yu, Y. Li and L. Gao, "Effect of thermal stress on the space charge distribution of 160 kV HVDC cable insulation material," IEEE Trans. Dielectr. Electr. Insul., vol. 24, no. 3, pp. 1355-1364, Jun. 2017.

[39] A. M. Nobrega, M. L. B. Martinez and A. A. A. de Queiroz, "Investigation and analysis of electrical aging of XLPE insulation for medium voltage covered conductors manufactured in Brazil," IEEE Trans. Dielectr. Electr. Insul., vol. 20, no. 2, pp. 628-640, Apr. 2013.

[40] X. Chi et al. "Thermal-oxidative aging effects on the dielectric properties of nuclear cable insulation," Materials, vol. 13, no. 10, pp. 2215, 2020.

[41] Y. Kemari, A. Mekhaldi, G. Teyssèdre and M. Teguar, "Correlations between structural changes and dielectric behavior of thermally aged XLPE," IEEE Trans. Dielectr. Electr. Insul., vol. 26, no. 6, pp. 1859-1866, 2019.

[42] L. Sanche, "Nanoscopic aspects of electronic aging in dielectrics," IEEE Trans. Dielectr. Electric. Insul., vol. 4, no. 5, pp. 507-543, Oct. 1997.

[43] G. Mazzanti and G. C. Montanari, "Electrical aging and life models: the role of space charge," IEEE Trans. Dielectr. Electr. Insul., vol. 12, no. 5, pp. 876-890, Oct. 2005.

[44] L. A. Dissado, G. Mazzanti and G. C. Montanari, "The role of trapped space charges in the electrical aging of insulating materials," IEEE Trans. Dielectr. Electr. Insul., vol. 4, no. 5, pp. 496-506, Oct. 1997.

[45] J. -. Crine, "A molecular model to evaluate the impact of aging on space charges in polymer dielectrics," IEEE Trans. Dielectr. Electr. Insul., vol. 4, no. 5, pp. 487-495, Oct. 1997.

[46] G.C. Montanari, "Bringing an insulation to failure: the role of space charge", IEEE Trans. Dielectr. Electr. Insul., vol. 18, pp.339–364, 2011.

[47] G. C. Montanari, P. Seri and L. A. Dissado, "Aging mechanisms of polymeric materials under DC electrical stress: A new approach and similarities to mechanical aging," IEEE Trans. Dielectr. Electr. Insul., vol. 26, no. 2, pp. 634-641, April 2019.

[48] Battaglia, A.; Marzinotto, M.; Mazzanti, G. A Deeper Insight in Predicting the Effect of Voltage Polarity Reversal on HVDC Cables. 2019 IEEE Conference on Electrical Insulation and Dielectric Phenomena (CEIDP), Richland, Washington, USA, 20- 23 Oct. 2019, doi: 10.1109/CEIDP47102.2019.9010572.

[49] Li, G.; et al. Power reversal strategies for hybrid LCC/MMC HVDC systems. *CSEE J. Power Energy Syst.*, 2020, *Volume*. 6, no. 1, pp. 203-21, doi: 10.17775/CSEEJPES.2019.01050.

[50] Recommendations to improve HVDC cable systems reliability. Available online: https://europacable.eu/wp-content/uploads/2021/01/Joint-paper-HVDC-Cable-Reliability-ENTSO-E-Europacable_FINAL_13.06.2019_.pdf

[51] 50Hertz Transmission GmbH; Amprion GmbH; Tennet TSO GmbH; TransentBw GmbH. Grid Development Plan. (GDP) 2030, 2nd Draft; Technical Report; German TSOs: Berlin, Germany, 2019

[52] B. Diban, G. Mazzanti and P. Seri, "Life-based Geometric Design of HVDC cables. Part 1: Parametric Analysis," in IEEE Transactions on Dielectrics and Electrical Insulation, doi: 10.1109/TDEI.2022.3168369.

[53] B. Diban, G. Mazzanti and P. Seri, "Life-based Geometric Design of HVDC Cables. Part 2: Effect of Electrical and Thermal Transients," in IEEE Transactions on Dielectrics and Electrical Insulation, 2022, doi: 10.1109/TDEI.2022.3212974.

[54] R. N. Hampton, “Some of the considerations for materials operating under high-voltage, direct-current stresses,” IEEE Electr. Insul. Mag., vol. 24, no. 1, pp. 5–13, 2008.
[55] H. Naderiallaf, P. Seri and G. C. Montanari, "Designing a HVDC Insulation System to Endure Electrical and Thermal Stresses Under Operation. Part I: Partial Discharge Magnitude and Repetition Rate During Transients and in DC Steady State," in IEEE Access, vol. 9, pp. 35730-35739, 2021.
[56] M. J. P. Jeroense and P. H. F. Morshuis, "Electric fields in HVDC paper insulated cables," IEEE Trans. Dielectr. Electr. Insul., vol. 5, no. 2, pp. 225-236, April 1998.
[57] Y. Zhang, X. Zhou, H. Niu, X. Wang, Y. Tang, J. Zhao, and Yo. Fan, “Theoretical calculation and experimental research on thermal time constant of single-core cables,” High Voltage Engineering, vol. 35, no. 11, pp. 2801-2806, Nov. 2009.
[58] I. Garniwa and A. Burhani, ‘‘Thermal incremental and time constant analysis on 20 kv XLPE cable with current vary,’’ in Proc. IEEE 8th Int. Conf. Properties Appl. Dielectr. Mater., Jun. 2006, pp. 566–569.
[59] A. Henke, and S. Frei. "Transient temperature calculation in a single cable using an analytic approach.," Int. J. Heat Fluid Flow (JFFHMT) , vol. 7, no. 1, pp. 58-65, 2020.
[60] H. Naderiallaf, P. Seri and G. C. Montanari, "Investigating Conditions for an Unexpected Additional Source of Partial Discharges in DC Cables: Load Power Variations," in IEEE Trans. Power Del., vol. 36, no. 5, pp. 3082-3090, Oct. 2021.
[61] G. Mazzanti, “The effects of seasonal factors on life and reliability of high voltage AC cables subjected to load cycles,” IEEE Trans. Power Deliv., vol. 35, no. 4, pp. 2080-2088, Aug. 2020.
[62] R. Huang, “Dynamic Rating for Improved Operational Performance,” PhD dissertation, University of Southampton, 2015.
[63] P. Chatzipanagiotou, V. Chatziathanasiou, G.D. Mey, B. Wiecek, “Influence of soil humidity on the thermal impedance, time constant and structure function of underground cables: a laboratory experiment,” Appl. Therm. Eng., vol. 113, pp. 1444-1451, 2017.
[64] B. Diban, G. Mazzanti, I. Troia, and N. Guerrini, “The Effect of Ambient Thermal Properties on Transient Electric Field Distribution and Life Estimation in HVDC Cable Insulation,” presented at the Conference on Electrical Insulation and Dielectric Phenomena (CEIDP), virtual conference, 2021.
[65] IEC 60287-3-1:2017, Electric cables - Calculation of the current rating - Part 3-1: Operating conditions - Site reference conditions. Ed. 2.0, 2017-06-08.
[66] Diban, B.; Mazzanti, G. The Effect of Insulation Characteristics on Thermal Instability in HVDC Extruded Cables. *Energies* 2021, *14*, 550. https://doi.org/10.3390/en14030550.
[67] N. Guerrini, G. Mazzanti, B. Diban, I. Troia, “Validation of Mechanical Features of HPTE Insulation for EHV DC Land Cable Systems,” 2021

[68] B. Diban, G. Mazzanti, I. Troia, “Preliminary Estimation of The Effect of Insulation Losses on HVDC Cable Reliability.,” In Proceedings of the Conference on Electrical Insulation and Dielectric Phenomena CEIDP, virtual event, 18–30 October 2020.
[69] S. Whitehead, *Dielectric Breakdown of Solids*; Oxford University Press: London, UK, 1951.
[70] J.J. O’Dwyer, *The Theory of Dielectric Breakdown of Solids*; Oxford University Press: London, UK, 1964.
[71] Fallou, M.M. Perforration dielectrique par instabilite thermique des cables a courant continu. Rev. Gen. De L’Electricite 1959, 693–695.
[72] Brazier, L.G. The breakdown of cables by thermal instability. J. Inst. Electr. Eng. 1935, 77, 104–115, doi:10.1049/jiee-1.1935.0128.
[73] Reddy, C.C.; Ramu, T.S. On the intrinsic thermal stability in HVDC cables. IEEE Trans. Dielectr. Electr. Insul. 2007, 14, 1509–1515, doi:10.1109/TDEI.2007.4401235.
[74] Recommendations for testing DC extruded cable systems for power transmission at a rated voltage up to and including 800 kV, CIGRÉ Technical Brochure 852, 2021.
[75] B. Diban and G. Mazzanti, "The Effect of Different Macroscopic Conductivity Equations on Life Estimation of HVDC Cables," 2022 IEEE Conference on Electrical Insulation and Dielectric Phenomena (CEIDP), 2022, pp. 455-458, doi: 10.1109/CEIDP55452.2022.9985353.
[76] G. Teyssedre and C. Laurent, "Charge transport modeling in insulating polymers: from molecular to macroscopic scale," in IEEE Transactions on Dielectrics and Electrical Insulation, vol. 12, no. 5, pp. 857-875, Oct. 2005, doi: 10.1109/TDEI.2005.1522182.
[77] L. Boyer, P.P. Buddaraju, M. Henriksen, L. Chemartin, and X. Festaz, “HVDC dielectric material comparison from cable characterizations as a mean for material selection,” 10’th International Conference on Insulated Power Cables Jicable’19, Paris, Versailles, 2019.
[78] N. Adi, T.T.N. Vu, G. Teyssèdre, F. Baudoin, N. Sinisuka, “DC model cable under polarity inversion and thermal gradient: build-up of design-related space charge,” Technologies, vol. 5, pp. 46, 2017.
[79] S. Kumara, Y. V. Serdyuk and M. Jeroense, "Calculation of Electric Fields in HVDC Cables: Comparison of Different Models," in IEEE Transactions on Dielectrics and Electrical Insulation, vol. 28, no. 3, pp. 1070-1078, June 2021.
[80] G. Mazzanti and M. Marzinotto, “Main Principles of HVDC Extruded Cable Design,” in Extruded Cables for HVDC Transmission: Advances in Research and Development,” 1st ed., IEEE, 2013, pp. 41–98.

[81] A. Fujimori, T. Tanaka, H. Takashima, T. Imajo, R. Hata, T. Tanabe, S.Yoshida, T.Kakihana, “Development of 500 kV DC PPLP-Insulated Oil-Filled Submarine Cable”, IEEE Transactions on Power Delivery,Vol. 11, No. 1, Jan 1996

[82] Z. Li and B. Du, “Polymeric insulation for high-voltage dc extruded cables: challenges and development directions,” IEEE Trans. Dielectr. Electr. Insul., vol. 34, no. 6, pp. 30–43, 2018

[83] J. Gu, X. Li and Y. Yin, “Calculation of electric field and temperature field distribution in MVDC polymeric power cable,” IEEE Int. Conf. on the Prop. and App. of Diel. Materials (ICPADM), 2009, pp. 105–108.

[84] S. Boggs et al, “Effect of insulation properties on the field grading of solid dielectric DC cable,” IEEE Trans. on Power Delivery, vol. 16, no. 4, pp. 456–461, Oct. 2001.

[85] Y. Zhan et al, “Comparison of two models on simulating electric field in HVDC cable insulation,” IEEE Trans. Dielectr. Electr. Insul., vol. 26, no. 4, pp. 1107–1115, 2019.

[86] C. C. Reddy and T. S. Ramu, “On the computation of electric field and temperature distribution in HVDC cable insulation,” IEEE Trans. Dielectr. Electr. Insul., vol. 13, no. 6, pp. 1236–1244, 2006.

[87] C. C. Reddy and T. S. Ramu, “On the DC Conductivity of HV DC Cable Insulation – Cautions in using the Empirical Models,” Annu. Rep. Conf. Electr. Insul. Dielect. Phenom. (CEIDP), 2008, vol. 1, pp. 39–42.

Annex A: The derivation of Eoll's formula

$$E = J.\rho = \frac{I}{2\pi r}\rho_0 \, ex\,p[-(a(T-T_0)+bE)]$$

By introducing the following approximation:

$$exp[bE(r)] \approx \left[\frac{eE(r)}{E_m}\right]^{-bE_m} = \left[\frac{eE(r)}{E_m}\right]^{-B}$$

where:

$$E_m = \frac{U_0}{r_o - r_i}$$

Yields:

$$E = J.\rho = \frac{I}{2\pi r}\rho_0 \, ex\,p[-a(T-T_0)]\left(\frac{eE}{E_m}\right)^{-B}$$

$$E = \frac{I\,\rho_0}{2\pi r}\, ex\,p[-a(T-T_0)]\left(\frac{eE}{E_m}\right)^{-B}$$

$$T(r) = T(r_o) + \frac{W_c}{2\pi\lambda_T} ln(r_o/r)$$

$$E^{B+1} = \frac{I\,\rho_0}{2\pi r}\, ex\,p\left[-a\left(T(r_o) + \frac{W_c}{2\pi\lambda_T} ln(r_o/r) - T_0\right)\right]\left(\frac{E_m}{e}\right)^{B}$$

$$E = \left(\frac{I\,\rho_0}{2\pi r}\right)^{\frac{1}{B+1}}\left(\frac{E_m}{e}\right)^{\frac{B}{B+1}}(\,ex\,p[-a(T(r_o)-T_0)])^{\frac{1}{B+1}}\left(ex\,p\left[-a\left(\frac{W_c}{2\pi\lambda_T} ln(r_o/r)\right)\right]\right)^{\frac{1}{B+1}}$$

One can call:

$$A = \frac{a\,W_c}{2\pi\lambda_T}$$

Yields:

$$E = \left(\frac{I\,\rho_0}{2\pi r}\right)^{\frac{1}{B+1}} \left(\frac{E_m}{e}\right)^{\frac{B}{B+1}} (\,exp[-a(T(r_o) - T_0)])^{\frac{1}{B+1}}\,(exp[-A\,ln(r_o/r)])^{\frac{1}{B+1}}$$

$$E = \left(\frac{I\,\rho_0}{2\pi r}\right)^{\frac{1}{B+1}} \left(\frac{E_m}{e}\right)^{\frac{B}{B+1}} (\,exp[-a(T(r_o) - T_0)])^{\frac{1}{B+1}}\,(exp[ln(r_o/r)])^{-\frac{A}{B+1}}$$

$$E = \left(\frac{I\,\rho_0}{2\pi r}\right)^{\frac{1}{B+1}} \left(\frac{E_m}{e}\right)^{\frac{B}{B+1}} \left(\,exp\left[-\frac{a}{B+1}(T(r_o) - T_0)\right]\right)\left(\frac{r_o}{r}\right)^{-\frac{A}{B+1}}$$

$$E = \left(\frac{I\,\rho_0}{2\pi r_o}\right)^{\frac{1}{B+1}} \left(\frac{E_m}{e}\right)^{\frac{B}{B+1}} \left(\,exp\left[-\frac{a}{B+1}(T(r_o) - T_0)\right]\right)\left(\frac{r_o}{r}\right)^{-\frac{A}{B+1}+\frac{1}{B+1}}$$

$$E = \left(\frac{I\,\rho_0}{2\pi r_o}\right)^{\frac{1}{B+1}} \left(\frac{E_m}{e}\right)^{\frac{B}{B+1}}\,exp\left[-\frac{a}{B+1}(T(r_o) - T_0)\right]\left(\frac{r}{r_o}\right)^{\frac{A-1}{B+1}}$$

$$E = \left(\frac{I\,\rho_0}{2\pi r_o}\right)^{\frac{1}{B+1}} \left(\frac{E_m}{e}\right)^{\frac{B}{B+1}}\,exp\left[-\frac{a}{B+1}(T(r_o) - T_0)\right]\left(\frac{r}{r_o}\right)^{\frac{A-1}{B+1}}$$

$$\delta = \frac{A+B}{B+1}$$

$$\delta - 1 = \frac{A-1}{B+1}$$

$$E = \left(\frac{I\,\rho_0}{2\pi r_o}\right)^{\frac{1}{B+1}} \left(\frac{E_m}{e}\right)^{\frac{B}{B+1}}\,exp\left[-\frac{a}{B+1}(T(r_o) - T_0)\right]\left(\frac{r}{r_o}\right)^{\delta-1} \qquad (A.1)$$

$$U = \int_{r_i}^{r_o} E\,dr = \left(\frac{I\,\rho_0}{2\pi r_o}\right)^{\frac{1}{B+1}} \left(\frac{E_m}{e}\right)^{\frac{B}{B+1}}\,exp\left[-\frac{a}{B+1}(T(r_o) - T_0)\right]\frac{(\,r_o - r_i)^{\delta}}{\delta\,{r_o}^{\delta-1}}$$

$$\left(\frac{I\,\rho_0}{2\pi r_o}\right)^{\frac{1}{B+1}} \left(\frac{E_m}{e}\right)^{\frac{B}{B+1}}\,exp\left[-\frac{a}{B+1}(T(r_o) - T_0)\right] = \frac{\delta U {r_o}^{\delta-1}}{(\,r_o - r_i)^{\delta}} \qquad (A.2)$$

Substitute (2) in (1) yields:

$$E = \frac{\delta U(r/r_o)^{\delta-1}}{r_o(1 - r_i/r_o)^{\delta}}$$

where:

$$\delta = \frac{A + B}{B + 1}$$

$$A = \frac{a\, W_c}{2\pi\lambda_T}$$

$$B = bE_m = \frac{bU_0}{r_o - r_i}$$

Annex B: The derivation of life expression as a function of the design parameters

$$L(E_D, T_D) = L_0 \left(\frac{E_D}{E_0}\right)^{-(n_0 - b_{ET} T_D')} exp[-B T_D']$$

Where $T_D' = \frac{1}{T_0} - \frac{1}{T_D}$

$$\frac{L(E,T)}{L(E_D, T_D)} = \left(\frac{E}{E_0}\right)^{-n_0} \left(\frac{E}{E_0}\right)^{b_{ET} T'} \left(\frac{E_D}{E_0}\right)^{n_0} \left(\frac{E_D}{E_0}\right)^{-b_{ET} T_D'} exp[-B(T' - T_D')]$$

$$L(E,T) = L_D \left(\frac{E}{E_0}\right)^{-n_0} \left(\frac{E}{E_0}\right)^{b_{ET} T'} \left(\frac{E_D}{E_0}\right)^{n_0} \left(\frac{E_D}{E_0}\right)^{-b_{ET} T_D'} exp[-B(T' - T_D')] =$$

$$= L_D \left(\frac{E}{E_D}\right)^{-n_0} \left(\frac{E}{E_0}\right)^{b_{ET} T'} \left(\frac{E_D}{E_0}\right)^{-b_{ET} T_D'} exp[-B(T' - T_D')] =$$

$$= L_D \left(\frac{E}{E_D}\right)^{-n_0} \left(\frac{E}{E_0}\right)^{b_{ET}\left(\frac{1}{T_0} - \frac{1}{T}\right)} \left(\frac{E_D}{E_0}\right)^{-b_{ET}\left(\frac{1}{T_0} - \frac{1}{T_D}\right)} exp\left[-B\left(\frac{1}{T_0} - \frac{1}{T} - \frac{1}{T_0} + \frac{1}{T_D}\right)\right] =$$

$$= L_D \left(\frac{E}{E_D}\right)^{-n_0} \left(\frac{E}{E_0}\right)^{b_{ET}\left(\frac{1}{T_0} - \frac{1}{T}\right)} \left(\frac{E_D}{E_0}\right)^{-b_{ET}\left(\frac{1}{T_0} - \frac{1}{T_D}\right)} exp\left[-B\left(\frac{1}{T_D} - \frac{1}{T}\right)\right]$$

$$L(E,T) = L_D \left(\frac{E}{E_D}\right)^{-n_0} \left(\frac{E}{E_D}\frac{E_D}{E_0}\right)^{b_{ET}\left(\frac{1}{T_0} - \frac{1}{T}\right)} \left(\frac{E_D}{E_0}\right)^{-b_{ET}\left(\frac{1}{T_0} - \frac{1}{T_D}\right)} exp\left[-B\left(\frac{1}{T_D} - \frac{1}{T}\right)\right] =$$

$$= L_D \left(\frac{E}{E_D}\right)^{-n_0} \left(\frac{E}{E_D}\right)^{b_{ET}\left(\frac{1}{T_0} - \frac{1}{T}\right)} \left(\frac{E_D}{E_0}\right)^{\frac{b_{ET}}{T_0}} \left(\frac{E_D}{E_0}\right)^{-\frac{b_{ET}}{T}} \left(\frac{E_D}{E_0}\right)^{-\frac{b_{ET}}{T_0}} \left(\frac{E_D}{E_0}\right)^{\frac{b_{ET}}{T_D}} exp\left[-B\left(\frac{1}{T_D} - \frac{1}{T}\right)\right]$$

$$= L_D \left(\frac{E}{E_D}\right)^{-n_0} \left(\frac{E}{E_D}\right)^{b_{ET}\left(\frac{1}{T_0} - \frac{1}{T}\right)} \left(\frac{E_D}{E_0}\right)^{b_{ET}\left(\frac{1}{T_D} - \frac{1}{T}\right)} exp\left[-B\left(\frac{1}{T_D} - \frac{1}{T}\right)\right]$$

By defining VEC at the design temperature $n_D = n_0 - b\left(\frac{1}{T_0} - \frac{1}{T_D}\right)$, one gets:

$$L(E,T) = L_D \left(\frac{E}{E_D}\right)^{-n_0} \left(\frac{E}{E_D}\right)^{b_{ET}\left(\frac{1}{T_0}-\frac{1}{T}\right)} \left(\frac{E_D}{E_0}\right)^{b_{ET}\left(\frac{1}{T_D}-\frac{1}{T}\right)} exp\left[-B\left(\frac{1}{T_D}-\frac{1}{T}\right)\right] =$$

$$= L_D \left(\frac{E}{E_D}\right)^{-\left[n_0 - b_{ET}\left(\frac{1}{T_0}-\frac{1}{T}\right)\right]} \left(\frac{E_D}{E_0}\right)^{b_{ET}\left(\frac{1}{T_D}-\frac{1}{T}\right)} exp\left[-B\left(\frac{1}{T_D}-\frac{1}{T}\right)\right] =$$

$$= L_D \left(\frac{E}{E_D}\right)^{-\left[n_0 - b_{ET}\left(\frac{1}{T_0}-\frac{1}{T_D}+\frac{1}{T_D}-\frac{1}{T}\right)\right]} \left(\frac{E_D}{E_0}\right)^{b_{ET}\left(\frac{1}{T_D}-\frac{1}{T}\right)} exp\left[-B\left(\frac{1}{T_D}-\frac{1}{T}\right)\right] =$$

$$= L_D \left(\frac{E}{E_D}\right)^{-\left[n_0 - b_{ET}\left(\frac{1}{T_0}-\frac{1}{T_D}\right) - b\left(\frac{1}{T_D}-\frac{1}{T}\right)\right]} \left(\frac{E_D}{E_0}\right)^{b_{ET}\left(\frac{1}{T_D}-\frac{1}{T}\right)} exp\left[-B\left(\frac{1}{T_D}-\frac{1}{T}\right)\right] =$$

$$= L_D \left(\frac{E}{E_D}\right)^{-\left[n_D - b_{ET}\left(\frac{1}{T_D}-\frac{1}{T}\right)\right]} \left(\frac{E_D}{E_0}\right)^{b_{ET}\left(\frac{1}{T_D}-\frac{1}{T}\right)} exp\left[-B\left(\frac{1}{T_D}-\frac{1}{T}\right)\right]$$

$$L(E,T) = L_D \left(\frac{E}{E_D}\right)^{-[n_D - b_{ET}T'']} \left(\frac{E_D}{E_0}\right)^{b_{ET}T''} exp[-BT'']$$

it is also possible to express the life with certain failure probability F (when $F \neq P_D$):

$$t_{D,F}\,(E,T) = \left[\frac{-ln\,(1-F)}{-ln\,(1-\,P_D)}\right]^{1/\beta_t} L_D \left(\frac{E}{E_D}\right)^{-[n_D - b_{ET}T'']} \left(\frac{E_D}{E_0}\right)^{b_{ET}T''} exp[-BT'']$$

Annex C: Calculation of temperature rise due to both conductor and insulation losses in MATLAB:

Starting from (4.3):

$$\frac{d^2T}{dr^2} + \frac{1}{r}\frac{dT}{dr} = -\rho_{th} w_p$$

by substituting the following in (4.3):

$$\frac{d^2T}{dr^2} = \frac{T_{k+1}^j - 2T_k^j + T_{k-1}^j}{\Delta r^2}$$

$$\frac{dT}{dr} = \frac{T_{k+1}^j + T_{k-1}^j}{2\Delta r}$$

yields:

$$\frac{T_{k+1}^j - 2T_k^j + T_{k-1}^j}{\Delta r^2} + \frac{T_{k+1}^j - T_{k-1}^j}{2r\Delta r} = -\rho_{th} w_p$$

$$\frac{2rT_{k+1}^j - 4rT_k^j + 2rT_{k-1}^j + \Delta rT_{k+1}^j - \Delta rT_{k-1}^j}{2r\Delta r^2} = -\rho_{th} w_p$$

$$2rT_{k+1}^j - 4rT_k^j + 2rT_{k-1}^j + \Delta rT_{k+1}^j - \Delta rT_{k-1}^j = -\rho_{th} w_p \, 2r\Delta r^2$$

$$(2r - \Delta r)T_{k-1}^j + (-4\mathrm{r})T_k^j + (2r + \Delta r)T_{k+1}^j = -\rho_{th} w_p \, 2r\Delta r^2$$

$$\begin{matrix} r_{in} \rightarrow \\ r_2 \rightarrow \\ \vdots \\ r_{k-1} \rightarrow \\ r_k \rightarrow \\ r_{k+1} \rightarrow \\ \vdots \\ r_{out} \rightarrow \end{matrix} \begin{bmatrix} BC & 0 & \cdots & 0 & 0 & 0 & 0 & 0 \\ 2r - \Delta r & -4\mathrm{r} & 2r + \Delta r & 0 & 0 & 0 & 0 & 0 \\ 0 & 2r - \Delta r & -4\mathrm{r} & 2r + \Delta r & 0 & 0 & 0 & 0 \\ 0 & 0 & \ddots & \ddots & \ddots & \vdots & \vdots & \vdots \\ \vdots & \vdots & \ddots & \ddots & \ddots & \vdots & \vdots & \vdots \\ \vdots & \vdots & \ddots & \ddots & 2r - \Delta r & -4r & 2r + \Delta r & 0 \\ 0 & 0 & \ddots & 0 & 0 & 2r - \Delta r & -4r & 2r + \Delta r \\ 0 & 0 & \cdots & 0 & 0 & 0 & 0 & BC \end{bmatrix} \begin{bmatrix} T_1 \\ \vdots \\ T_{k-1}^j \\ T_k^j \\ T_{k+1}^j \\ \vdots \\ T_n \end{bmatrix} = \begin{bmatrix} (B.C)_{inner} \\ \vdots \\ -\rho_{th} w_p \, 2r_{k-1}\Delta r^2 \\ -\rho_{th} w_p \, 2r_k \Delta r^2 \\ -\rho_{th} w_p \, 2r_{k+1}\Delta r^2 \\ \vdots \\ (B.C)_{outer} \end{bmatrix}$$

Boundary Conditions:

1) At the conductor

$$-T_1 + T_2 = \frac{\Delta r\ \rho_{th}\ w_c}{2\pi\ r_{in}} \tag{A1}$$

2) At the metallic sheath

$$\frac{T_{n+1} - T_n}{\Delta r} = -(W_c + W_d)\frac{\rho_{th}}{2\pi\ r_o}$$

$$T_n = T_{n+1} + (W_c + W_d)\frac{\Delta r\ \rho_{th}}{2\pi\ r_o}$$

$$T_n = \left[(W_c + W_d)(R_{T,sh} + R_{T,So})\right] + \left(W_c + W_{p,total}\right)\frac{\Delta r\ \rho_{th}}{2\pi\ r_o} \tag{A2}$$

$$\begin{matrix} r_{in} \rightarrow \\ r_2 \rightarrow \\ \vdots \\ r_{k-1} \rightarrow \\ r_k \rightarrow \\ r_{k+1} \rightarrow \\ \vdots \\ r_{out} \rightarrow \end{matrix}\begin{bmatrix} -1 & 1 & \cdots & 0 & 0 & 0 & 0 & 0 \\ 2r - \Delta r & -4\mathrm{r} & 2r + \Delta r & 0 & 0 & 0 & 0 & 0 \\ 0 & 2r - \Delta r & -4\mathrm{r} & 2r + \Delta r & 0 & 0 & 0 & 0 \\ 0 & 0 & \ddots & \ddots & \ddots & \vdots & \vdots & \vdots \\ \vdots & \vdots & \ddots & \ddots & \ddots & \vdots & \vdots & \vdots \\ \vdots & \vdots & \ddots & \ddots & 2r - \Delta r & -4r & 2r + \Delta r & 0 \\ 0 & 0 & \ddots & 0 & 0 & 2r - \Delta r & -4r & 2r + \Delta r \\ 0 & 0 & \cdots & 0 & 0 & 0 & 0 & 1 \end{bmatrix}\begin{bmatrix} T_1 \\ \vdots \\ T_{k-1}^j \\ T_k^j \\ T_{k+1}^j \\ \vdots \\ T_n \end{bmatrix} = \begin{bmatrix} eq\ (A.1) \\ \vdots \\ -\rho_{th} w_p\ 2r_{k-1}\Delta r^2 \\ -\rho_{th} w_p\ 2r_k \Delta r^2 \\ -\rho_{th} w_p\ 2r_{k+1}\Delta r^2 \\ -\rho_{th} w_p\ 2r_{k+1}\Delta r^2 \\ eq\ (A.2) \end{bmatrix}$$

Annex D: The part of the MATLAB code dedicated for the application of the matrix in Annex C:

%%The part of the MATLAB code specified for the temperature matrices illustrated in Annex C is reported here below.

```
%% calculate the temperature rise due to insulation losses:
%% generating the tri diagonal matrix “MATR2” using sparse matrix %%
MATR2 = diag ((2 * r_m (2:end)′-dr_m).* ones (nr-1,1),-1) + diag((-4 * r_m′).* ones(nr,1),0) +
diag ((2*r_m(1:end-1)′ + dr_m).* ones(nr-1,1), + 1);
MATR2 (end,1:end-1) = 0;
MATR2 (end-1,1:end-3) = 0;
MATR2 (1,3:end) = 0;
MATR2 (end,end) = 1; %Neumann BC with ghost point last point
MATR2 (1,1) = -1/dr_m; %Neumann BC first point
MATR2 (1,2) = 1/dr_m; %Neumann BC first point
%% generating the Right-Hand Side vector %%
T_tt2 (j,:) = -(Wp_Per_unit_V(j,:).* rhoTd).* (dr_m^2.* 2.* r_m); %All points
T_tt2 (j,1) = -(rhoTd.* Wc_total(1,j))./(2 *  pi * r_m(1,1)); %first point
T_tt2 (j,end) = (dr_m.* rhoTd. * (Wc_total(1,j) + Wp_tot(j,1)))/(2 * pi * r_m(1,end)) +
(thetafGt(j,end) + Wp_tot(j,1).* (RTg+RTt)); %last point
T_ttt2 = T_tt2′;
T_Losses (j,:) = MATR2\T_ttt2(:,j);
```